EXPERIMENTAL CHARACTERIZATION OF THE SEMIPERMEABLE MEMBRANE BEHAVIOUR OF PIERRE SHALE AT SOUTHERN SASKATCHEWAN

A Thesis Submitted to the College of
Graduate and Postdoctoral Studies
In Partial Fulfilment of the Requirements
For the Degree of Master of Science
In the Department of Civil, Geological and Environmental Engineering
University of Saskatchewan
Saskatoon, SK

By

Yuk Lun Yolanda Tang

PERMISSION TO USE

In presenting this thesis in partial fulfilment of the requirements for a Postgraduate degree from the University of Saskatchewan, I agree that the Libraries of this University may make it freely available for inspection. I further agree that permission for copying of this thesis in any manner, in whole or in part, for scholarly purposes may be granted by the professor or professors who supervised my thesis work or, in their absence, by the Head of the Department or the Dean of the College in which my thesis work was done. It is understood that any copying or publication or use of this thesis or parts thereof for financial gain shall not be allowed without my written permission. It is also understood that due recognition shall be given to me and to the University of Saskatchewan in any scholarly use which may be made of any material in my thesis.

DISCLAIMER

Reference in this thesis to any specific commercial products, process, or service by trade name, trademark, manufacturer, or otherwise, does not constitute or imply its endorsement, recommendation, or favouring by the University of Saskatchewan. The views and opinions of the author expressed herein do not state or reflect those of the University of Saskatchewan, and shall not be used for advertising or product endorsement purposes.

Requests for permission to copy or to make other uses of material in this thesis in whole or part should be addressed to:

Department of Civil, Geological and Environmental Engineering
University of Saskatchewan
3B48 Engineering building 57 Campus Drive
Saskatoon, Saskatchewan S7N 5A9

Alternatively, requests for permission to copy or to make other use of material in this thesis in whole or part may also be addressed to:

College of Graduate and Postdoctoral Studies
Room 116 Thorvaldsen Building, 110 Science Place
Saskatoon, Saskatchewan S7N 5E2

ABSTRACT

Chemical osmosis is a process in which fluid movement occurs through a porous media in response to a chemical concentration gradient (ΔC) within the pore fluid. The porous media acts as a semipermeable membrane that restricts solute transport while allowing pore fluid flow in response to osmotic gradients. Knowledge of the semipermeability character and the factors governing the semipermeability of a membrane is required to fully assess the impact of chemical osmosis. In this study the semipermeable membrane was a sample of Cretaceous-aged Pierre Shale collected at a depth of 121 m from Mosaic Company's K2 mine, located approximately 15 km east of the town of Esterhazy, Saskatchewan within the Williston Basin. Two approaches were used to characterize the semipermeability of the samples. The main approach was through direct measurements of osmotic pressure (ΔP, $\Delta\pi$) which could then be used to calculate the osmotic efficiency (ω). The value of ω ranges from zero (indicating no restriction to pore fluid flow) to one (indicating a perfect membrane that inhibits pore fluid flow). The second approach was through back analyses of the observed solute transport. The observed solutes were cations and anions transported in and out of the sample as a result of advection, diffusion as well as partitioning with the solid phase.

The experimental apparatus was designed to monitor the differential pressure (ΔP) in response to an applied concentration gradient within a closed testing circuit. Different values of concentration gradient were applied within three phases of testing. The concentration gradient was established across the top and bottom boundaries of the sample using synthetic fluids prepared with known concentrations. The solutions circulated along the top boundary of sample had KCl concentrations of 0 M, 0.0037 M, and 0.0082 M KCl, while the bottom boundary was maintained near a concentration of zero. Fluid samples were collected every 1.5 days. Due to solute transport, the cation and anion concentrations of the synthetic fluids were different from that of the collected samples. The chemistry of synthetic fluids and collected fluid samples were characterized using chemical testing (e.g. AAS, AES, IC, alkalinity tests).

It was observed that a 'peak' ΔP of 1.7 kPa and 1.6 kPa, as well as a 'residual' ΔP of 0.9 kPa and 1.0 kPa, developed in response to the applied concentration gradient. These correspond to the osmotic pressure differentials, based on the Van't Hoff equation, of 35 – 37 kPa and 80 – 83 kPa, respectively. The ω calculated through the comparison between the $\Delta\pi$ and the 'peak' ΔP were 0.047 and 0.020, while the ω calculated using the 'residual' ΔP were 0.025 and 0.012. These values were slightly lower than those reported by Neuzil (2000) and Garavito, Kooi, and Neuzil (2006) (0.038 – 0.14). It is expected that the slight difference in ΔP

might be due to the differences in clay composition, solute chemistry, and the cation exchange between K^+ and Na^+.

Since Cl^- was a non-reactive solute species, there was no Cl^- adsorption within the sample. All Cl^- within the sample was in pore fluid. Anion exclusion effects (Cl^- influx restrictions) were evident during chemical osmosis. Since K^+ was a reactive solute species, adsorption-desorption reactions occurred among K^+ and other major cations originally adsorbed within the sample. The influx of K^+ resulted in the desorption and the outflux of Na^+ and Ca^{2+}. The estimated values of partitioning (or distribution) coefficient (K_d) and the concomitant retardation factor (R_d) indicated a strong affinity for K^+ adsorption by the shale.

The diffusive double layer theory developed by Bresler (1973) indicates that the semipermeability of clayey materials is highly related to the electrical double layer (EDL) thickness. Bresler (1973) suggests that the ω of clayey materials is highly related to pore size and equilibrium anion concentration. Other previous researchers suggest that the semipermeability of clayey materials is highly related to pore size distribution, confining pressure, temperature, mineralogy, and pore fluid chemistry. In this study, the vertical confining stress (σ_v) was set constant at 1660 kPa during the entire chemical osmosis testing. The temperature factor affecting the fluctuation of osmotic pressure was minimized. Therefore, the most important factors that governed the ω of Pierre Shale were pore size distribution, clay mineralogy, and pore fluid chemistry.

ACKNOWLEDGEMENT

My sincere gratitude to God Almighty for giving me the strength, wisdom, and ability to achieve this feat. I would like to thank the numerous academics that helped me in various ways through my journey as a researcher. I am sincerely appreciative for all the contributions. I would like to thank my supervisor, Dr. David Elwood, for providing me with the wonderful research opportunities, for providing supports and guidance, and for nudging me towards scientific truths. My co-supervisors and committee members, Dr. Laura Smith, Dr. Lee Barbour, and Dr. Ian Fleming, for assisted in advising me and guiding me towards the success of this work. I am thankful to the University of Saskatchewan's College of Graduate Studies and Research for the scholarship and stipends. The success of this thesis has been possible by the funds provided by NSERC.

I could not have persevered through this endeavour without the support and encouragement of many people. Adam Hammerlindl, Helen Yin, the staffs in the machine shop assisted and mentored me on many occasions with great kindness. I am grateful for the many friends and memories I made in the Civil Engineering Department. I would like to thank my parents and my sister Jasmine for their support in diverse ways. I am particularly thankful for my church friends and my childhood friends Natalie, Candy and Minnie for helping me solve problems outside academia, and my peers Matthew and Shahabul for empowering me and inspiring me to move forward in this particularly long academic journey. They have been the source of motivation for the successful completion of my degree.

TABLE OF CONTENTS

LIST OF FIGURES

LIST OF TABLES

CHAPTER 1: INTRODUCTION

1.1 General Background

Chemical osmosis is a process in which fluid flow occurs in response to a chemical concentration gradient (ΔC) (Yeung & Mitchell, 1993). During chemical osmosis, solutes move from regions of higher concentrations to lower concentrations, while pore fluid move in the opposite direction in response to osmotic pressures within the fluid (Malusis, Shackelford, & Olsen, 2003). This transient process continues until the ΔC no longer exists.

The chemical osmosis behaviour through a membrane is highly related to the semipermeability of the membrane. A semipermeable membrane restricts solute transportation while allowing pore fluid flow during chemical osmosis (Malusis, Shackelford, & Olsen, 2001; Shackelford & Lee, 2003). If the movement of fluid is restricted as a result of the low hydraulic conductivity (K) of the porous media, a differential pressure (ΔP) can develop across the media resulting in what has been described as pore pressure anomalies within the geologic unit (Fritz, 1986; Neuzil, 2000). Therefore, a semipermeable membrane can be characterized by both the pressure anomalies and the solute transport behaviour.

The study of shale acting as a semipermeable membrane is relatively recent. Neuzil (2000) first suggests the potential of low K shales to act as semipermeable membranes after observing pore pressure anomalies in the Pierre Shale in the Williston Basin. Neuzil and Provost (2009) suggest that pore pressure anomalies are common in the semipermeable argillaceous formations hydraulically isolated by low hydraulic conductivity barriers. Numerous studies have also focused on chemical osmosis in various clay-rich formations, such as Opalinus clay (Horseman, Harrington, & Noy, 2007), Callovo-Oxfordian argillite (Rousseau-Gueutin, Gonçalvès, & Violette, 2008; Rousseau-Gueutin, de Greef, & Gonçalvès, 2009), and Wakkanai mudstones (Takeda, Hiratsuka, Manaka, Finsterle, & Ito, 2014).

Mosaic's K1 and K2 mines at Esterhazy in southern Saskatchewan comprise one of the largest potash production facilities in the world. According to Hatch (2018), Mosaic's K1 and K2 mine expansion project has increased the annual production capacity to 2.7 million tons in 2012, 3.3 million tons from 2013 to 2017, and 4.4 million tons in 2018. According to Baird (2017), the construction of a shaft at Mosaic's K3 potash mine is ongoing. The K3 shaft will make Esterhazy the largest underground potash mine in the world, with an annual production capacity of 21 million tons by 2024. The expansion of K1 and K2 has resulted in an increased output of tailings to the Tailings Management Area (TMA). Since increasing tailings output is

expected due to the expansion of K3 shaft, it is expected that more TMA capacity is required to store the increasing volume of tailings output. Due to the minimal fracturing and the low K of the Pierre Shale at Esterhazy, the release of contaminants from the TMA is expected to be limited to diffusion dominated transport with further attenuation due to the inward migration of fluid as a result of chemical osmosis. Therefore, it is beneficial to understand the chemical osmosis mechanism and to study the effectiveness of the Pierre Shale at Esterhazy to act as a semipermeable membrane and restrict solute transport.

For the purpose of this research, the ability of the Pierre Shale to act as a semipermeable membrane will be studied in a laboratory scale experiment using core obtained near the Mosaic's Esterhazy K2 Potash Mine in southern Saskatchewan (Figure 1.1). The Pierre Shale core will be characterized following three methods using pressure anomalies (Fritz, 1986), solute transport (Malusis *et al.*, 2001), and double diffuse layer behaviour (Bresler, 1973).

Figure 1.1. The location of Esterhazy (star) in southern Saskatchewan

Fritz (1986) observed that chemical osmosis induces a differential pressure across a semipermeable membrane (ΔP), and derived a method to approximate the theoretical osmotic pressure ($\Delta\pi$) across semipermeable membrane using the Van't Hoff equation. Fritz and Marine (1983) suggests that the osmotic efficiency (ω), which indicates the ideality of a semipermeable membrane, can be approximated using the ratio of ΔP to $\Delta\pi$. A ω of a semipermeable membrane can range from zero to one. This method has been followed by many researchers, including Yeung and Mitchell (1993), Cey, Barbour, and Hendry (2001),

Neuzil (2000), Malusis *et al.* (2001), Shackelford and Lee (2003), Neuzil and Provost (2009), Takeda *et al.* (2014).

Malusis *et al.* (2001) designed a chemical osmotic / diffusion system to study the transport of KCl through geosynthetic clay liner. Since the geosynthetic clay liner is a low permeability clay-rich membrane, solutes are mainly transported by diffusion (Malusis *et al.*, 2003). However, if osmotic flow develops in response to osmotic gradients, an additional restriction to diffusive transport can occur in a semipermeable membrane (Malusis *et al.*, 2001).

The diffusive double layer theory developed by Bresler (1973) indicates that the semipermeability of clayey materials is highly related to the electrical double layer (EDL) thickness. According to Berner (1971), the EDL is formed due to the electrical charge on the surface of clay particle when imperfections or substitutions occur within the clay crystal structure. The electrical charge is balanced by an excess concentration of opposite-charged ions (cations) from the surrounding solution. Specifically, the EDL around the clay particles consists of the negatively charged clay surface (fixed layer) and the balancing cations (mobile layer). If the pores sizes stay constant, the mobile layer of the EDL is more likely to overlap, leading to a more severe solute transport restriction. The diffusive double layer theory is a theory that explains the distribution of balancing cations in the mobile layer. The theory suggests that the diffusive double layer consists of the stern layer and the diffuse layer. The stern layer is a compacted layer that contains highly concentrated cations to balance the negative charge at the clay surface. The diffuse layer is a layer in which the number of cations exceeds the number of anions to balance the remaining negative charge.

The diffusive double layer theory has been widely used by many researchers to characterize the membrane characteristics of clay soils and clay-rich formations (Barbour & Fredlund, 1989; Neuzil, 2000; Cey *et al.*, 2001; Rahman, Chen, & Rahman, 2005; Al-Bazali, Zhang, Atlas, Chenevert, & Sharma, 2006; Gonçalvès, Rousseau-Gueutin, & Revil, 2007; Rousseau-Gueutin *et al.*, 2008; Neuzil & Provost, 2009; Rousseau-Gueutin *et al.*, 2009; Takeda *et al.*, 2014). The Bresler (1973) model suggests that the ω of clayey materials is highly related to pore size and equilibrium anion concentration. The later studies further suggest that the ω of clayey materials is influenced by the pore size distribution, confining pressure (σ_v), temperature, mineralogy, and pore fluid chemistry. In addition to the ω of clayey materials, pore fluid chemistry also affects the volume of clay-rich sample through osmotic swelling and osmotic consolidation.

This study differs from previous work due to the nature of the semi-permeable membrane being tested. before. Most previous work was conducted using geosynthetic clays such as bentonite and reconstituted shale for the purposes of characterizing geosynthetic liners (i.e. Kemper & Rollins, 1966; Fritz & Marine, 1983; Keijzer, Kleingeld, & Loch, 1999; Malusis *et al.*, 2001). In this study, the core sample was obtained from in-situ and altered as little as possible during collection. The results of this study can inform further work on how well natural clay-rich aquitards act as semi-permeable membranes and implications it may have towards relying on these formations as confining layers for deep geological repositories or protective layers for adjacent freshwater aquifers.

1.2 Study Objectives

The goal of this research is to characterize the semipermeability of the Pierre Shale in southern Saskatchewan using core obtained near the Mosaic's Esterhazy K2 Potash Mine and understand the factors that govern the observed semipermeability. The specific objectives are as follows:

1. Measure the differential pressure across the shale sample in response to a range of applied concentration differentials (ΔC);
2. Measure the solute transport within the shale sample to establish the osmotic efficiency (ω) through interpretation of the observed solute transport.

1.3 Thesis Layout

The thesis outline is as follow:

- Literature review (Chapter 2) - a summary of relevant literature with a focus on the osmotic pressure and efficiency, the solute transport mechanism, the double diffusive theory, the factors that affect the semipermeability of clay-rich material, the osmotic swelling and consolidation, and previous research findings related to the osmotic efficiencies of Pierre Shale
- Study site description (Chapter 3) - a description of the study site, the physical and electrochemical properties of Pierre Shale, and the actual Pierre Shale sample used for the chemical osmosis testing
- Methodology (Chapter 4) - a description of the shale sample and synthetic fluids preparation, the chemical osmosis circulation system, the osmotic pressure and osmotic

efficiency approximation, the series of chemical laboratory tests and numerical analyses for understanding the solute transport mechanism

- Presentation of Data (Chapter 5) - a synthesis of data collected from the chemical osmosis circulation system and the series of chemical laboratory tests, the approximated osmotic pressure and efficiency, also the results from the solute transport numerical analyses
- Discussion (Chapter 6) - a discussion to explain the evidences that supported the Pierre Shale as an efficient semipermeable membrane, as well as the important factors and processes that controlled the osmotic efficiencies of Pierre Shale during the chemical osmosis testing
- Conclusions and Recommendations (Chapter 7)

CHAPTER 2: LITERATURE REVIEW

2.1 Introduction

This chapter summaries the relevant literature describing the factors and processes controlling chemical osmosis in a semipermeable, unfractured, low-permeability clay-rich formation, as well as the descriptions of commonly used test methods to characterize the semipermeability (Section 2.2). Solute transport behavior in a unfractured, low-permeability clay-rich formation is discussed in Section 2.3. The colloid chemistry, specifically the electrical double layers in clay-rich material and its impact on pore fluid flow and solute transport, is discussed in Section 2.4. The factors affecting the semipermeability of clay-rich materials is discussed in Section 2.5. The mechanisms of osmotic swelling, osmotic consolidation, and osmotic induced consolidation is discussed in Section 2.6. Previous research findings related to the osmotic efficiencies of Cretaceous-aged Pierre Shale (Bearpaw Formation) is provided in Section 2.7.

2.2 Parameters for Membrane Characteristics Approximation

2.2.1 Osmotic Pressure

Osmotic pressure ($\Delta\pi$) is a measure of the chemical potential difference across a semipermeable membrane due to the difference in solute concentration (Fritz, 1986). The induced osmotic pressure (ΔP) is the fluid pressure that develops within a formation in response to $\Delta\pi$ if fluid flow is restricted (Figure 2.1). The maximum value of ΔP that can develop across a perfect semipermeable membrane is equal to $\Delta\pi$ (Fritz, 1986). The observable differential pressure (ΔP) across the semipermeable membrane induced by osmotic flow is generally less than $\Delta\pi$, unless the semipermeable membrane is a perfect membrane (Fritz, 1986). ΔP is determined by measuring the difference in pore pressure on either side of the membrane, and is subjected to change according to the physical properties of shale and electrochemical properties of pore fluid.

During chemical osmosis, pore fluid will flow from a reservoir of lower concentration towards a reservoir with higher concentrations in response to the osmotic pressure gradient (Malusis *et al.*, 2003). Many researchers suggest ΔP is induced by the semipermeability of nanoscale pores (Fritz & Marine, 1983; Fritz, 1986; Neuzil, 2000; Neuzil & Provost, 2009; Takeda *et al.*, 2014). If the sample is not a perfect semipermeable membrane, ongoing

diffusion of chemical constituents will occur across the semipermeable membrane resulting in a gradual dissipation the concentration gradient and the induced pressure head. At the same time, an advective water counter-flow may occur across the membrane which acts to dissipate the induced gradient in pressure. The pore-size diameter generally associated with this water flow are 20 – 30 nm (Takeda *et al.*, 2014).

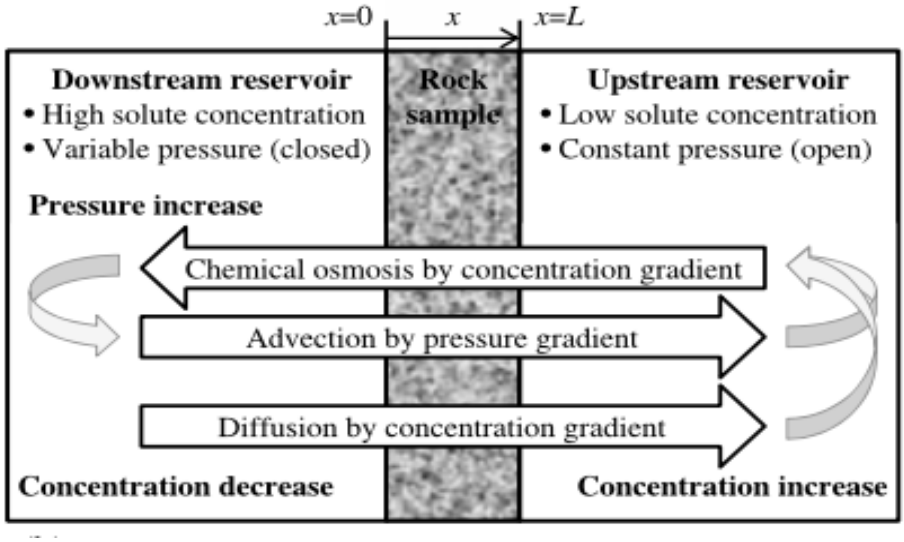

Figure 2.1. The conceptual model for chemical osmosis (Takeda *et al.*, 2014)

2.2.1.1 Osmotic Pressure Calculation

The theoretical value of $\Delta\pi$ is approximated using Eq. 2.1 (Fritz & Marine, 1983).

$$\Delta\pi = \nu RT\Delta C \qquad \text{(Eq. 2.1)}$$

where $\Delta\pi$ is the theoretical osmotic pressure across semipermeable membrane (kPa), ν is the number of ions per molecule of salt (i.e. $\nu = 2$ for KCl), R is the gas constant (0.0083145 $m^3 \cdot kPa \cdot mol^{-1} \cdot K^{-1}$), T is the surrounding temperature (degrees K), and ΔC is the concentration gradient across the semipermeable membrane ($mol \cdot m^{-3}$).

2.2.2 Osmotic Efficiency

Osmotic efficiency (ω) is an indicator of the ideality of a semipermeable membrane, and measures the ability of a membrane to restrict pore fluid flow relative to water (Fritz, 1986). The value of ω ranges from zero (indicating no restriction to pore fluid flow) to one (indicating a perfect membrane that inhibits pore fluid flow) (Fritz, 1986). The theoretical model of ω was developed by Kemper and Rollins (1966) and modified by Bresler (1973). Kemper and Rollins

(1966) first recognized the existence of osmotic gradients in soil and clays, and suggest the osmotic gradient is usually attributed to the anion exclusions from negatively charged soil pores acting as a semipermeable membrane. Based on this finding, Kemper and Rollins (1966) expressed ω as a function of anion concentration in the solution (c) and volumetric water content (θ), using Eq. 2.2.

$$\omega(\theta, c) = \frac{\int_b (1-c'(y)/c)(2by-y^2)dy}{\int_b (2by-y^2)dy} \qquad \text{(Eq. 2.2)}$$

where ω (dimensionless), 2b is the average effective thickness of the films (Angstroms, Å, equivalent to 10^{-10} m), c'(y) is the anion concentration at distance y (normality, N, eq/L), c is the anion concentration in the solution (normality, N, eq/L); the term $[1- c'(y)/c]$ is the salt exclusion factor at distance y.

Bresler (1973) followed the expression developed by Kemper and Rollins (1966), reduced the two independent variables θ and c into a single variable $b\sqrt{c}$, and developed a functional relationship between ω and $b\sqrt{c}$ for monovalent cation (Na^+) and divalent cation (Ca^{2+}) (Figure 2.2).

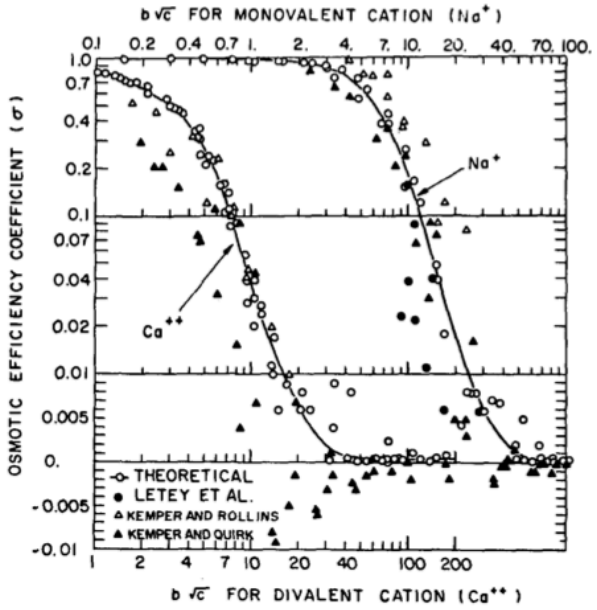

Figure 2.2. Osmotic efficiency (ω) as a function of pore size and equilibrium anion concentration for monovalent and divalent cation (Na^+ and Ca^{2+} respectively). The solid lines represent the best fit lines for a range of c between 0.001 and 2 N and for b greater than 5 Å. Note that in y-axis log scale is changed to linear scale at ω less than 0.01 (Bresler, 1973)

Many researchers have used ω determined from laboratory tests to characterize the osmotic properties of clay-rich materials, such as refined clays (Marine & Fritz, 1981; Fritz & Marine, 1983), geosynthetic liner materials (Malusis *et al.*, 2001), natural clay-rich formations (Rahman *et al.*, 2005), Opalinus clay (Horseman *et al.*, 2007), and Wakkanai mudstones (Takeda *et al.*, 2014).

In the Marine and Fritz (1981) research, ω is determined based on the premise that under steady state conditions, thermodynamic forces acting across the membrane are counterbalanced by the sum of mechanical frictional forces acting on the solution within the membrane. In this approach, ω is related to the physical membrane and the chemical properties of pore fluid (i.e. membrane porosity, cation exchange capacity of the membrane matrix, and the solute concentration of pore fluid) (Eq. 2.3).

$$\omega = 1 - \frac{(R_w+1)K_s}{\{\left[R_w\left(\frac{\bar{C}_a}{\bar{C}_c}\right)+1\right]+R_{wm}\left[R_m\left(\frac{\bar{C}_a}{\bar{C}_c}\right)+1\right]\}\theta} \qquad \text{(Eq. 2.3)}$$

where ω (dimensionless), θ is the water content of membrane (dimensionless), (R_w, R_{wm}, R_m) are the frictional coefficients (dimensionless), K_s is the distribution coefficient of the solute in the membrane (dimensionless), $\bar{C}_a$ is the concentration of the anion in the membrane pores (mole · cm^{-3}), $\bar{C}_c$ is the concentration of the cation in the membrane pores (mole · cm^{-3}).

Although the method described above can be used to determine ω, it is not the most common method. The determination of ω commonly relies on two approaches that are derived from the expression of pore fluid flow in clays, described by a generalized version of Darcy's law (Eq. 2.4) (Neuzil & Provost, 2009).

$$q = -\frac{k}{\mu}(\rho g \Delta z + \Delta P) + \omega\frac{k}{\mu}\Delta\pi \qquad \text{(Eq. 2.4)}$$

where q is the Darcy flux of pore fluid ($m^3 \cdot m^{-2} \cdot s^{-1}$), k is the intrinsic permeability of the medium (m^2), μ is the fluid dynamic viscosity (Pa · s), ΔP is the observable osmotic pressure (Pa), ρ is the pore fluid density (kg · m^{-3}), g is the gravitational acceleration (m · s^{-2}), Δz is the elevation gradient (m), ω is the osmotic efficiency (dimensionless), Δπ is the theoretical osmotic pressure (Pa).

The first approach is to place a sample between two reservoirs containing different solute concentrations, allow the pore fluid to flow in one direction, and monitor the osmotic differential pressure (ΔP) across the sample. When only the equilibrium ΔP is considered, the

approach is called an "equilibrium pressure" test. When the build-up of ΔP is also considered, the approach is called a "transient pressure" test. This approach is first suggested by Fritz and Marine (1983), and followed by many researchers such as Malusis *et al.* (2001), Al-Bazali (2005), Horseman *et al.* (2007) and Takeda *et al.* (2014). In this approach, the Δz is negligible. When the dynamic equilibrium is achieved (q = 0), the pressure applied to the higher-concentration reservoir is counterbalanced by the effective osmotic pressure acting in the opposite side (Fritz, 1986). Therefore, ΔP will become stable and the generalized Darcy flux expression (Eq. 2.2) can be applied to calculate ω using Eq. 2.5.

$$\omega = \Delta P/\Delta\pi \qquad \text{(Eq. 2.5)}$$

where ω (dimensionless), ΔP (Pa), and Δπ (Pa).

The second approach is to maintain both a higher concentration reservoir and a lower concentration reservoir at equal pressure, and monitor the fluid flux (q) after it has reached a steady state. The approach is called the "transient flow" test and is followed by researchers such as Cey *et al.* (2001). In this approach, the ΔP is zero. The μ, k, and ω are assumed to be constant, so Δπ across the sample must also be constant. By integrating and manipulating Eq. 2.4, ω can be calculated using Eq. 2.6.

$$\omega = (q\mu L/k\Delta\pi) \qquad \text{(Eq. 2.6)}$$

where ω (dimensionless), q ($m^3 \cdot m^{-2} \cdot s^{-1}$), μ ($Pa \cdot s$), L is the sample length (m), k (m^2), Δπ (Pa)

Neuzil and Provost (2009) suggest that these two approaches assume ω is constant across the sample. However, ω will generally vary spatially in the membrane because osmosis only occurs when there is a concentration gradient in the membrane. Therefore, the ω calculated using Eq. 2.5 and Eq. 2.6 are actually apparent values that lie in between the maximum ω and the minimum ω during the experiment.

Neuzil and Provost (2009) suggest a third approach, that accounts for the strong dependence of ω on solute concentrations, can be used to determine ω. This method is particularly useful when the extremes of solute concentration in the membrane (C_{min} and C_{max}) differentiate significantly. In this approach, the sample is placed between reservoirs with different solute concentrations. The sample-reservoir boundaries are set as $x = x_1, x_2$. When

the dynamic equilibrium is reached (q = 0), the integration of Eq. 2.4 between x_1 and x_2 with a concentration-dependent ω yields Eq. 2.7, and subsequently yields Eq. 2.8.

$$\int_{x_1}^{x_2} \frac{dP}{dx} dx = \int_{x_1}^{x_2} \omega(C) \frac{d\pi}{dx} dx \quad \text{(Eq. 2.7)}$$

$$\Delta P = \int_{C_{max}}^{C_{min}} \omega(C) \frac{d\pi}{dC} dC \quad \text{(Eq. 2.8)}$$

where ΔP (Pa), ω (dimensionless), dP/dx is the gradient of actual osmotic pressure across specific distance of the membrane (Pa), $d\pi/dx$ is the gradient of theoretical osmotic pressure across specific distance of the membrane (Pa), $d\pi/dC$ is the change of theoretical osmotic pressure with respect to the solute concentration, x_1, x_2 are the distances of membrane boundaries from datum (m), C_{min} and C_{max} are the extremes of solute concentration in the membrane ($mol \cdot m^{-3}$).

Besides laboratory tests, the ω of clay-rich materials can be determined through in-situ tests. The in-situ tests are usually done by adding solutions with known concentrations to capped boreholes (or the borehole sections sealed by packers), and monitoring the change of fluid pressures (or water levels) until the osmotic flow reaches dynamic equilibrium (q = 0). In some studies, such as the one conducted by Neuzil (2000), pore fluids are also collected to monitor the change of solute concentrations over time. In-situ tests are mainly conducted in natural clay-rich formations such as Pierre Shale (Neuzil, 2000), Opalinus Clay (Noy, Horseman, Harrington, Bossart, & Fis, 2004), and Boom Clay (Garavito, de Cannière, & Kooi, 2007). Due to the low K's of clay-rich formations, monitoring time frames are usually very long (9 years for the Neuzil (2000) research and 2 years in each stage (a total of 3 stages) for the Noy *et al.* (2004) research).

Using the results collected from laboratory and in-situ tests, ω can be determined in numerical models. For example, in the numerical model developed by Garavito *et al.* (2006), ω was determined based on the fluid pressures and the solute concentrations collected from the in-situ osmosis experiment in the Pierre Shale, south Dakota (Neuzil, 2000).

2.3 Solute Transport

2.3.1 The Overview of solute transport mechanism

The solute concentrations in groundwater are primarily governed by the amount of solute present at the source, the rate of release from the source, the hydrologic factors

(including dispersion, advection, and diffusion), and the geochemical processes (including aqueous geochemical processes, such as adsorption / desorption, precipitation, and dissolution) (Krupka, Kaplan, Whelan, Serne, & Mattigod, 1999).

Hydraulic fluxes are characterized by dispersive flux, advective flux, and diffusive flux. Dispersive flux addresses the effects of departure of individual particle velocities from the average seepage velocity (Zheng & Bennett, 2002). When dispersion happens, the solute concentration decreases but the solutes spreads to an increasingly larger area. Dispersive flux is generally described in two components : a longitudinal component in the direction of the flow, and a transverse component normal to the flow (Figure 2.3). Longitudinal dispersive flux (J_{DisL}) and transverse dispersive flux (J_{DisT}) can be expressed through Eq.2.9 and Eq. 2.10.

$$J_{DisL} = -D_L \frac{dC}{dx} \quad \text{(Eq. 2.9)}$$

$$J_{DisT} = -D_T \frac{dC}{dx} \quad \text{(Eq. 2.10)}$$

where J_{DisL} ($kg \cdot m^{-2} \cdot s^{-1}$), J_{DisT} ($kg \cdot m^{-2} \cdot s^{-1}$), D_L is the longitudinal dispersion coefficient ($m^2 \cdot s^{-1}$), D_T is the transverse dispersion coefficient ($m^2 \cdot s^{-1}$), dC/dx is the concentration gradient across the membrane ($kg \cdot m^{-3} \cdot m^{-1}$).

D_L and D_T can be expressed respectively through Eq.2.11 and Eq. 2.12.

$$D_L = \alpha_L \nu \quad \text{(Eq. 2.11)}$$

$$D_T = \alpha_T \nu \quad \text{(Eq. 2.12)}$$

where D_L ($m^2 \cdot s^{-1}$), D_T ($m^2 \cdot s^{-1}$), α_L is the longitudinal dispersity (m), α_T is the transverse dispersity (m), ν is the average seepage velocity.

α_L governs the spreading of solutes in the flow of direction, and affects only a small degree to the spreading of a continuous source leaching into an aquifer. The effect of α_L is crucial in order to describe the first arrival or the breakthrough of solutes. α_T governs the spreading of a continuous source leaching into an aquifer.

In laboratory experiments, the α is determined by the microscopic factors of a granular porous medium. In microscopic scale, the seepage velocity within an individual pore vary from a maximum along the centerline of the pore to essentially zero along the pore walls. On a slightly larger scale, the seepage velocities in an assemblage of pores vary in direction from one point to another because of the microscopic heterogeneity and tortuosity associated with

the pore structure. The disparity caused by pore-scale heterogeneity is generally very limited. α_L in the range of 0.01 – 1 cm are not uncommon. However, in field situations, the disparity is usually more pronounced. α_L are typically two to four orders because the dispersion is primarily affected by macroscopic heterogeneities characterized by hydraulic conductivity and porosity, while α_T is hardly affected by the heterogeneity of the aquifer. Depending on the spatial distribution of macroscopic heterogeneities, flow may tend to concentrate along pathways of higher conductivity, to diverge around areas of low conductivity, and to be refracted at conductivity boundaries.

Both advective flux and diffusive flux are fluxes that advance the solutes at the average seepage velocity (Figure 2.3) (Zheng & Bennett, 2002). Advective flux is predominant in high-permeability zones and diffusive flux is predominant in low-permeability zones. Advective - diffusive models represent a special case in which the transport regime is separated into local zones dominated by either advection or molecular diffusion due to macroscopic heterogeneities. In a fractured bedrock system, advective transport may dominate within the fracture network, while molecular diffusion may dominate in the matrix blocks between fractures.

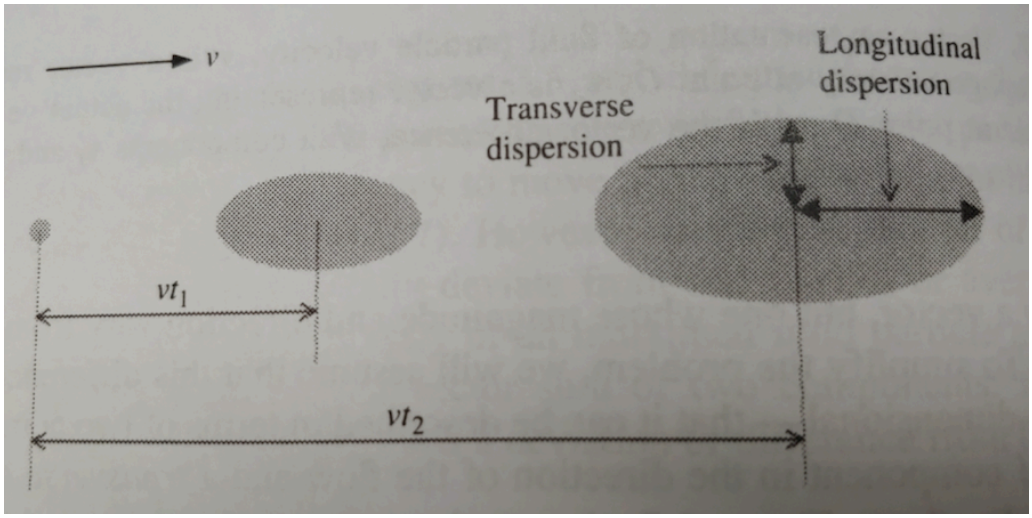

Figure 2.3. Solute transport as the result of advective flux and dispersive flux. The advective flux advances the solutes at the average seepage velocity (v), and the dispersive flux causes the solutes to spread out in both longitudinal and transverse directions (Zheng & Bennett, 2002).

In unfractured, low-permeability clay-rich formations, both dispersive flux and advective flux are negligible. Diffusive flux is the predominant solute transport mechanism. Advective flux becomes more significant in the system when advective water counter-flow occurs. The pore-sizes generally associated with this water flow are 20 – 30 nm diameter (Takeda *et al.*, 2014).

2.3.2 Diffusion Mechanism

In unfractured, low-permeability clay-rich formations, diffusion is the predominant mechanism of solute transport. Shackelford and Daniel (1991) studied the diffusion of inorganic chemicals in saturated soil, and suggest that the steady-state solute diffusion in response to a concentration gradient (ΔC) is governed by the Fick's first law as expressed through Eq. 2.13 and Eq. 2.14.

$$J_D = -D_0 \alpha \gamma \tau \theta \frac{dC}{dx} \quad \text{(Eq. 2.13)}$$

$$J_D = -D^* \frac{dC}{dx} \quad \text{(Eq. 2.14)}$$

where J_D is the diffusive mass flux ($kg \cdot m^{-2} \cdot s^{-1}$), D_0 is the free-solution diffusion coefficient of chemical species ($m^2 \cdot s^{-1}$), D^* is the coefficient of molecular diffusion ($m^2 \cdot s^{-1}$), τ is the tortuosity factor (dimensionless), α is the viscosity factor (dimensionless), γ is the anion exclusion factor (dimensionless), θ is the volumetric water content (dimensionless), dC/dx is the concentration gradient across the membrane ($kg \cdot m^{-3} \cdot m^{-1}$).

Solute diffusion is controlled by the effective porosity (n_e) instead of the total porosity (n_t). n_e only considers the pores that allow solute diffusion, and excludes isolated pores, pores restricting solute diffusion, and pores occupied by the water adsorbed on clay minerals.

D_0 only represents the maximum values attainable for an individual chemical species in free solution under ideal conditions. The coefficient of molecular diffusion (D^*) is different from D_0. The difference between D^* and D_0 is due to the tortuosity factor (τ), the viscosity factor (α), the anion exclusion factor (γ), and the saturation of soils. τ accounts for the tortuous flow paths around the solid particles that occupy some cross-sectional area of the soil. The flow paths tend to be more tortuous when the n_e is reduced. α accounts for the increased viscosity of water adjacent to the clay mineral surfaces. γ accounts for the restriction of solute diffusion due to anion exclusion. Anion exclusion is favoured by dilute external water (low m_{Cl^-}) and / or high concentration of negatively charged clay sites (high $\bar{m}_{Clay^-}$) brought by high clay content, high compaction, or high charge on clay. Anion exclusion should occur when the average porosity of soil is about 0.3 (lower values for pure illite and kaolinite; higher values for smectite) (Berner, 1971). The saturation of soils accounts for the restriction of solute diffusion due to the gas in porous media. Flow paths are much more tortuous in unsaturated soil, since diffusion cannot go through the gas in porous media. Diffusion is the fastest when

the soil is saturated ($\theta = n_t$). According to Shackelford and Daniel (1991), it is difficult to quantify and separate the effects of τ, α, and γ in most soil diffusion studies. It is because τ, α, and γ are mainly controlled by the pore properties (e.g. porosity, pore type, pore structure) of the membrane. These pore properties are difficult to be monitored without ultrasonic wave (e.g. x-ray CT scanning). The expression of D^* can be described through Eq. 2.15.

$$D^* = D_0 \alpha \gamma \tau \theta \qquad \text{(Eq. 2.15)}$$

Although Fick's first law is useful in steady-state diffusive system, it may not be useful in cases where the composition at a particular position of a system changes with time. A new relation is required to relate time along with concentration and position. Fick's second law is derived from the conservation of mass and the Fick's first law, in absence of any chemical reactions, for transient-state diffusive system. Fick's second law states that the rate of accumulation of concentration (dC/dt) is proportional to the local curvature of concentration gradient (d^2C/dx^2). D^* is the proportionality constant. Fick's second law can be expressed through Eq. 2.16.

$$\frac{dC}{dt} = \left(D^* \frac{dC}{dx}\right) \frac{d}{dx} \qquad \text{(Eq. 2.16)}$$

where dC/dt is the rate of accumulation (or depletion) of concentration within the membrane ($kg \cdot m^{-3} \cdot s^{-1}$), D^* ($m^2 \cdot s^{-1}$), d^2C/dx^2 is the local curvature of concentration gradient ($kg \cdot m^{-3} \cdot m^{-2}$).

2.3.3 The Classification of Solute Species

Solutes can be classified as nonreactive species and reactive species. Nonreactive (or conservative) solutes are those that remain in the fluid phase without any losses or gains to the fluid phase from chemical reactions or partitioning to the solid phase (e.g. adsorption). Chemical and / or physical reactions include adsorption-desorption reactions, radioactive decay, dissolution, oxidation-reduction, and ion pairing. An example of nonreactive species would be chloride (Cl^-). Reactive solutes are those that are subject to chemical and / or physical reactions, with part of the solutes in the fluid phase partitioned to the solid phase (e.g. adsorption). An example of reactive species would be potassium (K^+) (Shackelford & Daniel, 1991).

2.3.4 Partitioning

Partitioning in saturated flow is a process that separates the solutes between the fluid and solid phases (Krupka *et al.*, 1999). An adsorption isotherm describes the relationship between the quantity of solutes retained in pore fluids and adsorbed on soil particles. Different adsorbate-adsorbent pairs have different isotherms. The most common ones are favourable adsorption, linear adsorption, and unfavourable adsorption (Figure 2.4) (Weber, McGinley, & Katz, 1991). In a linear isotherm sorption model, the quantity of solutes adsorbed on the soil particles (S) has a directly proportional relationship with the quantity of solutes retained in pore fluids (C), at a fixed temperature, under chemical equilibrium conditions (Bear and Cheng, 2010). In adsorption, any increase in the quantity of solutes retained in the pore fluids is associated with an appropriate increase in the quantity of solutes adsorbed on the soil particles. In desorption, the decrease in the quantity of solutes adsorbed on the soil particles is associated with the appropriate decrease in the quantity of solutes retained in the pore fluids. The linear isotherm is appropriate for describing adsorption most commonly at very low solute concentrations and for soil particles with low sorption potential (Weber *et al.*, 1991).

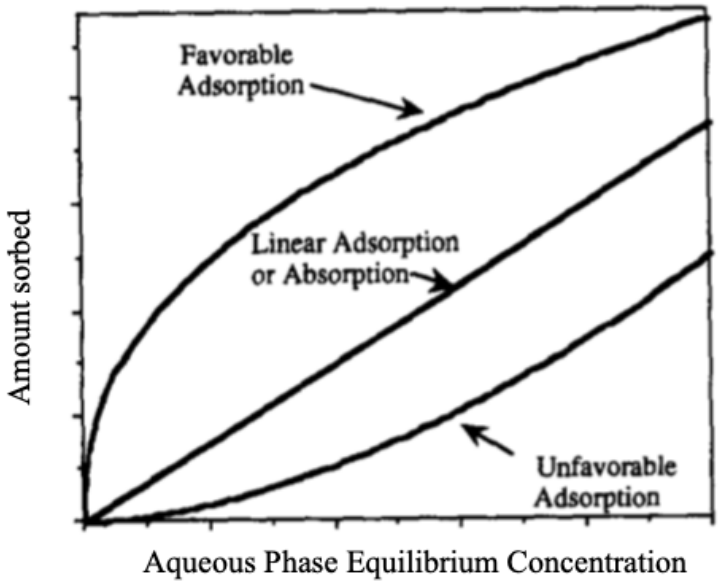

Figure 2.4. The most common adsorption isotherm models (Weber *et al*., 1991)

2.3.5 Adsorption-Desorption Reactions

The important geochemical processes affecting partitioning include adsorption / desorption, precipitation, and dissolution. Dissolution / precipitation is more likely to be the key process where chemical non-equilibrium exists, such as areas near to the point source

where high solute concentrations exist, or where steep pH or oxidation-reduction gradients exist. Adsorption / desorption is more likely to be the key process in areas where chemical steady state exists, such as in areas far from the point source (Krupka *et al.*, 1999).

Adsorption-desorption reactions are an exchange of solute mass between the mobile fluid and the immobile regions that exist in the porous medium (Brusseau & Rao, 1989; Mojid & Vereecken, 2005; Sardin, Schweich, Leij, & van Genuchten, 1991). Cation exchange is the dominant type of adsorption-desorption reactions during chemical osmosis. According to Langmuir (1997) and Mitchell and Soga (2005), cation exchange normally occurs in three mechanisms. The first mechanism, also the primary mechanism, occurs when cations with higher valence replace cations with lower valence. Cations with valence of +2, such as calcium (Ca^{2+}) and magnesium (Mg^{2+}), can replace cations with valence of +1, such as potassium (K^{+}) and sodium (Na^{+}). The second mechanism occurs when cations with larger dehydrated radii (smaller hydrated radius) replace cations with smaller dehydrated radii (larger hydrated radius). Although both K^{+} and Na^{+} have a valence of +1, K^{+} can replace Na^{+} because the dehydrated diameter of K^{+} is larger than Na^{+} (Table 2.1). The third mechanism occurs when higher concentrated cations replace lower concentrated cations. Monovalent cations, such as K^{+} and Na^{+}, can replace divalent cations, such as Ca^{2+} and Mg^{2+}, when the concentrations of monovalent cations are significantly higher.

Table 2.1. The dehydrated and hydrated diameters of major cations in pore fluid (Al-Bazali *et al.*, 2006)

	Dehydrated Diameter (Angstrom)	**Hydrated Diameter (Angstrom)**	**Average Hydrated Diameter (Angstrom)**
Sodium (Na^{+})	1.9	5.5 – 11.2	8.35
Potassium (K^{+})	2.66	4.64 – 7.6	6.12
Cesium (Cs^{+})	3.34	4.6 – 7.2	5.9
Magnesium (Mg^{2+})	1.3	21.6	21.6
Calcium (Ca^{2+})	1.9	19	19

2.3.6 Partition Coefficient and Retardation Factor

The partitioning (or distribution) coefficient (K_d) is an important parameter used in estimating the migration potential of solutes present in pore fluids in contact with surface, subsurface, and suspended solids (Krupka *et al.*, 1999). A few assumptions are made in the K_d

construction in a linear isotherm sorption model. First, only trace amount of solutes exist in the fluid and solid phases. Second, the relationship between the amount of solutes in the fluid and solid phases is linear. Third, equilibrium conditions exist. Fourth, the kinetics of adsorption and desorption are equally rapid. Fifth, K_d describes the solute partitioning between one sorbate (pore fluids) and one sorbent (soil particles). Sixth, all adsorption sites in soil are accessible and have equal strengths. Last, the K_d measured in the laboratory tests is only applicable to predict solute transport in chemically identical systems (Krupka *et al.*, 1999).

According to Section 2.3.4, for the linear isotherm sorption model, K_d in saturated flow can be defined using the ratio between the quantity of solutes adsorbed on the soil particles (S) and the quantity of solutes retained in pore fluids (C), using Eq. 2.17.

$$K_d = S/C \qquad \text{(Eq. 2.17)}$$

where K_d ($L \cdot g^{-1}$), S ($mg \cdot g^{-1}$), C ($mg \cdot L^{-1}$).

Retardation factor (R_d) is a coefficient that expresses the partitioning of solutes within a unit volume of porous medium (Bear & Cheng, 2010). For the linear isotherm sorption model, R_d is related to K_d through Eq. 2.18.

$$R_d = 1 + \frac{\rho_b K_d}{n} \qquad \text{(Eq. 2.18)}$$

where R_d (dimensionless), ρ_b is the bulk density of soil ($g \cdot L^{-1}$), K_d ($L \cdot g^{-1}$), n is the porosity (dimensionless).

2.3.7 The Relationship between Pore Fluid Flow and Solute Transport

During chemical osmosis, pore fluid flow and solute transport occur in opposite directions (Malusis *et al.*, 2003). ω represents the ability of a membrane to restrict pore fluid flow relative to water, and the reflection coefficient (Γ) represents the ability of a membrane to restrict solute transport (Fritz & Marine, 1983). Solute transport and pore fluid flow have to occur at the same speed to maintain electroneutrality during chemical osmosis (Shackelford & Daniel, 1991). Any restriction of solute transport results in the restriction of pore fluid flow at the same magnitude. Therefore, ω has a 1 : 1 relationship with Γ (i.e. semipermeable membrane with the $\omega = 0.8$ has the $\Gamma = 0.8$).

2.4 Colloid Chemistry

2.4.1 Electrical Double Layer

Electrical double layer (EDL) is a fundamental theory applicable to colloid chemistry of sediment particles. An EDL exists at the surface of clay particle when the clay particle is suspended in an electrolyte solution. When the specific surface area of clay particle is high, the double-layer effects becomes important (Berner, 1971).

According to Berner (1971), an EDL is formed due to the electrical charge on the surface of clay particle when imperfections or substitutions occur within the clay crystal structure. The electrical charge is balanced by an excess concentration of opposite-charged ions (cations) from the surrounding solution. Therefore, the EDL around the clay particles consists of the negatively charged clay surface (fixed layer) and the balancing cations (mobile layer). Since the electrical charge on the surface is formed by crystallographic causes, the charge is independent of solution composition.

2.4.2 The Gouy-Chapman-Stern Double Layer Model

In the Gouy-Chapman-Stern double layer model, the cations in EDL are distributed in a combination of the Stern layer and the diffuse layer (Stern, 1924) (Figure 2.5). The Stern layer is a compacted layer that contains highly concentrated cations to balance the negative charge at the clay surface. The diffuse layer is a layer in which the number of cations exceeds the number of anions to balance the remaining negative charge. While there are no anions in the Stern layer, the number of anions is much higher in the diffuse layer. This distribution of cations and anions in the EDL leads to a highly positive zeta potential in the Stern layer, and a less positive zeta potential in the diffuse layer. A highly positive zeta potential indicates that a larger force is required to pull the cations out from the Stern layer. In the diffuse layer, the electrostatic attractive force is much stronger, allowing the cations to form attractive bonds with the anions. The diffuse layer is able to freely exchange cations with external solution (Berner, 1971). Therefore, the diffuse layer can be referred to as the mobile layer.

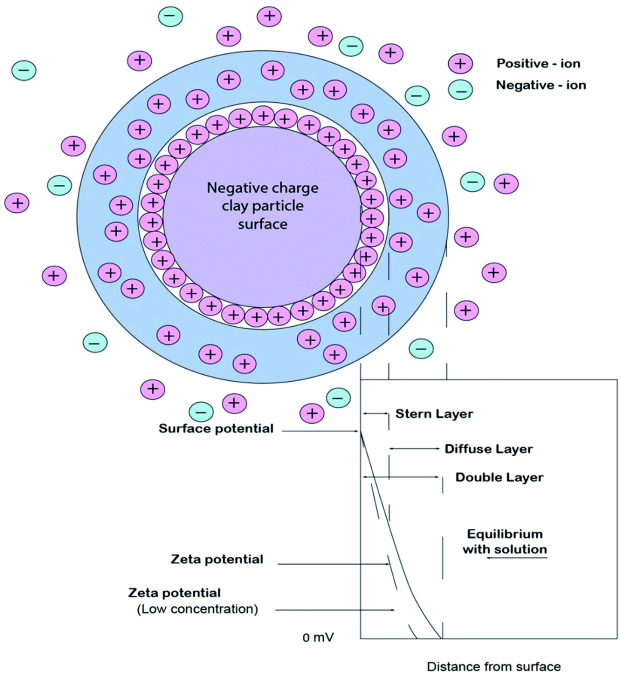

Figure 2.5. The Gouy-Chapman-Stern double layer conceptual model (Jafarbeglou, Abdouss, Shoushtari, & Jafarbeglou, 2016)

2.4.3 The Impact of EDL on Pore Fluid Flow and Solute Transport

Pore fluid in a clay-rich formation can be classified into three types: interlayer water, EDL water, and free pore water (Tournassat & Appelo, 2011). Interlayer water is defined as water molecules intercalated between clay layers to create an interlayer ionic solution. EDL water usually exists in the Stern layer and the diffuse layer, and the water molecules tend to be adsorbed to cations through Van der Waal forces or hydrogen bonds when the attractive force is greater than the repulsive force (Sposito et al., 1999). Free pore water usually exists outside the EDL. The numbers of cations and anions in the water are approximately the same to maintain the electrical neutrality. Both interlayer water and EDL water have a much higher viscosity due to the strong adhesive forces acted on the water molecules. However, the free pore water has a much lower viscosity due to the weak adhesive forces acting on the water molecules. Therefore, the capability of pore fluid flow in clay-rich media is inversely proportional to the EDL thickness.

The migration of cations in the diffuse layer is affected by the forces of diffusion and electrostatic attraction (Berner, 1971). The electrostatic attraction causes the cations to be attracted to the negatively charged clay surfaces, leading to the increase of cation concentration in the EDL. On the other hand, the electrostatic gradient across the EDL causes the cations to diffuse away from the clay surfaces. At equilibrium, the forces of diffusion and electrostatic

attraction are equal. The migration of anions through pores is also affected by the diffusion forces and electrostatic forces (Berner, 1971). Since anions have the same charge as the negatively charged clay surfaces, the electrostatic repulsion causes the anions to be repulsed from the clay surfaces. However, the anions experience the diffusion forces because of the electrical charge difference between the clay surface and the diffuse layer. As a result, anion exclusion occurs until the anion distribution reaches equilibrium. The capability of solute transport in clay-rich media is inversely proportional to the EDL thickness. When the EDL is thicker, the electrostatic gradient in EDL becomes greater, and the diffusion force in EDL becomes stronger. Therefore, the solute diffusion through pores is more restricted. The EDL is also more likely to overlap when it is thicker. The diffusion forces and electrostatic forces only affect the migration of charged species, and do not affect the migration of neutral components of the solution (such as water molecules and uncharged species) (Takeda *et al.*, 2014).

2.5 Factors that Affect the Membrane Characteristics

2.5.1 Pore Size Distribution

Pore size distribution is a significant factor affecting the ω of a semipermeable membrane. The theoretical model of ω was developed by Kemper and Rollins (1966) and modified by Bresler (1973) shows that ω has a unique relationship with pore size (Eq. 2.2 and Figure 2.2). Due to the heterogeneity of pore sizes within a clay-rich formation, the restriction of solute transport usually only occurs in the fraction of smaller pore sizes. Preferential solute migration occurs where pore sizes are wider, the overlap of EDL does not exist, and electrical restrictions happen to a lesser extent.

2.5.2 Confining Pressure

The dependency of ω on pore-size distribution also makes ω dependent on confining pressure (σ_v) since increasing σ_v will result in smaller pore sizes (Fredlund & Xing, 1994) with concomitant reductions in porosity (n) and void ratio (e) (Schiffman & Gibson, 1964). When σ_v is applied to the semipermeable membrane, the pores are the primary media being compressed, because the pore compressibility (β_p) is much larger than the particle compressibility (β_m). The pore compression behaviour in saturated semipermeable membranes is similar to the volumetric water content (θ) condition described in soil-water characteristic curve (Fredlund & Xing, 1994). The bigger pores are the first to be compressed when a load is applied to the sample because the pore-fluid in bigger pores dissipates more easily. The

medium sized pores are second to compress, followed by the smallest pores. As a result, the number of smaller pores increases with time when σ_v is applied to the semipermeable membrane. The EDL thickness should not change unless the clay mineralogy or pore-water chemistry has changed. As a result, the effective EDL is more likely to overlap when the semipermeable membrane is subjected to a higher σ_v (Rahman *et al.*, 2005), leading to a higher Γ (Figure 2.6). The relationship between Γ and σ_v is not linear. It is very likely because the impact of σ_v on solute transport restriction is much less once the majority of pore size is sufficiently small that the overlap between EDL occurs.

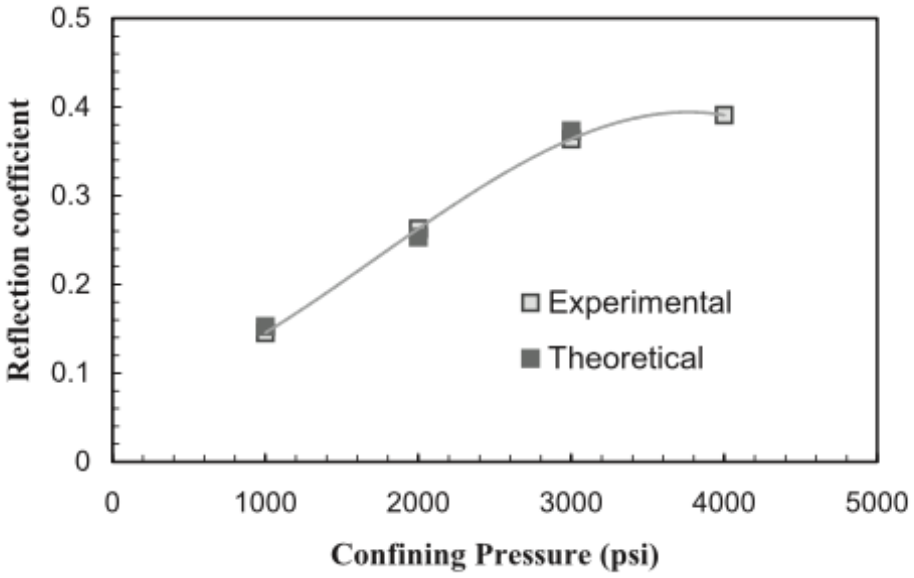

Figure 2.6. Γ with respect to σ_v (1000, 2000, 3000, 4000 psi) (Rahman *et al.*, 2005)

2.5.3 Temperature

Temperature is an important factor to determine the thermo-poroelastic behaviour of shale. In a thermo-poroelastic medium, porosity is affected by changes in fluid pressure, normal stresses, and temperature. According to Ingebritsen, Sanford, and Neuzil (2006), there are competing responses of fluid and porous medium in response to temperature changes. On one hand, a temperature increase leads to a decrease in fluid storage through a fluid expansion and a fluid density decrease. As the fluid expands, the thickness of EDL also increases. On the other hand, a temperature increase leads to an increase in fluid storage through a pore volume increase and a porous media expansion. Fluid storage is only possible in areas which the EDL does not overlap. Since the shale is located deep in subsurface and is subjected to high σ_v, the change of pore volume induced by temperature change is limited. As a result, the Γ of shale is

affected mainly by the fluid expansion and EDL expansion induced by temperature change. When the EDL expansion occurs, the EDL is more likely to overlap with each other, leading to a greater Γ.

According to Fritz and Marine (1983), the $\Delta\pi$ is proportional to the temperature (Eq. 2.1). According to Yeung and Mitchell (1993), the ΔP is also proportional to the temperature. In an experiment that measures the ΔP induced by the concentration difference across a semipermeable membrane, where the volumetric flow and electrical current density flow are zero, the ΔP can be expressed through Eq. 2.19.

$$\Delta P = \left(\frac{L_{13}L_{22} - L_{12}L_{23}}{L_{11}L_{22} - L_{12}L_{21}}\right)\frac{RT}{C_c}\Delta(-C_c) + \left(\frac{L_{14}L_{22} - L_{12}L_{24}}{L_{11}L_{22} - L_{12}L_{21}}\right)\frac{RT}{C_a}\Delta(-C_a) \qquad \text{(Eq. 2.19)}$$

where ΔP (Pa), L_{11} and L_{22} are the conductivity coefficients for volumetric flow and electrical current density flow, L_{12}, L_{13}, L_{14}, L_{21}, L_{23} and L_{24} are the coupling coefficients, R (0.0083145 $m^3 \cdot kPa \cdot mol^{-1} \cdot K^{-1}$), T (degrees K), C_c and C_a ($kg \cdot m^{-3}$), $\Delta(-C_c)$ and $\Delta(-C_a)$ ($kg \cdot m^{-3} \cdot m^{-1}$).

2.5.4 Mineralogy

The interaction between clay minerals and water varies with mineralogy (Grim, 1953; Dolinar & Trauner, 2004; Dolinar, Mišič, & Trauner, 2007). There are three groups of clay minerals, kaolinite, illite and smectite; all of which have different forming mechanisms and mineral structures (Langmuir, 1997). Kaolinite has a 1 : 1 tetrahedral sheet – octahedral sheet ratio, and the mineral structure is very platy (Figure 2.7). Illite has a 2 : 1 tetrahedral sheet – octahedral sheet ratio, and the mineral structure is fibrous (Figure 2.8). Smectite has a 2 : 1 tetrahedral sheet – octahedral sheet ratio, and the mineral structure has a lot of porous space in between (Figure 2.9).

Both kaolinite and illite have strong bonds in the EDL, low swelling potential, and only have active external surfaces. This implies that in kaolinite and illite the inner-sphere surface complex has no water molecule interposed between the surface functional group and the small cation or molecule it binds, whereas the outer-surface complex has at least one such interposed water molecule. Therefore, outer-sphere surface complexes comprise solvated adsorbed cations (Sposito et al., 1999).

Although smectite has the same 2:1 group as illite, the layer charge of smectite is much lower than illite. Due to the much weaker bonds (Van der Waals forces) in the EDL formed between any cation in the layer and anion from water molecules, smectite has a high swelling

potential and both active external and internal surfaces (Holtz & Kovacs, 1981; Dolinar & Trauner, 2004; Dolinar *et al.*, 2007). This implies that in smectite both inner-sphere surface complex and outer-sphere surface complex have at least one interposed water molecule between the surface functional group and the small cation or molecule it binds. Ions bound in surface complexes are distinguished from those adsorbed in the diffuse portion of the EDL because the former ones remain immobilized on a siloxane surface over long molecular time scales (Sposito et al., 1999). As the inner-sphere surface complex expands, the diffuse layer shrinks in sample. Since cation exchange normally occurs between diffuse layer and external solution, the shrinkage of diffuse layer leads to an increase in cation exchange capacity (CEC). According to Shainberg & Levy (2005), kaolinite has a low CEC (1 – 10 $cmol_c \cdot kg^{-1}$), smectite has a high CEC (80 – 120 $cmol_c \cdot kg^{-1}$), and illite has an intermediate CEC (20 – 40 $cmol_c \cdot kg^{-1}$). Due to the high smectite content in the sample, it will dominate the CEC in the sample. As the inner-sphere surface complex expands, the pore volume occupied by free pore water decreases in the sample. Since free pore water has a much lower viscosity, the permeability of sample highly relates to the pore volume occupied by free pore water. The reduction of pore volume leads to the reduction of permeability.

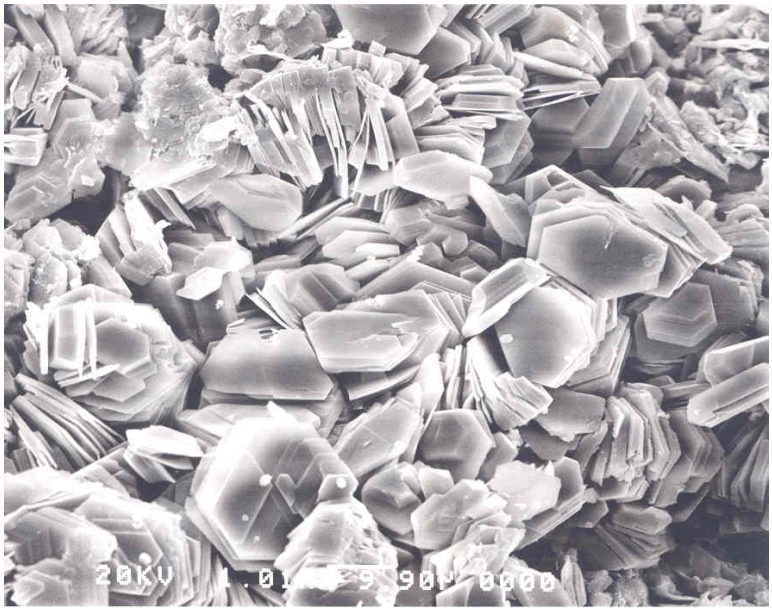

Figure 2.7. The scanning electron microscope image of kaolinite (PetroTech Associates, 2004)

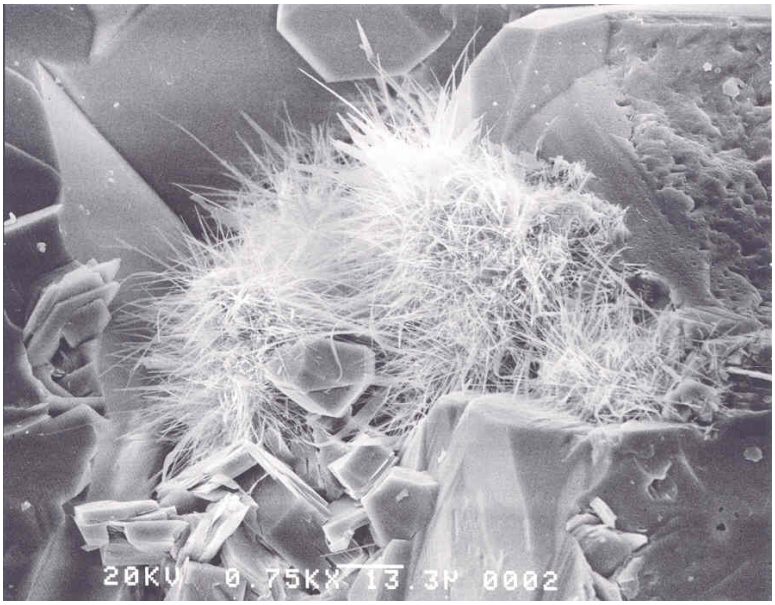

Figure 2.8. The scanning electron microscope image of illite (PetroTech Associates, 2004)

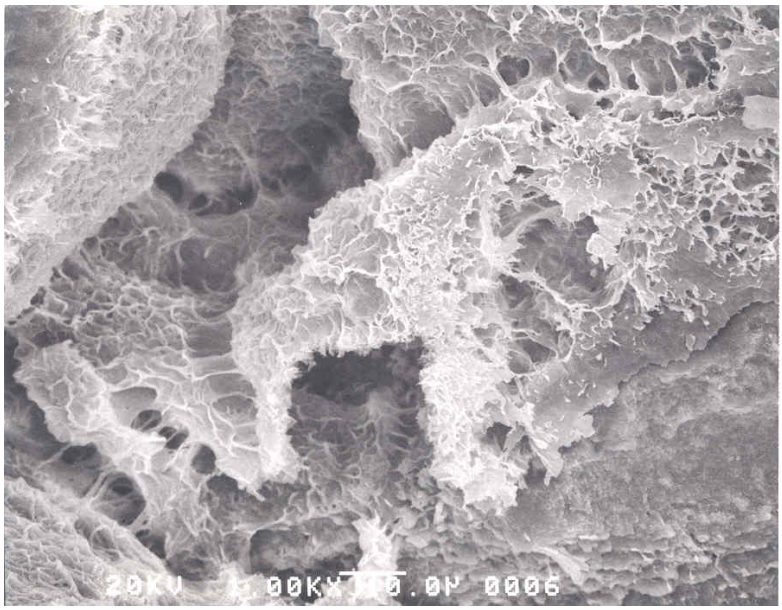

Figure 2.9. The scanning electron microscope image of smectite (PetroTech Associates, 2004)

2.5.5 Pore Fluid Chemistry

Many researchers have recognized that the Γ of a semipermeable membrane is largely controlled by pore fluid chemistry (Bresler, 1973; Fritz, 1986; Neuzil, 2000; Cey *et al.*, 2001; Mitchell & Soga, 2005; Al-Bazali *et al.*, 2006; Neuzil & Provost, 2009; Takeda *et al.*, 2014). The EDL (diffuse layer) thickness is highly related to the cation type, electrolyte concentration, and adsorption-desorption reaction (Langmuir, 1997; Mitchell & Soga, 2005). Cation type is classified by cation valence and cation radius. When cations around the negative clay particle surface have a higher valence and / or a larger dehydrated radius, the EDL thickness tends to

be thinner (Langmuir, 1997; Mitchell & Soga, 2005). When the valence of cations is higher, fewer cations are required to compensate for the negative charge at clay surface. In addition, the cations with a higher valence and / or a larger dehydrated radius tend to form stronger bonds with the anions. When the bonds are stronger, the bonding lengths tend to be shorter, and as a result, the cations and anions become more closely packed, leading to a thinner EDL thickness. For example, as compared to a concentrated Na^+ brine, the EDL would be much thinner in concentrated Ca^{2+} brine. Less restrictions would be imposed by the EDL to restrict the pore fluid flow through the sample, and the permeability of sample would increase. According to Kharaka and Berry (1973) and Malusis and Shackelford (2002), cations with a larger hydrated radius are more likely to be restricted to move through the pores of a given size. The hydrated ionic radii of monovalent cations vary in the order of $Na^+ > K^+ > Cs^+$, as shown in Table 2.1. Therefore, the Γ should vary in the same order.

The salinity of pore fluid significantly affects the EDL thickness (Berner, 1971). When the semipermeable membrane is immersed in dilute (fresh) pore fluid (low electrolyte concentration), the EDL thickness is large and on the order of same distance as the dimensions of clay particles. Solute transport restriction may occur in surficial loosely compacted sediments. On the other hand, when the semipermeable membrane is immersed in typical sea water (higher electrolyte concentration), the EDL thickness is thin and on the order of only a few angstroms. A high degree of compaction is necessary so that the EDL may overlap. Table 2.2 shows the relationship between EDL (diffuse layer) thickness and electrolyte concentration for a constant surface charge density (11.7 $\mu C/cm^2$) typical for smectite.

Table 2.2. The EDL (diffuse layer) thickness as a function of electrolyte concentration for a constant surface charge density (11.7 $\mu C/cm^2$) (Berner, 1971)

Electrolyte Concentration (Normality)	**Diffuse Layer Thickness (1 - 1 valent electrolyte) (Angstrom)**	**Diffuse Layer Thickness (2 - 2 valent electrolyte) (Angstrom)**
10^{-5}	1000	500
10^{-3}	100	50
10^{-1}	10	5

The adsorption-desorption reactions, such as cation exchange reactions, tend to reduce the EDL thickness (Rahman *et al.*, 2005; Al-Bazali *et al.*, 2006; Neuzil & Provost, 2009; Takeda *et al.*, 2014). A semipermeable membrane with a high CEC implies that the membrane

has a high capacity to hold exchangeable cations. As a result, a semipermeable membrane with a higher CEC tends to have a thicker EDL and a greater Γ. Figure 2.10 shows the linear relationship between CEC and Γ.

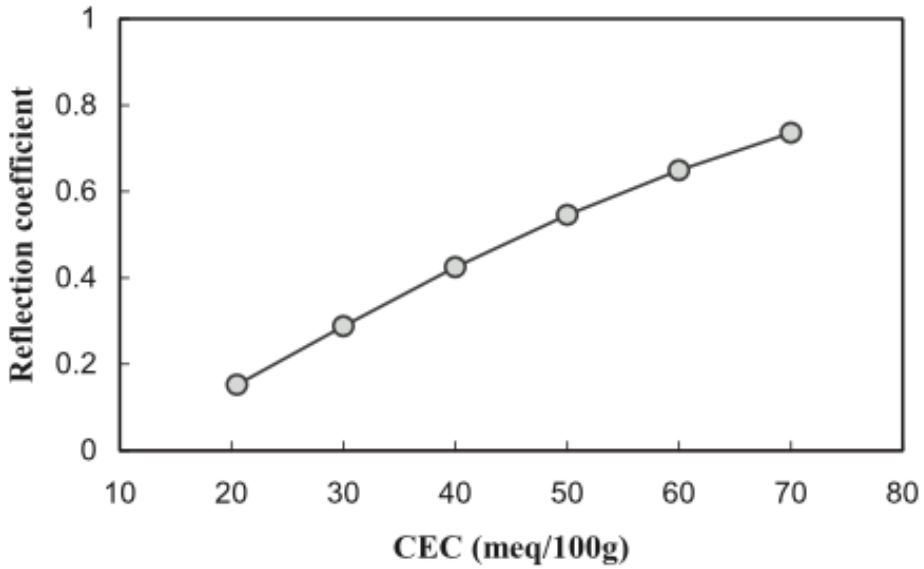

Figure 2.10. Γ with respect to CEC (Rahman *et al.*, 2005)

2.6 Osmotic Swelling and Consolidation

Many researchers have studied the influence of pore fluid chemistry on the mechanical behaviour of clays (Grim, 1958; Barbour & Fredlund, 1989; Curtin, Steppuhn, Mermut, & Selles, 1994; di Maio, 1996). When clay specimens are exposed to fluids different from their pore fluids, the clays undergo noticeable volume changes. There are two main types of osmotic volume change. The first type is osmotically induced consolidation, and the second type is osmotic consolidation.

Osmotically induced consolidation is consolidation that arises because of the decrease in fluid pressure and resulting increase in effective stress caused by osmotic flows out of the clay in response to osmotic gradients. di Maio (1996) suggests that when clay behaves as a semipermeable membrane, it allows outward flow of water but restricts inward diffusion of solutes. Barbour and Fredlund (1989) suggest that negative pore pressure is developed within the clay sample when water flows out of the sample.

Osmotic consolidation is caused by suppression of the EDL and results in a change in electrostatic repulsive-minus-attractive stresses between clay particles. Barbour and Fredlund (1989) suggest that even under a constant σ_v, changes in the pore fluid chemistry can lead to the volume change of clay due to the alteration of electrostatic interactions between clay

particles and the alteration of charged ions distribution in pore fluid adjacent to the clay particles. Osmotic consolidation is particularly noticeable in smectite with a high proportion of exchangeable Na^+. Smectite with high Na^+ concentration has the highest swelling potential (Curtin *et al.*, 1994). In an air-dried state, Na^+ favours the development of a single adsorbed water molecular layer. However, if water is available, Na^+ favours the development of probably tens of adsorbed water molecular layers (Grim, 1958). Due to the weak bonds between particles, the EDL is the thickest in Na-smectite. The experiment conducted by di Maio (1996) shows that when the Na-smectite is exposed to KCl, the exchangeable Na^+ would be substituted by K^+. As a result, the Na-smectite would be converted to K-smectite. This ion exchange leads to the decrease in EDL thickness and clay specimen volume. Due to the tight bonds between particles, the potential for the growth of thick, oriented water layers in K-smectite is very small (Grim, 1958).

2.7 Osmotic Efficiencies of Cretaceous-aged Pierre Shale (Bearpaw Formation)

Neuzil and Provost (2009) compiled the results from a number of osmotic tests on the Pierre Shale (Table 2.3). The ω of the Pierre Shale is 0.038 – 0.14 (Neuzil, 2000; Garavito *et al.*, 2006), 0.0051 – 0.025 (Al-Bazali, 2005), and 0.0028 – 0.035 (Cey *et al.*, 2001). The ω of Pierre Shale in the Al-Bazali (2005) research is lower because the shale is subjected to solutions with higher electrolyte concentrations. The Cey *et al.* (2001) research shows that as the concentration of electrolyte in solution increases, the ω of shale tends to decrease.

Table 2.3. The physical properties, the electro-chemical properties, and the osmotic efficiencies of Pierre Shale

Formation	**Lithology/ Clay Mineralogy (%)** [a]	**Permeability (m/s)**	**Porosity**	**Type of Test** [b]	**Electrolyte Type and Concentration (M)**	**ω**	**Reference**
Pierre Shale	Claystone, 70-80% (ML: 80%)	$10^{-13} – 10^{-14}$	0.34	In-situ; equilibrated pressure	NaCl, 0.06 – 0.11 M	0.038 – 0.14	Neuzil (2000)
Pierre Shale	Claystone, 70-80% (ML: 80%)	$10^{-13} – 10^{-14}$	0.34	In-situ; transient pressure	NaCl, 0.06 – 0.11 M	0.038 – 0.14	Garavito *et al.* (2006)
Pierre Shale	Claystone, 64% (ML: 49%)	6.2×10^{-14}	0.26	Lab; equilibrated pressure	NaCl, 0.6 – 1.97 M	0.0051 – 0.025	Al-Bazali (2005)

Formation	Lithology/ Clay Mineralogy (%) [a]	Permeability (m/s)	Porosity	Type of Test [b]	Electrolyte Type and Concentration (M)	ω	Reference
Bearpaw Formation	Claystone, 57% (S: 50-60%) (I: 10-20%)	2.1 – 3.7 × 10^{-12}	0.38 – 0.43	Lab; equilibrated flow	NaCl, 0.105 M (mean)	0.027 – 0.035	Cey *et al.* (2001)
Bearpaw Formation	Claystone, 57% (S: 50-60%) (I: 10-20%)	4.0 – 4.7 × 10^{-12}	0.38 – 0.43	Lab; equilibrated flow	NaCl, 0.210 M (mean)	0.0076 – 0.012	Cey *et al.* (2001)
Bearpaw Formation	Claystone, 57% (S: 50-60%) (I: 10-20%)	4.3 – 6.6 × 10^{-12}	0.38 – 0.43	Lab; equilibrated flow	NaCl, 0.420 M (mean)	0.0028 – 0.004	Cey *et al.* (2001)

[a] C: total clay, ML: mixed layer smectite/illite, S: smectite, I: illite, K: kaolinite.

[b] "equilibrated pressure" tests: only considered the equilibrium or maximum osmotically generated pressure; "transient pressure" tests: also consider the change of osmotic pressure; "equilibrated flow" tests: based on equilibrated osmotically generated fluid flux while the osmotic pressure is not permitted to change.

CHAPTER 3: STUDY SITE AND SAMPLE CHARACTERIZATION

3.1 Introduction

This chapter provides general background knowledge related to the study area and the Pierre Shale based on the previous studies conducted in southern Saskatchewan. The information provides some general insights into the actual shale sample being tested in the chemical osmosis testing. The study area is described in Section 3.2. Details of the mineralogy and the physical properties of Pierre Shale is discussed in Section 3.3. The pore fluid chemistry and the solute transport properties of Pierre Shale is discussed in Section 3.4. The consolidation history of Pierre Shale is discussed in Section 3.5. The actual Pierre Shale sample used in the chemical osmosis testing is described in Section 3.6.

3.2 Study Area

The study area is located near the Mosaic's K2 Potash mine (N5617477.62 E295357.89), approximately 15 km east of the town of Esterhazy, Saskatchewan within the Williston Basin. The Williston Basin underlies approximately 250,000 km^2 of North Dakota, South Dakota, and Montana in the USA, and Manitoba and Saskatchewan in Canada (Kuhn, di Primio, & Horsfield, 2010) (Figure 3.1). At this location, the Cretaceous-aged shale in the study area extends from 11 to 392 m BGS, and Pierre Shale (11 – 184 m BGS) is the top-most formation of the Cretaceous-aged shale (Hendry & Harrington 2014). The Cretaceous-aged shale is overlain by clay-rich Quaternary-aged glacial till (<11 m BGS) and underlain by sandy and shaley Mannville (aquifer) (392 – 485 m BGS) (Figure 3.2).

Hendry and Harrington (2014) suggest that the hydrogeology of present-day Williston Basin is characterized as a gravity-driven southwest to northeast-directed groundwater flow system. The vertical hydraulic gradients are downward at 0.22 through the Pierre Shale at the K2 mine and the vertical hydraulic conductivity (K_v) of Pierre Shale at the K2 mine ranges from (2 to 10) $\times 10^{-12}$ $m \cdot s^{-1}$ (Smith, van der Kamp, & Henry, 2013). This K_v range is consistent with the K_v of Pierre Shale in North Dakota (10^{-11} to 10^{-13} $m \cdot s^{-1}$) and South Dakota (4×10^{-12} to 10^{-11} $m \cdot s^{-1}$) (Bredehoeft, Neuzil, & Milly, 1983; Neuzil, 1986).

Clay-rich aquitards with low K_v ($\leq 10^{-8}$ $m \cdot s^{-1}$) control recharge and contaminant transport to adjacent aquifers (Cherry *et al*. 2004). Therefore, the Pierre Shale at the study area could be a suitable host formation for sequestration of hazardous wastes and can act as an

isolation unit to potentially protect shallow groundwater from contaminations injected into deeper formations.

Figure 3.1. Map of the Esterhazy site location (star), and the distribution of Williston Basin in west-central Canada and the United States of America (modified from Kuhn *et al.* (2010))

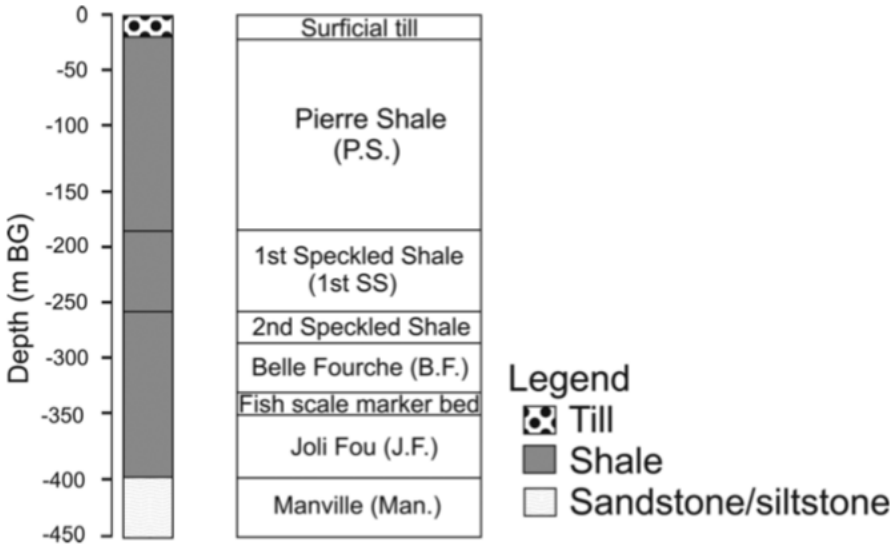

Figure 3.2. Stratigraphy of the borehole at Mosaic's Esterhazy K2 mine in Saskatchewan, Canada based on geological and geophysical logging (Smith *et al.*, 2013)

3.3 Mineralogy and Physical Properties of the Pierre Shale

In North America Western Interior, the late Cretaceous sedimentary pattern is intertonguing continental strata and marine shales due to the continual transgression and

regression of the Bearpaw Sea. Bearpaw Formation is formed by the primarily marine clays and some marine sands deposited during the final transgression and regression (Caldwell, 1968). Dawson (1882) first recognized the Pierre age of Bearpaw Shale through the fossils and termed them "Pierre Shale" (Irwin, 1931). Yet, Bearpaw Shale is not the only formation being termed as Pierre Shale. Pierre Shale is a term that can be generally applied to all Pierre-aged formations.

The Pierre Shale is primarily a grey-dark grey, non-calcareous, over-consolidated silt and clay. Shell fragments, fossils, and pyrite mineralization are observable throughout the formation and thin layers (<50 mm) of bentonite are common throughout the formation (Smith, Elwood, Barbour, & Hendry, 2018). Williams and Bayliss (1988) suggest that the clay mineralogy of the Pierre Shale (Millwood unit, Pembina unit, and Gammon Ferruginous unit) is mainly composed of kaolinite (25%), illite (20%) and smectite (30%) (Figure 3.3); and the chemical components are mainly silica and aluminium, with minor iron, calcium, magnesium, potassium (Figure 3.4).

The mean total porosities (n_T) of Pierre Shale are 0.33 ± 0.05, 0.33 ± 0.04, and 0.33 ± 0.02 respectively at Mosaic's Esterhazy K2 mine and two sites in southern Saskatchewan; one in the northern portion of the Williston Basin (site 1) and another closer to the center of the Williston Basin (site 2) (Smith *et al.*, 2013; Smith *et al.*, 2018).

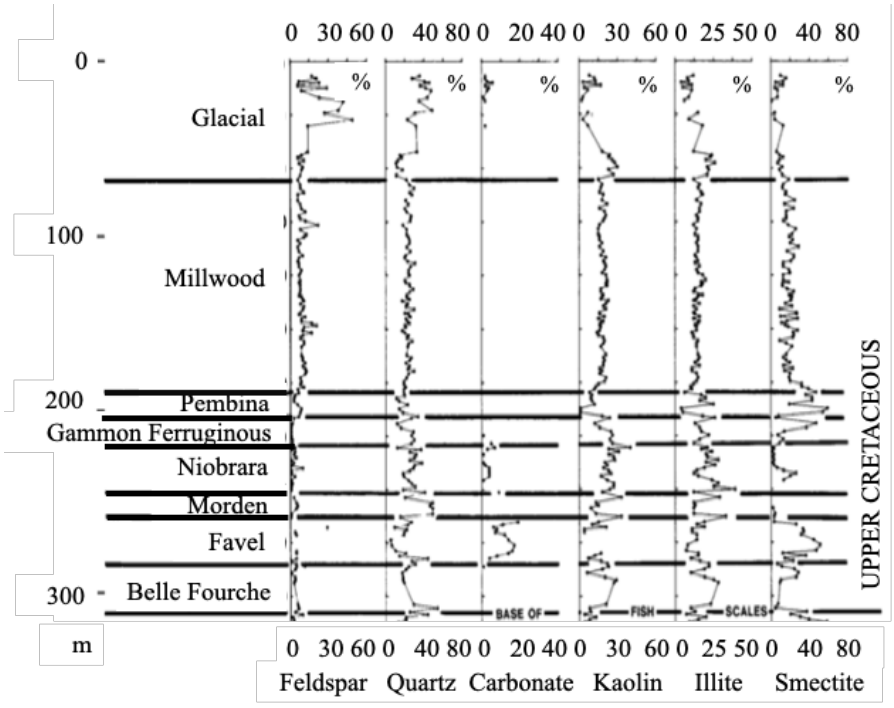

Figure 3.3. The mineral logs of Upper Cretaceous-aged shale in southern Saskatchewan (after Williams & Bayliss, 1988)

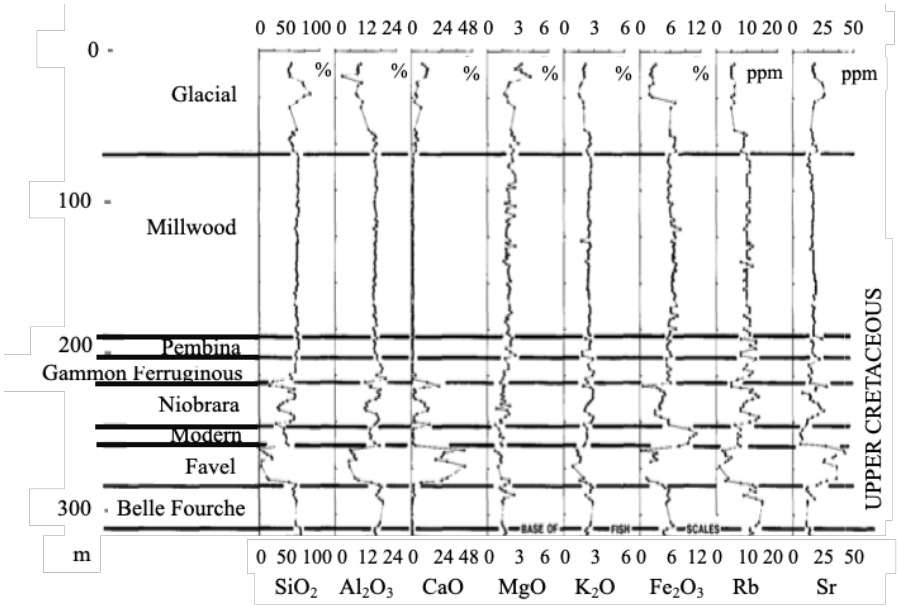

Figure 3.4. The chemical element logs of Upper Cretaceous-aged shale in southern Saskatchewan (after Williams & Bayliss, 1988)

3.4 Pore Fluid Chemistry and Solute Transport Properties

Solute transport through the Pierre Shale in southern Saskatchewan is diffusion dominated due to its low K. According to Hendry *et al.* (2017), there has been a very long period (>1 Ma) of diffusion dominated solute transport through Pierre Shale. Based on the clay composition of Pierre Shale (25% kaolinite; 20% illite; 30% smectite) and the typical CEC values of each clay mineral described in Section 2.5.4, the CEC of Pierre Shale should be approximately 40 – 60 $cmol_c \cdot kg^{-1}$. This range falls in between the typical CEC values for illite and smectite and indicates Pierre Shale has intermediate to high CEC.

Na^+ is the dominant cation in the pore fluids of Pierre Shale. Na^+ likely originated from the hydrolysis of mirabilite, a hydrous sodium sulphate mineral ($Na_2SO_4 \cdot 10H_2O$) (Tomkins, 1954). The high exchangeable Na^+ concentration is confirmed by the presence of Na-rich jarosite (natrojarosite) as the dominant alteration product of pyrite and the high Na / K ratio in pore fluids (Curtin, Steppuhn, Mermut, & Selles, 1995). Despite the high Na^+ concentration, a considerable amount of exchangeable K^+, Ca^{2+} and Mg^{2+} also exists in the pore fluids. K^+ likely originated from the buried potash (KCl) migrating upward through the overlying formations in the form of salt domes, while Mg^{2+} likely originated from the dissolution of Mg^{2+} bearing minerals, dolomite and calcite, under the low pH conditions, and Ca^{2+} likely originated from the dissolution of gypsum under the low pH conditions (Mermut & Arshad, 1987).

Sulphate (SO_4^{2-}) is the dominant anion in the pore fluids of Pierre Shale, likely originated from the pyrite (FeS_2) oxidation and the hydrolysis of natrojarosite ($NaFe_3(SO_4)_2(OH)_6$) (Curtin *et al.*, 1995; Mermut & Arshad, 1987; van Breemen *et al.*, 1982), following:

$$FeS_2 + 15/4\ O_2 + 7/2\ H_2O \rightarrow Fe(OH)_3 + 2SO_4^{2-} + 4H^+$$

$$NaFe_3(SO_4)_2(OH)_6 + 3H_2O \rightarrow 3Fe(OH)_3 + 2SO_4^{2-} + 3H^+ + Na^+$$

In coastal areas, SO_4^{2-} concentrations are less than Cl^- in soils due to the influx of seawater. However, there is no influx of seawater in upland areas, so the SO_4^{2-} concentration is much higher than Cl^- in soils (Mermut & Arshad, 1987). Bangsund (2016a) studied the pore waters and sediments within the Cretaceous-aged clay – Quaternary-aged glacial till aquitard system in southwestern Saskatchewan (King site located approximately 140 km southwest of Saskatoon, Saskatchewan). Bangsund (2016a) provides an extensive list of the anion and cation concentrations of pore fluids from core obtained from the 2013 King site core, obtained from 1 to 239 m BGS. Table 3.1 and Table 3.2 show the major anion and cation concentrations, respectively. SO_4^{2-} is the dominant anion, followed by Cl^-. Na^+ is the dominant cation, followed by Ca^{2+} and Mg^{2+}.

Table 3.1. Major anion concentrations of the squeezed pore fluids from the 2013 King site core (Bangsund, 2016a)

Depth (m BGS)	**F^- (mg/L)**	**Cl^- (mg/L)**	**NO_2^- (mg/L)**	**Br^- (mg/L)**	**NO_3^- (mg/L)**	**SO_4^{2-} (mg/L)**	**PO_4^{3-} (mg/L)**
112	<0.60	339	<0.3	2.14	1.55	6540	<0.60
119	8.83	739	<0.05	2.60	3.48	8740	<0.05
128	<0.60	360	<0.3	4.09	0.99	6000	<0.60
129	<0.60	326	<0.3	4.37	1.34	6210	<0.60

Table 3.2. Major cation concentrations of the squeezed pore fluids from the 2013 King site core (Bangsund, 2016a)

Depth (m BGS)	**Na^+ (mg/L)**	**K^+ (mg/L)**	**Mg^{2+} (mg/L)**	**Ca^{2+} (mg/L)**	**Fe^{3+} (mg/L)**	**Al^{3+} (mg/L)**	**Si^{4+} (mg/L)**
113	3020	ud	63.4	174	0.95	0.06	9.20
120	3490	ud	94.4	239	0.06	0.02	7.30
120	3720	ud	97.2	242	0.07	0.02	7.48

Depth (m BGS)	Na^+ (mg/L)	K^+ (mg/L)	Mg^{2+} (mg/L)	Ca^{2+} (mg/L)	Fe^{3+} (mg/L)	Al^{3+} (mg/L)	Si^{4+} (mg/L)
129	3050	ud	46.5	181	0.25	0.02	11.7
130	2690	ud	56.2	131	0.11	0.03	12.0
ud: the concentration is undetectable							

Table 3.3 shows the major anion concentrations of the squeezed pore fluids from the Pierre Shale sample collected near Mosaic's Esterhazy K2 mine at a depth of 45 – 47 m BGS. The pattern of data presented in Table 3.3 is close to the data presented in Table 3.1. SO_4^{2-} is the dominant anion, followed by Cl^-, within the sample.

Table 3.3. Major anion concentrations of the squeezed pore fluids extracted from the Pierre Shale sample collected near Mosaic's Esterhazy K2 mine at a depth of 45 – 47 m BGS (self-squeezed)

Depth (m BGS)	F^- (mg/L)	Cl^- (mg/L)	NO_2^- (mg/L)	Br^- (mg/L)	NO_3^- (mg/L)	SO_4^{2-} (mg/L)	PO_4^{3-} (mg/L)
45 – 47	4.8	307	0	0	0	2230	0

3.5 Consolidation History of the Pierre Shale

Four major glaciation periods occurred in North America during the Quaternary period with the most recent being the Wisconsin Glaciation (Benn & Evans, 2010). At the height of the Wisconsin Glaciation period, the ice sheet height relative to sea level in southern Saskatchewan was approximately 1500 to 2000 m (Peltier, 1994). As a result, the Pierre Shale in southern Saskatchewan was subjected to increased σ_v during the Quaternary glaciations. Based on traditional oedometer tests conducted on core samples from the Pierre Shale at Site 1, the maximum pre-consolidation pressure (P_C') is estimated to be approximately 6000 to 7000 kPa at up to 200 m BGS, and the current effective stress (σ_v') up to the same depth is around 1000 to 2500 kPa (Table 3.4) (Smith *et al.*, 2018). Increasing σ_v' with depth results in decreasing bulk compressibility (β), and spans about one order of magnitude, ranging from 3.0×10^{-6} to 2.0×10^{-7} kPa^{-1} between 25 and 325 m BGS.

Table 3.4. Summary of geomechanical parameters obtained from the Pierre Shale core samples in southern Saskatchewan (Smith *et al.*, 2018)

Sample (m BGS)	Estimated* σ_v' (kPa)	e	Pc' (kPa)	OCR	Cc	Cr
47	526	0.79	2500	4.75	0.32	n.d.
87	1130	0.31	10000	8.87	0.20	0.035
128	1690	0.46	3000	1.77	0.12	0.045
175	2260	0.51	6000	2.66	0.27	0.069
185	2400	0.52	6000	2.49	0.41	0.006
212	3350	0.6	7000	2.08	0.39	0.088

*estimated by subtracting pore pressure measurements near each sample from calculated total stress

3.6 Description of the Pierre Shale Sample for Test Program

The Pierre Shale sample used in this study was collected from borehole M1870-01 near the Mosaic's K2 Potash mine on October 14, 2009. The coordinates of the borehole location was N5617477.62 E295357.89 (NAD83 / UTM zone 13).

The borehole was a continuously cored borehole using the rotary drilling rig ((Failing CF – 15TD). The sizes of drill bits used to drill through the clay-rich Quaternary-aged glacial till (0 to 12.2 m BGS) and the Cretaceous-aged shale (12.2 to 323 m BGS) were 159 mm and 140 mm, respectively. The total depth of the borehole was 323 m. The elevations of ground surface and borehole end were 510 m and 187 m above sea level, respectively. Samples were collected throughout the borehole. According to the borehole log in Appendix A (Figure A.1 to A.3), the Pierre Shale was generally an unoxidized, hard, non-calcareous, grey silty clay shale. Although the shale was generally non-calcareous, the shale from 221 to 280 m BGS was weakly to moderately calcareous. The strength of shale increased along with increasing depth. The core from 12.2 to 48 m BGS was disturbed. The core occurred from 41 to 48 m BGS transitioned from disturbed to intact. The core below 48 m BGS was intact. Shale is a type of rock that demonstrates strong anisotropic behaviours with tensile strengths perpendicular to bedding plane much higher than that parallel to bedding plane. This behaviour was observable in the entire intact shale core. From 48 to 88 m BGS, the core strength was weak along the bedding planes. From 88 to 189 m BGS, the core broke easily long the bedding planes. From 189 to 323 m BGS, the core broke preferentially along the bedding planes.

The shale sample used in this study was collected at depth 121 m BGS (elevation 389 m above sea level). According to the borehole log in Appendix A (Figure A.2), the Pierre Shale at that specific depth was unoxidized, hard, non-calcareous, very brittle, dark grey clay shale with trace to no silt (silt interbedding). Core also breaks easily along bedding planes. The core collected at depth 121 m BGS was chosen as the sample because it was in the best condition after storage. Most of the samples collected at site were damaged during the drilling, sampling and storage phases. Once the samples were damaged, they could not be used in the chemical osmosis testing because it was essential for the chemical osmosis testing to be conducted in a closed environment. Any leakage in the sample would lead to preferential dissipation of osmotic pressure and pore fluid. Osmotic pressure would not be able to build up in the testing system, and the sample would be much less semipermeable.

The semipermeability of shale primarily depends on the physical and electrochemical properties of shales described in Section 2.5. The clay and shale layers are regionally extensive throughout southern Saskatchewan, and the physical and electrochemical properties of shales within each sublayers are expected to be relatively consistent. However, it should be noted that there was only one sample used in this study and the sample was collected from one single borehole. The applicability of the results collected from this study in other locations of southern Saskatchewan are subjected to the heterogeneity of the physical and electrochemical properties of shales.

Once the sample was collected the sample was trimmed to remove any drill fluid, wrapped in plastic wrap, waxed in the field, and stored in a cooler at ambient surface temperature (5 – 10 ℃) until transported to the University of Saskatchewan. The sample was stored in a temperature-regulated room (5 – 10 ℃) until the sample was taken out for preparation.

Although drilling, sampling, and storage was conducted to introduce as little damage as possible, the formation of fractures in the sample was inevitable. First, the flushing of drilling fluids into boreholes during rotary drilling could enlarge the existing fractures in sample and introduce a different pore fluid to the core. Second, during retrieval, the lateral and vertical confining pressures originally applied to the sample decreased significantly resulting in swelling. Third, although the sample was wrapped in plastic wrap and waxed in the field, the evaporation of pore fluid resulted in a reduction of moisture content. Shales tended to be more brittle when the moisture contents of shales decreased causing fractures to form easily. If fractures were formed during collection and storage, it is expected that the K of the sample would increase, and reduce the semipermeability of the sample.

CHAPTER 4: METHODOLOGY

4.1 Introduction

This chapter describes the methods used to approximate the semipermeability of the Pierre Shale sample. Two different approaches were applied in this research. The first approach was to measure the osmotic efficiency by comparing the observed differential pressure that built up in response to a concentration gradient across the sample to the calculated osmotic pressure differential. The second approach was to analyze the solute transport across the sample over time during the chemical osmosis testing.

The method of the test sample and circulation fluid preparation is discussed in Section 4.2. The chemical osmosis testing apparatus set-up is discussed in Section 4.3. The method of osmotic efficiency approximation is discussed in Section 4.4. The methods of chemical laboratory tests to determine the cation and anion concentrations of synthetic fluids and collected fluids is discussed in Section 4.5. The methods of data analyses to construct the solute transport model is discussed in Section 4.6.

4.2 Preparation of Test Sample and Synthetic Fluids

The test sample was prepared by shaving, saturation and consolidation. The shale sample was shaved to a 63.5 mm diameter and a 8.7 mm height using a machining lathe operating at room temperature and dry environment to fit the internal surface of the steel test ring. The sample was then concurrently saturated with the synthetic in-situ pore fluid using the capillary rise method and consolidated using the seepage-induced consolidation method. The synthetic in-situ pore fluid used for sample saturation contained the major cation and anion concentrations as shown in Table 4.1. The synthetic in-situ pore fluid was produced to mimicked the anion concentrations of the squeezed pore fluids extracted from the Mosaic's Esterhazy K2 mine 138 m BGS shale sample (Bangsund, 2016b) (Table 4.3). Details of the shale saturation method and the shale consolidation method are provided in Section 4.2.1.

Table 4.1. The major cation and anion concentrations of synthetic fluids for sample saturation

	K^+	Na^+	Mg^{2+}	F^-	Cl^-	SO_4^{2-}	HCO_3^-
Concentration (mg/L)	0	178	3.9	0	272	16.6	6.6

Synthetic fluids were produced to circulate within the chemical osmotic circulation system during the testing period. As the synthetic fluids circulated within the system, it passed along the top and bottom boundaries of test sample. Three types of synthetic fluids were produced in this study, each had the same concentrations of NaCl and $MgSO_4$, and various concentrations of KCl. The difference of KCl concentrations between the synthetic fluids circulated at the top boundary and that at the bottom boundary resulted in a concentration gradient across the test sample, which led to the generation of osmotic pressure. The detail of synthetic fluid production method and the type of synthetic fluid used for top and bottom circulations during each osmotic cycle are provided in Section 4.2.2.

4.2.1 Shale Sample Preparation

The sample was saturated through the capillary rise method (Schmitt, Forsans, & Santarelli, 1994). A small amount of suction was applied across the sample to draw water up into the sample from bottom to the top using the synthetic in-situ pore fluid. This method pushed the air out of the sample through connected pores, and filled the void spaces with the synthetic pore fluid.

The sample was primarily consolidated through the seepage-induced consolidation method (Basc, 2014). The seepage force (j_s) played an important role in this consolidation method. When the synthetic in-situ pore fluid moved upward, j_s was in the opposite direction to the gravitational effective stresses (p_g'). For upward seepage, the impact of j_s towards the effective normal stress (σ'_z) on a plane within the sample is expressed using Eq. 4.1 (Budhu, 2010).

$$\sigma'_z = \gamma' z - iz\gamma_w = \gamma' z - j_s z \qquad \text{(Eq. 4.1)}$$

where σ'_z is the effective normal stress (kPa), γ' is the buoyant unit weight ($kN \cdot m^{-3}$) (the total unit weight (γ_t) minus the unit weight of water (γ_w)), j_s is the seepage force per unit volume ($kN \cdot m^{-3}$), z is the depth below surface datum (m), i is the hydraulic gradient (dimensionless) (Δp across the 0.0087 m shale sample height).

Eq. 4.1 shows that σ'_z decreases when j_s increases during upward seepage. Since the total stress (σ_z) remained constant, any reduction of σ'_z must be balanced by a corresponding increase in pore-water pressure (μ) (Budhu, 2010). However, μ in the shale sample should remain constant because the consolidation system was drained. As a result, no excess pore-water could accumulate in the sample. This process led to a continual change of sample volume

(ΔV_{shale}). ΔV_{shale} ceased when the steady state of flow (constant rate of synthetic pore fluid volumetric upward flow) was reached (Basc, 2014).

Sample saturation and consolidation were done concurrently over a 1870 hour period. The testing apparatus used is shown in Figure 4.1 (schematic diagram) and Figure 4.2 (actual apparatus). The sample was laterally confined by the steel ring, and vertically confined by the top piston and the bottom pedestal. The sample was vertically loaded within a Karol-Warner 555 Conbel pneumatic consolidation loading frame. A pressure/volume (P/V) controller was connected to the bottom pedestal, and supplied continuous pressure (p_b) and synthetic pore fluid (see Table 4.1) at the bottom of the sample. Atmospheric pressure (p_t = 0 kPa) was maintained for 1220 hours at the top of the sample. This apparatus created a continuous Δp across the sample and an open system in which no excess pore-water pressure could build up. The apparatus system was closed at 1220 hour to terminate the creation of Δp across the shale sample, when the sample was near to fully saturated and consolidated.

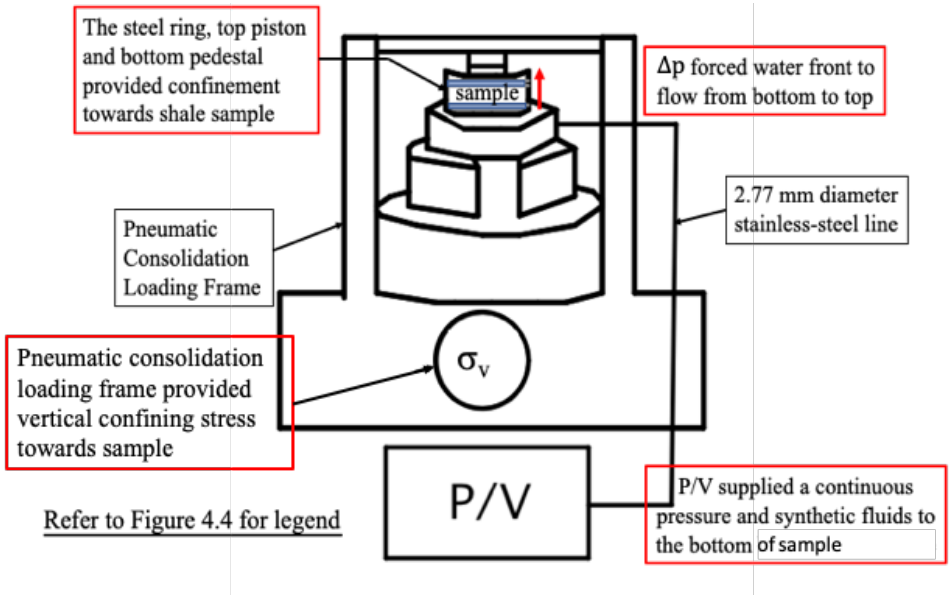

Figure 4.1. The apparatus system for shale sample saturation and consolidation (schematic diagram)

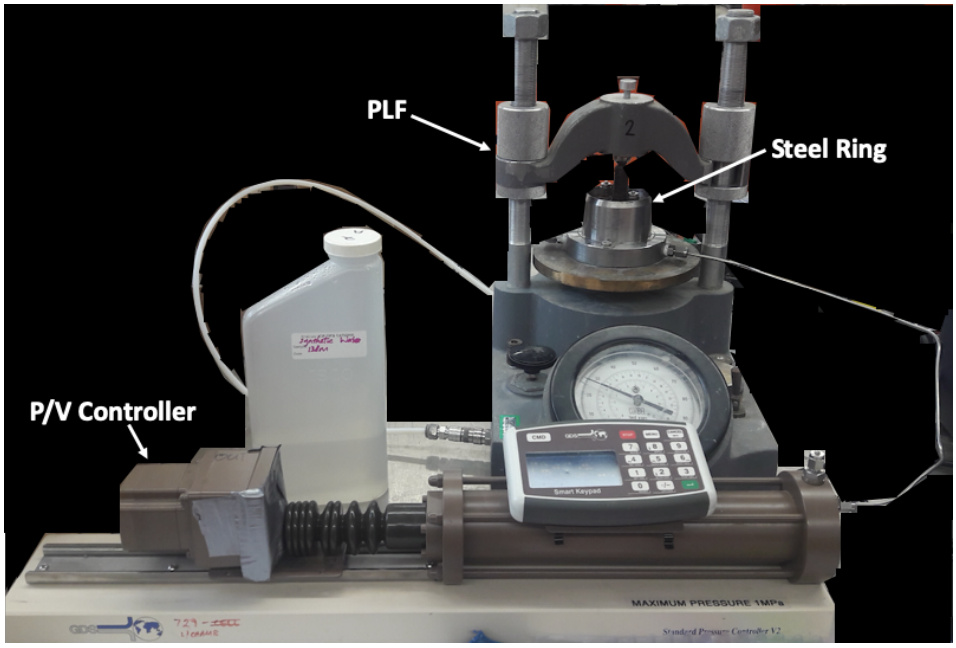

Figure 4.2. The apparatus system for shale sample saturation and consolidation (actual apparatus system)

The K of the shale sample was approximated during sample saturation, using the volumetric flow rate of the synthetic in-situ pore fluid from the P/V controller to the bottom of sample (Q), the pressure head difference (Δp), the sample height (h) and the cross-sectional area of the sample (A), through Eq. 4.2. The elevation head difference (Δz) was zero.

$$Q = -KiA = -K\frac{(\Delta p+\Delta z)}{h}A \qquad \text{(Eq. 4.2)}$$

where Q ($m^3 \cdot s^{-1}$), K ($m^3 \cdot m^{-2} \cdot s^{-1}$), Δp (m), Δz (m), h (m), A (m^2).

A back-pressure test was carried out at the end of sample consolidation for 48 days and 22.5 hours to ensure that the shale sample was fully saturated. The supply of fluid pressure at the bottom of sample by P/V controller ceased and the total vertical stress (σ_v) applied by the pneumatic consolidation loading frame was manually increased by 73.9 kPa (i.e. from 917 to 991 kPa). For a saturated sample, the increase of σ_v should lead to the increase of fluid pressure at the bottom of sample. Therefore, the pressure within P/V controller should increase over time. The pressure response within the P/V controller was monitored daily over time (n = 66).

4.2.2 Circulation Fluid Preparation

Three types of synthetic fluids (Type A, B, and C) were circulated in the chemical osmotic circulation system. Each type had the same concentrations of NaCl and $MgSO_4$, while

the fluids flushed at the top and bottom boundaries had various concentrations of KCl. KCl was chosen as the chemical to generate the concentration gradient across the sample because the sample had trace amount of pre-existing K^+ and it was easier to keep track of the solute transport through the sample during the chemical osmosis testing. If Na^+ was used instead of K^+, it would be difficult to know if the Na^+ transported to bottom boundary was originated from the sample or from the synthetic fluids circulating at the top boundary.

The three types of synthetic fluids (Type A, B, and C) were characterized by the variations of KCl concentrations. Table 4.2 shows the desired KCl molar concentrations, as well as the desired amount of KCl in 1000 mL of ultrapure (type 1) water to produce each type of synthetic fluid.

Table 4.2. The desired KCl concentration and amount in each type of synthetic fluid

Synthetic fluid type	**KCl molar concentration (M)**	**KCl amount (g)**
A	0	0
B	0.0039	0.291
C	0.0087	0.649

All three types of synthetic fluids (Type A, B, and C) had the same amount of NaCl (0.446 g) and $MgSO_4$ (0.035 g) in 1000 mL of ultrapure (type 1) water. Therefore, all synthetic fluids had the same NaCl and $MgSO_4$ concentrations. The desired amount of NaCl and $MgSO_4$ within the synthetic fluids was determined based on the anion concentrations of the squeezed pore fluids extracted from the Mosaic's Esterhazy K2 mine 138 m BGS shale sample (Bangsund 2016b) (Table 4.3).

Table 4.3. The desired anion concentrations of synthetic fluids based on the squeezed pore fluids extracted from the Mosaic's Esterhazy K2 mine 138 m BGS shale sample (Bangsund 2016b)

	F^-	**Cl^-**	**NO_2^-**	**Br^-**	**SO_4^{2-}**	**NO_3^-**	**PO_4^{3-}**
Concentration (mg/L)	0	271	0	0	14	0	0

The comparison between synthetic fluid (Table 4.3) and squeezed pore fluids from 2013 King site (Table 3.2) and Mosaic's Esterhazy K2 mine 45 – 47 m BGS sample (Table 3.4) shows that the Cl^- concentration of synthetic fluid (271 mg/L) was consistent with the Cl^-

concentrations of squeezed pore fluids (360 mg/L, 326 mg/L, from King site core; 307 mg/L, from Esterhazy sample). However, the SO_4^{2-} concentration of synthetic fluid (14 mg/L) was significantly lower than the SO_4^{2-} concentrations of squeezed pore fluids (6000 mg/L, 6210 mg/L, from King site core; 2230 mg/L, from Esterhazy sample).

The three types of synthetic fluids (Type A, B, and C) had the same concentrations of Na^+, Mg^{2+} and SO_4^{2-} and various concentrations of K^+ and Cl^-. Table 4.4 shows the desired cation and anion concentrations, as well as the TDS concentration, in each type of synthetic fluid.

Table 4.4. The desired cation and anion concentrations in each type of synthetic fluid

Synthetic fluid type	**K^+ (mg/L)**	**Na^+ (mg/L)**	**Mg^{2+} (mg/L)**	**Cl^- (mg/L)**	**SO_4^{2-} (mg/L)**	**TDS (mg/L)**	**TDS (kg/m^3)**
A	0	176	3.5	271	14.0	464	0.464
B	153	176	3.5	409	14.0	755	0.755
C	340	176	3.5	579	14.0	1110	1.11

The comparison between the test sample saturation fluid (Table 4.1) and the synthetic fluids (Table 4.4) shows that the major cation and anion concentrations of the sample saturation fluid were very close to the Type A synthetic fluid.

A total 18 bottles of synthetic fluid were produced for the chemical osmosis testing. Table 4.5 shows the type of synthetic fluid used for top and bottom circulation, and the desired TDS concentration difference, in each osmotic cycle. There were three osmotic cycles in this study. The 1st, 2nd, and 3rd osmotic cycles occurred respectively from day 1 to day 22, day 22 to day 85, and day 85 to day 149. Each time after producing the synthetic fluid, an EC measurement was taken to ensure the synthetic fluids had a roughly consistent TDS concentration (±10 uS/cm or ±20 mg/L). Atomic absorption spectrometry (AAS) tests (after ASTM D4691–17), ion chromatography (IC) tests (after ASTM D4327–17), and alkalinity tests (Hach method 8221) were also done for actual cation and anion concentrations of synthetic fluids.

Table 4.5. The type of synthetic fluid used for top and bottom circulation in each osmotic cycle

Cycle	Top Circulation	Bottom Circulation	TDS Concentration Difference (kg/m^3)
1st	Type A	Type A	0
2nd	Type B	Type A	0.291
3rd	Type C	Type A	0.649

4.3 Chemical Osmotic Circulation System

Following sample preparation, the test sample in the steel ring, along with the top piston and bottom pedestal, were transferred to the chemical osmotic circulation system and loaded until fully consolidated under a confining stress of 1660 kPa. The confining stress was determined based on the estimate σ_v' of Pierre Shale in southern Saskatchewan at depth 128 m (Table 3.4). Dial gauge readings were taken during the loading process, and used to determine the compressibility of shale sample (after ASTM D2435–11). The one-dimensional constrained compressibility (m_v) is defined as the compression of the shale, per unit of original thickness, per unit increase of effective stress in the load.

The chemical osmotic circulation system (Figure 4.5 and Figure 4.6 for schematic diagram and legend; Figure 4.7 for actual apparatus) was designed to create an osmotic pressure differential across a confined sample within a closed fluid volume system. The system was comprised of three elements: the consolidation system, the circulation system, and the monitoring system.

In the consolidation system (Figure 4.8), a Karol-Warner 555 Conbel pneumatic consolidation loading frame (PLF) was used to maintain the σ_v at 1660 kPa. The steel ring, top piston and bottom pedestal provided lateral and vertical confinement towards the shale sample.

In the circulation system, the synthetic fluids with known concentrations of KCl, NaCl and $MgSO_4$ were pumped through a 2.77 mm diameter top and bottom stainless steel circulation lines using a Harvard apparatus 906 infusion/withdrawal pump acting on stainless-steel reservoirs. Spiral channels were scoured into the top piston and base pedestal to ensure uniform fluid application to the sample. The fluid was then circulated back into storage within the stainless-steel cylinders at the pump.

During the circulation period, synthetic fluids (inflow fluids) flowed out from the pump at the same speed as the collected fluids (outflow fluids) flowed towards the pump. The

pumping speed was set to 0.01 mL/min for the first 5 days, and increased to 0.02 mL/min for the remaining 144 days. The pumping speed was doubled to monitor solute transport through shale sample more closely. The pumping speed was chosen so that the circulation rate was sufficiently rapid to minimize changes in the boundary concentration due to solute transport, while remaining sufficiently slow to capture changes in mass flux at the boundaries of the sample.

The monitoring system monitored multiple parameters during the circulation period (Figure 4.9). Laboratory temperature (T_{lab}, ℃) was monitored by a hand-held digital thermometer (HB Instrument). No adjustment was required for the T_{lab} because the thermometer was placed very close to the chemical osmotic circulation system and the output was in ℃. The change in line pressures (LP) (measured as inches of water) at the top and bottom boundaries was monitored by line pressure transducers (LPT). There were two types of LPT in the system, the high LPT and the low LPT. The pressure range measured by high LPT for the top and bottom boundaries was 0 to 400 kPa. Each increment of the high LPT was 2 kPa. The pressure range measured by the low LPT (Series 2000 Magnehelic Gages) was 0 to 15 inches of water (0 to 3.73 kPa) for the top boundary and 0 to 20 inches of water (0 to 4.97 kPa) for the bottom boundary. The accuracy of the low LPT was within 2%. The change of sample height (Δh) was monitored by a dial gauge attached to the PLF during the 3rd osmotic cycle.

The change of actual osmotic pressure across the shale sample, also termed differential pressure (DP), was monitored by a differential pressure transducer (DPT) Validyne D15-42N1S5A. A DPT had two ends, one end attached to the top boundary and another end attached to the bottom boundary. The output of the DPT was the direct measurement of DP between the top and bottom boundaries. LP and Δh were manually monitored on a daily basis (n = 169 for LP; n = 70 for Δh). Temperature and DP were recorded every half hour by the Optimum Instruments data dolphin model 400 (DD2) (n = 7008). The output of DPT was recorded by DD2 (measured as volts). This data was then converted to DP (as kPa) using Eq. 4.3.

$$\mathrm{DP} = 0.0147\ (\mathrm{DD2\ data}) - 0.4399 \qquad \text{(Eq. 4.3)}$$

where DP (kPa), DD2 data (Volts).

Due to the reasons described in Section 2.5.3, the change of T_{lab} during the chemical osmosis testing continuously affected the DP fluctuation. DP was lower when the T_{lab} was lower during the day, and higher when the T_{lab} was higher during the night. DP correction was completed to minimize this temperature effect towards DP so that the actual osmotic pressure

(ΔP) (the difference between the initial DP and the equilibrated DP across the sample in each osmotic cycle) could better reflect the semipermeable characteristics of shale induced by the pore-fluid chemistry and the physical properties.

The DP variation induced by the temperature effect (Δp) was approximated following a 4-step procedure. In the first step, the water density (ρ_w) corresponding to each T_{lab} recorded during the chemical osmosis testing was approximated using Eq. 4.4 based on the relationship between ρ_w and temperature (Figure 4.3). Eq. 4.4 shows the relationship between ρ_w and T_{lab} at room temperature (within the range of T_{lab} between 20 ℃ and 35 ℃).

$$\rho_w = 1003.9 - 0.2788 * T_{lab} \quad \text{(Eq. 4.4)}$$

where ρ_w ($kg \cdot m^{-3}$), T_{lab} (℃).

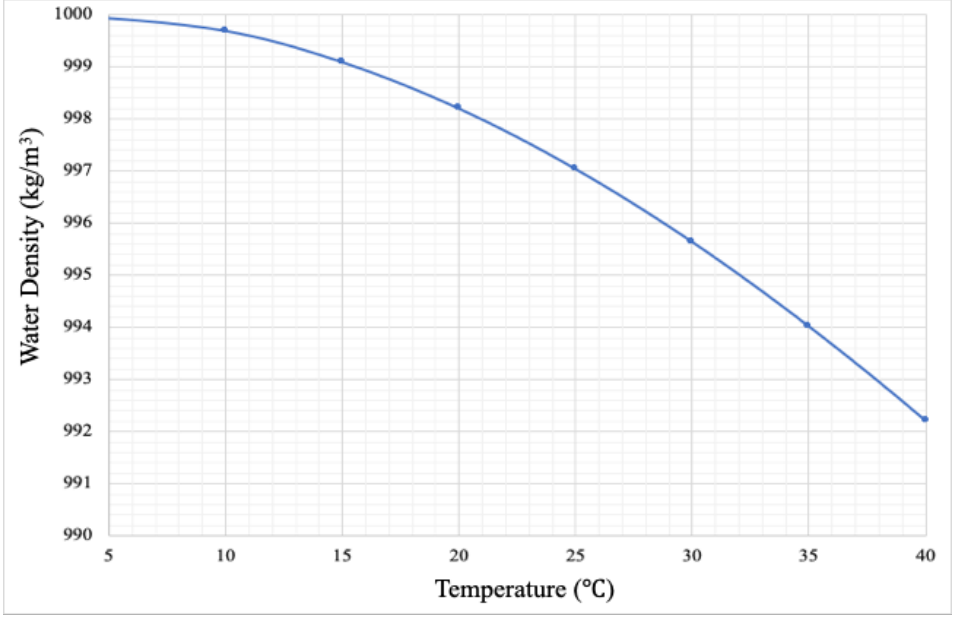

Figure 4.3. The relationship between water density and temperature

In the second step, the fluid volume within the closed system (V_w) corresponding to each calculated ρ_w during the chemical osmosis testing was approximated using Eq. 4.5, with the assumption that the initial fluid volume in the closed system (V_w) was 1.4×10^{-5} m^3.

$$V_{w2} = \rho_{w1} \times V_{w1}/\rho_{w2} \quad \text{(Eq. 4.5)}$$

where ρ_{w1} is the ρ_w at previous time step ($kg \cdot m^{-3}$), V_{w1} is the V_w at previous time step (m^3), ρ_{w2} is the ρ_w at current time step ($kg \cdot m^{-3}$), V_{w2} is the V_w at current time step (m^3).

In the third step, the DP variation induced by the temperature effect (Δp) was approximated using the relationship between the change of pressure and the change of fluid volume developed in the P/V controller compliance test (Figure 4.4).

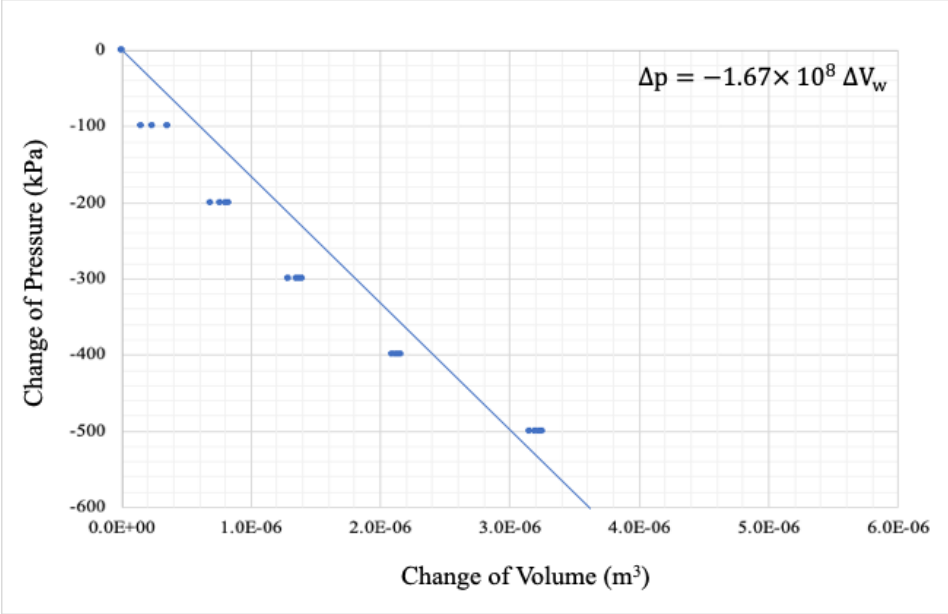

Figure 4.4. The relationship between the change of pressure and the change of fluid volume

In the last step, the Δp was taken out from the DP, though Eq. 4.6.

$$\text{Corrected DP} = \text{DP} - \Delta p \qquad \text{(Eq. 4.6)}$$

where corrected DP is the DP with the temperature effect minimized (kPa), DP is the DP from DPT (kPa), Δp is the change of pressure induced by the change of T_{lab} (kPa)

Since the V_w as 1.4×10^{-5} m^3 was an estimated value, sensitivity analyses were done with a variance of initial fluid volume in the closed system. The values of V_w chosen for sensitivity analyses were 1.0×10^{-5} m^3, 1.4×10^{-5} m^3, 2.0×10^{-5} m^3, and 3.0×10^{-5} m^3.

The supply of synthetic fluids for circulations in the top and bottom boundaries of sample was unlimited and the chemical components of synthetic fluids stayed the same in each osmotic cycle. The top boundary was a constant-source boundary, and the bottom boundary was a constant-flushing boundary (Malusis, 2001). The circulation system was a closed system, and absolutely no leakage was allowed during the circulation period. Any permeable connection to normally pressured surroundings would lead to ΔP very close to zero at all times (Neuzil & Provost, 2009).

The fluid volume capacity inside each pump cylinder was 64 mL. Synthetic fluids were normally stored in the P/V controllers and de-aired under 400 kPa. The volume in the pump

cylinders was then topped up from the P/V controllers every 1.5 days. When the synthetic fluids were replenished, the fluids stored in the pump cylinders were collected for further chemical analyses.

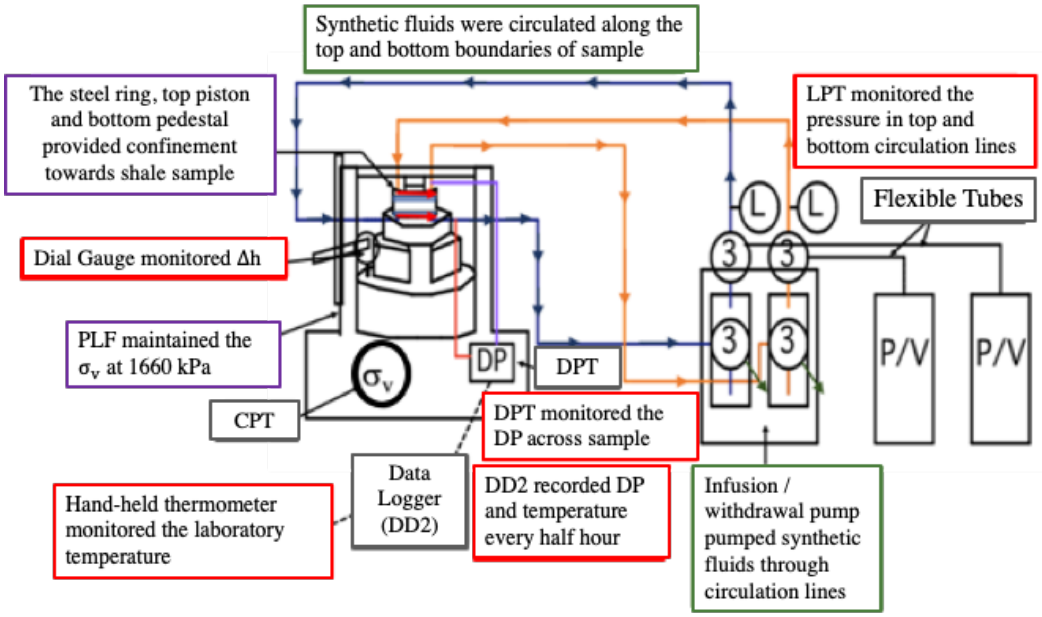

Figure 4.5. The chemical osmotic circulation system (schematic diagram); the consolidation system is described in purple boxes, the circulating system is described in green boxes, the monitoring system is described in red boxes.

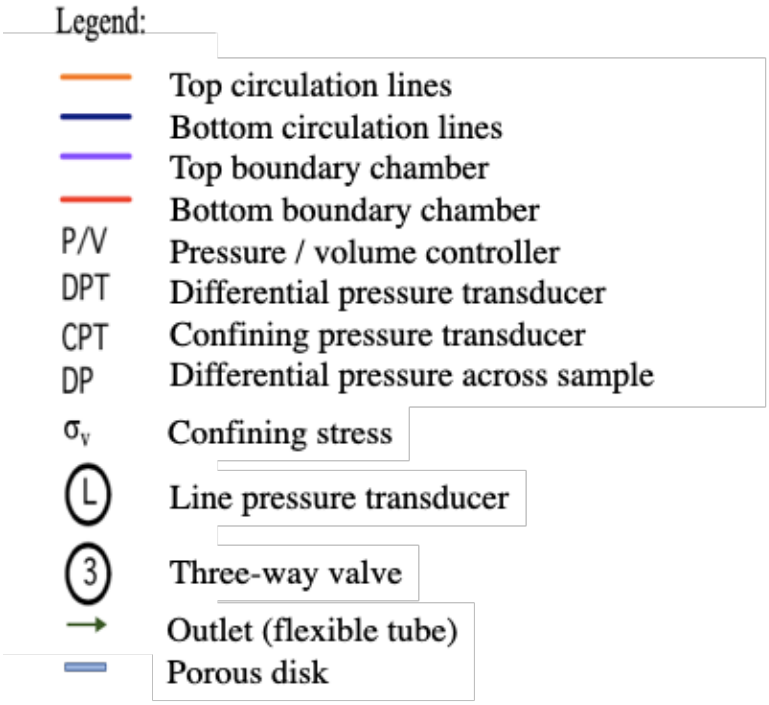

Figure 4.6. Legend for the schematic diagram of chemical osmotic circulation system

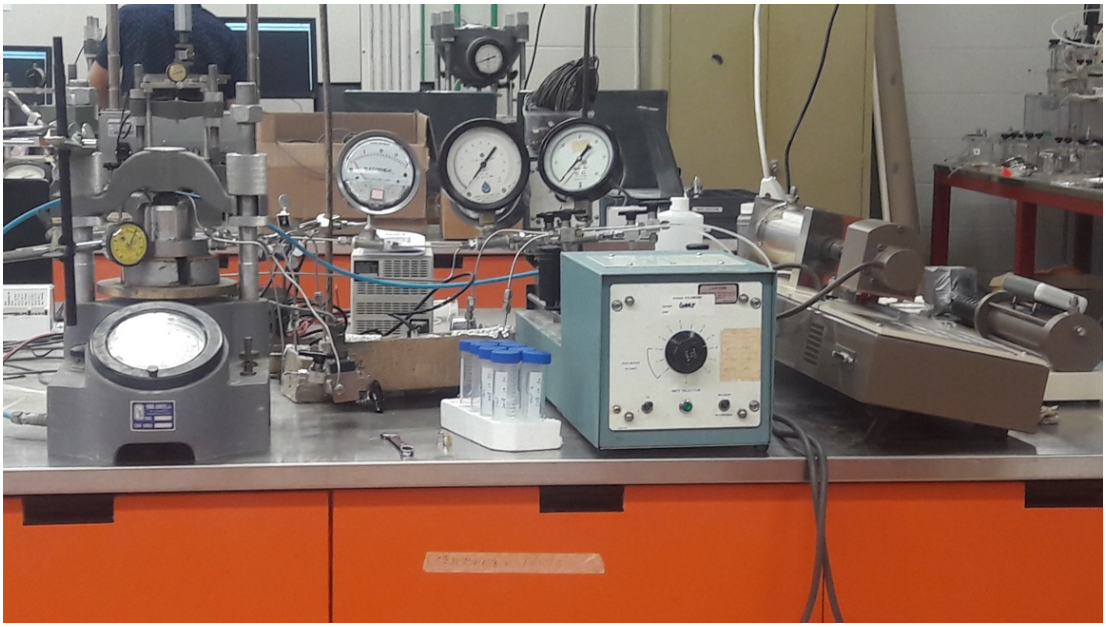

Figure 4.7. The overall view of the chemical osmotic circulation system (actual apparatus system)

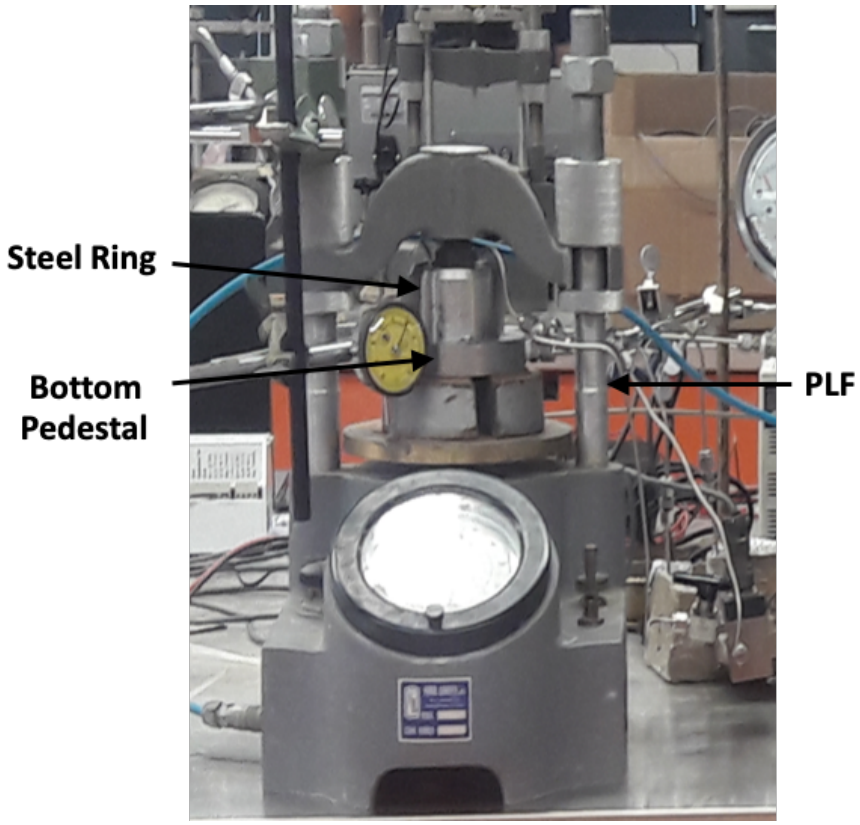

Figure 4.8. The consolidation system apparatus; the top piston is confined within the steel ring

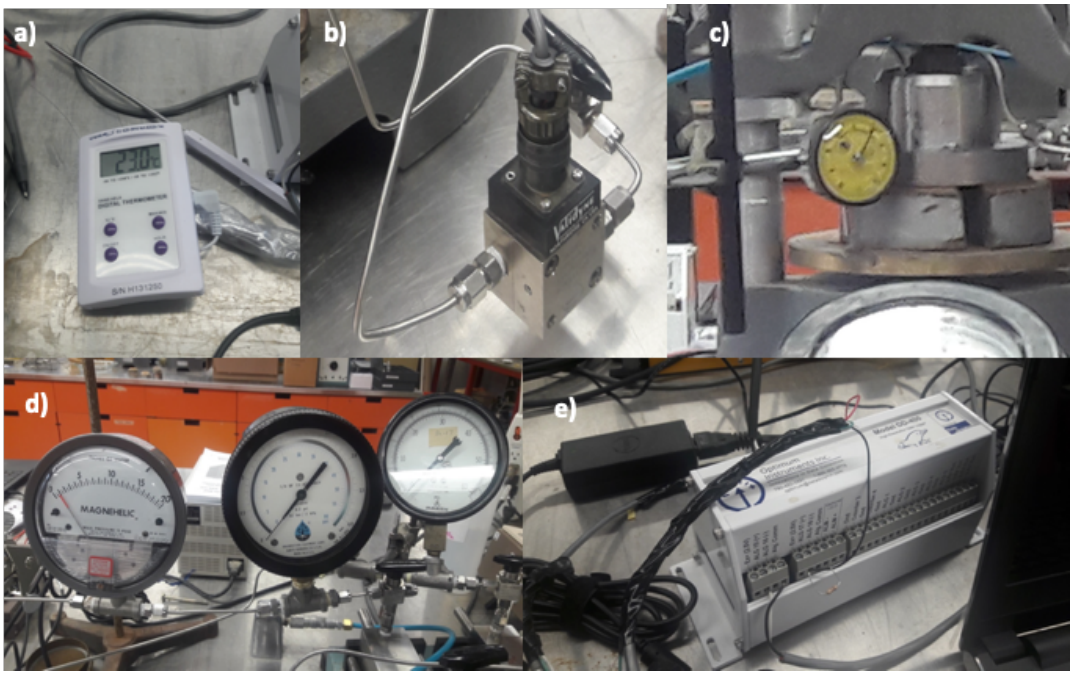

Figure 4.9. The monitoring system apparatus, including (a) the HB Instrument VWR hand-held digital thermometer, (b) the differential pressure transducer Validyne D15-42N1S5A, (c) the dial gauge, (d) the line pressure transducers, and (e) the Optimum Instruments data dolphin model 400.

4.4 Approximation of Osmotic Pressure and Osmotic Efficiency

The theoretical osmotic pressure ($\Delta\pi$) during chemical osmosis was approximated using Eq. 2.1, based on the total major cation and anion concentration difference of the synthetic fluids (Na^+, K^+, Mg^{2+}, Cl^-, SO_4^{2-}, HCO_3^-) circulated at the top and bottom boundaries. The actual osmotic pressure (ΔP) during chemical osmosis was approximated based on the DP fluctuation monitored by the DPT during the chemical osmosis testing.

The osmotic efficiency (ω) of sample was approximated using the "equilibrium pressure" method (see Section 2.2.2 for detail). This method was chosen because it was the most convenient and most widely used laboratory testing method in the literature. According to Neuzil and Provost (2009), the ω determined by the "equilibrium pressure" method was actually an apparent value that lied in between the maximum ω and the minimum ω during the experiment. However, the ω should be reasonably accurate to show the semipermeability of Pierre Shale in this study. The height and cross-sectional area of sample for testing were 0.0087 m and 0.00317 m^2, so it was unlikely that the physical properties of sample were significantly heterogeneous. The KCl concentrations of synthetic fluids used for the chemical osmosis

testing were diluted (< 0.01 M), so it was unlikely that the C_{max} and C_{min} within the sample were significantly different from the C_{avg} when the chemical osmotic flow reached equilibrium.

4.5 Chemical Analyses

Chemical analyses were done on the fluids synthesized for the chemical osmotic circulations, as well as the fluids collected from the chemical osmotic circulation system. The chemical analyses consisted of atomic absorption spectrometry (AAS) tests (after ASTM D4691–17), atomic emission spectrometry (AES) tests (after ASTM D1976–18), ion chromatography (IC) tests (after ASTM D4327–17), and alkalinity tests (Hach method 8221). The results describe the chemical components of synthetic fluids and collected fluids. Charge-balance calculations were completed for synthetic fluids and collected fluids to ensure that the results from chemical analyses are representative. The TDS concentration approximations by EC probe provide a quick and reliable indicator for the change of TDS concentration in top circulation and bottom circulation over time.

4.5.1 Cation Concentration Analyses

The cation concentration analyses used the atomic absorption spectrometry method (AAS). After day 130, the cation concentration analyses of K^+ used the atomic emission spectrometry method (AES) due to a break-down of the K^+ hollow cathode lamp. The Thermo Scientific iCE 3000 series atomic absorption spectrometer (Figure 4.10) was used for both AAS and AES tests, which can be classified as examples of optical spectrometry (Andrade-Garda, 2009).

4.5.1.1 Atomic Absorption Spectrometry Tests

AAS tests were used to determine the major cation concentrations of collected fluids and synthetic fluids. The major cation species analyzed by the AAS tests were Na^+, K^+, Mg^{2+}, Ca^{2+}, Fe^{3+}. The samples collected during day 9 to 149 (n = 148), as well as the fluids synthesized during day 0 to 149 (n = 18) were analyzed using AAS tests.

During AAS analyses, hollow cathode lamps emitted element specific spectral lines and supplied an electromagnetic radiation source. This radiation was absorbed by the free atoms in gaseous state to excite the atoms to the vapour state with a higher energy level. The vaporized atoms were subsequently drawn into a flame provided by a universal finned 50 mm titanium burner (Andrade-Garda, 2009; Thermo Fisher Scientific Inc., 2011). The cation concentration in an unknown sample was determined based on the comparison between the

amount of radiation absorbed in the unknown sample and the calibrated radiation absorption curve constructed with standard solutions (samples of known concentrations) under the same conditions.

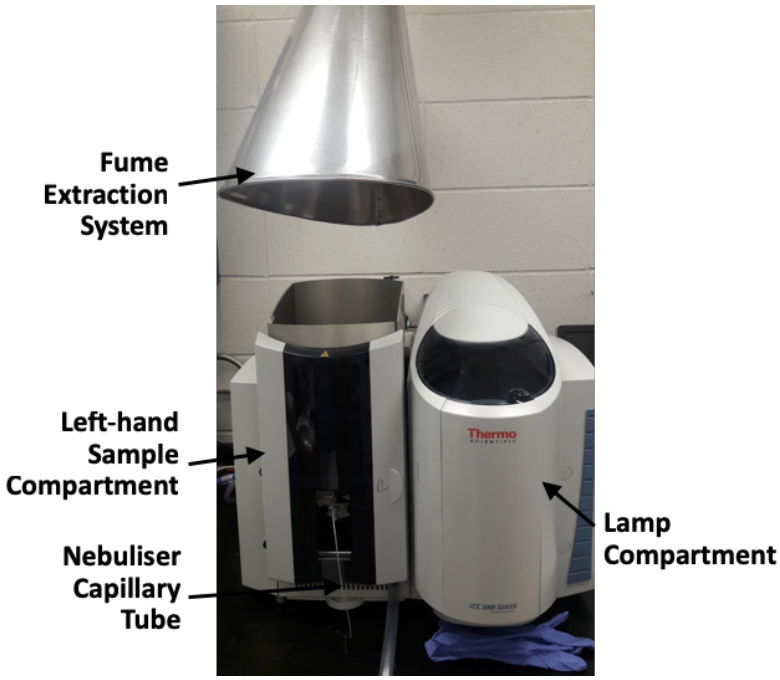

Figure 4.10. The Thermo Scientific iCE 3000 series Atomic Absorption Spectrometer

Dilution of the testing solutions with 2% (0.5 N) nitric acids was required because the detection accuracy in AAS tests becomes much lower when the radiation absorbance exceeds 0.8 A (Thermo Fisher Scientific Inc., 2011). Table 4.6 shows the concentration – radiation absorbance relationship for each cation species and the maximum concentration in which AAS tests can maintain a high accuracy. All dilutions were carried out using pipettes designed for transporting liquids with various ranges of volume. The volumetric ranges were 1 – 10 µL, 10 – 100 µL, 100 – 1000 µL, 1 – 10 mL. The pipettes were carefully chosen to match the transported liquid volumes.

Table 4.6. The concentration – radiation absorbance relationship and the maximum concentration for each cation species (AAS test)

Cation Species	**Concentration – Radiation Absorbance**	**Maximum Concentration (mg/L)**
Na^+	0.5 mg/L ~ 0.4 A	1.0
K^+	0.8 mg/L ~ 0.4 A	1.6

Cation Species	Concentration – Radiation Absorbance	Maximum Concentration (mg/L)
Mg^{2+}	0.3 mg/L ~ 0.4 A	0.6
Ca^{2+}	1.0 mg/L ~ 0.4 A	2.0
Fe^{3+}	5.0 mg/L ~ 0.4 A	10.0

All AAS tests began with calibration tests using three standard solutions, which consisted of concentrations 25%, 50% and 100% of the maximum concentration. Standard solutions were renewed every week to maintain good concentration accuracies. Following solution renewals, the calibration results may be slightly different, but all calibration curves should be linear. When the calibration curves were not linear, there was a high probability that the AAS test results were not accurate. If this occurred, the standard solutions were remade and the spectrometer was checked to make sure the calibration could work properly.

AAS tests with synthetic fluids and collected fluids were completed after calibration tests. The cation concentrations of the synthetic fluids and collected fluids were determined based on the calibrated radiation absorption curve constructed with standard solutions. A proper dilution of the testing solutions was important for an accurate measurement in the AAS tests. Table 4.7 shows the dilution ratio assigned for each cation concentration range, as well as the volume of fluid sample, and the volume of 2% (0.5 N) nitric acid required in 30 mL testing solutions to achieve the required dilution ratio.

Table 4.7. The dilution ratio assigned for each testing solution concentration range (AAS test)

Concentration Range (mg/L)	Dilution Factor	Volume of Fluid Sample (mL)	Volume of 2% (0.5 N) nitric acid (mL)
≤50; ≤30 (for Mg^{2+})	51	0.588	29.4
50 to 200	201	0.149	29.9
200 to 400	401	0.075	29.9

4.5.1.2 Atomic Emission Spectrometry Tests

AES tests were used to determine the K^+ concentrations of collected fluids and synthetic fluids, due to a break-down of the K^+ hollow cathode lamp. The samples collected during day

70 to 82 (n = 8) and after day 130 (n = 24), as well as the fluids synthesized after day 130 (n = 1) were analyzed using AES tests.

During the AES analyses, the testing solution was drawn into the flame through a nebuliser tube. The heat from the flame provided by a universal finned 50 mm titanium burner evaporated the solvent and broke the chemical bonds to create free atoms in a gaseous state. The thermal energy excited the atoms into excited electronic states that emitted light when they returned to the grounded electronic state. The wavelengths of atomic spectral lines identified the cation species. A hollow cathode lamp was not required for the AES analyses (Andrade-Garda, 2009; Thermo Fisher Scientific Inc., 2011). The intensity of emitted lights generated from an unknown sample was compared with the calibrated optical emission curve constructed with standard solutions to obtain the cation concentrations.

All AES tests started with calibration tests using standard solutions with known concentrations. The preparation of the standard solutions required the dilution with 3 g/L lanthanum (III) chloride heptahydrate ($LaCl_3 \cdot 7H_2O$) solution in a 1 to 10 ratio. The standard solution preparation was first carried out at the lowest concentration (11.4 mg/L) solution and the highest concentration (90.9 mg/L) solution. The other standard solutions were prepared by mixing these two standard solutions to varying degrees. The detail of the standard solution preparation method is shown in Table 4.8.

Table 4.8. The AES test standard solutions preparation method

Standard Solutions (mg/L)	**11.4 mg/L standard solution (mL)**	**90.9 mg/L standard solution (mL)**
11.4	30	/
22.7	30	5
37.9	20	10
68.2	10	25
90.9	/	30

The preparation of testing solutions also required the dilution with 3 g/L $LaCl_3 \cdot 7H_2O$ solution in a 1 to 10 ratio. The synthetic fluid and top collected fluid testing solutions were prepared by combining 1 mL of synthetic or collected fluids with 10 mL of $LaCl_3 \cdot 7H_2O$ solution. The dilution factor of solutions prepared by this method was 11. The bottom collected fluid testing solutions were prepared by adding $LaCl_3 \cdot 7H_2O$ powder into the fluids to adhere a 1 to 10 ratio. The dilution factor of solutions prepared by this method was 1.

4.5.2 Anion Concentration Analyses

The anion concentration analyses used the ion chromatography method (IC) and the alkalinity analyses method. IC is a common method for determining major anion concentrations. Alkalinity analyses is a common method for determining the ability of fluids to neutralize acids. The total alkalinity is generally contributed by the bicarbonate, carbonate and hydroxide components dissolved in the fluids.

4.5.2.1 Ion Chromatography Tests

Thermo Scientific ion chromatography system (IC system) (Figure 4.11) was used to determine the major anion concentrations. The IC system can be divided into two components. The first component is the Dionex AS-DV Autosampler and the second component is the Dionex Integrion HPIC System. The Dionex AS-DV Autosampler is a compact autosampler used to load the PolyVials containing testing solutions or rinse solutions (ultrapure (type 1) water), and to deliver the solutions to the Dionex Integrion HPIC System that runs the IC tests when the pump pressure and CD value become stable (Thermo Fisher Scientific Inc., 2012, 2016).

The IC system separated individual ion species, and detected and quantified trace elements using the conductivity detection method (CDM) (Fritz & Gjerde, 2009). The separation of ions was based on ionic exchange. The time required for sample ions to transport out of the ion exchange column (retention time) depended on the ionic size and charge. Therefore, ions were separated by the difference in retention times. After ion separation, CDM detected the analyte concentration through the linear relationship between the conductivity and the ionic concentration. The major anion species to be tested were F^-, Cl^-, NO_2^-, Br^-, NO_3^-, SO_4^{2-} and PO_4^{3-}. Among these anions, F^-, Cl^- and SO_4^{2-} were the species of interest. The anion concentrations of the samples collected during day 9 to 149 (n = 148), as well as the fluids synthesized during day 0 to 149 (n = 18) were analyzed using IC tests.

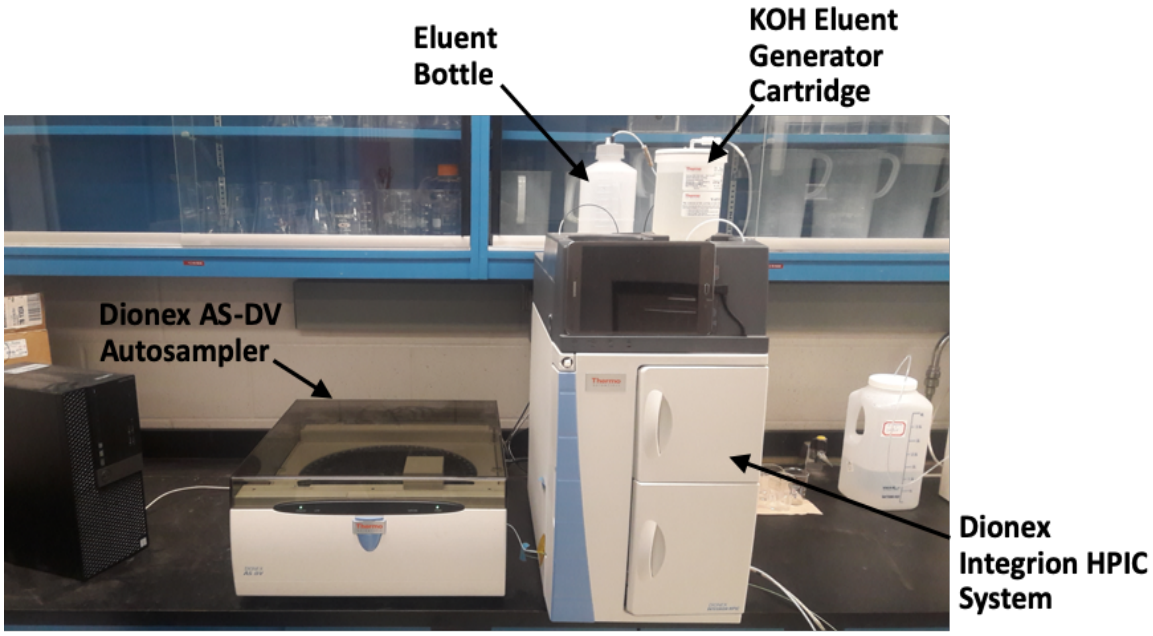

Figure 4.11. The Thermo Scientific ion chromatography system

Dilution with ultrapure water (type 1) was required because the detection accuracy of IC tests would be reduced when the anion concentrations of testing solutions were too high. All dilutions were done automatically with a Fisher Scientific Hamilton™ Microlab™ 600 Diluter / Dispenser System. This diluter / dispenser system has two high precision bubble-free prime syringes with greater than 99% accuracy. The small syringe has a volumetric range of 1 to 1000 µL, and the large syringe has a volumetric range of 50 to 50000 µL (Hamilton Company, 2008). The range of concentration suitable for IC tests depended on the specific anion type. Table 4.9 shows the maximum concentration allowed for each major anion species in IC tests.

Table 4.9. The maximum anion concentrations allowed in IC tests

	F^-	Cl^-	NO_2^-	Br^-	NO_3^-	SO_4^{2-}	PO_4^{3-}
Max. Concentration (mg/L)	4	20	20	20	20	20	40

IC tests were calibrated using three standard solutions diluted from the Dionex™ Combined Seven Anion Standard II solution. The dilution ratios were 1 : 100, 1 : 19 and 1 : 4. Each calibration test is valid for approximately four months.

The anion concentrations of synthetic fluids and collected fluids were determined based on the calibration curves constructed with standard solutions. A proper dilution was important

for an accurate detection in AAS tests. Table 4.10 shows the dilution ratio assigned for each anion concentration range, also the volume of fluid sample and ultrapure water (type 1) required in 5 mL testing solutions to achieve such dilution ratio.

Table 4.10. The dilution ratio assigned for each testing solution concentration range (IC test)

Concentration Range (mg/L)	**Dilution Factor**	**Volume of Fluid Sample (mL)**	**Volume of Ultrapure (Type 1) Water (mL)**
≤80 (for F^-)	21	0.238	4.76
≤400	26	0.192	4.81
80 to 200 (for F^-) 400 to 1000	51	0.098	4.90

4.5.2.2 Alkalinity Analyses

Alkalinity analyses used the titration-based method (Hach method 8221) (Hach Company, 2017) to determine the ability of fluids to neutralize acids (Figure 4.12). In this method, 0.02 N sulphuric acid (H_2SO_4) was slowly added to the testing solution mixed with bromcresol green – methyl red indicator through a burette, until the pH of testing solution reached 4.5. By knowing the volume of 0.02 N H_2SO_4 added to the testing solution (A_{H2SO4}) and the volume of original testing solution (V_{alk}), the concentration of calcium carbonate ($CaCO_3$) could be calculated using Eq. 4.7.

$$CaCO_3 \text{ concentration} = \frac{A_{H2SO4} \times N_{H2SO4} \times 50{,}000}{V_{alk}} \quad \text{(Eq. 4.7)}$$

where $CaCO_3$ concentration ($mg \cdot L^{-1}$), A_{H2SO4} (mL), N_{H2SO4} is the normality of sulphuric acid (0.02 N), V_{alk} (mL).

The $CaCO_3$ concentration measured by the alkalinity does not imply that there is $CaCO_3$ in the fluids. The $CaCO_3$ concentration is a summary term for hydrogen carbonate (HCO_3^-), carbonate (CO_3^{2-}) and hydroxide (OH^-) concentrations (Snoeyink & Jenkins, 1980). The fluid pH has to be measured before performing each alkalinity test. If the amount of acid required to reach pH 8.3 is equal to the amount of acid required to change the pH from pH 8.3 to pH 4.5, the fluid only contains CO_3^{2-} (no OH^-). If the pH is lower than 8.3, and a certain amount of acid is required to reach pH 4.5, the fluid only contains HCO_3^- (no CO_3^{2-} and OH^-). If a certain amount of acid is required to reach pH 8.3, but no acid is required from pH 8.3 to pH 4.5, the

fluid only contains OH^-. The conversion between $CaCO_3$ and HCO_3^- could be calculated using Eq. 4.8.

$$HCO_3^- \text{ concentration } = 1.22 \times CaCO_3 \text{ concentration} \qquad \text{(Eq. 4.8)}$$

where HCO_3^- concentration ($mg \cdot L^{-1}$), $CaCO_3$ concentration ($mg \cdot L^{-1}$).

All pH measurements were completed using a Thermo Scientific Orion 3-Star pH meter (Thermo Fisher Scientific Inc., 2010). Calibration of the Thermo Scientific Orion 3-Star pH meter was completed weekly using pH 4.01, 7.00 and 10.0 buffer solutions. At least 96% accuracy was required for a successful pH meter calibration. If the accuracy was less than 96%, calibration would be repeated until the accuracy reached 96%.

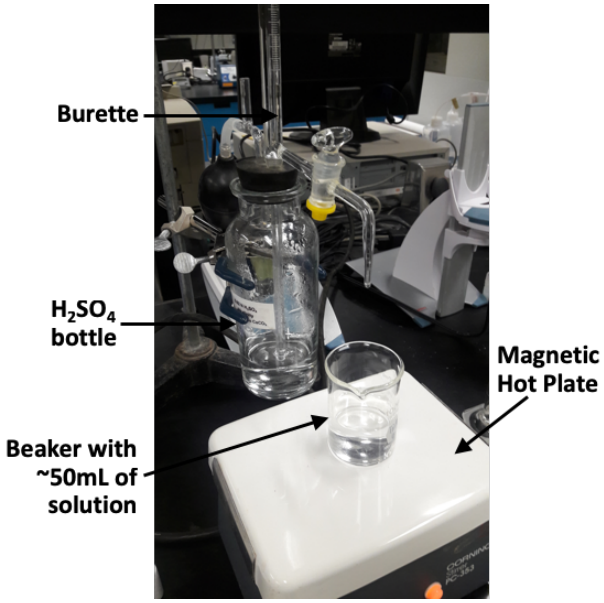

Figure 4.12. The alkalinity analyses apparatus set-up

The HCO_3^- concentrations of fluids synthesized during day 0 to 149 (n = 18), as well as the samples collected during day 9 to 149 (n = 132) were analyzed using alkalinity tests. It should be noted that alkalinity tests could not be carried out for the bottom collected fluids during day 70 to 82 (n = 4) and after day 130 (n = 12) because the K^+ concentration testing method changed from AAS to AES. $LaCl_3 \cdot 7H_2O$ powder was added to the bottom collected fluids during the testing solution preparation process. This step was necessary to produce testing solutions suitable for the AES tests. However, the fluids were altered and therefore not suitable for alkalinity tests.

4.5.3 Charge Balance Calculation

Due to electroneutrality, the total sum of all positive charges (cations) should have equaled to the total sum of all negative charges (anions) in solution. However, analytical errors and / or unanalyzed constituents cause electrical imbalances. Charge balance error (CBE) is the extent of electrical imbalance. The cation and anion concentrations are considered representative when the CBE is within ±5%. The CBE was calculated using Eq. 4.9 (Appelo & Postma, 2005).

$$\mathrm{CBE} = \frac{\sum \mathrm{cations} + \sum \mathrm{anions}}{\sum \mathrm{cations} - \sum \mathrm{anions}} \times 100\% \qquad \text{(Eq. 4.9)}$$

where CBE is the charge balance error (%), $\sum \mathrm{cations}$ is the total cation electrochemical equivalence (meq · L^{-1}), $\sum \mathrm{anions}$ is the total anion electrochemical equivalence (meq · L^{-1}).

The CBE of the samples collected during day 9 to 149 (n = 132), as well as the fluids synthesized during day 0 to 149 (n = 18) were calculated using Eq. 4.9. It should be noted that the CBE could not be calculated for the bottom collected fluids during day 70 to 82 (n = 4), and after day 130 (n = 12) due to the reason described above in Section 4.5.2.2. Therefore, the collected data was not sufficient for CBE calculations.

4.5.4 Total Dissolved Solutes Concentration Approximation

EC measurements are a quick and reliable indicator for the change of TDS concentration in the top and bottom circulation fluid over time. EC (μS/cm) is approximately twice the TDS (mg/L). The Hach HQ40d EC probe was calibrated using a Hach standard NaCl solution with an EC of 1000 μS/cm and a TDS concentration of 491 mg/L. Calibration was completed by dipping the EC probe into the Hach standard NaCl solution (Hach Company, 2019). After calibration, the EC value should be exactly or very close (±10 μS/cm) to 1000 μS/cm.

The TDS concentrations of the samples collected during day 9 to 149 (n = 148), as well as the fluids synthesized during day 0 to 149 (n = 18) were measured using the EC probe. The deviation of EC measurements should be within ±20 μS/cm from the actual value. It should be noted that the TDS concentrations measured by the EC meter did not represent actual TDS concentrations of testing solutions, because the EC measurements were based on standard NaCl solution.

4.6 Solute Transport Numerical Analyses

Solute transport numerical analyses were done analytically based on the results from chemical analyses. The numerical analyses consisted of the change of solute mass within shale due to solute inflow and solute outflow, and the cumulative change of stored solute mass within shale. Fick's first law was used to approximate the diffusion coefficients. The important geochemical processes that affected the partitioning within shale (adsorption and desorption of cations) during chemical osmosis were also considered. The partitioning within shale was characterized using the partitioning coefficient and the concomitant retardation factor. Due to the sorption reactions, the quantities of cations stored within shale changed over time. The numerical analyses provide insights to understand the change of electrochemical properties of pore fluids over time, and the effectiveness of shale as a semipermeable membrane to restrict contaminant spreading.

4.6.1 Mass Balance Theory

In this study, the synthetic fluids circulated in the chemical osmotic circulation system and passed along the spiral channels at the ports of the top piston and base pedestal placed horizontally above and below the porous disks and the shale sample (Figure 4.13). The concentrations of fluids before passing along the top and bottom boundaries of sample are respectively represented by symbols C_{0t} and C_{0b}. The C_{0t} and C_{0b} should be equivalent to the concentrations of synthetic fluids produced for chemical osmosis circulation. The concentrations of synthetic fluids in each osmotic cycle were very consistent (see detail in Section 4.2.2), so both C_{0t} and C_{0b} in each osmotic cycle were very consistent. The C_{0t} and C_{0b} formed the concentration gradient across the sample at the initial time step (before the sample was subjected to solute diffusion).

The concentrations of fluids after passing along the top and bottom boundaries of sample are respectively represented by symbols C_t and C_b. Due to the solute diffusion across the sample, the C_t and C_b were not equivalent to the C_{0t} and C_{0b}. The C_t and C_b were subject to change depending on the K^+ and Cl^- diffusion during chemical osmosis. Cl^- is a non-reactive species and K^+ is a reactive species (Fetter, Boving, & Kreamer, 2018). The K^+ and Cl^- diffusion was initiated as a result of concentration differences (K^+ and Cl^-) between the top and bottom boundaries.

Under normal conditions, K^+ and Cl^- diffused through the sample from top to bottom since solutes always transport from higher to lower concentrations (Malusis *et al.*, 2003)

(Figure 4.13). The K^+ and Cl^- concentrations within porous disks were assumed to be equal to the K^+ and Cl^- concentrations of the fluids after passing along the sample (C_t and C_b).

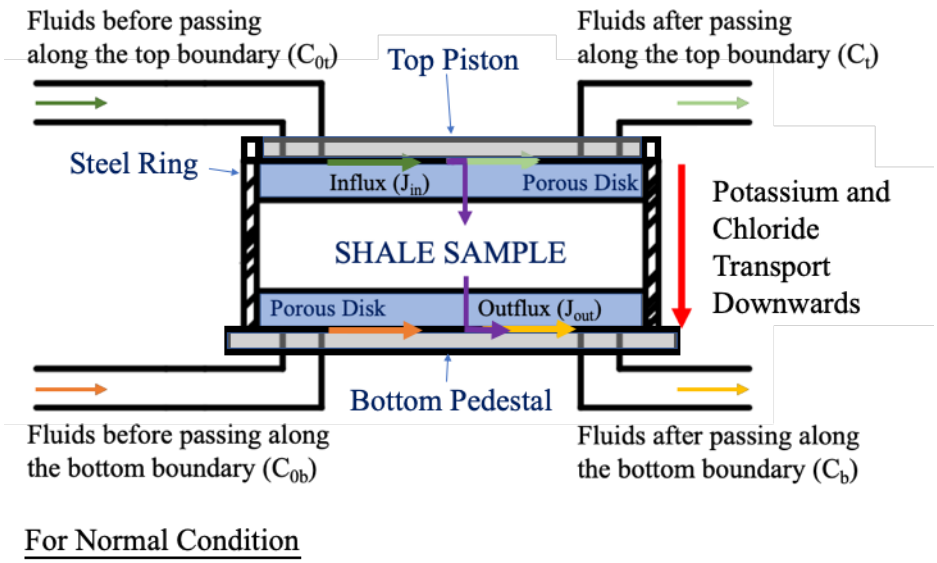

Figure 4.13. Schematic diagram of K^+ and Cl^- diffusion under normal conditions

There were two types of restrictions, partial restriction and complete restriction. The pattern of Cl^- diffusion during the partial anion exclusion period followed the Figure 4.13, except the influx were significantly lower than that under normal conditions (Figure 4.14). The pattern of Cl^- diffusion during the complete anion exclusion period was different from that shown in Figure 4.13. The influx of Cl^- from the synthetic fluids to the shale sample through the top boundary was completely prohibited. Instead, Cl^- flowed through the shale sample and exited at the top boundary (Figure 4.15). As a result, Cl^- exited the shale sample through both the top and bottom boundaries during the complete anion exclusion period.

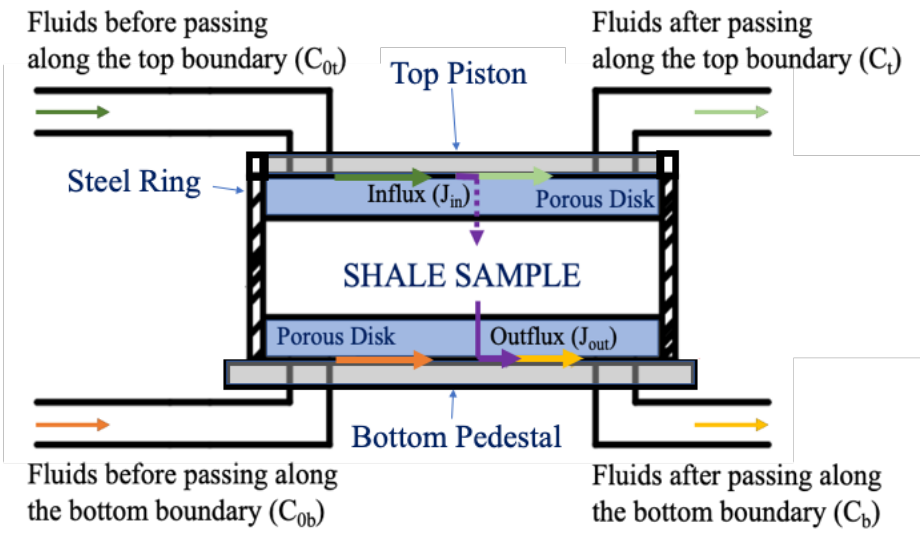

Figure 4.14. Schematic diagram of Cl^- diffusion during the partial anion exclusion period

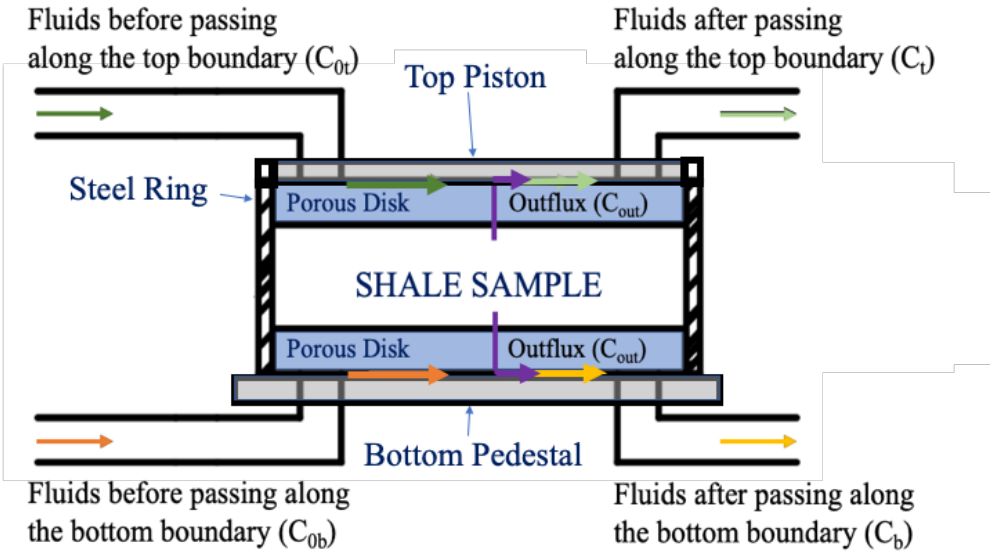

Figure 4.15. Schematic diagram of Cl^- diffusion during the complete anion exclusion period

The changes of K^+ and Cl^- mass within shale sample due to solute inflow (M_{in}) and solute outflow (M_{out}) during each circulation period were governed by the solute diffusion and the effective pore volume within shale sample. The changes of K^+ and Cl^- mass were calculated using Eq. 4.10 and Eq. 4.11. Negative values indicate that the outflow of solutes through the sample boundary was greater than the inflow of solutes.

$$M_{in} = (C_{0t} - C_t)(V_{shale} \times n_e)/A_{shale} \quad \text{(Eq. 4.10)}$$

$$M_{out} = (C_{0b} - C_b)(V_{shale} \times n_e)/A_{shale} \quad \text{(Eq. 4.11)}$$

where M_{in} ($kg \cdot m^{-2}$), M_{out} ($kg \cdot m^{-2}$), C_{0t} ($kg \cdot m^{-3}$), C_t ($kg \cdot m^{-3}$), C_{0b} ($kg \cdot m^{-3}$), C_b ($kg \cdot m^{-3}$), V_{shale} is the total volume of shale sample during chemical osmosis (m^3), n_e is the effective porosity (dimensionless), A_{shale} is the cross-sectional area of shale sample (m^2).

The summaries of M_{in} and M_{out} ($\sum M_{in}$ and $\sum M_{out}$) were calculated for the 2nd and 3rd osmotic cycles to understand how the K^+ and Cl^- influx and outflux brought the cumulative change of K^+ and Cl^- stored mass within shale sample ($\sum M_{stored}$) during each osmotic cycle. Followed up was the slope constructions between the cumulative change of K^+ and Cl^- mass within shale sample ($\sum M_{in}$ and $\sum M_{out}$) and the duration of experiment. These slopes could easily reflect how the M_{in} and M_{out} changed over time, and whether these parameters had reached the steady state condition. When the changes of K^+ and Cl^- mass within shale sample due to mass influx and mass outflux became steady, the slopes also became steady and consistent. The steady portions of slopes were used to determine the rate of K^+ and Cl^- mass influx (J_{in}) and mass outflux (J_{out}).

Mass balance theory governs the transport of non-reactive species and reactive species, through Eq. 4.12 and Eq. 4.13.

Non-reactive species:

$$J_{in} = J_{out} \quad \text{(Eq. 4.12)}$$

Reactive species:

$$J_{in} > J_{out} \quad \text{(Eq. 4.13)}$$

J_{out} is always significantly less than J_{in} for the transport of reactive species, since part of the solutes is adsorbed onto the mineral surfaces (Shackelford & Daniel, 1991).

4.6.2 Solute Diffusion

The transport of K^+ and Cl^- through the shale sample were governed by diffusion. (Shackelford & Daniel, 1991). The concentration gradient ($\frac{dC}{dx}$) was induced by the difference between the concentrations of synthetic fluids, with the consideration of solute diffusion. Fick's first law can only approximate D^* at steady-state ($J_{in} = J_{out}$). Therefore, Fick's first law was

used to approximate the D^* of non-reactive species (i.e. Cl^-) at steady-state (Eq. 4.14 and Eq. 4.15). Fick's first law was used to approximate the average D^* of reactive species (i.e. K^+), assuming that the rate of K^+ mass flux within sample was within the range of J_{in} and J_{out}.

Diffusion coefficient of non-reactive species (i.e. Cl^-):
Through the top boundary:

$$J_{in} = -n_e D^* \frac{C_b - C_t}{h} \quad \text{(Eq. 4.14)}$$

Through the bottom boundary:

$$J_{out} = -n_e D^* \frac{C_b - C_t}{h} \quad \text{(Eq. 4.15)}$$

Average diffusion coefficient of reactive species (i.e. K^+):

$$\left(\frac{J_{in} + J_{out}}{2}\right) = -n_e D^* \frac{C_b - C_t}{h} \quad \text{(Eq. 4.16)}$$

where J_{in} ($kg \cdot m^{-2} \cdot s^{-1}$), J_{out} ($kg \cdot m^{-2} \cdot s^{-1}$), n_e (dimensionless), D^* ($m^2 \cdot s^{-1}$), C_b ($kg \cdot m^{-3}$), C_t ($kg \cdot m^{-3}$), h is the sample height (m).

4.6.3 Sorption Reactions

The important geochemical processes affecting partitioning include adsorption / desorption, precipitation, and dissolution. The consideration of partitioning is important when the J_{in} is greater than J_{out}, which is common for the diffusion of reactive species (ie. K^+). The partitioning is limited when J_{in} is close to J_{out}, which is common for the diffusion of non-reactive species (i.e. Cl^-). In this study, the key geochemical processes were sorption reactions (adsorption / desorption) (see Section 2.3.5), because the synthetic fluids circulated at the top and bottom boundaries of sample were very diluted (< 0.01 M), and the pH or oxidation-reduction gradients were also very gentle.

As K^+ was transported downward through the sample, adsorption-desorption reactions occurred between K^+ and other major cations in the shale. When K^+ was adsorbed onto the mineral surfaces, it occupied the regions that were originally occupied by other major cations. The sorption reactions led to the desorption of the other major cations from the mineral surfaces. The desorbed cations were subsequently transported out of the sample (Langmuir, 1997; Mitchell & Soga, 2005).

According to Section 2.3.4, the partitioning of solutes within shale is a process that separates a contaminant between the solid and fluid phases. The cumulative change of K^+ and Cl^- stored mass within shale sample ($\sum M_{stored}$) was the difference induced by the mass influx and the mass outflux (Eq. 4.17). $\sum M_{stored}$ was equal to the change of total K^+ and Cl^- mass stored within sample. The change of 'average' K^+ and Cl^- mass stored in the pore fluid (M_{fluid}) was determined using Eq. 4.18, as well as the change of 'average' solute concentration in pore fluid and the total pore volume. It was assumed that the 'average' solute concentration in pore fluid was the average between the synthetic fluids circulated at the top and bottom boundaries. The total pore volume was the volume of pores within shale sample effective for solute transport. Since Cl^- was a non-reactive solute species, there was not any Cl^- adsorption within the sample. All Cl^- stored within the sample was in fluid phase. The volume required to store the Cl^- in pore fluid (V_{Cl}) was approximated using Eq. 4.19, as well as the 'average' solute concentration in pore fluid and the total stored mass in sample. Then a comparison was done between the V_{Cl} and the total pore volume within sample. On the other hand, since K^+ was a reactive solute species, adsorption-desorption reactions occurred among K^+ and the major cations originally adsorbed within the sample. The cumulative change of K^+ mass involved in cation exchange (adsorbed on soil particles) ($\sum M_{solid}$) was determined using Eq. 4.20.

$$\sum M_{stored} = \sum M_{in} + \sum M_{out} \quad \text{(Eq. 4.17)}$$

where $\sum M_{stored}$ (kg), $\sum M_{in}$ (kg), $\sum M_{out}$ (kg).

$$M_{fluid} = \left(\left(\frac{C_{0t_2} + C_{0b_2}}{2}\right) - \left(\frac{C_{0t_1} + C_{0b_1}}{2}\right)\right)(V_{shale} \times n_e) \quad \text{(Eq. 4.18)}$$

where M_{fluid} (kg), C_{0t_2} and C_{0b_2} are the concentrations of synthetic fluids at the top and bottom boundaries at current osmotic cycle ($kg \cdot m^{-3}$), C_{0t_1} and C_{0b_1} are the concentrations of synthetic fluids at the top and bottom boundaries at previous osmotic cycle ($kg \cdot m^{-3}$), V_{shale} (m^3), n_e (dimensionless).

$$V_{Cl} = \frac{M_{stored}}{\left(\frac{C_{0t_2} + C_{0b_2}}{2}\right)} \quad \text{(Eq. 4.19)}$$

where V_{Cl} (m^3), M_{stored} is the mass of Cl^- stored in pore fluid in each circulation period (kg), C_{0t_2} ($kg \cdot m^{-3}$), C_{0b_2} ($kg \cdot m^{-3}$).

$$\sum M_{solid} = \sum M_{stored} - M_{fluid} \quad \text{(Eq. 4.20)}$$

where $\sum M_{solid}$ (kg), $\sum M_{stored}$ (kg), M_{fluid} (kg).

The partitioning (or distribution) coefficient (K_d) is defined as the ratio between the quantity of a solute species adsorbed on the soil particles (S) and the concentration of a solute species retained in pore fluids (C) (Eq. 2.17). The K_d of K^+ during chemical osmosis were calculated using Eq. 4.21.

$$K_d = \frac{S}{C} = \frac{\sum M_{solid}/M_{dry}}{(\frac{C_{0t_2}+C_{0b_2}}{2})-(\frac{C_{0t_1}+C_{0b_1}}{2})} \quad \text{(Eq. 4.21)}$$

where K_d ($m^3 \cdot kg^{-1}$), S ($kg \cdot kg^{-1}$), C ($kg \cdot m^{-3}$), $\sum M_{solid}$ (kg), M_{dry} is the dry mass of shale sample (kg), C_{0t_2} ($kg \cdot m^{-3}$), C_{0b_2} ($kg \cdot m^{-3}$), C_{0t_1} ($kg \cdot m^{-3}$), C_{0b_1} ($kg \cdot m^{-3}$).

Eq. 4.21 shows that M_{dry} was required for the determination of K_d. However, M_{dry} was not measured before the start of chemical osmosis testing. Therefore, the calculated M_{dry} was applied to determine K_d. The calculated $M_{dry}$was determined using Eq. 4.22, as well as the void ratio (e), bulk density (ρ_b) and V_{shale},. The typical range of ρ_b of shale is 2060 kg/m^3 to 2670 kg/m^3. It was assumed that the ρ_b of sample was 2550 kg/m^3 in the calculation of M_{dry}.

$$M_{dry} = \frac{\rho_b}{1+e} V_{shale} \quad \text{(Eq. 4.22)}$$

where M_{dry} (kg), ρ_b ($kg \cdot m^{-3}$), e (dimensionless), V_{shale} (m^3).

The retardation factor (R_d) was directly proportional to K_d. In this study, R_d was determined based on K_d using Eq. 4.23.

$$R_d = 1 + \frac{\rho_b K_d}{n} \quad \text{(Eq. 4.23)}$$

where R_d (dimensionless), ρ_b ($kg \cdot m^{-3}$), K_d ($m^3 \cdot kg^{-1}$), n (dimensionless).

Due to the adsorption-desorption reactions within sample, the amount of major cations (K^+, Na^+, Mg^{2+}, Ca^{2+}, Fe^{3+}) stored within the shale sample changed over time. Since each cation type has a different molar mass and electric charge, it is better to standardize and compare the change of cation amounts stored within shale sample by equivalent. An equivalent is the amount of solute that reacts with an arbitrary amount of another solute in a given chemical reaction. The cumulative change of cation amounts stored within the sample ($\sum Q_{stored}$) was

determined using Eq. 4.24. Negative values indicate that the amount of solutes stored within the sample decreased.

$$\sum Q_{stored} = (\sum M_{stored} / M) \times z \qquad \text{(Eq. 4.24)}$$

where $\sum Q_{stored}$ (Eq), $\sum M_{stored}$ (kg), M is the molar mass of cations (kg · mol^{-1}), z is the electric charge of cations (Eq · mol^{-1}).

4.7 Validity of Chemical Osmosis Testing

Since there is no conventional system set-up for chemical osmosis testing, the chemical osmosis circulation system used in this study was designed following the Malusis *et al.* (2001) . Four compliance tests were completed prior to the actual testing to review the testing method and system, and to optimize the validity of chemical osmosis testing. In the first compliance test, leakage occurred during each fluid replenishment. As a result, the osmotic pressures fluctuated violently and did not reflect the semipermeability of sample. In the second, third, and fourth compliance tests, the osmotic pressures could not build up and preferential solute transport occurred because either there was crack in the sample or the sample was not placed properly into the chemical osmosis circulation system. During the second and third compliance tests, two separate P/V controllers were placed within the chemical osmosis circulation system to collect fluids during each circulation period. These two P/V controllers were removed from the circulation system during the actual testing because these fluids could be stored within the pump and collected during each fluid replenishment period. These compliance tests are important to the successful performance of chemical osmosis testing and the optimization of testing results' repeatability.

The repeatability of the chemical osmosis testing results highly depends on the test sample and circulation fluid preparations. The sample has to be placed horizontally, perfectly fit to the steel ring, and absolutely no gap between the sample and top piston & bottom pedestal. The sample has to be fully saturated and consolidated prior to the chemical osmosis testing. Damage has to be kept to minimum during test sample preparation. Any fractures in the sample would lead to the dissipation of osmotic pressure and the preferential solute transport. Since chemical osmosis testing is very sensitive to the concentration gradient across the sample, circulation fluids have to be prepared with accuracy and precision to keep the concentrations of fluids circulated at the top and bottom boundaries stable and consistent during each osmotic cycle of chemical osmosis testing. Stainless-steel porous disks should be placed on both sides

of sample to ensure the consistency of concentration gradient across the sample. The set-up of chemical osmosis circulation system is also very important to ensure the repeatability of the chemical osmosis testing results. The chemical osmosis circulation system has to be a closed system. Any leakage in the circulation system would lead to the dissipation of osmotic pressure. The set-up needs to be carefully designed to ensure that there is no osmotic flow due to the difference in pressure head or elevation head. The confining pressure applied to sample has to be consistent during the entire chemical osmosis testing. The pumping rates for the circulation at the top and bottom boundaries have to always be the same and consistent during the entire chemical osmosis testing to optimize the accuracy of the solute transport model.

CHAPTER 5: PRESENTATION OF DATA AND RESULTS

5.1 Introduction

This chapter presents the data collected from testing of the sample and fluid preparation phase, as well as the chemical osmosis testing phase. The osmotic pressures and osmotic efficiencies estimated from these test results are also provided along with the results of the quantitative interpretation of the solute transport rates across the shale during the chemical osmosis testing phase. The data collected from the testing of the sample and fluid preparation phase are provided in Section 5.2. The data collected from the testing of the chemical osmosis testing phase are provided in Section 5.3. The osmotic pressures and osmotic efficiencies of Pierre Shale are presented in Section 5.4. The chemistry test data is provided in Section 5.5. The solute transport interpretation is provided in Section 5.6.

5.2 Shale Sample and Circulation Fluid Preparation

5.2.1 Shale Sample Preparation

The first total vertical stress (σ_v) and fluid pressure at the bottom of sample (p_b) were 141 kPa and 25 kPa respectively. The σ_v and p_b were manually adjusted and increased over time during shale saturation and consolidation, as shown in Table 5.1. As the σ_v increased, the consolidation loading frame increased the vertical confinement towards the sample. As the p_b increased, the seepage force increased and the effective normal stress reduced. Both processes led to further sample consolidation. In the last adjustment, the σ_v and p_b were respectively 917 kPa and 200 kPa.

Table 5.1. The p_b and σ_v during the shale sample saturation and consolidation period

p_b (kPa)	**Δp (m)**	**σ_v (kPa)**	**Start time**	**End time**
25	2.51	141	0 hr	19 hr
50	5.03	252	19 hr	42.5 hr
75	7.54	363	42.5 hr	67.5 hr
150	15.1	695	67.5 hr	117.5 hr
250	25.1*	1320*	117.5 hr	118 hr*
80	8.04	725	118 hr	139 hr
90	9.05	954	139 hr	1320 hr

p_b (kPa)	Δp (m)	σ_v (kPa)	Start time	End time
100	0**	917	1360 hr	1720 hr
200	0**	917	1750 hr	1870 hr
* Steel ring popped out 118 hrs after the sample preparation started ** The system was closed at 1220 hr to terminate the creation of $\Delta\psi$ across sample				

The shale sample saturation and consolidation procedure continued for 1870 hours. The volumetric flow rate was monitored from 0 hour to 1220 hour. The Δp became zero after closing the system at 1220 hour. The K of shale sample was approximated using Eq. 4.2 based on the volumetric flow rate. Figure 5.1 shows the hydraulic conductivity of shale sample between 0 hour to 1220 hour. The figure shows that the accident at 118 hour (steel ring popped out) slightly altered the K, from 0.5×10^{-11} m/s before the accident to 4.5×10^{-11} m/s after the accident. The figure also shows that the K increased during the saturation phase, from 3.5×10^{-11} m/s to 6×10^{-11} m/s, and became stable, at 6×10^{-11} m/s, when the sample was close to fully saturation. A period of approximately 840 hours was required for the K to reach stability.

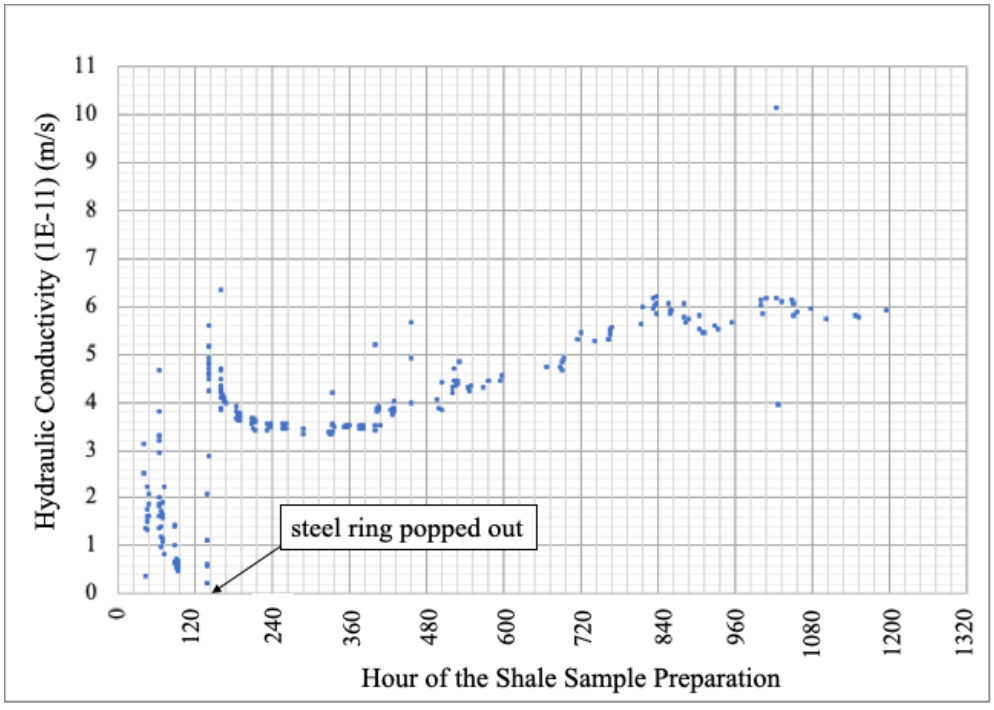

Figure 5.1. The hydraulic conductivity of shale sample (0 Hour to 1220 Hour)

During the shale sample preparation period, two back pressure tests were done, from 1320 hour to 1360 hour and from 1720 hour to 1750 hour. In both cases, the results indicated that the test specimen was not fully saturated. The third attempt of back pressure test started at

1870 hour and stopped at 3040 hour. The back-pressure test started by manually increased the σ_v applied by the pneumatic consolidation loading frame by 73.9 kPa (i.e. from 917 to 991 kPa), while ceased the impact of P/V controller towards the fluid pressure at the bottom of sample. Figure 5.2 shows the change of pressure in P/V controller, which reflected the change of fluid pressure at the bottom of sample over time. The pressure showed a steady increase and a concave curve when the pressure was reaching steady state. The pressure in P/V controller overall increased by 250 kPa.

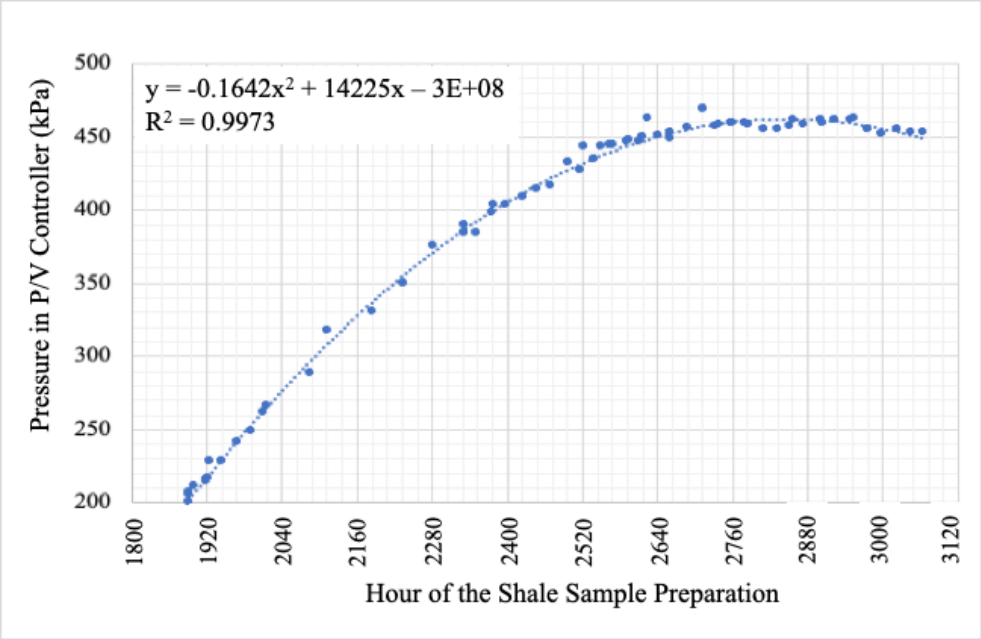

Figure 5.2. The pressure response of fully saturated shale (1870 hour to 3040 hour)

5.2.2 Circulation Fluid Preparation

The chemical osmosis circulation continued for 149 days. Since KCl, NaCl and $MgSO_4$ were the only chemicals added to the synthetic fluids, K^+, Na^+ and Mg^{2+} were the major cations in the fluids while Cl^-, SO_4^{2-} were the major anions in the fluids. Alkalinity analyses show that there was 4 – 10 mg/L of HCO_3^- in the synthetic fluids. The actual cation and anion concentrations of synthetic fluids circulated along the top and bottom boundaries are respectively provided in Appendix B (Tables B.1 and B.2). The concentration differences between the top and bottom boundaries are provided in Appendix B (Table B.3). Figures 5.3 to 5.5 show the actual major cation concentrations of the synthetic fluids for both the top circulation and bottom circulation. Figures 5.6 to 5.8 show the actual major anion concentrations of the synthetic fluids for top circulation and bottom circulation. The target cation and anion concentrations in the synthetic fluids (Table 4.4) are also shown in Figures

5.3 to 5.7 for comparison. Figure 5.3 to Figure 5.8 show that KCl was the main source of the ΔC. The KCl concentrations of the Type B and Type C synthetic fluids circulating at the top boundary were respectively 275 mg/L (0.0037 M) and 609 mg/L (0.0082 M) in the 2nd and 3rd osmotic cycles.

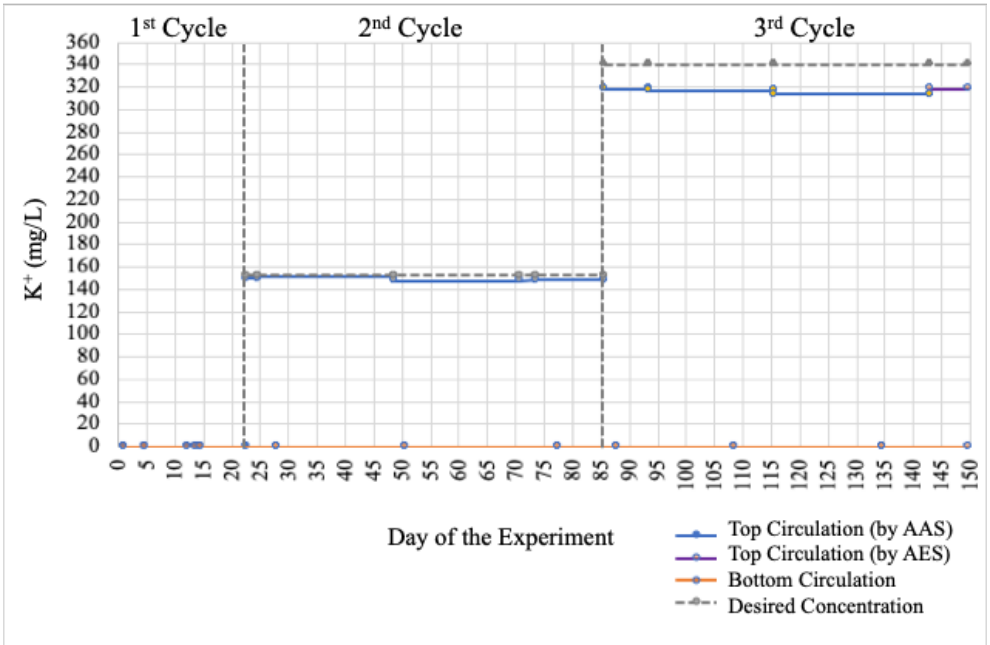

Figure 5.3. K^+ concentrations of synthetic fluids circulated at top and bottom boundaries

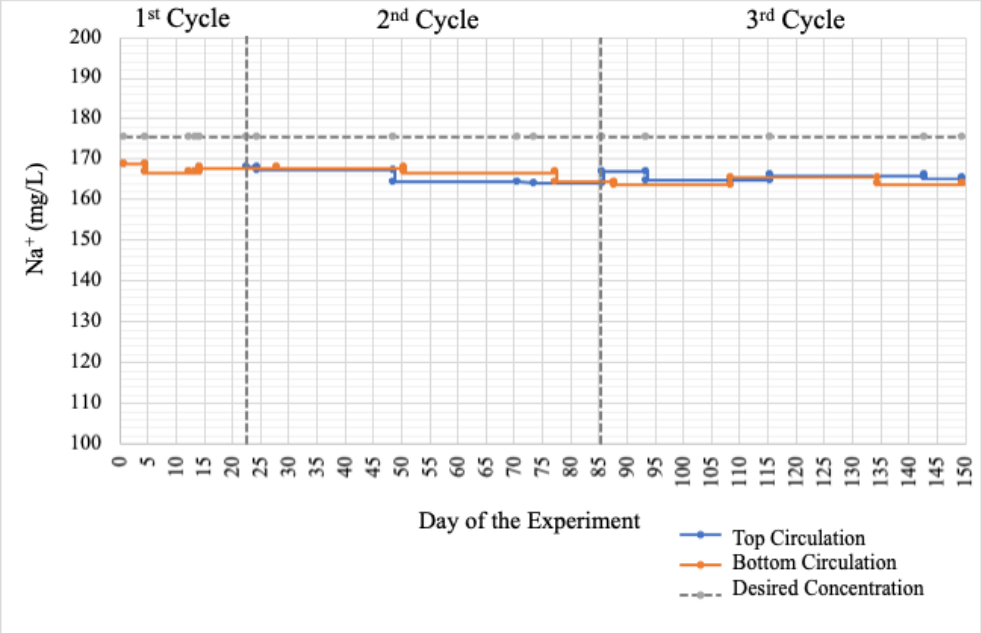

Figure 5.4. Na^+ concentrations of synthetic fluids circulated at top and bottom boundaries

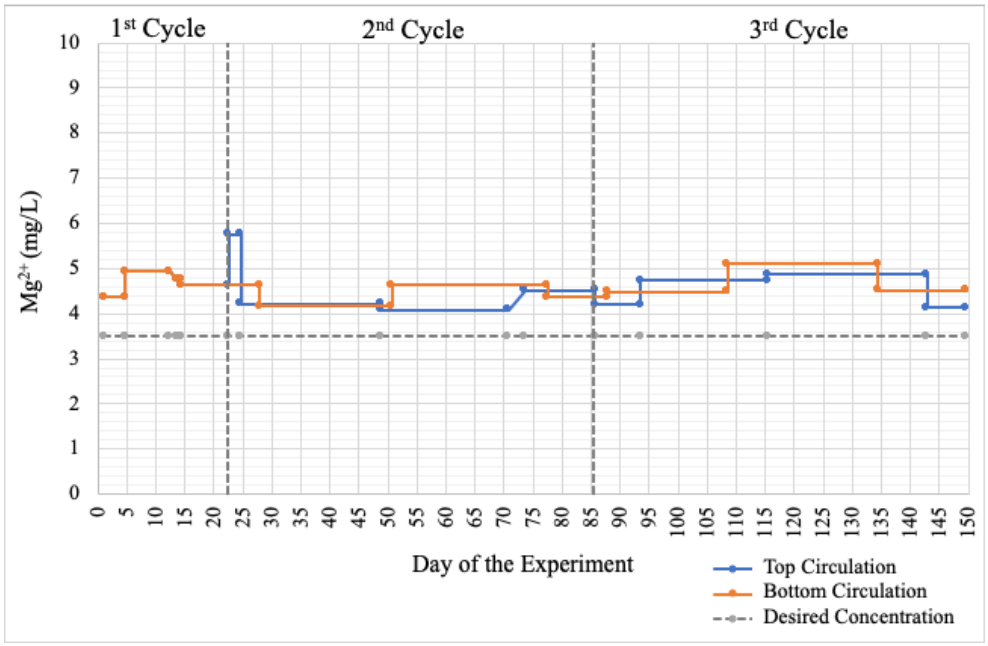

Figure 5.5. Mg^{2+} concentrations of synthetic fluids circulated at top and bottom boundaries

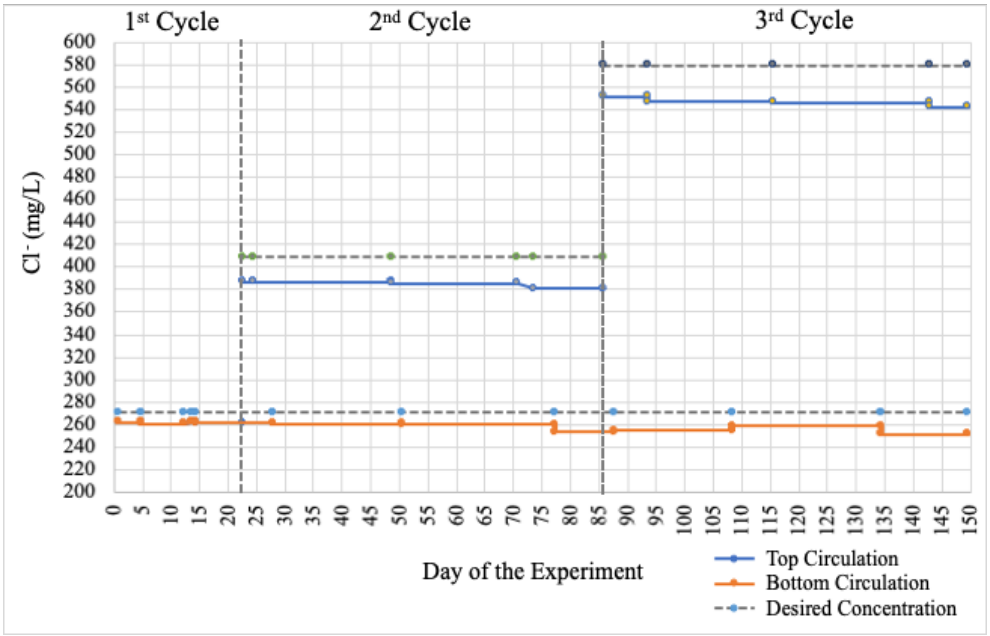

Figure 5.6. Cl^- concentrations of synthetic fluids circulated at top and bottom boundaries

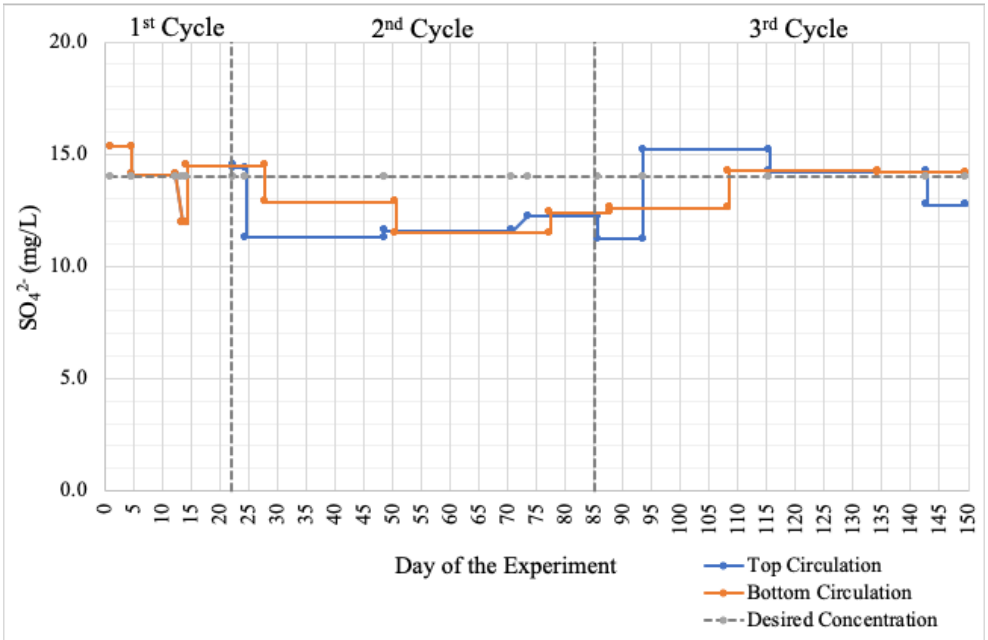

Figure 5.7. SO_4^{2-} concentrations of synthetic fluids circulated at top and bottom boundaries

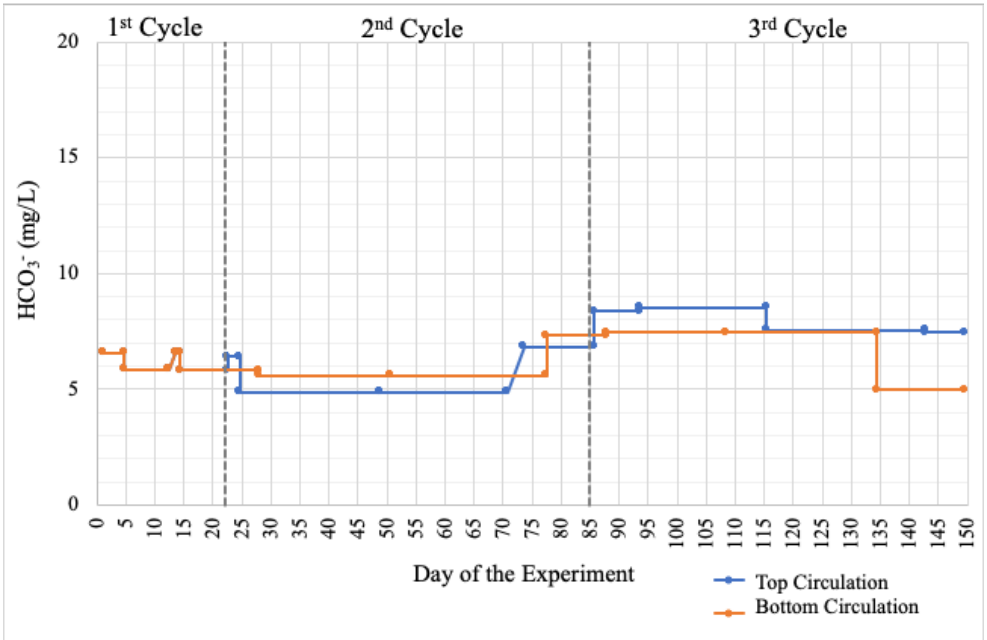

Figure 5.8. HCO_3^- concentrations of synthetic fluids circulated at top and bottom boundaries

5.3 Chemical Osmosis Testing

The value of σ_v was increased gradually on the shale sample until it reached 1660 kPa in preparation for the chemical osmosis testing phase. The shale height (h) decreased from 0.0087 m (initial, prior to loading) to 0.00584 m (following application of the load). Table 5.2 shows the one-dimensional constrained compressibility of shale sample (m_v) approximated during each step of loading. The results show that the m_v decreased gradually from 2.0×10^{-4}

kPa^{-1} to 9.0×10^{-5} kPa^{-1} as σ_v increased from 125 kPa to 1660 kPa. The m_v was assumed to be 9.0×10^{-5} kPa^{-1} (or 9.0×10^{-8} Pa^{-1}) during the chemical osmosis test when the σ_v was maintained at 1660 kPa. This value was slightly higher than the compressibility of shale in southern Saskatchewan (3.0×10^{-6} to 2.0×10^{-7} kPa^{-1}) (L. Smith et al., 2018).

Table 5.2. The approximation of the one-dimensional constrained compressibility of shale sample

σ_v (kPa)	$\Delta\sigma_v$ (kPa)	Δh (m)	h_i (m)	h_f (m)	m_v (kPa^{-1})	m_v (Pa^{-1})
125	125	2.08E-04	8.70E-03	8.49E-03	1.95E-04	1.95E-7
215	90	8.57E-04	8.49E-03	7.64E-03	1.09E-03	1.09E-6
400	185	7.05E-04	7.64E-03	6.93E-03	5.00E-04	5.00E-7
585	185	3.45E-04	6.93E-03	6.59E-03	2.70E-04	2.70E-7
770	185	2.32E-04	6.59E-03	6.35E-03	1.91E-04	1.91E-7
955	185	1.53E-04	6.35E-03	6.20E-03	1.30E-04	1.30E-7
1140	185	1.30E-04	6.20E-03	6.07E-03	1.14E-04	1.14E-7
1330	190	1.05E-04	6.07E-03	5.97E-03	9.37E-05	9.37E-8
1510	180	4.50E-05	5.97E-03	5.92E-03	4.09E-05	4.09E-8
1660	150	7.80E-05	5.92E-03	5.84E-03	8.92E-05	8.92E-8

There were three osmotic cycles in this study. In each osmotic cycle, the concentration gradient across the sample was different due to the different combinations of synthetic fluids being circulated along the top and bottom boundaries (Table 4.5). The 1st, 2nd, and 3rd osmotic cycles started respectively on day 1, day 22, and day 85. The testing data was collected up to day 149. T_{lab}, DP, Δh and LP were monitored during the chemical osmosis testing. Figure 5.9 shows the T_{lab} over time. During the experiment, T_{lab} mainly varied between 22 ℃ to 25 ℃, and sometimes went up to 26 ℃. The daily variation of T_{lab} was 2 – 3 ℃, but was lower during the day, and higher during the night. The exceptions occurred between day 56 to day 70, and day 105 to day 149 due to the operation of air-conditioning system (the daily variation of T_{lab} was 1 ℃ in these periods).

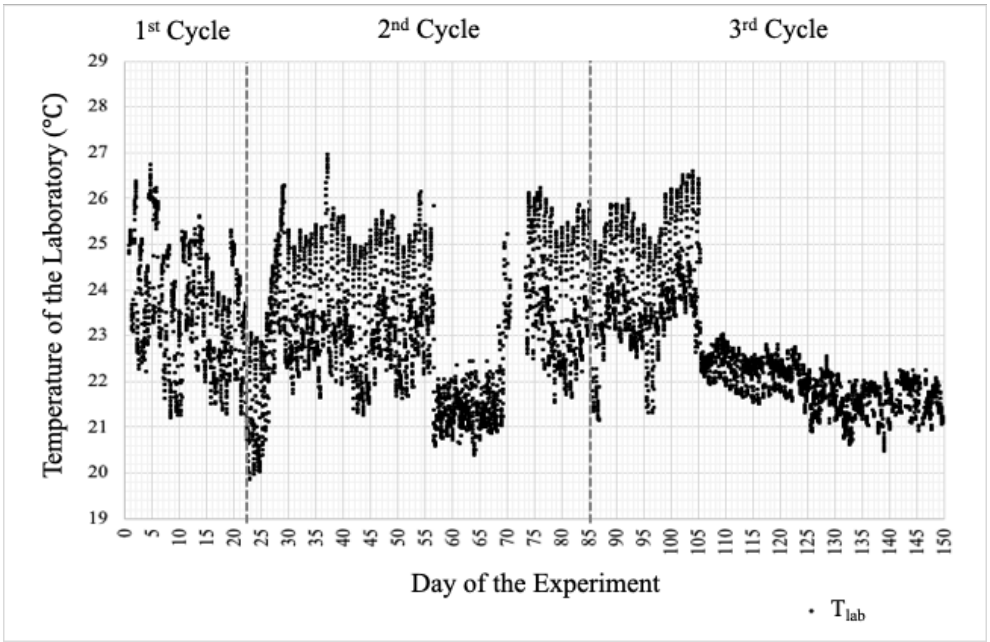

Figure 5.9. T_{lab} variation during the chemical osmosis testing

The water density (ρ_w) and the fluid volume within the closed system (V_w) variated corresponding to the T_{lab} variation during the chemical osmosis testing. Figure 5.10 shows the ρ_w over time, and Figure 5.11 shows the V_w over time. Figure 5.10 shows that the daily variation of ρ_w was 1 kg/m^3. The daily variation of ρ_w was 0.5 kg/m^3 between day 56 to day 70, and day 105 to day 149. The initial V_w was 1.4×10^{-5} m^3. Figure 5.11 shows that the daily variation of V_w was 1.0×10^{-8} m^3. The daily variation of V_w was 5.0×10^{-9} m^3 between day 56 to day 70, and day 105 to day 149.

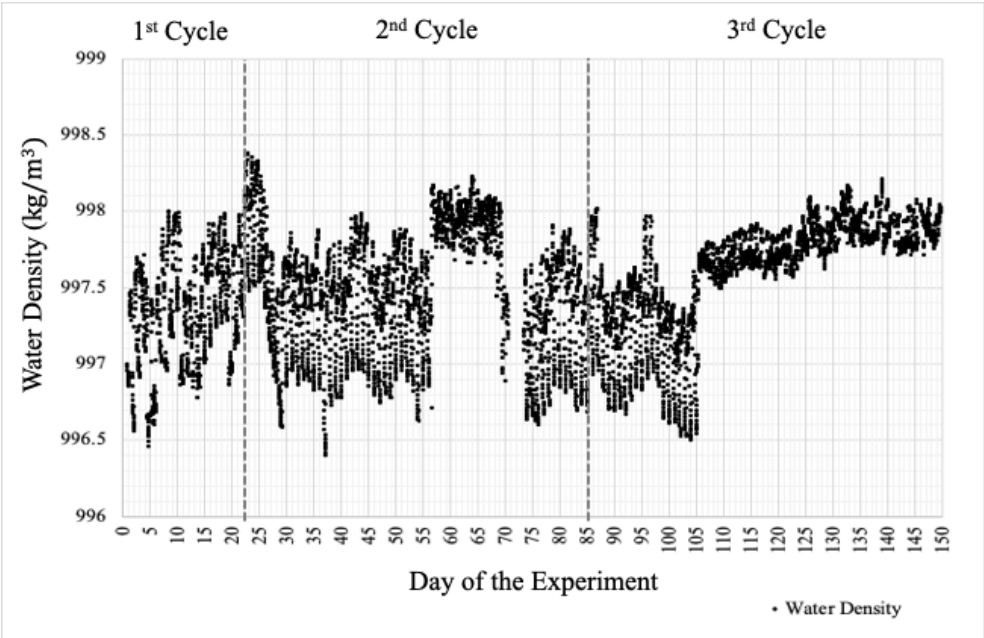

Figure 5.10. ρ_w variation corresponding to the change of T_{lab}

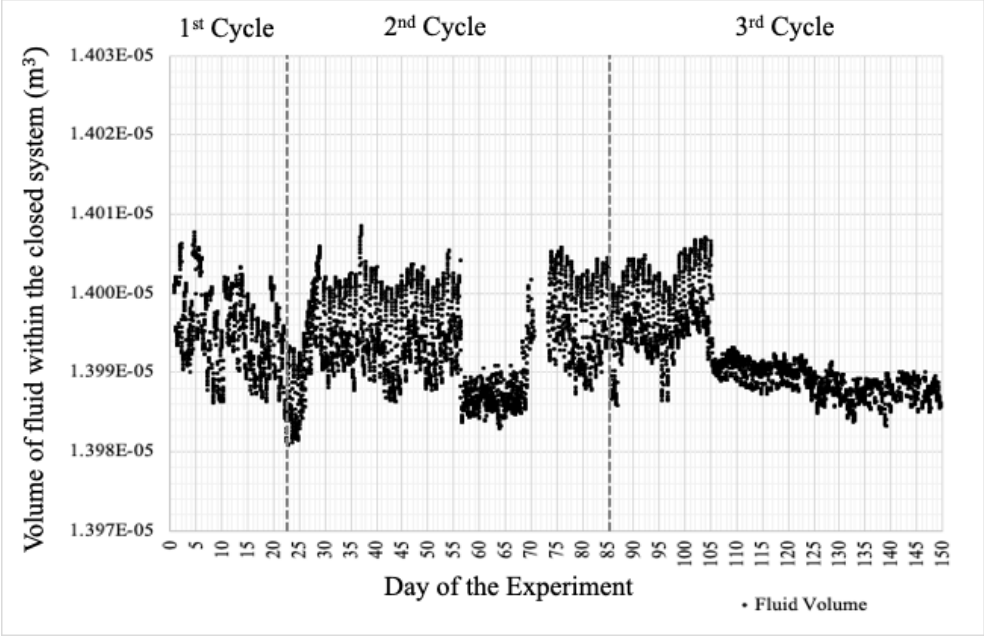

Figure 5.11. V_w variation corresponding to the change of T_{lab}

The Δp induced by the change of T_{lab} was calculated from the change of V_w. Therefore, Δp did not show direct relationship with T_{lab} (Figure 5.12). Instead, the Δp was directly related to the change of T_{lab} (the difference of T_{lab} between current record and previous record) (Figure 5.13).

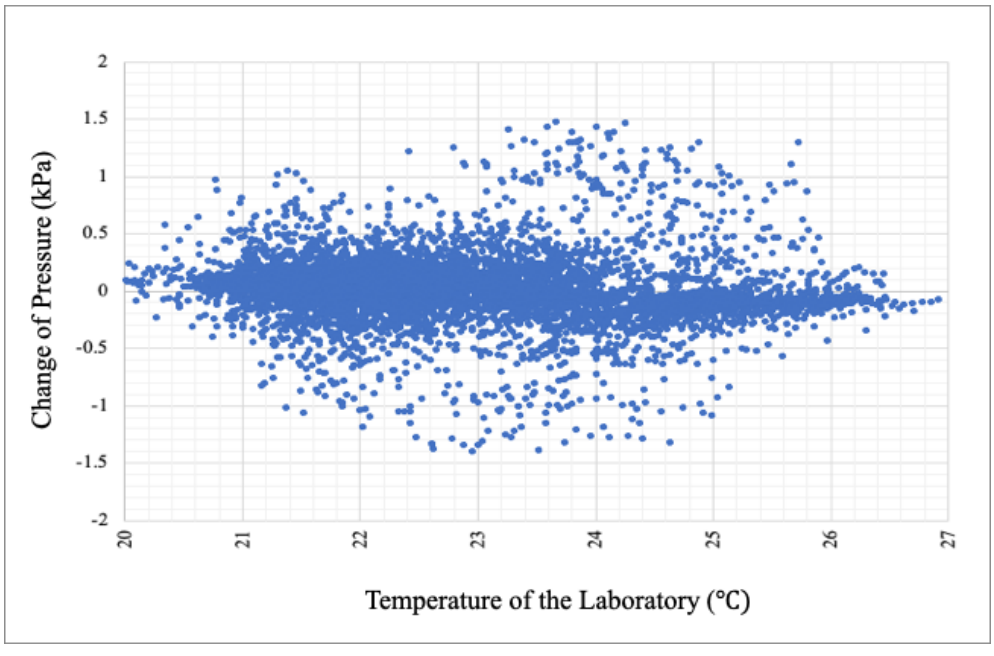

Figure 5.12. The change of Δp corresponding to T_{lab}

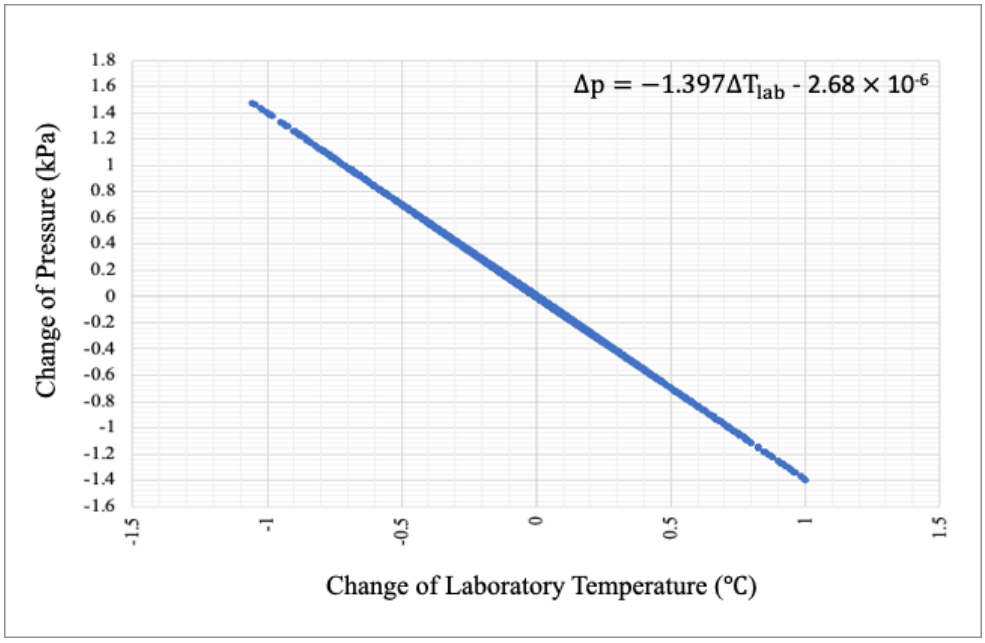

Figure 5.13. The change of Δp corresponding to the change of T_{lab}

During the 1st osmotic cycle (Figure 5.14), Type A solution was circulated along both the top and the bottom boundaries; therefore, there was no concentration gradient created and theoretically no DP should be present across the shale sample. Figure 5.14 shows the DP variation during the 1st osmotic cycle with the temperature effect minimized.

The DP decreased gradually for 8 days (from day 1 to day 9) until it reached -2.4 kPa. On day 10, the test apparatus was disassembled and the circulation system was opened to the atomosphere for 3 hours. The chemical osmosis test resumed on the same day. The apparatus was disassembled again on day 12, and the test resumed on day 13. The DP gradually decreased for 4 days (from day 14 to day 18) until it reached -2.4 kPa. The time required for the DP to stabilize at -2.4 kPa was half the time required during the first time due to the increase of pumping speed to 0.02 mL/min (twice as fast as the first time 0.01 mL/min). The DP fluctuated between -2.0 kPa to -2.4 kPa for 93.5 hours. It appears that when there was no ΔC across the sample (i.e. no concentration gradient), the DP was -2.4 kPa (-9.6 inches of water). Based on the results in the 1st osmotic cycle, the threshold could be any value within the range between -2.0 kPa and -2.4 kPa. The threshold was chosen to be -2.4 kPa since DP started at -2.4 kPa in both 2nd and 3rd osmotic cycles. Although theoretically no DP should be present across the sample due to the absence of ΔC, the presence of DP in this study was not an inaccuracy. The DP was generated due to the heterogeneity of pore size, pore structure, and mineralogy within the sample.

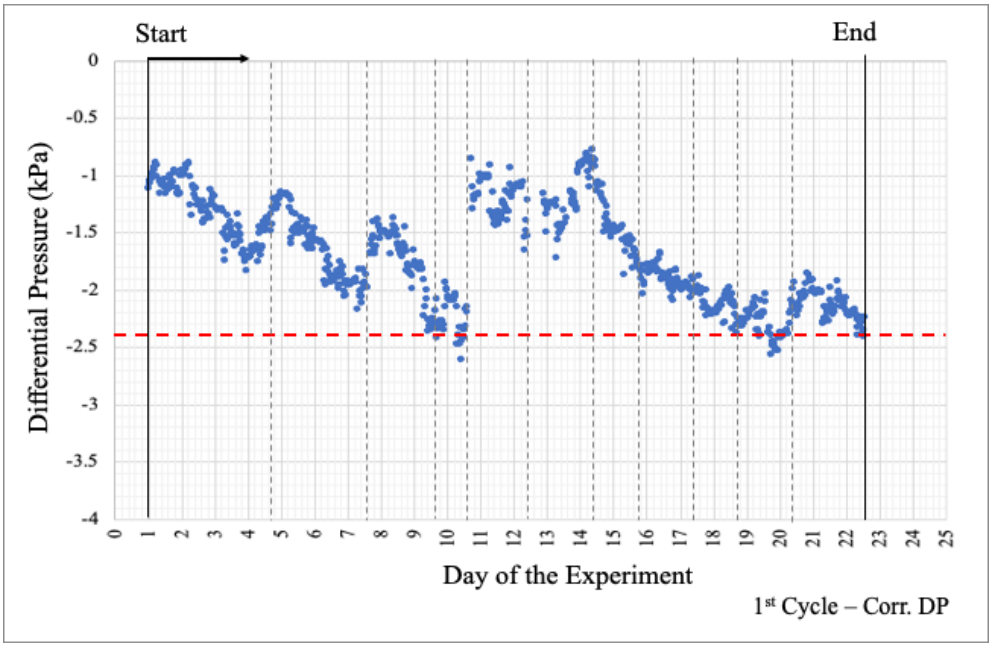

Figure 5.14. Corrected DP variation during the 1st osmotic cycle; grey dash lines represent fluid replenishing; red dash line represents the DP threshold

During the 2nd osmotic cycle (Figure 5.15), Type B solution (0.0037 M KCl) was circulated along the top boundary while Type A solution (0 M KCl) was circulated along the bottom boundary. In this case, the DP across the shale sample was influenced by both the ΔC and the physical properties of the sample. Based on the results from the 1st osmotic cycle, it was assumed that any DP higher than -2.4 kPa was induced by ΔC. Figure 5.15 shows the DP variation during the 2nd osmotic cycle with the temperature effect minimized.

After the 2nd osmotic cycle, the DP remained stable at -2.4 kPa for two days (day 22 to day 24). From day 24 to day 31, the DP increased from -2.4 kPa to -0.7 kPa. After the DP reached its peak, it gradually decreased from -0.7 kPa to -1.5 kPa between day 35 to 39. The decrease of DP started when the cumulative mass outflux of Cl^- reached steady state. From day 39 to day 70, the DP fluctuated around -1.5 kPa. The pump was found to be not working properly on day 70. The test apparatus was disassembled and the circulation system was opened to the atomosphere for 69 hours. The disassemblance of test apparatus led to the DP close to 0 kPa. The circulation resumed on day 73. On day 75, the DP returned to the same level before the break-down of the pump. The DP fluctuated around -1.5 kPa after day 75.

When the 'peak' DP was considered, DP increased from -2.4 kPa (-9.6 inches of water) to -0.7 kPa (-2.8 inches of water), therefore ΔP was 1.7 kPa (6.8 inches of water). When the 'residual' DP was considered, DP increased from -2.4 kPa (-9.6 inches of water) to -1.5 kPa (-6 inches of water), therefore ΔP was 0.9 kPa (3.6 inches of water).

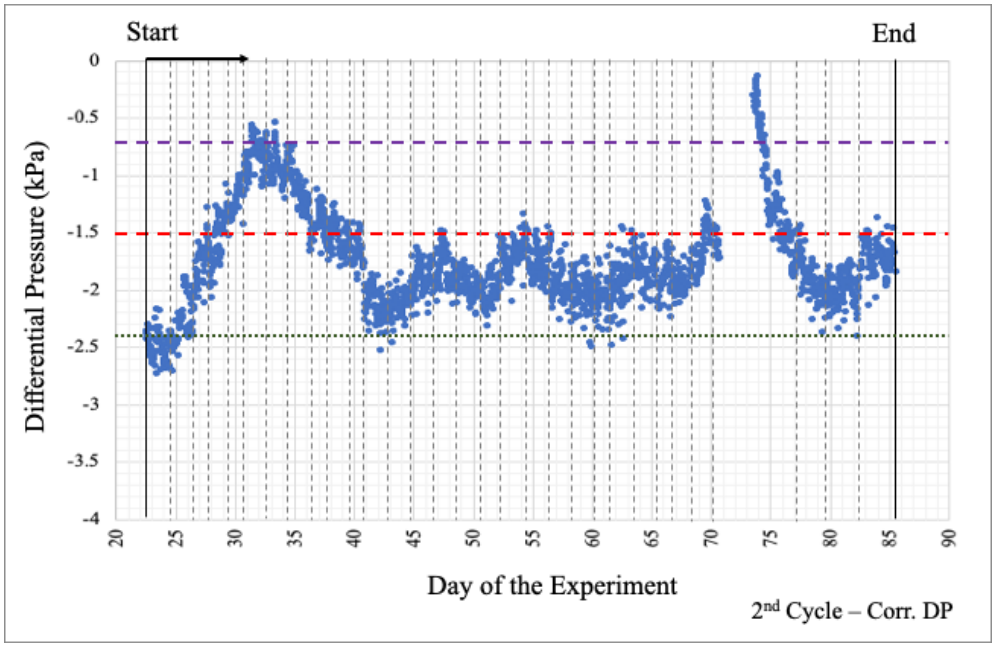

Figure 5.15. Corrected DP variation during the 2nd osmotic cycle; grey dash lines represent fluid replenishing; green dash line represents the threshold with concentration gradient; purple dash line represents the 'peak' DP; red dash line represents the 'residual' DP.

During the 3rd osmotic cycle (Figure 5.16), Type C solution (0.0082 M KCl) was circulated along the top boundary while Type A solution (0 M KCl) was circulated along the bottom boundary. In this case, the DP across the shale sample was influenced by both the ΔC and the physical properties of the sample. Based on the results from the 1st osmotic cycle, it was assumed that any DP higher than -2.4 kPa was induced by ΔC. Figure 5.16 shows the DP variation during the 3rd osmotic cycle with the temperature effect minimized.

After the 3rd osmotic cycle, the DP remained stable at -2.4 kPa for ten days (day 85 to day 95). DP in the 3rd osmotic cycle started at -2.4 kPa, which was the same as the 2nd osmotic cycle, due to the flushing of synthetic fluids through top and bottom circulation lines at a pumping speed of 1.83 mL/min. The increase of DP started on day 95. From day 95 to day 105, DP increased at a constant rate from -2.4 kPa to -0.9 kPa. The pump was replaced on day 105. The pump replacement induced the disruption of DP from day 105 to day 107. The DP increasing trend resumed at the same rate after day 107. The DP reached the peak at -0.8 kPa on day 110. After DP reached the peak,it decreased from -0.8 kPa to -1.4 kPa from day 110 to day 115. The decrease of DP started when the cumulative mass outflux of Cl^- reached steady state. The DP was stable at -1.4 kPa from day 115 to day 122. A second peak of DP occurred from day 124 to day 131, at -0.8 kPa. After the second peak of DP, DP dereased from -0.8 kPa to -1.7 kPa from day 131 to day 135. This DP decrease following the second peak (0.9 kPa)

was more than the DP decrease following the first peak (0.6 kPa). It was not evident that the DP decrease was related to the cumulative mass outflux of Cl^-. DP became stable at -1.4 kPa from day 145 to day 149.

When the 'peak' DP was considered, DP increased from -2.4 kPa (-9.6 inches of water) to -0.8 kPa (-3.2 inches of water), therefore ΔP was 1.6 kPa (6.4 inches of water). When the 'residual' DP was considered, DP increased from -2.4 kPa (-9.6 inches of water) to -1.4 kPa (-5.6 inches of water), therefore ΔP was 1.0 kPa (4 inches of water).

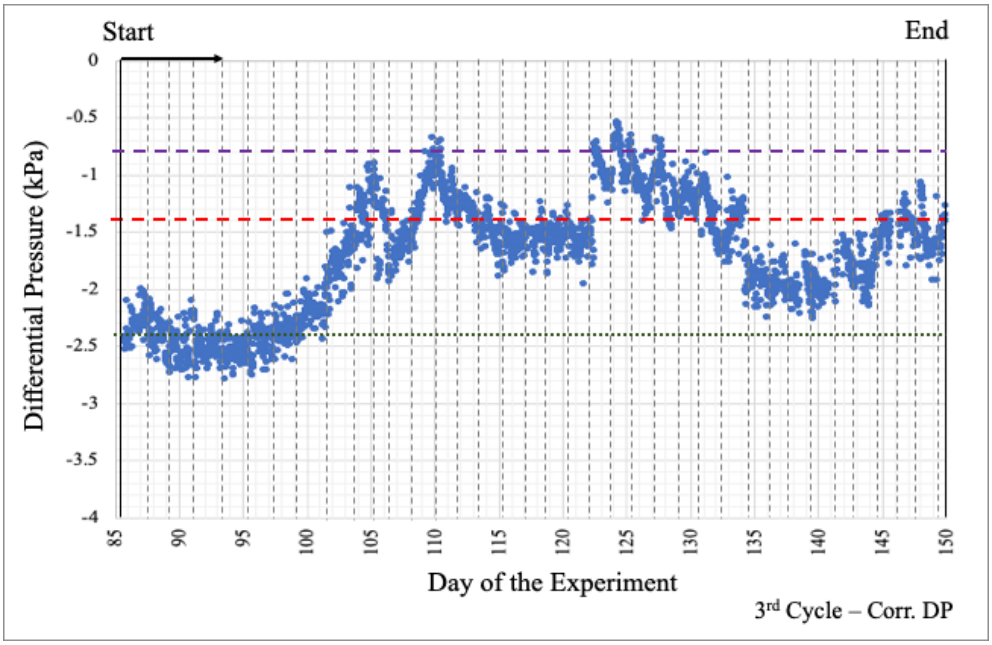

Figure 5.16. Corrected DP variation during the 3rd osmotic cycle; grey dash lines represent fluid replenishing; green dash line represents the threshold with concentration gradient; purple dash line represents the 'peak' DP; red dash line represents the 'residual' DP.

Sensitivity analyses were performed using the initial V_w values 1.0×10^{-5} m^3, 1.4×10^{-5} m^3, 2.0×10^{-5} m^3, and 3.0×10^{-5} m^3 (Figures 5.17 to 5.19). The separated graphs are provided in Appendix D. The combined graphs show that the general trends of corrected DP during the 1st, 2nd, and 3rd osmotic cycles were the same no matter the initial V_w values were assumed to be 1.0×10^{-5} m^3, 1.4×10^{-5} m^3, 2.0×10^{-5} m^3, and 3.0×10^{-5} m^3. However, as the initial V_w value increased, the variance belt (the difference between the maximum and the minimum DP) became thicker.

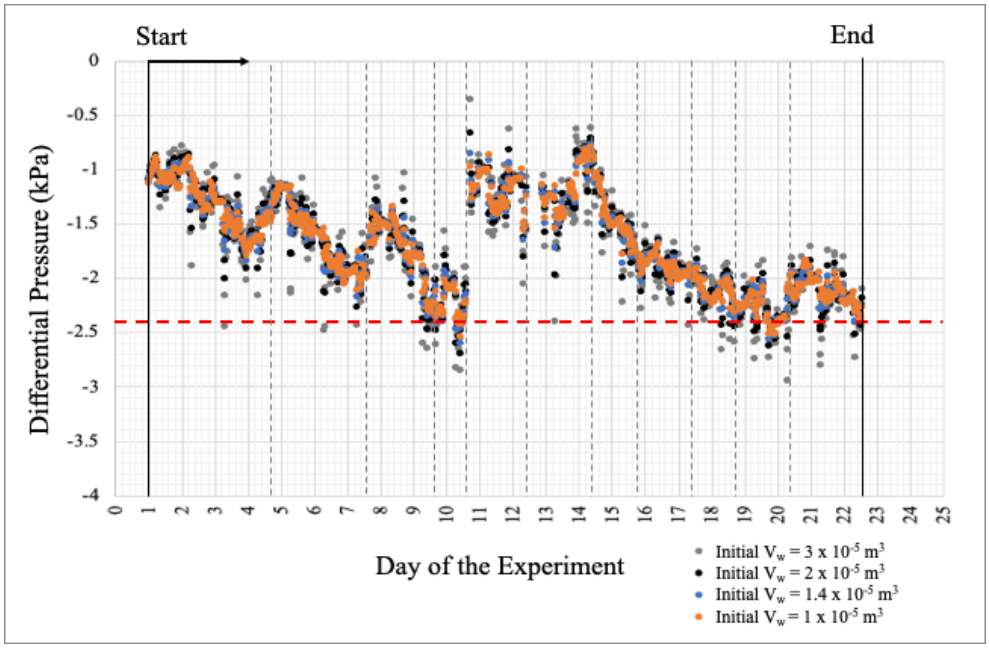

Figure 5.17. Sensitivity analyses for the 1st osmotic cycle

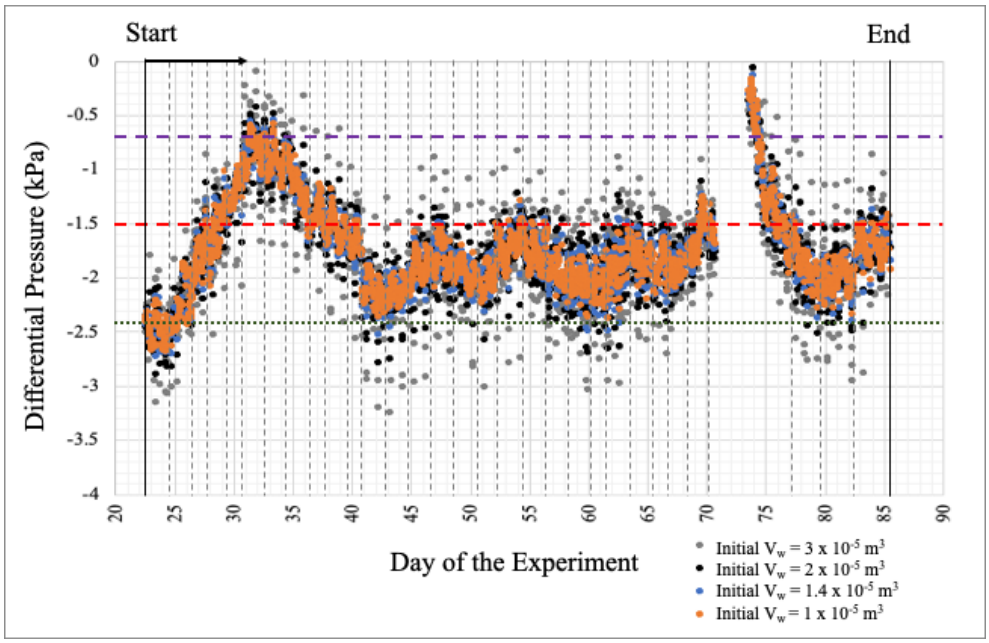

Figure 5.18. Sensitivity analyses for the 2nd osmotic cycle

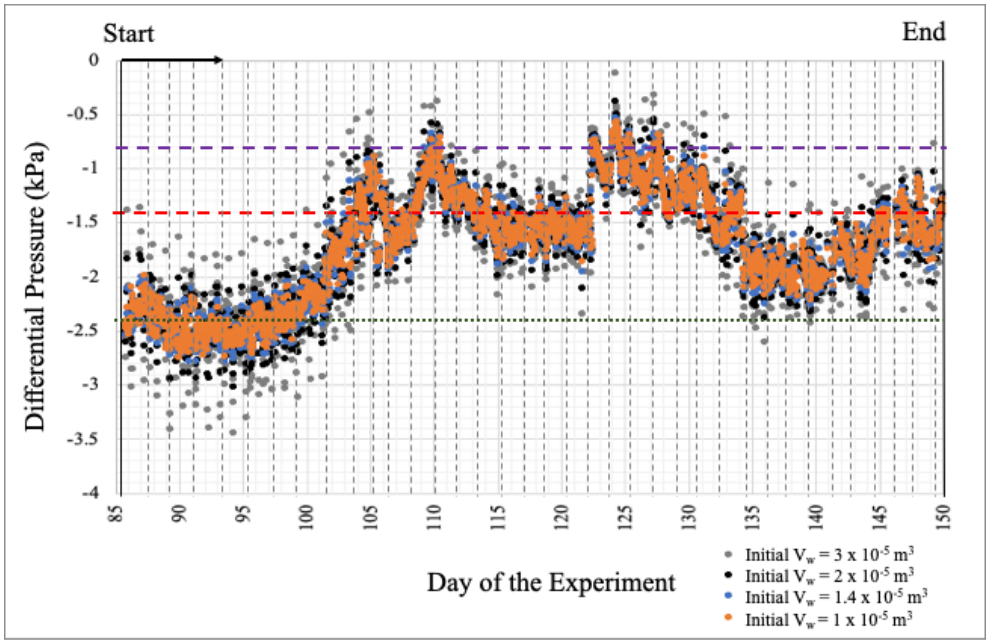

Figure 5.19. Sensitivity analyses for the 3rd osmotic cycle

During the chemical osmosis testing, the high LPT readings stayed at 0 kPa. The low LPT readings fluctuated between 0 kPa to 1 kPa. Figure 5.20 shows that the low LPT readings at the top boundary and the bottom boundary had very different patterns. The LPT readings at the top boundary were stable and close to 0 kPa while the LPT readings at the bottom boundary kept fluctuating.

During the 1st osmotic cycle, the LP at the bottom boundary always stayed at 0 kPa. During the 2nd osmotic cycle, the LP at bottom boundary initially stayed at 0 kPa (day 22 to day 30). The LP fluctuated mainly between 0.25 kPa to 0.5 kPa from day 32 to day 69. The LP fluctuation was less (0.2 kPa to 0.25 kPa) after day 69. During the 3rd osmotic cycle, the LP at the bottom boundary showed a general increasing trend from day 85 to day 99, ranging from 0.2 kPa to 0.8 kPa. The LP from day 100 to day 105 was much lower, between 0.1 kPa to 0.2 kPa. The LP between day 106 to 108 was abnormal due to the PUMP replacement on day 105. The LP returned to the range between 0.1 kPa to 0.2 kPa on day 109. The LP was greater than 0.3 kPa from day 111 to day 142, except the period between day 121 to day 131. After day 142, the LP stabilized at 0 kPa.

The LP readings at the top boundary were stable and very close to 0 kPa. During the 1st osmotic cycle, the LP at the top boundary was mainly within the range between 0.1 kPa to 0.2 kPa. During the 2nd and 3rd osmotic cycles, the LP at the top boundary remained less than 0.05 kPa and 0.1 kPa respectively.

The pore pressure at the regions of higher concentrations (top boundary) was stable throughout the 2nd and 3rd osmotic cycles. The pore pressure at the regions of lower concentrations (bottom boundary) tended to be much lower during the period with higher ΔP. Therefore, the fluctuation of ΔP was very likely to be controlled by osmotic suction instead of osmotic pressure build-up.

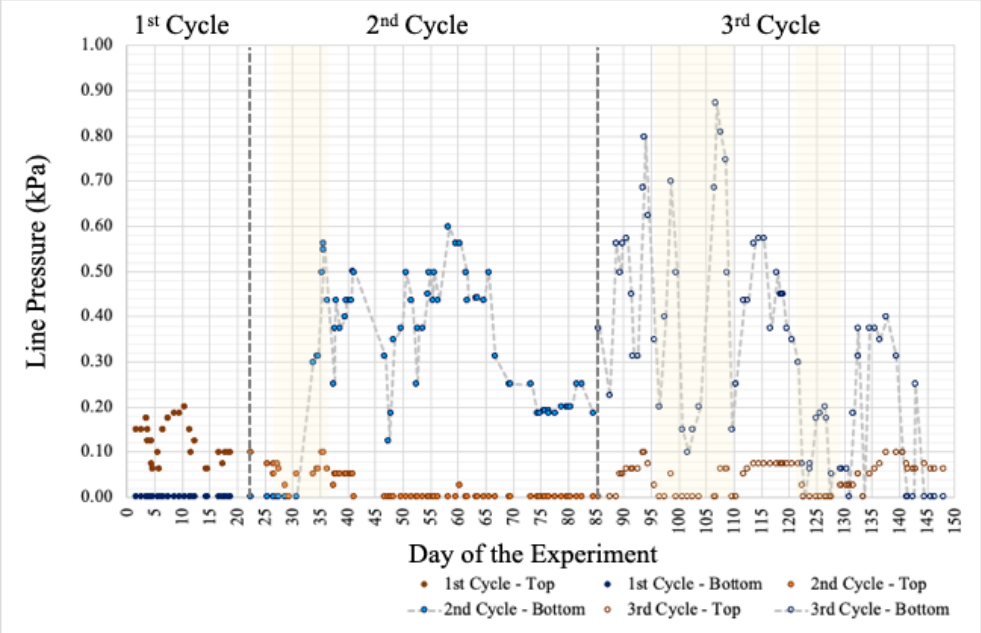

Figure 5.20. LP variation during chemical osmosis (the period with higher DP is highlighted)

The sample volume change recorded by dial gauge during chemical osmosis was induced by both osmotic induced consolidation and osmotic consolidation (see Section 2.6 for detail). No dial gauge reading was taken during the 1st and 2nd osmotic cycles. The sample volume change during the 1st osmotic cycle was expected to be small. During the 1st osmotic cycle, Type A solution was circulated along both the top and bottom boundaries, so there was no concentration gradient across the sample. The major cation and anion concentrations of Type A solution were very close to that of the sample saturation fluid. The solute transport within sample was limited so the osmotic induced consolidation and osmotic consolidation were also limited.

Both osmotic induced consolidation and osmotic consolidation were expected to occur in the 2nd osmotic cycle. During the 2nd osmotic cycle, Type B solution was circulated along the top boundary while Type A solution was circulated along the bottom boundary. Concentration gradient was present across the sample. The cumulative mass influx of K^+ occurred at a stable rate, while the rate of cumulative mass outflux of K^+ from day 22 to day 32 was much gentler than that after day 32 (Figure 5.39). Osmotic consolidation was expected

to occur from day 22 to day 32. Anion exclusion was observed from day 26 to day 36 (Figure 5.29). Osmotic induced consolidation was expected to occur from day 26 to day 36.

Dial gauge readings were taken manually every day during the 3rd osmotic cycle. Figure 5.21 shows the cumulative shale sample height change during the 3rd osmotic cycle, and shows that significant consolidation happened between day 87 to day 97, day 103 to day 110, and day 120 to day 124. During the 3rd osmotic cycle, Type C solution was circulated along the top boundary while Type A solution was circulated along the bottom boundary. Concentration gradient was present across the sample. The cumulative mass influx of K^+ occurred at a stable rate, while the rate of cumulative mass outflux of K^+ from day 85 to day 97 was much gentler than that after day 97 (Figure 5.40). The consolidation between day 87 to day 97 was primarily induced by osmotic consolidation. Anion exclusion was observed from day 97 to day 112, and day 120 to day 127 (Figure 5.29). The consolidation between day 103 to day 110 and day 120 to day 124 was primarily induced by osmotic induced consolidation. Overall, the shale sample height was consolidated by -0.33 mm (equivalent to 5.5%) throughout the cycle.

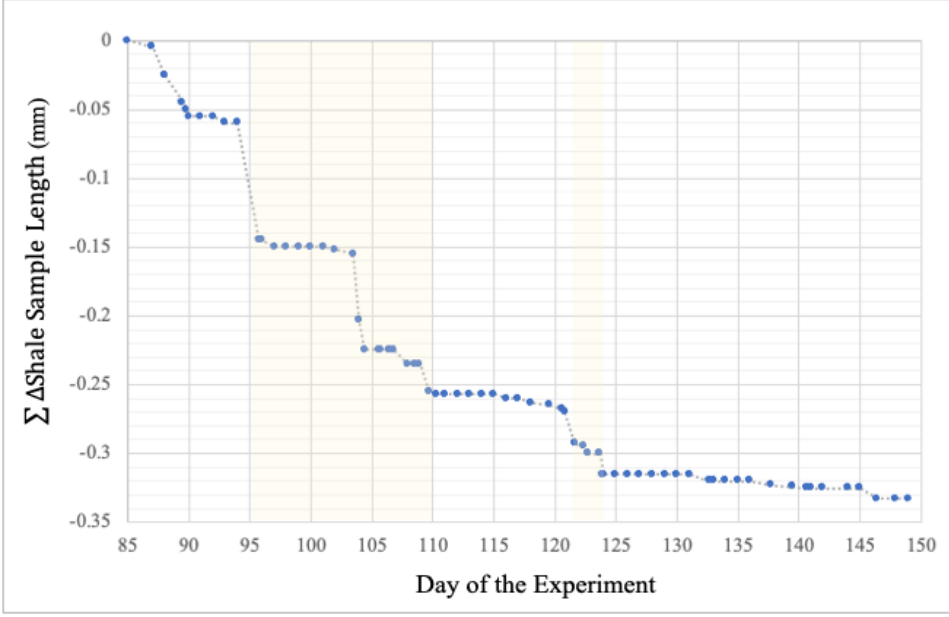

Figure 5.21. Cumulative change of the sample height during the 3rd osmotic cycle (the period with DP increase is highlighted)

5.4 Approximation of Osmotic Pressure and Osmotic Efficiency

The TDS molar concentration differences between the top and bottom boundaries during chemical osmosis were calculated based on the individual cation and anion concentration differences provided in Appendix B (Table B.4). $\Delta\pi$ was approximated based on the TDS molar concentration differences provided in Appendix B (Table B.5). Table B.5 shows

that Δπ was stable in each osmotic cycle. Figure 5.22 and Figure 5.23 show the Δπ in the 2nd and 3rd osmotic cycles. The Δπ was zero in the 1st osmotic cycle, ranged from 35.2 kPa to 36.9 kPa (36.0 kPa average) in the 2nd osmotic cycle, and ranged from 80 kPa to 82.6 kPa (81.4 kPa average) in the 3rd osmotic cycle. It was not evident that the change of Δπ in the 2nd and 3rd osmotic cycles affected the change of observed DP in the chemical osmosis testing (Figure 5.15 and Figure 5.16). As mentioned in Section 5.3, the ΔP calculated using the 'peak' DP were respectively 1.7 kPa and 1.6 kPa in the 2nd and 3rd osmotic cycles, while the ΔP calculated using the 'residual' DP were respectively 0.9 kPa and 1.0 kPa. The osmotic efficiencies of shale sample calculated based on the Δπ and the 'peak' ΔP were respectively 0.0472 and 0.0196 in the 2nd and 3rd osmotic cycles. The osmotic efficiencies of shale sample calculated using the Δπ and the 'residual' ΔP were respectively 0.0250 and 0.0123.

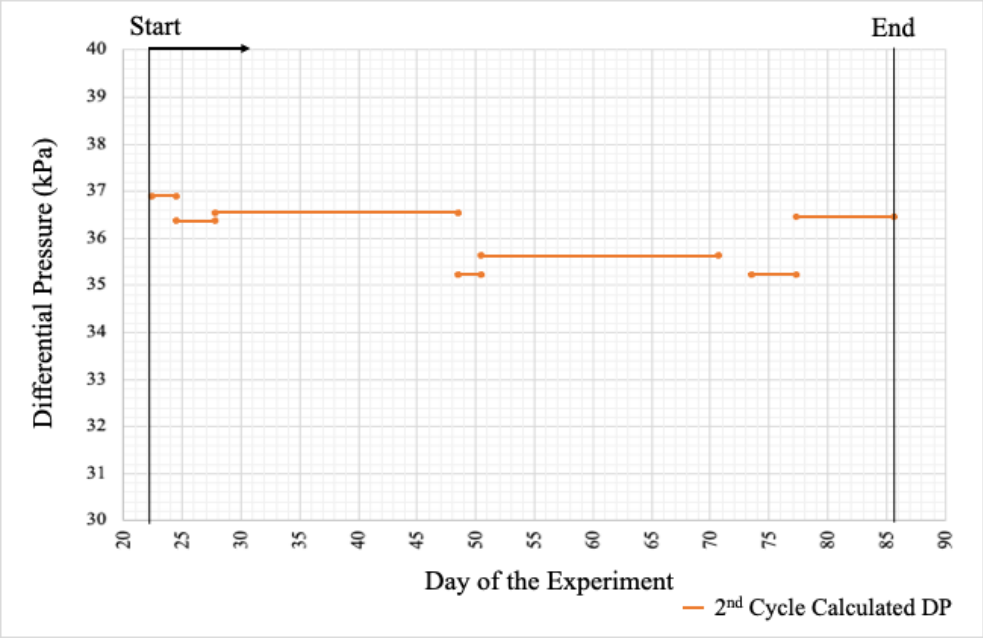

Figure 5.22. Calculated DP variation during the 2nd osmotic cycle

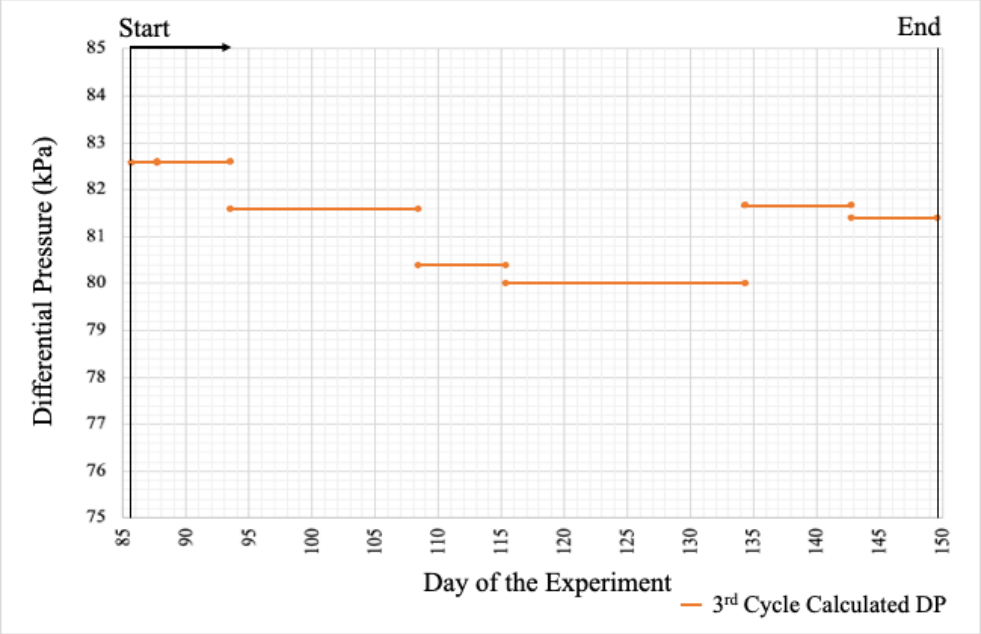

Figure 5.23. Calculated DP variation during the 3rd osmotic cycle

5.5 Chemical Analyses

The chemical analyses for the collected fluids started after day 9. From day 1 to day 6, the pumping speed for the chemical osmosis circulation system was 0.01 mL/min. Starting from day 6, the pumping speed was doubled to 0.02 mL/min. The rates of solute influx, transport and outflux were independent from the pumping speed. The solute diffusion rate was influenced by the intrinsic properties of shale and the ΔC. When the pumping speed increased from 0.01 mL/min to 0.02 mL/min, the length of each circulation period became shorter by 53 hours. Since less time was allowed for solute influx and solute outflux in each circulation period, there were less cations and anions influx and outflux through the shale sample. Therefore, the concentrations of fluid samples collected from the top boundary increased while the concentrations of fluid samples collected from the bottom boundary decreased.

5.5.1 Cation Concentration Analysis

Fluid samples collected were analyzed for K^+, Na^+, Mg^{2+}, Ca^{2+}, Fe^{3+}. Since none of the synthetic fluids (Type A, B, and C) contained Ca^{2+} or Fe^{3+}, the concentrations of these species collected in the fluids originated exclusively from the shale sample. The K^+, Na^+, and Mg^{2+} concentrations of the collected samples were also compared with that of the synthetic fluids to determine the contribution from the shale sample. The K^+, Na^+, Mg^{2+}, Ca^{2+}, and Fe^{3+} concentrations of the synthetic fluids and the collected samples are provided in Appendix B (Tables B.1, B.2, B.6, and B.7). Figures 5.24 to 5.28 show a comparison of major cation

concentrations of the synthetic fluids and the collected samples. If the cation concentration of the collected sample was lower than that of the synthetic fluid, it implies that cation influx occurred from the synthetic fluids to the shale sample. On the other hand, if the cation concentration of the collected sample was higher than that of the synthetic fluid, it implies that cation outflux occurred from the shale sample to synthetic fluids.

During the 1st osmotic cycle, the major cation concentrations of the collected samples were very close to that of the synthetic fluids. The results are reasonable because Type A solutions were circulated along both the top and bottom boundaries, so there was no concentration gradient across sample for chemical osmosis. The chemical components of Type A solutions (0 M KCl) were similar to that of the shale pore fluids.

Type B solutions (0.0037 M KCl) were circulated along the top boundary during the 2nd osmotic cycle while Type C solutions (0.0082 M KCl) were circulated along the top boundary during the 3rd osmotic cycle. Type A solutions (0 M KCl) were circulated along the bottom boundary in both cycles. Figure 5.24 shows that during the 2nd and 3rd osmotic cycles, the K^+ concentrations of the collected samples from the top boundary were respectively 30 mg/L and 60 mg/L lower than that of the synthetic fluids circulating at the top boundary. Conversely, the K^+ concentrations of the collected samples from the bottom boundary were respectively 4 – 11 mg/L and 12 – 20 mg/L higher than that of the synthetic fluids circulating at the bottom boundary. These observations illustrate the transport of K^+ into the sample from the top boundary and out of the bottom of sample in response to the ΔC.

Since K^+ is a reactive species, adsorption-desorption reactions took place within the shale when K^+ adsorbed. Figures 5.25 and 5.26 show that the Na^+ and Ca^{2+} concentrations of the collected samples were higher than that of the synthetic fluids, while Figures 5.27 and 5.28 show that the Mg^{2+} and Fe^{3+} concentrations of the collected samples were very close to that of the synthetic fluids. This suggests that the adsorption-desorption reactions mainly occurred by K^+ replacing Na^+ and Ca^{2+} at adsorption sites. These figures also show that the Na^+ and Ca^{2+} concentrations of the collected samples from the top boundary were higher than that of the collected samples from the bottom boundary. This is consistent with the higher K+ concentrations near the top boundary and consequently greater rates of desorption of Na^+ and Ca^{2+} from the mineral surfaces and transport across this boundary.

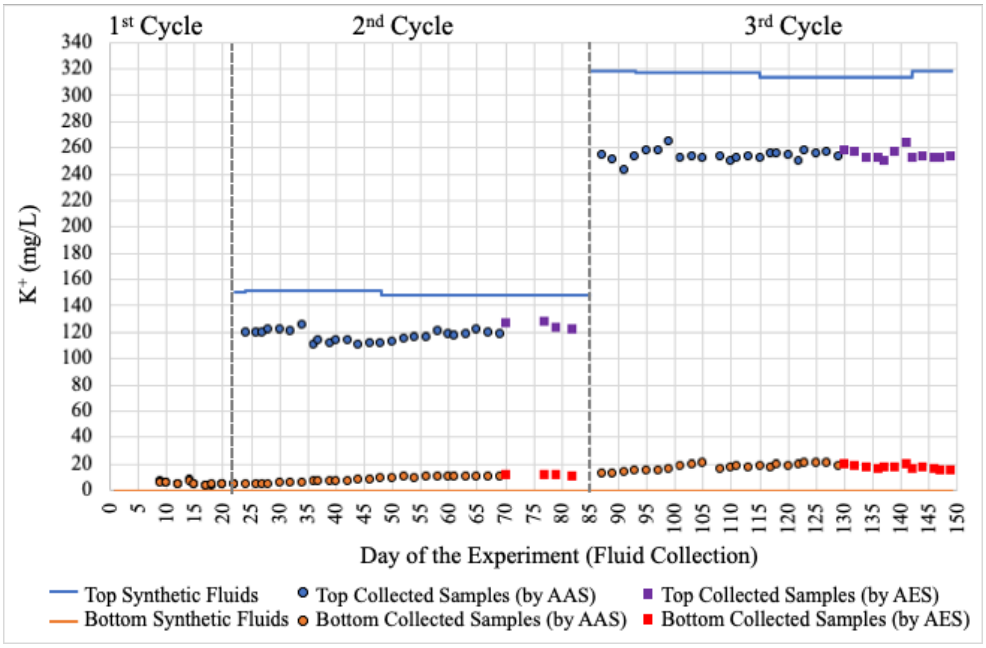

Figure 5.24. K^+ concentrations of synthetic fluids and collected samples

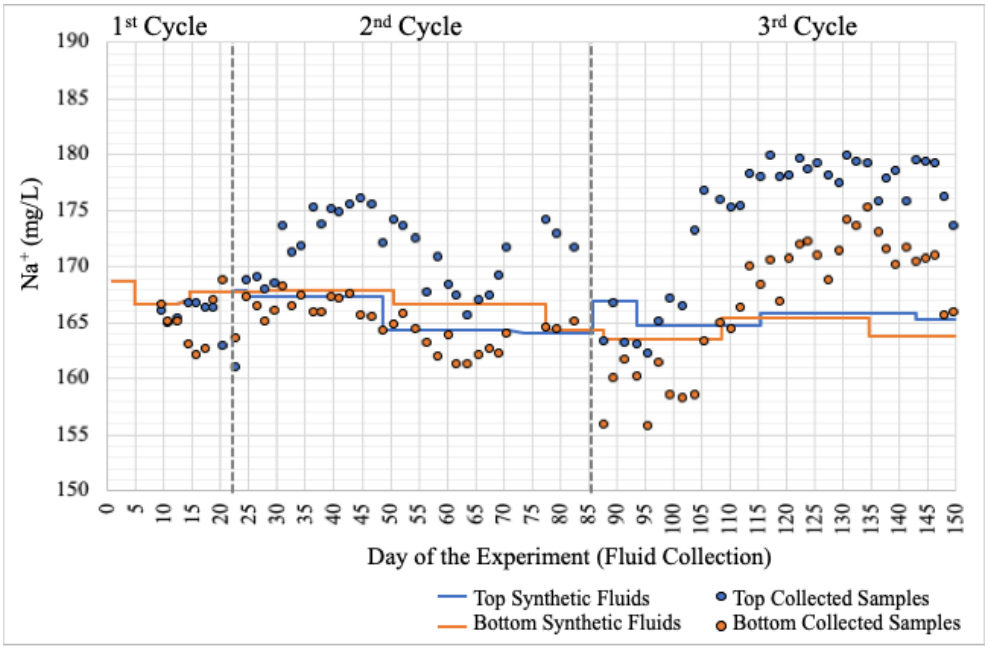

Figure 5.25. Na^+ concentrations of synthetic fluids and collected samples

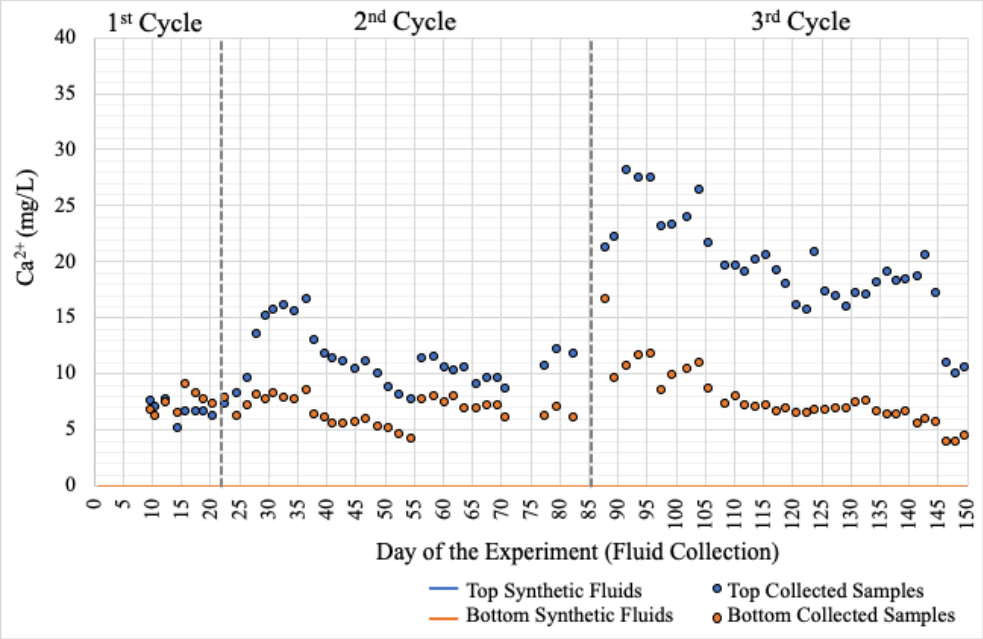

Figure 5.26. Ca^{2+} concentrations of synthetic fluids and collected samples

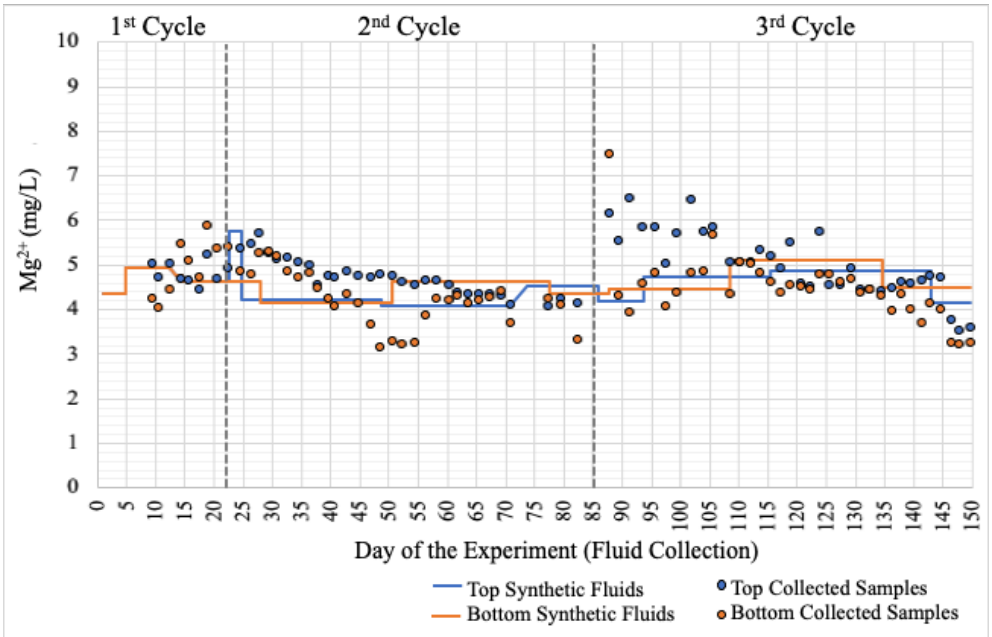

Figure 5.27. Mg^{2+} concentrations of synthetic fluids and collected samples

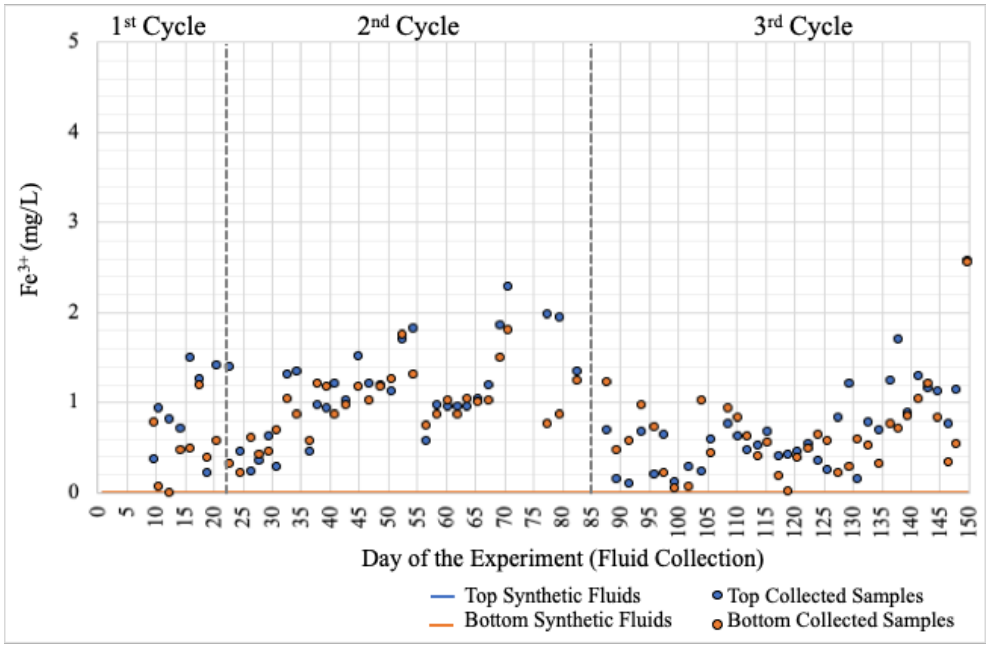

Figure 5.28. Fe^{3+} concentrations of synthetic fluids and collected samples

5.5.2 Anion Concentration Analysis

Fluid samples collected were analyzed for Cl^-, SO_4^{2-}, and F^-. Since none of the synthetic fluids (Type A, B, and C) contained F^-, the concentrations of the species collected in the fluids originated exclusively from the shale sample. The Cl^- and SO_4^{2-} concentrations of the collected samples were also compared with that of the synthetic fluids to determine the contribution from the shale sample. The Cl^-, SO_4^{2-}, and F^- concentrations of the synthetic fluids and the collected samples are provided in Appendix B (Tables B.1, B.2, B.8, and B.9). Figures 5.29 to 5.31 show a comparison of major anion concentrations of the synthetic fluids and the collected samples. If the anion concentration of the collected sample was lower than that of the synthetic fluid, it implies that cation influx occurred from the synthetic fluids to the shale sample. On the other hand, if the anion concentration of the collected sample was higher than that of the synthetic fluid, it implies that cation outflux occurred from the shale sample to synthetic fluids.

During the 1st osmotic cycle, the major anion concentrations of the collected fluids from both the top and bottom boundary were very close to that of the synthetic fluids for the reasons noted previously. Figure 5.29 shows that under normal condition (illustrated in Section 4.6.1) the Cl^- concentrations of the collected samples from the top boundary were 20 – 25 mg/L lower than that of the synthetic fluids circulating at the top boundary. Conversely, the Cl^- concentrations of the collected samples from the bottom boundary were 10 – 20 mg/L higher than that of the synthetic fluids circulating at the bottom boundary. These observations illustrate the transport of Cl^- from the top boundary, through the shale sample, to the bottom

boundary, corresponding to the ΔC. However, during the periods of anion exclusion, between day 26 to day 36, day 97 to day 112, and day 120 to day 127. The Cl^- concentrations of the collected samples from the top boundary during the anion exclusion periods were generally 20 mg/L higher than that under the normal condition.

Since Cl^- is a non-reactive species, Cl^- did not adsorb onto the mineral surfaces within the shale sample, and adsorption-desorption reactions did not take place within the shale sample. Figure 5.30 shows that the SO_4^{2-} concentrations of the collected samples were 0 – 5 mg/L lower than that of the synthetic fluids, while Figure 5.31 shows that the F^- concentrations of the collected samples were very close or at 0 mg/L (except day 87).

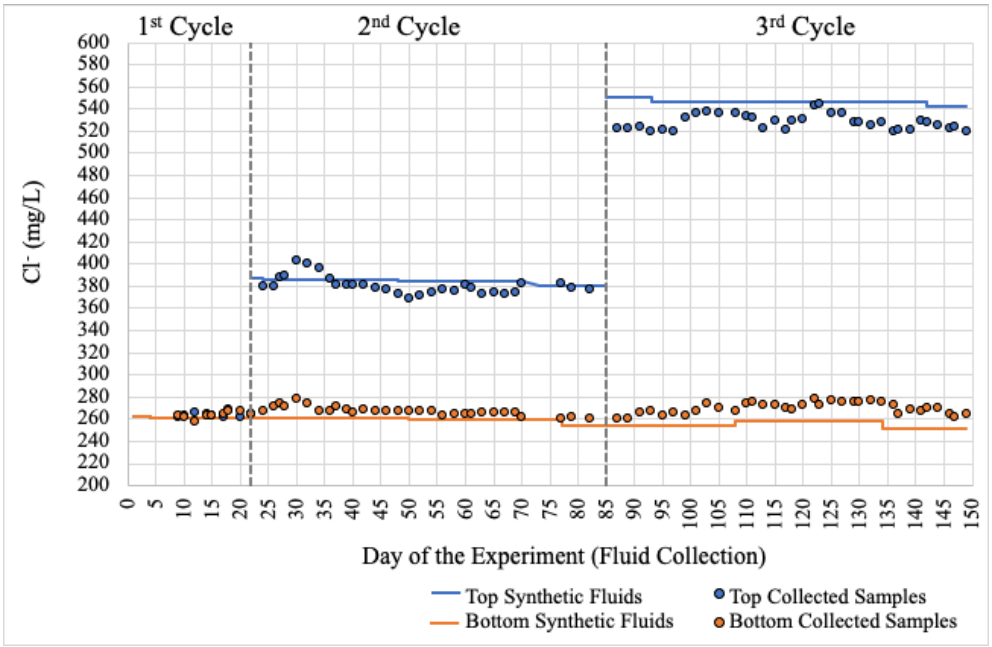

Figure 5.29. Cl^- concentrations of synthetic fluids and collected samples

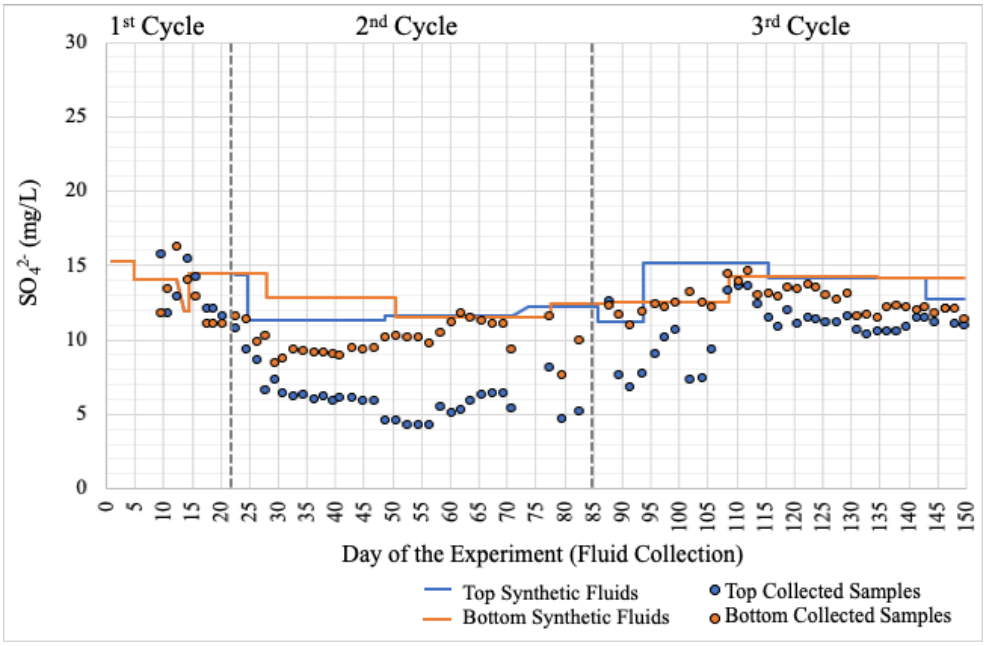

Figure 5.30. SO_4^{2-} concentrations of synthetic fluids and collected samples

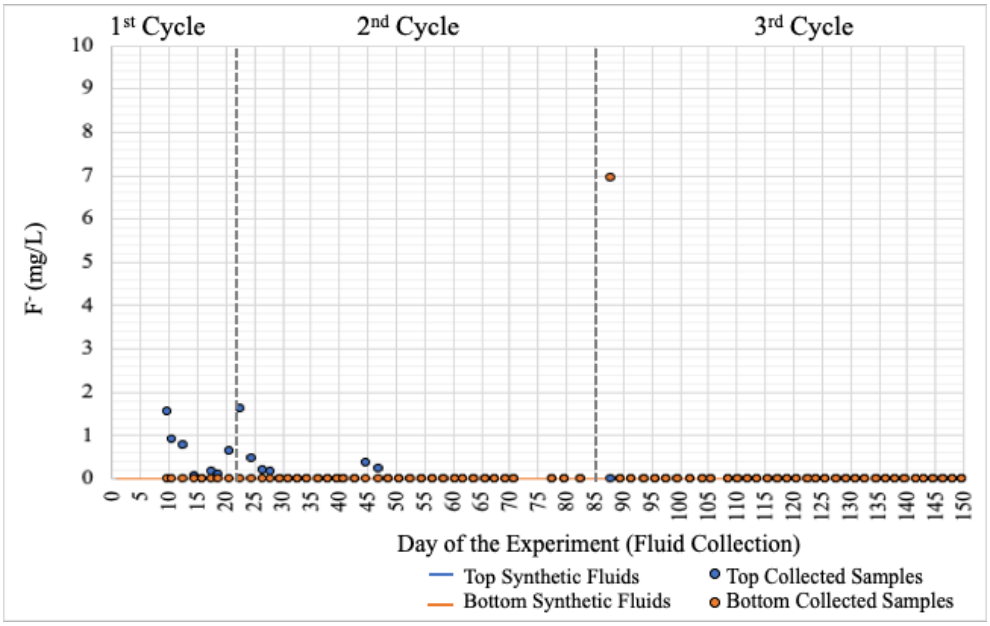

Figure 5.31. F^- concentrations of synthetic fluids and collected samples

Figures 5.32 and 5.33 show that the synthetic fluids and the collected samples were acidic. The pH of the synthetic fluids and collected samples were generally 4.7 – 6 and 5.8 – 6.5 respectively. Since the pH measurements were all below 8.3, the fluids only contained HCO_3^- and did not contain CO_3^{2-} and OH^-. The HCO_3^- concentrations of the synthetic fluids and the collected samples are provided in Appendix B (Tables B.1, B.2, B.8, and B.9). It should be noted that alkalinity tests could not be done for the collected samples from the bottom boundary between day 70 to day 82, and after day 130, due to the reason described in Section

4.5.2.2. It is likely that the HCO_3^- buffering capacity in water slowed the decline of pH to around 6 (Oram, 2014). However, a rapid pH drop occurred when the HCO_3^- buffering capacity exhausted at a pH of approximately 5.5. Eq. 4.8 was used to convert the $CaCO_3$ concentrations determined from the alkalinity test to HCO_3^- concentrations. Figure 5.34 shows that the HCO_3^- concentrations of the collected samples were generally higher than 20 mg/L, while the HCO_3^- concentrations of the synthetic fluids were less than 10 mg/L. This information illustrates that the synthetic fluids had weak buffering capacity while the collected samples had strong buffering capacity.

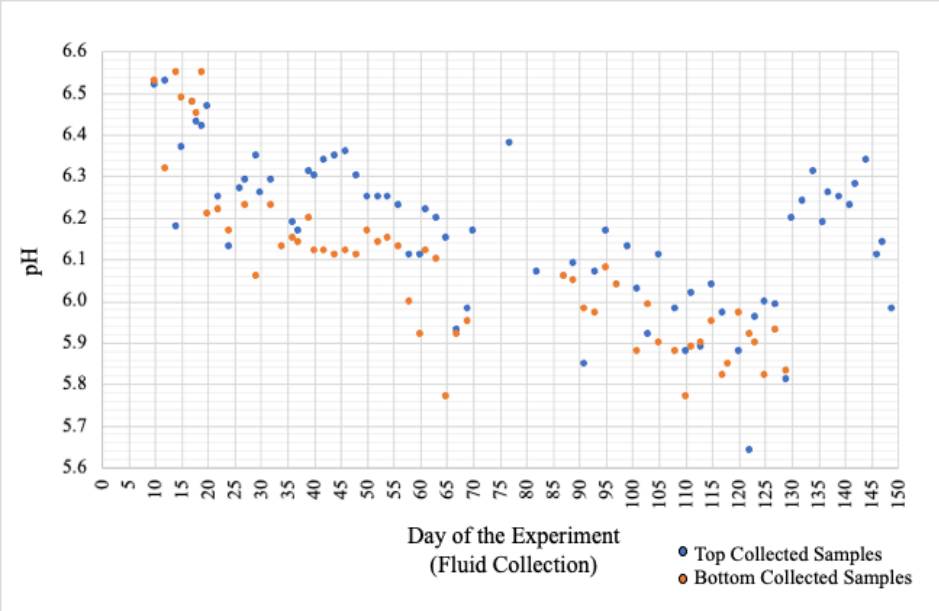

Figure 5.32. pH of the collected samples

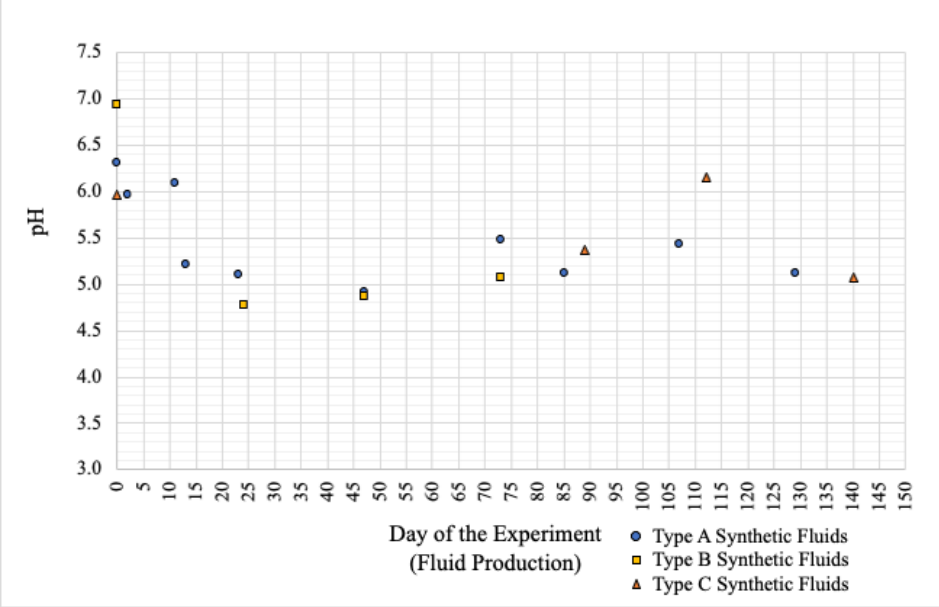

Figure 5.33. pH of the synthetic fluids

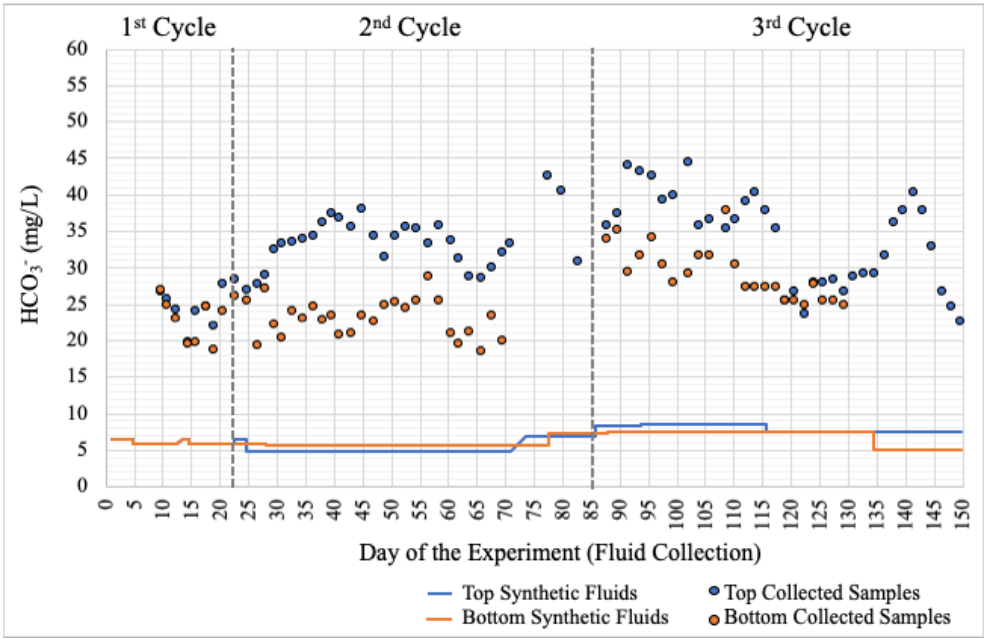

Figure 5.34. HCO_3^- concentrations of synthetic fluids and collected samples

5.5.3 Charge Balance Calculation

Charge balance calculations were carried out using Eq. 4.9 as well as the cation and anion concentrations of the synthetic fluids and collected samples. As mentioned in Section 4.5.3, the total sum of cations should have equaled to the total sum of anions due to electroneutrality. CBE is the extent of the electrical imbalance caused by analytical errors and / or unanalyzed constituents. The cation and anion concentrations are representative when the CBE is within ±5%. Figure 5.35 shows the CBE for the collected samples from the top and bottom boundaries. Figure 5.36 shows the CBE for the synthetic fluids. The CBE for synthetic fluids and collected samples are provided in Appendix B (Table B.10 to B.12). These figures show that all the CBE ranged between -2 to +2.2%. Since the errors were within ±5%, the cation concentrations and anion concentrations were representative to use for solute transport analyses. It should be noted that the charge balance calculations could not be done for the collected fluids from the bottom boundary between day 70 to day 82, and after day 130, due to the reason described in Section 4.5.3.

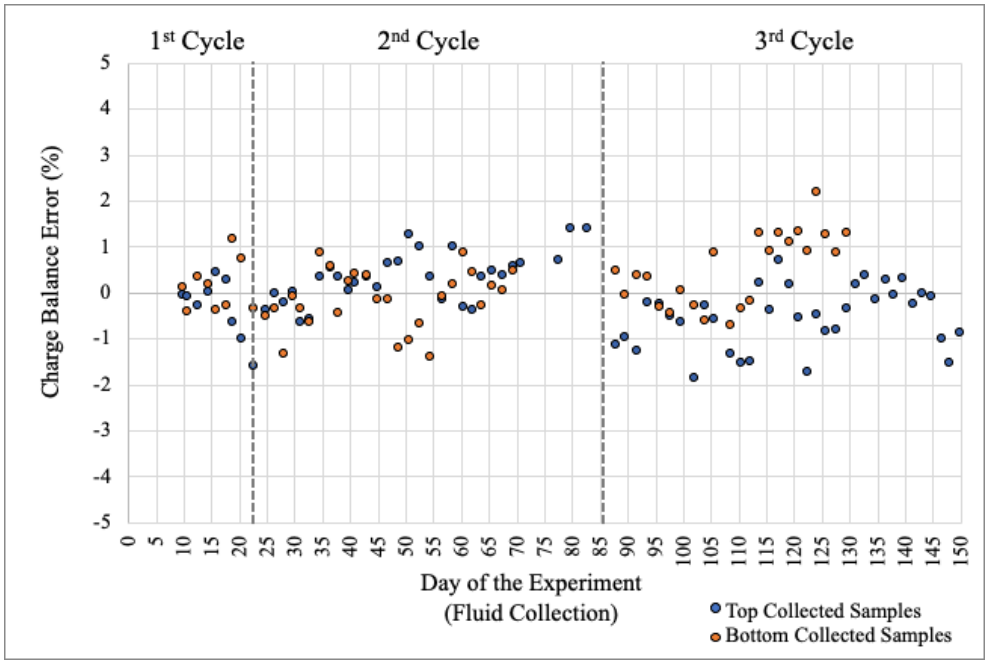

Figure 5.35. The CBE for the collected samples

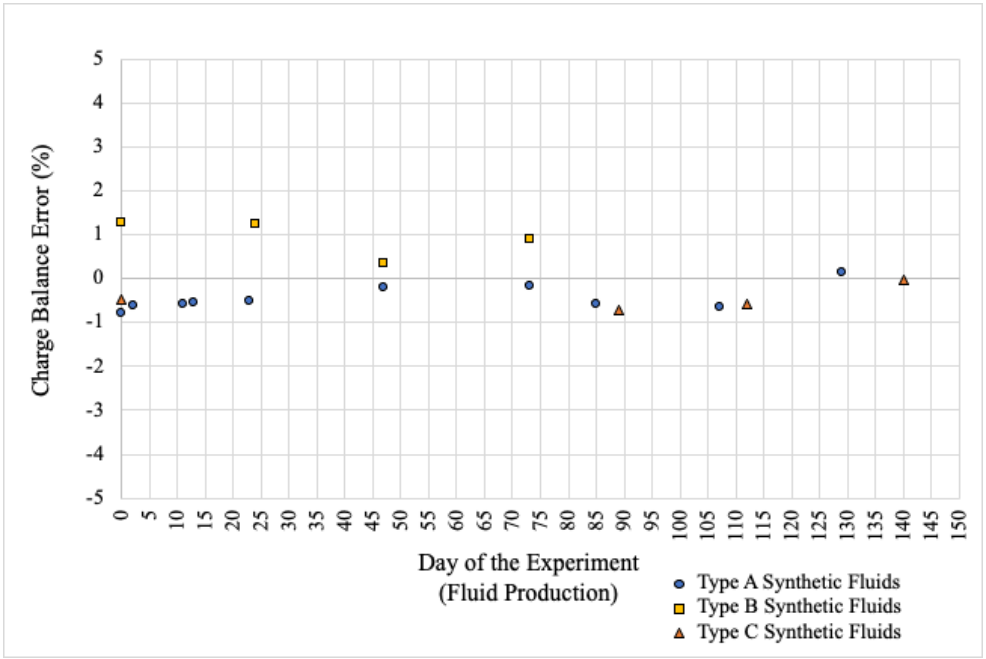

Figure 5.36. The CBE for the synthetic fluids

5.5.4 TDS Approximation

As discussed in Section 4.5.4, the TDS concentrations measured by the EC meter did not represent the actual TDS concentrations of the fluids. The TDS concentrations measured by the EC meter were compared with the actual TDS concentrations derived from the laboratory experiments (AAS, AES, IC, alkalinity tests), as shown in Figure 5.37. The figure

shows that the offset was linearly proportional and therefore meaningful calibration may have been derived.

Although the TDS concentrations measured by the EC meter were offset from the actual values, Figure 5.38 shows that the TDS concentrations of synthetic fluids and collected samples had a very similar pattern as the K^+ and Cl^- concentrations (Figures 5.24 and 5.29). The figure shows that during the 1st chemical osmotic cycle, the TDS concentrations of collected samples from the top and bottom boundaries were very close to that of the synthetic fluids. During the 2nd and 3rd osmotic cycles, the TDS concentrations of the collected samples from the top boundary were consistently lower than that of the synthetic fluids circulating at the top boundary, while the TDS concentrations of the collected samples from the bottom boundary were consistently higher than that of synthetic fluids circulating at the bottom boundary. The same pattern is observed in the K^+ and Cl^- concentrations (Figures 5.24 and 5.29). Figure 5.38 also shows that the TDS concentrations of collected samples from top boundary were higher between day 26 to day 34, and day 97 to day 113. These two periods matched the anion exclusion periods (Figure 5.29). However, the TDS concentrations were not able to capture the anion exclusion period between day 120 to day 127.

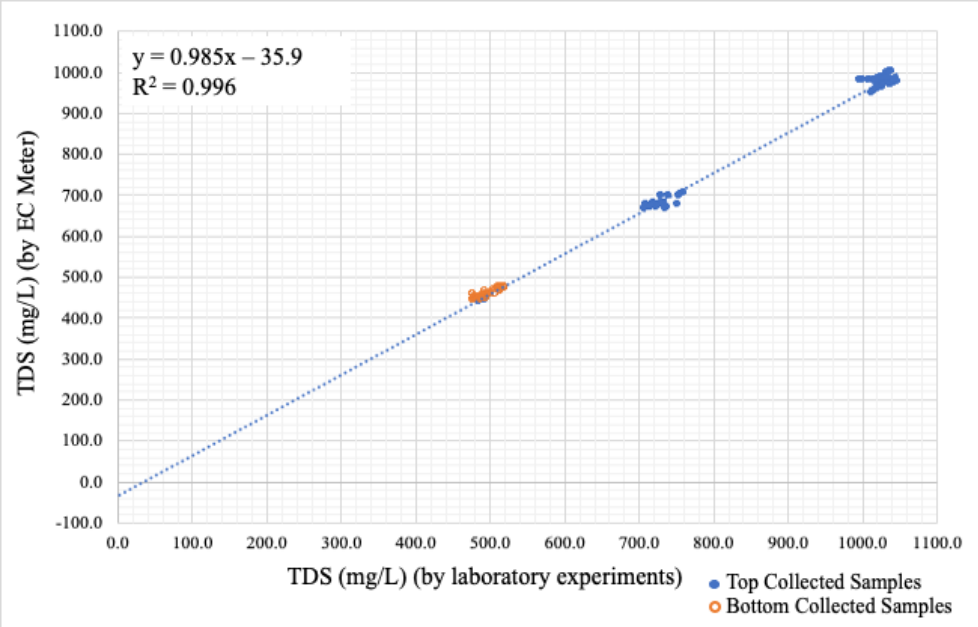

Figure 5.37. The offset between TDS measured by EC meter and the actual TDS

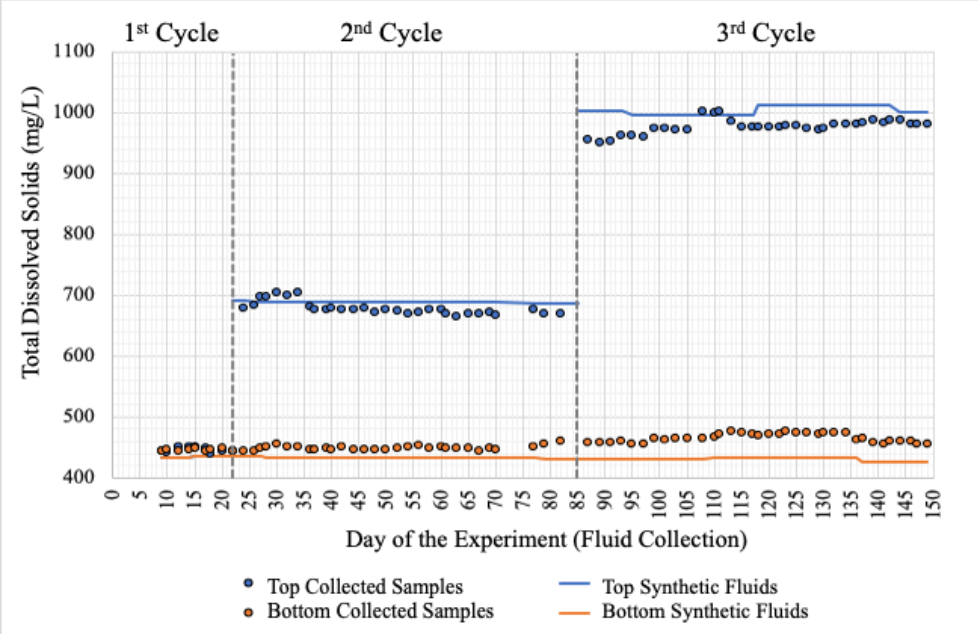

Figure 5.38. TDS concentrations of synthetic fluids and collected samples

5.6 Solute Transport Numerical Analyses

5.6.1 Mass Balance Theory

K^+ and Cl^- should be transported across the sample from top to bottom as a result of diffusive transport created by the concentration gradients across the sample. In the case of Cl^-, there will be differences in the rate of transport in and out of the sample initial to account for the change in Cl^- stored within the pore-water.

Figures 5.39 to 5.42 (also in Appendix C - Table C.1 to C.4) present the cumulative mass flux of K^+ and Cl^- in and out of the sample with time, as well as the cumulative change in mass stored within the sample calculated from the differences in the cumulative mass fluxes.

Figures 5.39 and 5.40 show that the $\sum M_{in}$ of K^+ increased steadily and consistently, by respectively 1.65×10^{-3} kg/m^2 and 4.16×10^{-3} kg/m^2 during the 2nd and 3rd osmotic cycles. The $\sum M_{out}$ of K^+ decreased consistently, respectively by 4.10×10^{-4} kg/m^2 and 1.17×10^{-3} kg/m^2 during the 2nd and 3rd osmotic cycles. The decrease of $\sum M_{out}$ started with a gentler slope and became steady with a steeper slope. The rate of K^+ $\sum M_{out}$ from day 22 to day 32 (-5.66×10^{-6} kg/m^{2}d) was much gentler than that after day 32 (-9.60×10^{-6} kg/m^{2}d) in the 2nd osmotic cycle. The rate of K^+ $\sum M_{out}$ from day 85 to day 97 (-1.37×10^{-5} kg/m^{2}d) was much gentler than that after day 97 (-1.93×10^{-5} kg/m^{2}d) in the 3rd osmotic cycle. In general, the K^+ $\sum M_{in}$ was much more than the K^+ $\sum M_{out}$. Therefore, the K^+ $\sum M_{stored}$ showed an consistent increasing trend. The K^+ $\sum M_{stored}$ was much closer to K^+ $\sum M_{in}$ from day 22 to day 32 and day

85 to day 97, due to the gentler rates of K^+ $\sum M_{out}$ in these periods. The K^+ $\sum M_{stored}$ increased by respectively 1.24×10^{-3} kg/m^2 and 2.99×10^{-3} kg/m^2 during the 2nd and 3rd osmotic cycles. It should be noted that the K^+ $\sum M_{stored}$ increasing trends observed in the 2nd and 3rd osmotic cycles cannot go on indefinitely. These increasing trends would cease once the cation exchange reaches equilibrium (the amount of K^+ adsorbed within sample reaches its maximum capacity), and the trends would subsequently become much gentler and steady.

Figures 5.41 and 5.42 show that the $\sum M_{in}$ of Cl^- increased with a generally consistent trend. The Cl^- $\sum M_{in}$ increased by respectively 2.68×10^{-4} kg/m^2 and 1.23×10^{-3} kg/m^2 during the 2nd and 3rd osmotic cycles. The exceptions occurred during the anion exclusion periods. During the complete anion exclusion period (day 26 to day 36), the $\sum M_{in}$ of Cl^- decreased from 2.42×10^{-5} kg/m^2 to -5.78×10^{-5} kg/m^2, implying that Cl^- fluxed out of the sample through the top boundary. During the partial anion exclusion periods (day 97 to day 112, and day 120 to day 127), the $\sum M_{in}$ of Cl^- kept the increasing trend but the rates of $\sum M_{in}$ were much gentler (1.14×10^{-5} kg/m^{2}d and 6.45×10^{-6} kg/m^{2}d respectively between day 97 to day 112 and day 120 to day 127). The rates of Cl^- $\sum M_{in}$ after reaching steady state on day 46 and day 127 were respectively 1.11×10^{-5} kg/m^{2}d and 2.27×10^{-5} kg/m^{2}d. The $\sum M_{out}$ of Cl^- decreased consistently, by respectively 3.73×10^{-4} kg/m^2 and 9.53×10^{-4} kg/m^2 during the 2nd and 3rd osmotic cycles. During the 2nd osmotic cycle, the rate of Cl^- $\sum M_{out}$ was steeper (-1.36×10^{-5} kg/m^{2}d) from day 22 to day 32, and the rate became gentler and steady (-6.40×10^{-6} kg/m^{2}d) after day 35. During the 3rd osmotic cycle, the rate of $\sum M_{out}$ of Cl^- was gentler (-8.50×10^{-6} kg/m^{2}d) from day 85 to day 96, and the rate became steeper and steady (-1.73×10^{-5} kg/m^{2}d) after day 110. When Cl^- mass flux reached the steady state, the mass influx was very close to mass outflux, and the change of Cl^- $\sum M_{stored}$ was very limited. Therefore, the fluctuation of Cl^- $\sum M_{stored}$ mainly occurred before Cl^- mass flux reached the steady state. During the 2nd osmotic cycle, the Cl^- $\sum M_{stored}$ decreased by 2.20×10^{-4} kg/m^2 (at the rate of -1.59×10^{-5} kg/m^2) from day 22 to day 36, and increased by 1.15×10^{-4} kg/m^2 (at the rate of 3.49×10^{-6} kg/m^2) from day 36 to day 69. During the 3rd osmotic cycle, the Cl^- $\sum M_{stored}$ increased by 2.20×10^{-4} kg/m^2 (at the rate of 1.86×10^{-5} kg/m^2) from day 85 to day 97, and increased by 5.40×10^{-5} kg/m^2 (at the rate of 1.03×10^{-6} kg/m^2) from day 97 to day 149. The Cl^- $\sum M_{stored}$ slightly decreased during the anion exclusion periods because the Cl^- $\sum M_{out}$ were much more than the Cl^- $\sum M_{in}$.

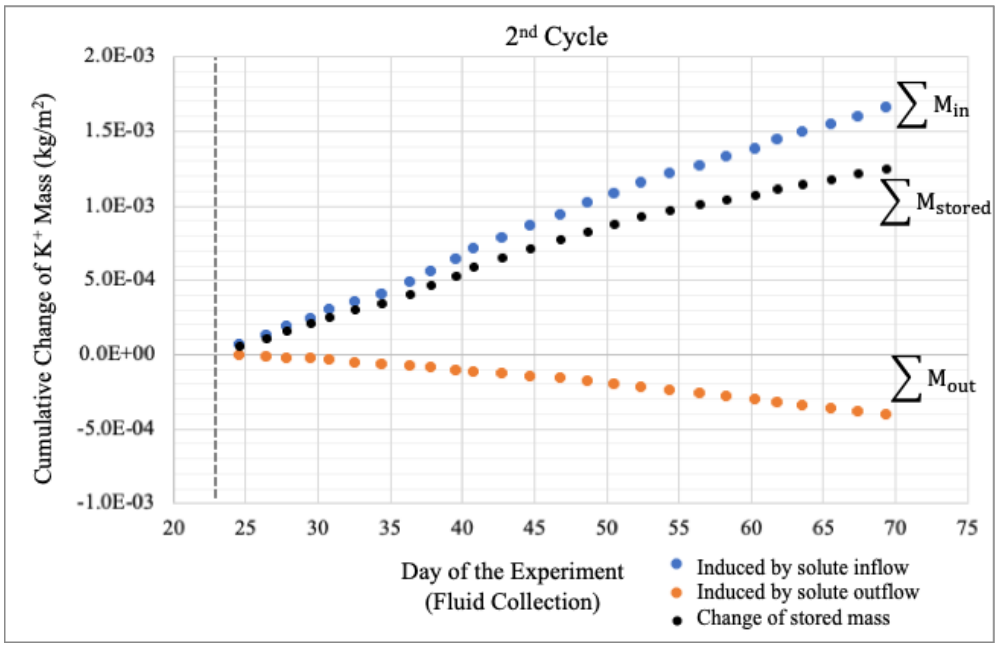

Figure 5.39. The cumulative change of K^+ stored mass within sample due to mass influx and mass outflux during the 2nd osmotic cycle

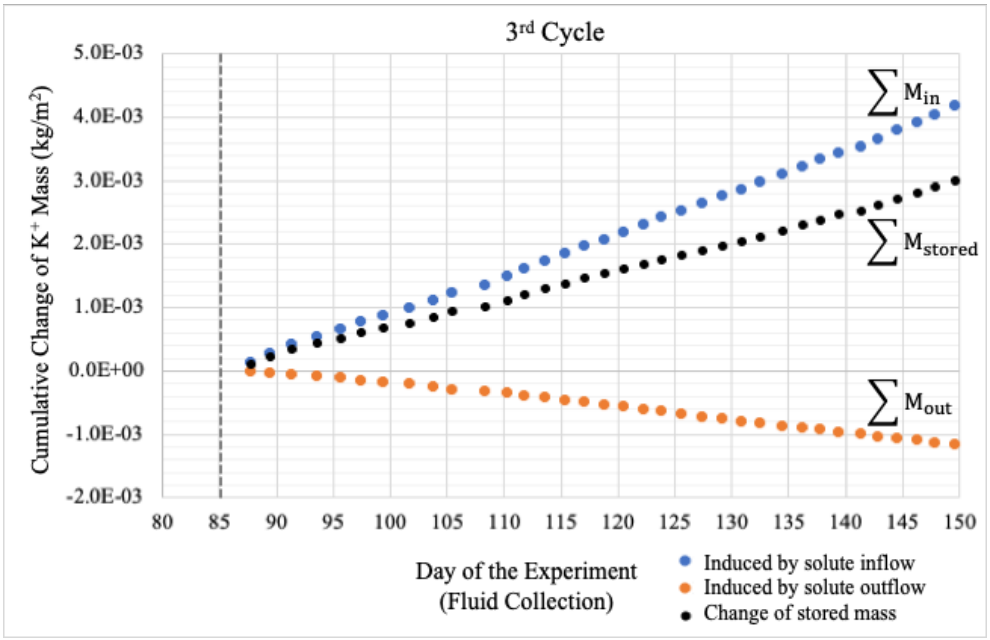

Figure 5.40. The cumulative change of K^+ stored mass within sample due to mass influx and mass outflux during the 3rd osmotic cycle

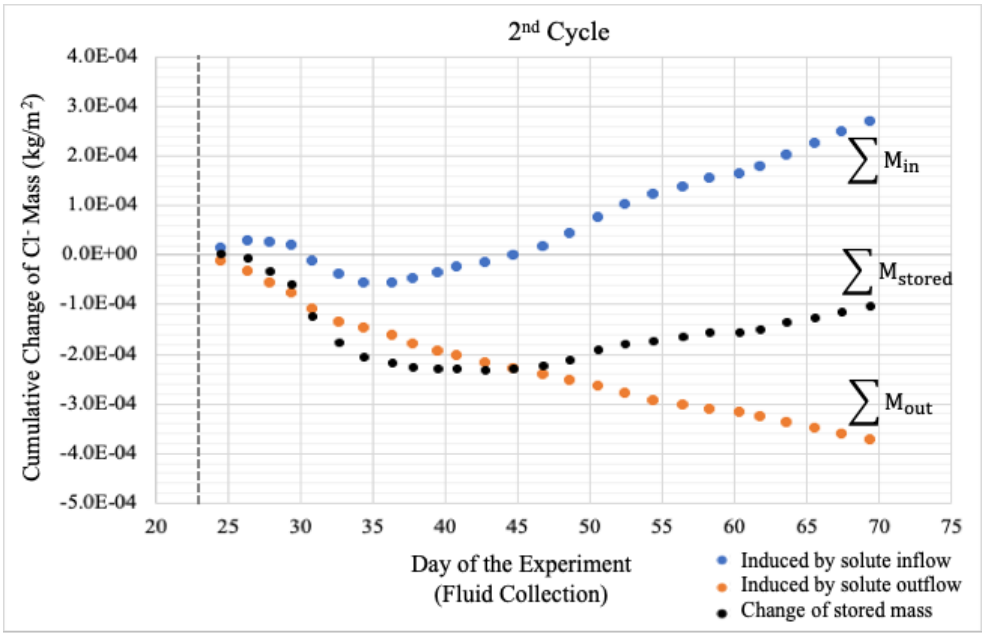

Figure 5.41. The cumulative change of Cl^- stored mass within sample due to mass influx and mass outflux during the 2nd osmotic cycle

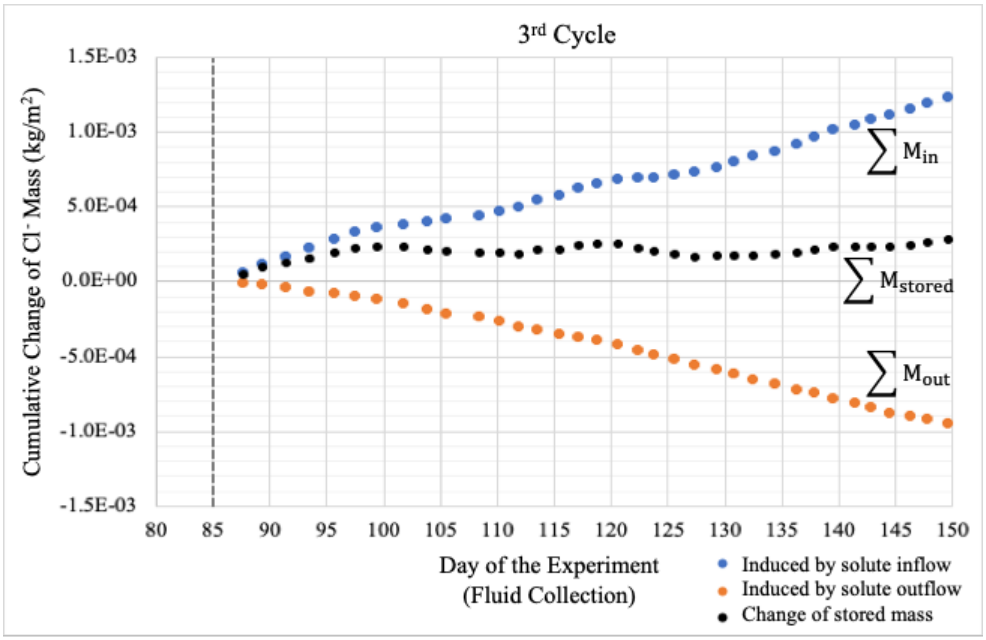

Figure 5.42. The cumulative change of Cl^- stored mass within sample due to mass influx and mass outflux during the 3rd osmotic cycle

As discussed in Section 4.6.1, the steady portions of $\sum M_{in}$ and $\sum M_{out}$ slopes shown in Figures 5.39 to 5.42 were used to determine the rates of K^+ and Cl^- mass influx (J_{in}) and mass outflux (J_{out}). The J_{in} and J_{out} of K^+ and Cl^- are shown in Table 5.3 and 5.4. The data contributed to the determinations of J_{in} and J_{out} are in purple colour in Appendix C - Table C.1 to C.4.

Table 5.3. The J_{in} of K^+ and Cl^- during the 2nd and 3rd osmotic cycles

Cycle	Element	Start day	End day	Start $\sum M_{in}$ (kg/m^2)	End $\sum M_{in}$ (kg/m^2)	J_{in} (kg/m^2s)
2	**K^+**	50.6	69.4	1.15E-03	1.65E-03	3.45E-10
3	**K^+**	119	150	2.18E-03	4.16E-03	7.87E-10
2	**Cl^-**	48.7	69.4	7.31E-05	2.68E-04	1.20E-10
3	**Cl^-**	129	150	7.93E-04	1.23E-03	2.68E-10

Table 5.4. The J_{out} of K^+ and Cl^- during the 2nd and 3rd osmotic cycles

Cycle	Element	Start day	End day	Start $\sum M_{out}$ (kg/m^2)	End $\sum M_{out}$ (kg/m^2)	J_{out} (kg/m^2s)
2	**K^+**	50.6	69.4	-2.24E-04	-4.10E-04	-1.27E-10
3	**K^+**	119	150	-5.82E-04	-1.17E-03	-2.34E-10
2	**Cl^-**	48.7	69.4	-2.66E-04	-3.73E-04	-6.61E-11
3	**Cl^-**	129	150	-6.24E-04	-9.53E-04	-2.03E-10

When comparing the J_{in} and J_{out} of K^+ and Cl^- in the 2nd and 3rd osmotic cycles, it was evident that the differences between the J_{in} and J_{out} of Cl^- were much smaller than that of K^+. The Cl^- J_{in} were respectively 1.82 and 1.32 times of the Cl^- J_{out} in the 2nd and 3rd osmotic cycles, while the K^+ J_{in} were respectively 2.72 and 3.36 times of the K^+ J_{out}. This phenomenon was as expected because Cl^- was a non-reactive species and K^+ was a reactive species.

5.6.2 Solute Diffusion

As discussed in Section 4.6.2, Fick's first law was used to approximate the D^* of non-reactive species (i.e. Cl^-) and the average D^* of reactive species (i.e. K^+) (Table 5.5). At steady state the J_{in} of Cl^- were very close to the J_{out} of Cl^-, so it was certain that the D^* of Cl^- within sample was close to the D^* of Cl^- at the top and bottom boundaries. However, the J_{in} of K^+ were significantly higher than the J_{out} of K^+. It could only be assumed that the D^* of K^+ within sample was the average between the D^* of K^+ at the top and bottom boundaries.

Table 5.5. The D^* of K^+ and Cl^- during the 2nd and 3rd osmotic cycles

Cycle	Species	J (kg/m^2s)	C_t (kg/m^3)	C_b (kg/m^3)	h (m)	dC/dh ($kg/m^3/m$)	n	D^* (m^2/s)
2	**Cl^- (Top)**	1.20E-10	0.375	0.266	0.00584	18.7	0.33	1.95E-11
2	**Cl^- (Bottom)**	6.61E-11	0.375	0.266	0.00584	18.7	0.33	1.07E-11
2	**K^+ (Average)**	2.36E-10	0.118	0.011	0.00584	18.4	0.33	3.88E-11
3	**Cl^- (Top)**	2.68E-10	0.524	0.269	0.00584	43.7	0.33	1.85E-11
3	**Cl^- (Bottom)**	2.03E-10	0.524	0.269	0.00584	43.7	0.33	1.41E-11
3	**K^+ (Average)**	5.11E-10	0.254	0.018	0.00584	40.5	0.33	3.82E-11

Table 5.5 shows that the D^* of Cl^- within sample was $1 - 2 \times 10^{-11}$ m^2/s and the D^* of K^+ within sample was 3.8×10^{-11} m^2/s. The D^* of K^+ was 2 – 3.5 times higher than that of Cl^-.

According to Malusis et al. (2001), the D^* of Cl^- and K^+ within the sample must be the same at steady-state diffusion due to electroneutrality. The D^* of K^+ was higher than that of Cl^- in this study because the diffusion of K^+ across sample had not reached steady state by the end of osmotic cycles (Figures 5.39 and 5.40). Neuzil did not perform D^* analyses with the Pierre Shale in North Dakota and South Dakota. Malusis et al. (2001) performed the D^* analyses with KCl using geosynthetic clay liner specimens (Na^+ bentonite). For the test in which $C_{0t} = 0.0087$ KCl, the D^* values of K^+ and Cl^- were respectively 1.16×10^{-10} m^2/s and 0.907×10^{-10} m^2/s. While the Pierre Shale core sample used in this study was subjected to an extremely high confining pressure (6000 to 7000 kPa) during the Quaternary glaciations, the clay liner specimen used in the Malusis et al. (2001) was a reconstituted sample subjected to a much lower confining pressure, so it is reasonable that there was more EDL overlap in Pierre Shale sample, subsequently leading to the lower D^* values of K^+ and Cl^- in this study compared to that reported by Malusis et al. (2001).

5.6.3 Sorption Reactions

The cumulative change of total K^+ stored mass within sample ($\sum M_{stored}$, in kg) during the 2nd and 3rd osmotic cycles (Figures 5.43 and 5.44) were calculated using Eq. 4.17. The K^+ $\sum M_{stored}$ results are provided in Appendix C (Tables C.5 and C.6). The patterns followed the K^+ $\sum M_{stored}$ shown in Figures 5.39 and 5.40.

The change of 'average' K^+ mass stored in pore fluid (M_{fluid}) during the 2nd and 3rd osmotic cycles (Figures 5.43 and 5.44) were calculated using Eq. 4.18. The K^+ M_{fluid} results are provided in Appendix C (Tables C.5 and C.6). Since the synthetic fluids circulated at the

top and bottom boundaries within each osmotic cycle had very consistent chemical concentrations, the K^+ M_{fluid} were very stable in both osmotic cycles. The K^+ M_{fluid} in the 2nd osmotic cycle (day 22 to day 69) and the 3rd osmotic cycle (day 85 to day 149) were respectively 4.58×10^{-7} kg and 5.06×10^{-7} kg.

The cumulative change of K^+ stored mass involved in cation exchange (adsorbed on soil particles) ($\sum M_{solid}$) during the 2nd and 3rd osmotic cycles (Figures 5.43 and 5.44) were calculated using Eq. 4.20. The K^+ $\sum M_{solid}$ results are provided in Appendix C (Tables C.5 and C.6).The K^+ $\sum M_{solid}$ in the 2nd osmotic cycle (day 22 to day 69) and the 3rd osmotic cycle (day 85 to day 149) were respectively 3.48×10^{-6} kg and 8.95×10^{-6} kg.

The K_d of K^+ during the 2nd and 3rd osmotic cycles were calculated using Eq. 4.21. The calculated dry mass of the sample (M_{dry}) was 0.0328 kg. The K_d of K^+ during the 2nd and 3rd osmotic cycles were respectively 1.41×10^{-3} m^3/kg and 3.29×10^{-3} m^3/kg. The concomitant R_d were respectively 12.3 and 27.4.

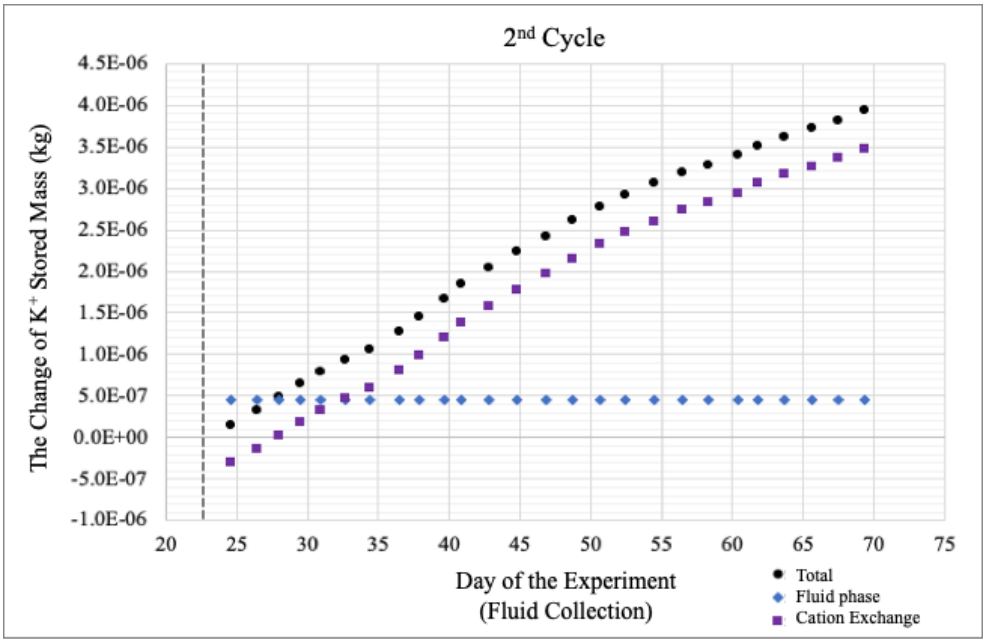

Figure 5.43. The cumulative change of K^+ stored mass (total, involved in cation exchange) and the change of 'average' K^+ mass stored in pore fluid during the 2nd osmotic cycle

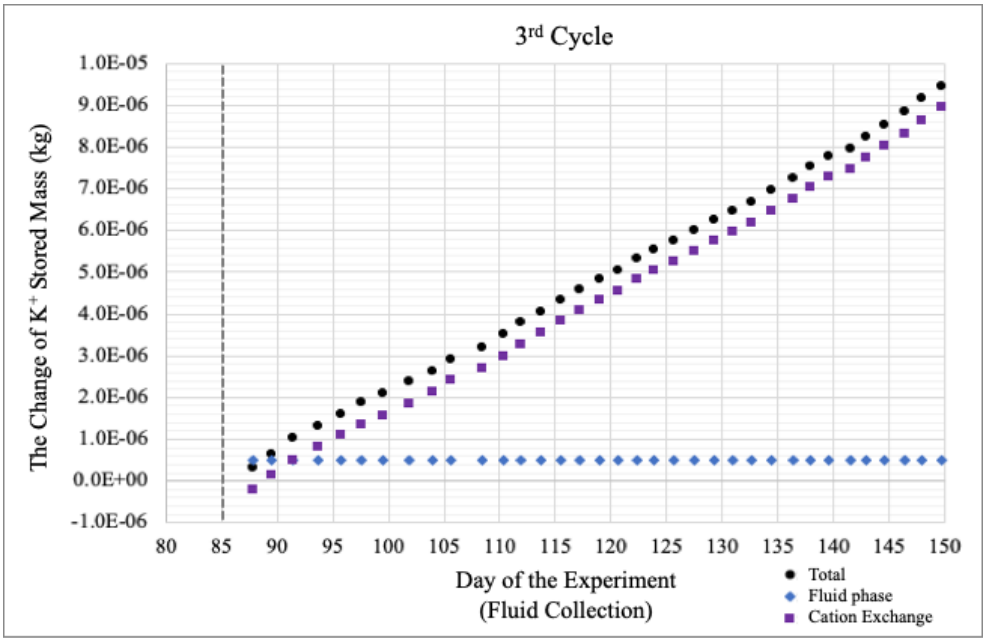

Figure 5.44. The cumulative change of K^+ stored mass (total, involved in cation exchange) and the change of 'average' K^+ mass stored in pore fluid during the 3rd osmotic cycle

The cumulative change of total Cl^- stored mass within sample ($\sum M_{stored}$, in kg) during the 2nd and 3rd osmotic cycles (Figures 5.45 and 5.46) were calculated using Eq. 4.17. The Cl^- $\sum M_{stored}$ results are provided in Appendix C (Tables C.7 and C.8). The patterns followed the Cl^- $\sum M_{stored}$ shown in Figures 5.41 and 5.42.

The change of 'average' Cl^- mass stored in pore fluid (M_{fluid}) during the 2nd and 3rd osmotic cycles (Figures 5.45 and 5.46) were calculated using Eq. 4.18. The Cl^- M_{fluid} results are provided in Appendix C (Tables C.7 and C.8). Since the synthetic fluids circulated at the top and bottom boundaries within each osmotic cycle had very consistent chemical concentrations, the Cl^- M_{fluid} were very stable in both osmotic cycles. The Cl^- M_{fluid} in the 2nd osmotic cycle (day 22 to day 69) and the 3rd osmotic cycle (day 85 to day 149) were respectively 3.81×10^{-7} kg and 4.74×10^{-7} kg.

Since Cl^- was a non-reactive solute species, all Cl^- stored within the sample was in fluid phase. The volume required to store Cl^- within the pore fluid during the 2nd and 3rd osmotic cycles (Figures 5.47 and 5.48) were calculated using Eq. 4.19. The V_{Cl} results are provided in Appendix C (Tables C.9 and C.10). Since solute transport in the 1st osmotic cycle was limited, it was assumed that V_{Cl} was equal to the total pore volume (6.10×10^{-6} m^3) at the beginning of 2nd osmotic cycle. The initial Cl^- stored mass during 2nd osmotic cycle was assumed to be 1.98×10^{-6} kg. Figure 5.47 shows that V_{Cl} decreased significantly from 6.10×10^{-6} m^3 to 3.95×10^{-6} m^3 from day 26 to day 36. The decrease of V_{Cl} supported that anion exclusions occurred

from day 26 to day 36. After the anion exclusion period, the influx and outflux of Cl^- reached steady state. Therefore, the increase of Cl^- stored mass was limited. The V_{Cl} was much less than the total pore volume during the rest of 2nd osmotic cycle. Figure 5.48 shows that the V_{Cl} increased back to the total pore volume from day 85 to day 97. The V_{Cl} decreased from 5.8 – 6.0 × 10^{-6} m^3 to 5.54 × 10^{-6} m^3 from day 97 to day 112. The decrease of V_{Cl} supported that anion exclusions occurred from day 97 to day 112. The V_{Cl} increased back to the total pore volume from day 112 to day 119. The second decrease of V_{Cl} occurred between day 120 to day 127, from 6.07 × 10^{-6} m^3 to 5.38 × 10^{-6} m^3. The decrease of V_{Cl} supported that anion exclusions occurred from day 120 to day 127. The V_{Cl} was stable at 5.4 – 5.5 × 10^{-6} m^3 from day 127 to day 135, and increased back to the total pore volume from day 134 to day 139. The V_{Cl} was stable and close to the total pore volume from day 139 to day 149.

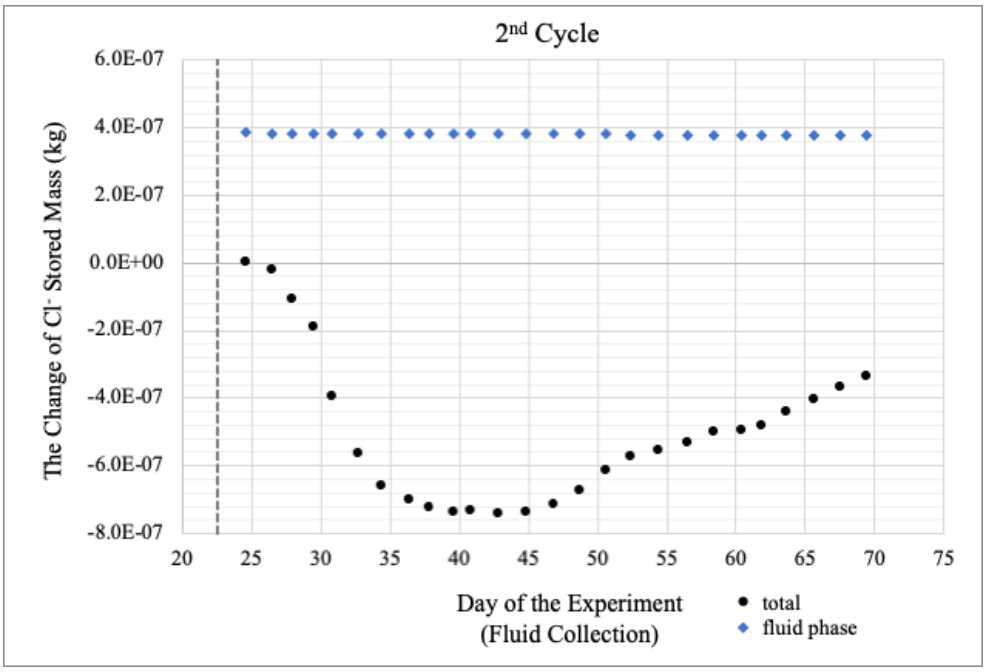

Figure 5.45. The cumulative change of total Cl^- stored mass and the change of 'average' Cl^- mass stored in pore fluid during the 2nd osmotic cycle

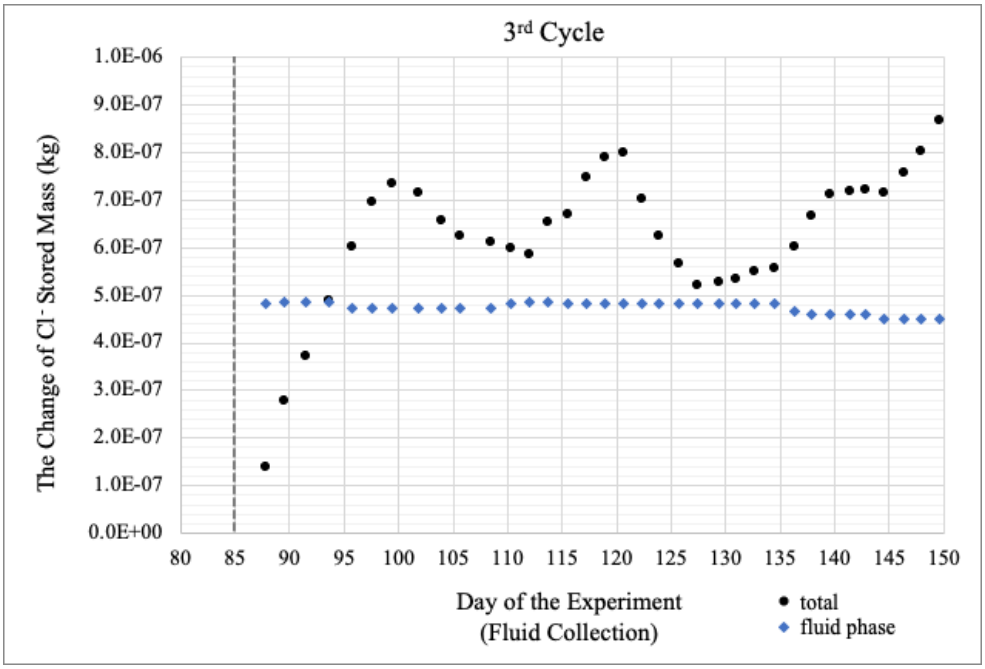

Figure 5.46. The cumulative change of total Cl^- stored mass and the change of 'average' Cl^- mass stored in pore fluid during the 2nd osmotic cycle

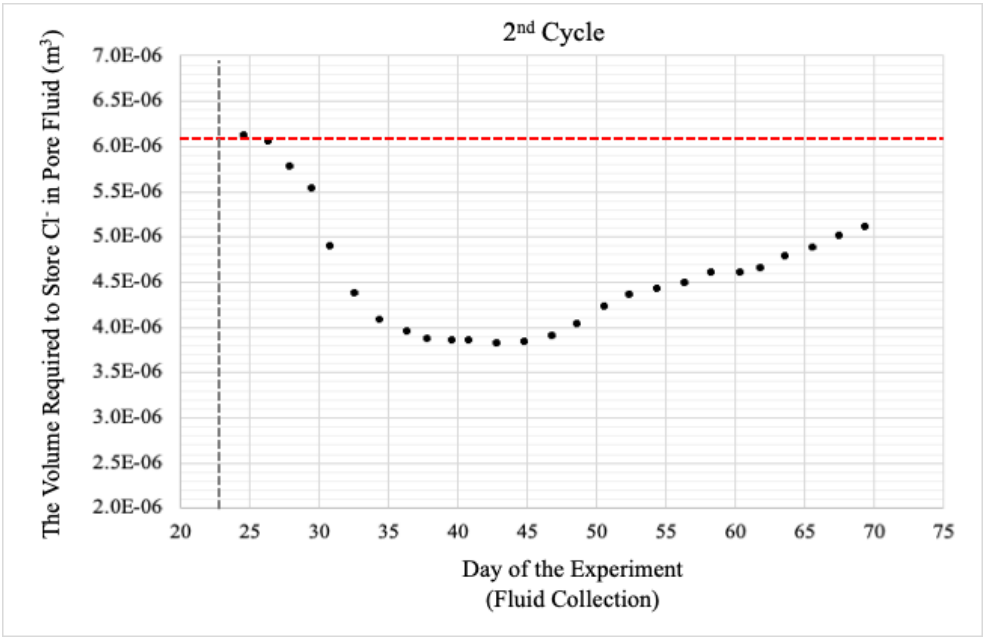

Figure 5.47. The volume required to store the Cl^- in pore fluid during the 2nd osmotic cycle; red dash line represents the total pore volume

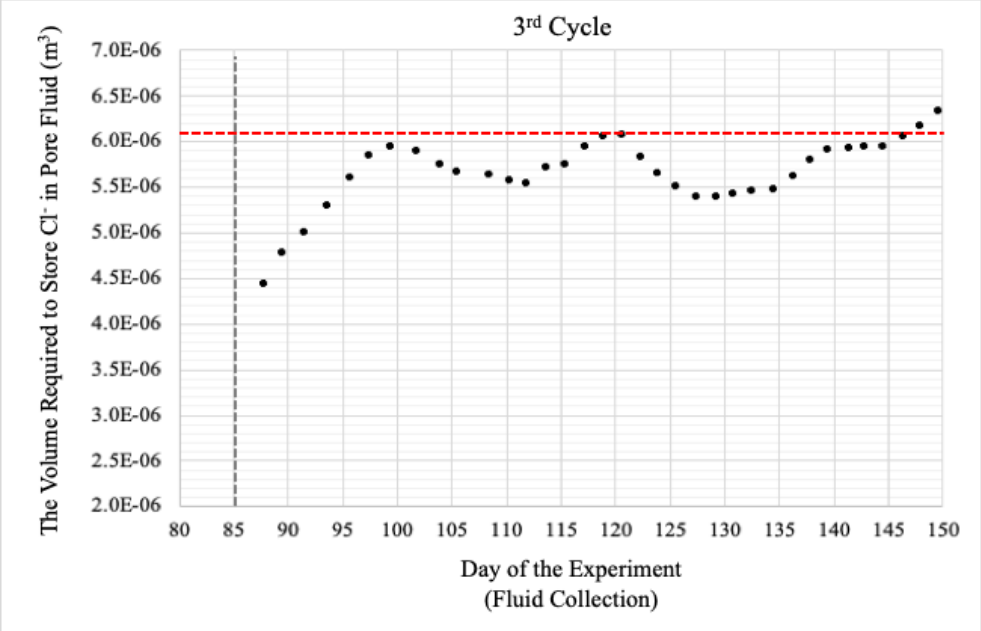

Figure 5.48. The volume required to store the Cl^- in pore fluid during the 3rd osmotic cycle; red dash line represents the total pore volume

The cumulative changes of cations (K^+, Na^+, Mg^{2+}, Ca^{2+}, Fe^{3+}) stored amounts ($\sum Q_{stored}$) involved in cation exchange during the 2nd and 3rd osmotic cycles are presented in Figures 5.49 and 5.50, and provided in Appendix C (Tables C.11 and C.12). Negative values meant the amount of certain cation species stored within the sample decreased. The net cation $\sum Q_{stored}$ was calculated by summarizing the $\sum Q_{stored}$ of major cations (K^+, Na^+, Mg^{2+}, Ca^{2+}, Fe^{3+}) (Figures 5.51 and 5.52; Appendix C - Tables C.11 and C.12). Negative values meant the amount of cations stored within the sample was less than that in the previous osmotic cycle.

During the 2nd osmotic cycle, K^+ was the major cation species adsorbed within the sample, and Ca^{2+} was the major cation species desorbed from the sample. The cumulative K^+ stored amount increased by 8.90×10^{-5} Eq, and the cumulative Ca^{2+} stored amount decreased by 1.44×10^{-4} Eq. The Na^+ desorption during the 2nd osmotic cycle was limited. The cumulative Na^+ desorbed amount was 1.79×10^{-5} Eq. The net cation $\sum Q_{stored}$ decreased consistently from -1.28×10^{-5} Eq to -9.55×10^{-5} Eq from day 22 to day 69. During the 3rd osmotic cycle, the cumulative K^+ stored amount increased by 2.29×10^{-4} Eq, and the cumulative Ca^{2+} stored amount decreased by 2.90×10^{-4} Eq. The cumulative change of Na^+ stored amount was limited from day 85 to day 115 (-8.98×10^{-6} Eq). A significant Na^+ desorption occurred from day 115 to day 149. The cumulative Na^+ desorbed amount was 1.07×10^{-4} Eq. The cumulative Na^+ desorbed amount was approximately 50% of the cumulative K^+ adsorbed amount. The net cation $\sum Q_{stored}$ decreased consistently from -1.63×10^{-5} Eq to -

1.83×10^{-5} Eq from day 85 to day 144, and became stable at -1.84×10^{-5} Eq from day 144 to day 149.

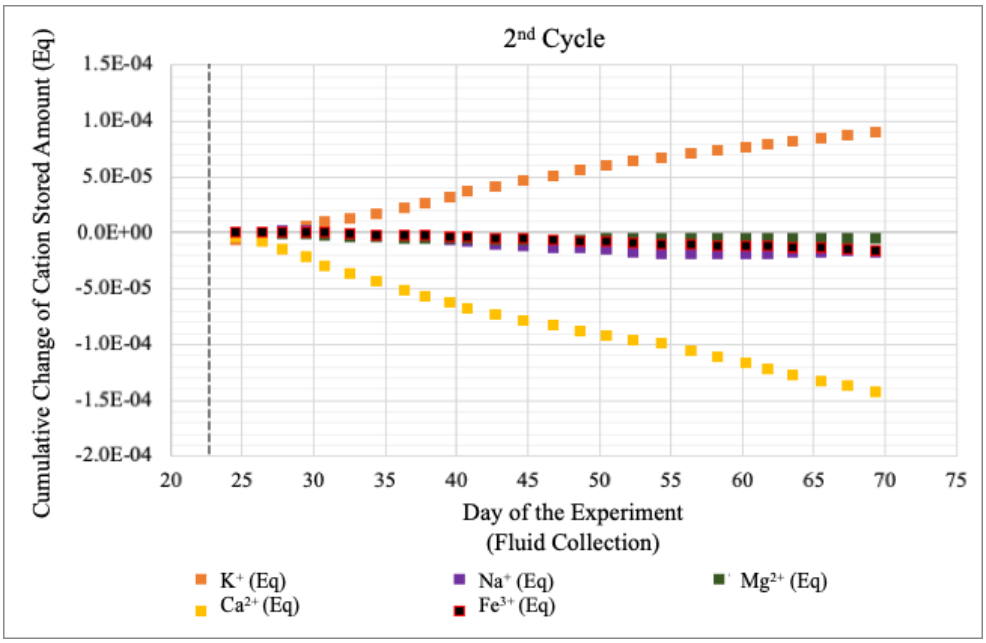

Figure 5.49. The cumulative change of K^+, Na^+, Ca^{2+}, Mg^{2+}, and Fe^{3+} stored amounts involved in cation exchange during the 2nd osmotic cycle

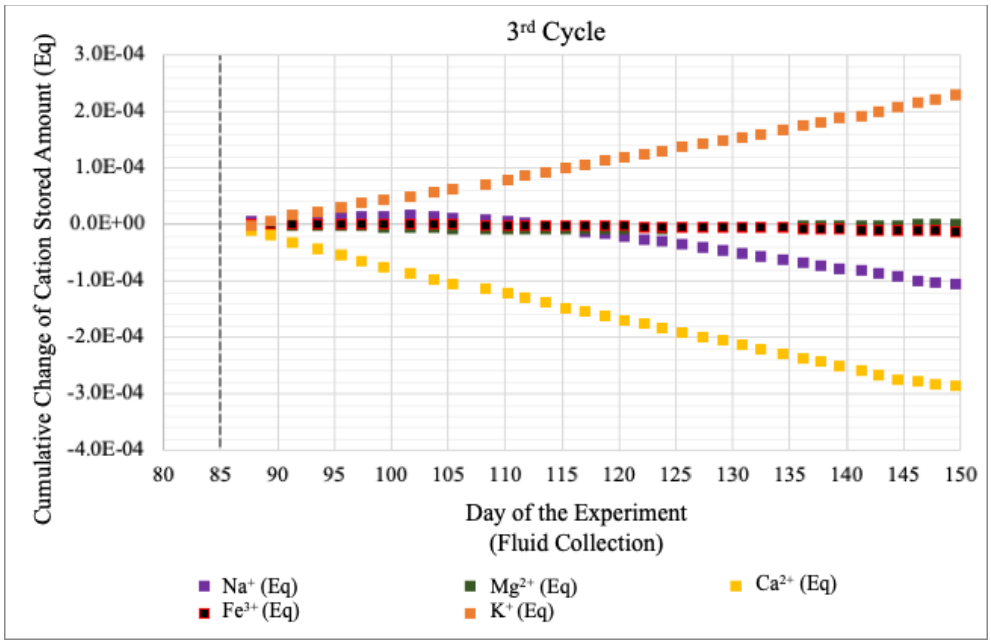

Figure 5.50. The cumulative change of K^+, Na^+, Ca^{2+}, Mg^{2+}, and Fe^{3+} stored amounts involved in cation exchange during the 3rd osmotic cycle

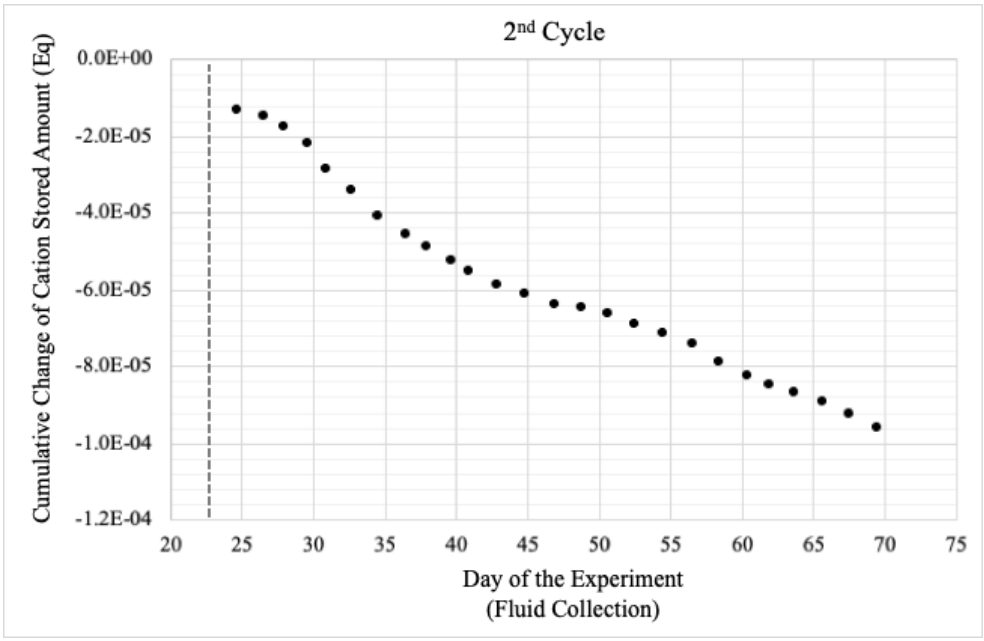

Figure 5.51. The net change of cations stored amount involved in cation exchange during the 2nd osmotic cycle

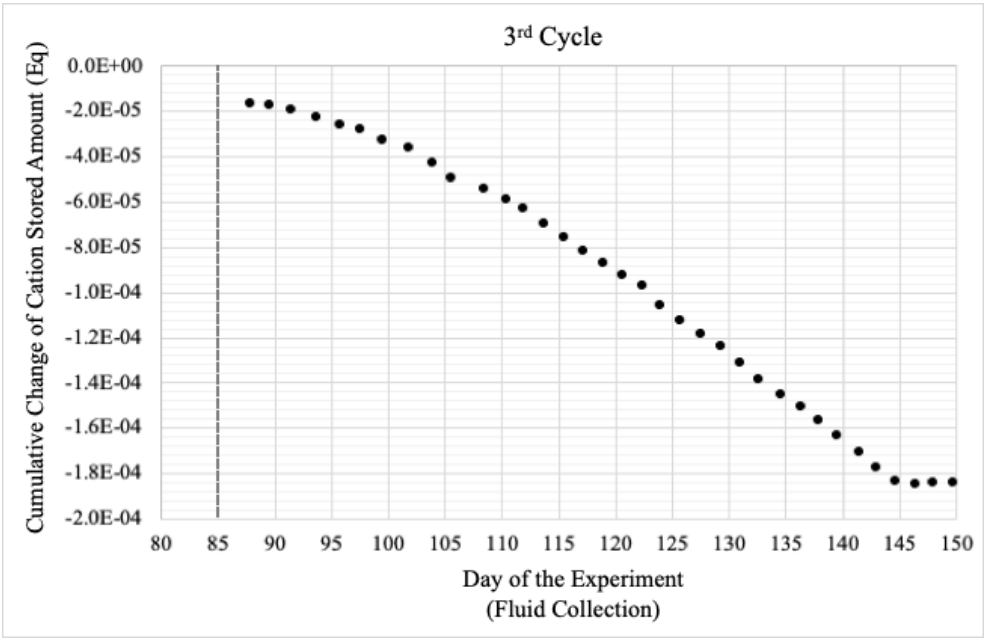

Figure 5.52. The net change of cations stored amount involved in cation exchange during the 3rd osmotic cycle

CHAPTER 6: DISCUSSION

6.1 Introduction

Two approaches were used to study the semipermeability of the Pierre Shale sample. The first approach was the direct measurements of osmotic pressure (ΔP, Δπ) to calculate the osmotic efficiency (ω). The second approach was the back analyses of solute transport model. This chapter discusses how the results from these two different approaches supported that the Pierre Shale sample was an efficient semipermeable membrane. This chapter also discusses the factors that controlled the semipermeability of Pierre Shale sample according to the diffusive double layer theory. The study of osmotic pressure and osmotic efficiency of the semipermeable shale sample discussed in Section 6.2. The study of solute transport within the semipermeable shale sample is discussed in Section 6.3. The influence of solute transport towards the fluctuation of observed differential pressure during the chemical osmosis testing is discussed in Section 6.4. The factors that differentiate the osmotic efficiencies of the Pierre Shale in this study from those reported by Neuzil (2000) and Garavito *et al.* (2006) are discussed in Section 6.5.

6.2 Osmotic Pressure and Osmotic Efficiency

The first approach to characterize the semipermeability of Pierre Shale is through osmotic pressure (ΔP, Δπ) and osmotic efficiency (ω). Theoretical osmotic pressures (Δπ) were calculated based on the total major cation and anion concentration difference of the synthetic fluids (Na^+, K^+, Mg^{2+}, Cl^-, SO_4^{2-}, HCO_3^-) circulated at the top and bottom boundaries. The concentration gradient across shale sample was almost constant (7.10 – 7.44 mol/m^3 and 16.1 – 16.7 mol/m^3, respectively) during the 2nd and 3rd osmotic cycles, so Δπ were stable, at 35.2 – 36.9 kPa and 80.0 – 82.6 kPa, respectively (Figure 5.22 and Figure 5.23). The 'peak' ΔP were observed from the difference between the initial DP and the 'peak' DP. The 'residual' ΔP were observed from the difference between the initial DP and the equilibrium DP. The 'peak' ΔP were 1.7 kPa and 1.6 kPa respectively, and the 'residual' ΔP were 0.9 kPa and 1.0 kPa respectively during the 2nd and 3rd osmotic cycles (Figure 5.15 and Figure 5.16). While Δπ was a controllable parameter because the major cation and anion concentrations of synthetic fluids were easily controllable, ΔP was not a controllable parameter. The ΔP was primarily governed by the solute transport within the shale sample. The 'peak' ω of shale sample calculated based on the Δπ and the 'peak' ΔP were respectively 0.0472 and 0.0196 during the

2nd and 3rd osmotic cycles, while the 'residual' ω calculated based on the Δπ and the 'residual' ΔP were respectively 0.0250 and 0.0123. Since the ω values were within the range of zero (indicating no restriction to pore fluid flow) and one (indicating a perfect membrane that inhibits pore fluid flow), these values supported that the shale sample was an efficient semipermeable membrane.

6.3 Solute Transport Model

The second approach to characterize the semipermeability of Pierre Shale is through the solute transport model. In this study, the chemical osmotic circulation system was designed that the synthetic fluids circulated at the top and bottom boundaries during the 2nd and 3rd osmotic cycles had different chemical concentrations. Type B and Type C synthetic fluids (0.0037 M and 0.0082 M KCl, respectively) were circulated at the top boundary during the 2nd and 3rd osmotic cycles while Type A synthetic fluid (0 M KCl) was circulated at the bottom boundary during both osmotic cycles. Since solutes always transport from regions of higher concentrations to regions of lower concentrations (Malusis *et al.*, 2003), KCl transported from the top boundary, through the shale sample, to the bottom boundary, corresponding to the concentration gradient during the 2nd and 3rd osmotic cycles. The exceptions occurred during the anion exclusion periods (day 26 to day 36, day 97 to day 112, day 120 to day 127). During these periods, the Cl^- influx was partially or completely prohibited.

The $\sum M_{in}$ and $\sum M_{out}$ of K^+ during the 2nd and 3rd osmotic cycles supported that the Pierre Shale sample was an efficient semipermeable membrane (Figures 5.39 and 5.40). The rate of K^+ $\sum M_{in}$ (J_{in}) should be close to the rate of K^+ $\sum M_{out}$ (J_{out}) for a sample at steady state with no restriction towards pore fluid flow. K^+ $\sum M_{out}$ should be close to zero for a perfect membrane that inhibits pore fluid flow. Figures 5.39 and 5.40 show that K^+ $\sum M_{out}$ was approximately 25% of K^+ $\sum M_{in}$. Also, the rate of K^+ $\sum M_{out}$ (J_{out}) was much lower than the rate of K^+ $\sum M_{in}$ (J_{in}) during the 2nd and 3rd osmotic cycles. Therefore, the results show that the Pierre Shale sample was neither a sample with no restrictions nor a perfect sample. Instead, the Pierre Shale sample was a semipermeable membrane. Since K^+ $\sum M_{in}$ was much higher than K^+ $\sum M_{out}$, K^+ $\sum M_{stored}$ increased consistently in the 2nd and 3rd osmotic cycles. Figures 5.43 to 5.44 show that most of the K^+ $\sum M_{stored}$ increase came from the K^+ adsorption. K^+ $\sum M_{solid}$ (K^+ involved in cation exchange) were 90 – 95% of K^+ $\sum M_{stored}$ in the 2nd and 3rd osmotic cycles (Figures 5.43 and 5.44).

The K_d and R_d of K^+ during the 2nd and 3rd osmotic cycles supported that the Pierre Shale sample was an efficient semipermeable membrane. The R_d should be close to unity for a sample with no restrictions. The K_d of K^+ during the 2nd and 3rd osmotic cycles were respectively 1.41×10^{-3} m^3/kg and 3.29×10^{-3} m^3/kg. The concomitant R_d were respectively 12.3 and 27.4. Since the R_d were significantly higher than unity, the Pierre Shale sample was a semipermeable membrane.

K^+ transport retardation was mainly due to the adsorption-desorption reactions among K^+, Ca^{2+}, and Na^+. Figures 5.49 and 5.50 show that K^+ was the major cations adsorbed within the shale sample. The adsorption of K^+ led to the desorption of cations, mainly Na^+ and Ca^{2+}. During the 2nd osmotic cycle, the adsorption-desorption reactions between Na^+ and K^+ were minor (Figure 5.49). During the 3rd osmotic cycle, the adsorption-desorption reactions between Na^+ and K^+ after day 115 were much more significant (Figure 5.50). The adsorption-desorption reactions between Na^+ and K^+ led to the osmotic consolidation, which subsequently reduced the mineral surface area. As a result, the mineral surface area available for cation adsorption reduced. The net cation $\sum Q_{stored}$ subsequently decreased more significantly after day 115 (Figure 5.52).

6.4 The Influence of Solute Transport on the Differential Pressure Fluctuation

Many previous researchers suggest that the increase of ΔP during chemical osmosis is due to the pore pressure build-up at the regions of higher concentrations (Fritz, 1986; Neuzil, 2000; Neuzil & Provost, 2009; Takeda *et al.*, 2014). However, the pressure build-up was not evident in both the top and bottom boundaries in this study (Figure 5.20). The pressure at the regions of higher concentrations (top boundary) was very stable (less than 0.2 kPa). The pressure at the regions of lower concentrations (bottom boundary) fluctuated between 0 kPa to 1 kPa, and tended to be much lower during the period with higher DP. Barbour and Fredlund (1989) suggest that negative pore pressure tends to develop within clay-rich sample during osmotic induced consolidation, and is correspondent to the strong osmotic gradient. Figure 5.21 shows the cumulative change of sample height due to both osmotic consolidation and osmotic induced consolidation during the 3rd osmotic cycle. Osmotic consolidation occurred between day 87 to day 97, and osmotic induced consolidation occurred between day 103 to day 110, and day 120 to day 124. Figure 5.16 shows that DP increased from day 95 to day 110, and day 122 to day 124. Therefore, the periods showing the periods of osmotic induced consolidation matched with the periods showing DP increase.

The DP increase during the 2nd and 3rd osmotic cycles (Figures 5.15 and 5.16) seemed to be directly related to anion exclusion (Cl^- influx restriction) (Figures 5.41 and 5.42). According to Barbour (1987), any factor that reduces the number of solute molecules impacting a solution inside small restricting pores will cause an increase in ΔP. Anion exclusion is such a factor. According to Figures 5.41 and 5.42, Cl^- influx was completely prohibited from day 26 to day 36 in the 2nd osmotic cycle, and partially prohibited from day 97 to day 112, and day 120 to 127 in the 3rd osmotic cycle. The periods where DP increased and stayed at the peak (Figure 5.15 and Figure 5.16) matched with the anion exclusion periods.

During the 2nd and 3rd osmotic cycles, there was a continuous K^+ influx. K^+ $\sum M_{Stored}$ in the sample increased consistently over time during both osmotic cycles (Figures 5.43 and 5.44). Cation exchange between K^+ and Na^+ was minor during the 2nd osmotic cycle, and it was significantly more after day 115 during the 3rd osmotic cycle (Figures 5.49 and 5.50). As discussed in Section 2.5.5, the EDL thickness tends to be thinner when the cations around the negative clay particle surface have higher valence and/or larger dehydrated radius (Langmuir, 1997; Mitchell & Soga, 2005). During the 3rd osmotic cycle, a significant amount of Na^+ stored within the sample was replaced by K^+. As a result, the EDL thickness decreased, and the ability of the shale to perform as a semipermeable membrane reduced drastically (Kharaka & Berry, 1973; Langmuir, 1997; Malusis & Shackelford, 2002; Mitchell & Soga, 2005). The reduced semipermeability of the shale sample was reflected by the observation that the 'peak' and the 'residual' ω in the 3rd osmotic cycle (0.0472 and 0.0250, respectively) was less than that in the 2nd osmotic cycle (0.0196 and 0.0123, respectively).

6.5 Important Factors that Control the Osmotic Efficiencies

The ω of Pierre Shale in this study was 0.0123 – 0.0472 (see Section 5.4 for detail). The ω of Pierre Shale in this study were slightly lower than those reported by Neuzil (2000) and Garavito *et al.* (2006) (0.038 – 0.14) (Table 2.3). The total clay % and porosities of the shale samples were 70 – 80% and 0.33 / 0.34, respectively, so these parameters were very similar. There are three main factors that contributed to the slight differences of ω between the shale samples in this study and the Neuzil (2000) and Garavito *et al.* (2006) studies : clay composition, solute chemistry, and cation exchange between K^+ and Na^+.

A semipermeable membrane tends to have a greater ω when the smectite proportion is larger, and a lower ω when the kaolinite proportion is larger (Holtz & Kovacs, 1981; Dolinar & Trauner, 2004; Dolinar *et al.*, 2007). The shale sample used in this study contained a total

50% smectite and illite (20% illite and 30% smectite), and 25% kaolinite. The shale sample used in Neuzil (2000) and Garavito *et al.* (2006) contained a total 70 – 80% of smectite and illite, and 0% kaolinite. Therefore, the shale sample used in this study contained a total 20 – 30% less of smectite and illite, and 25% more of kaolinite than the shale sample used in the Neuzil (2000) and Garavito *et al.* (2006). Due to the above stated behaviour of clay compositions and ω, it is reasonable that the ω of shale in this study were slightly lower than those reported by Neuzil (2000) and Garavito *et al.* (2006).

Solute chemistry is another important factor that causes the difference of ω between the shale samples. The solutes used to create a change in concentration across the shale sample in the Neuzil (2000) and Garavito *et al.* (2006) was NaCl, while the solutes used in this study was KCl. As discussed in Section 2.5.5, cations with larger hydrated radii are more likely to be restricted to move through the pores of a given size (Kharaka & Berry, 1973; Malusis & Shackelford, 2002). According to Table 2.1, the hydrated diameter of Na^+ (8.35 Å) is much larger than that of K^+ (6.12 Å), so it is reasonable that the Γ in this research is lower. Given that the ω of a semipermeable membrane has same value as the Γ, it is reasonable that the ω of shale in this study were slightly lower than those reported by Neuzil (2000) and Garavito *et al.* (2006).

Smectite with high Na^+ concentrations has the highest swelling potential (Curtin *et al.*, 1994) due to the weak bonding between particles; therefore, the EDL is the thickest in Na-smectite. NaCl was the type of solute used to create a change in concentration across the shale sample in the Neuzil (2000) and Garavito *et al.* (2006), so Na^+ remained as the primary cation species within the shale sample during the entire tests. Therefore, the EDL was consistently thick and the ω of shale sample was consistently high. KCl was the type of solute used to create a change in concentration across the shale sample in this study. An experiment conducted by di Maio (1996) shows that when the Na-smectite was exposed to KCl, the exchangeable Na^+ was substituted by K^+. As a result, the Na-smectite was converted to the K-smectite. The chemical analyses in this study show that the shale sample was dominated by NaCl during the 1st osmotic cycle. However, there was a minor cation exchange between K^+ and Na^+ during the 2nd osmotic cycle, and a more significant cation exchange between K^+ and Na^+ during the 3rd osmotic cycle. The potential for the growth of thick oriented water layers in K-smectite is very small due to the tight bonding between particles (Grim, 1958). As a result, the cation exchange between K^+ and Na^+ led to a decrease in EDL thickness within the shale sample, which led to a decrease in ω of the shale sample.

CHAPTER 7: CONCLUSIONS AND RECOMMENDATIONS

7.1 Conclusions

The goal of this research is to characterize the semipermeability of Pierre Shale in southern Saskatchewan using core obtained near the Mosaic's Esterhazy K2 Potash Mine at a depth of 121 m BGS. Two different approaches were adopted to characterize the semipermeability of Pierre Shale. The first approach was the direct measurements of osmotic pressure (ΔP, $\Delta\pi$) to calculate the osmotic efficiency (ω). The value of ω ranges from zero (indicating no restriction to the pore fluid drainage), to one (a perfect membrane that inhibits the pore fluid drainage) (Fritz, 1986). The second approach was the back analyses of solute transport model.

The porosity of sample was 0.33, with a clay mineralogy of a total 50% illite and smectite (20% illite and 30% smectite), and 25% kaolinite. The saturated K of the sample was 6×10^{-11} m/s determined by the rate of upward seepage during the saturation stage of sample preparation. The m_v of sample was 9.0×10^{-5} kPa^{-1} (or 9.0×10^{-8} Pa^{-1}) determined by the one-dimensional loading of sample in the chemical osmotic circulation system before the start of the chemical osmosis testing. In unfractured, low-permeability clay-rich formations, diffusion is the dominant mechanism of solute transport.

According to the diffusive double layer theory developed by Bresler (1973), the semipermeability of a clayey material is highly related to the EDL thickness. Given the pore structures and pore sizes of semipermeable membranes are similar, solute transport is more likely to be restricted when the EDL is thicker. Many previous researchers suggest that the ω of clayey materials is mainly influenced by the pore size distribution, confining pressure (σ_v), temperature, mineralogy, and pore fluid chemistry (Barbour & Fredlund, 1989; Neuzil, 2000; Cey *et al.*, 2001; Rahman *et al.*, 2005; Al-Bazali *et al.*, 2006; Gonçalvès *et al.*, 2007; Rousseau-Gueutin *et al.*, 2008; Neuzil & Provost, 2009; Rousseau-Gueutin *et al.*, 2009; Takeda *et al.*, 2014).

This research was designed to :

- Construct the chemical osmotic circulation system and observe the fluctuation of DP across the sample during multiple osmotic cycles;
- Characterize the semipermeability of Pierre Shale through the osmotic pressure (ΔP, $\Delta\pi$) and osmotic efficiency (ω), as well as the solute transport model; and

- Identify the important factors and processes that govern the semipermeability of Pierre Shale.

There were three osmotic cycles in the chemical osmosis testing. During the chemical osmosis testing, synthetic fluids were circulated along the top and bottom boundaries of sample, resulting in a controlled ΔC across sample (0 mol/m^3, 7.102 – 7.438 mol/m^3 and 16.133 – 16.656 mol/m^3, respectively). The differential pressure (DP) across sample, the osmotic pressure (LP) at the top and bottom boundaries, the laboratory temperature (T_{lab}), and the sample height (Δh) were monitored in the chemical osmotic circulation system. The observed DP (ΔP) and the calculated DP ($\Delta \pi$) were compared to determine the ω of sample. Fluids were collected from the chemical osmotic circulation system every 1.5 days for chemical analyses.

Due to the solute transport across the sample, the chemical components of collected fluid samples were different from the chemical components of synthetic fluids. A series of laboratory tests (AAS, AES, IC, alkalinity tests) were conducted to determine the major cation and anion concentrations of collected fluid samples and synthetic fluids. The CBE of collected fluid samples and synthetic fluids showed that the data collected from the laboratory tests were representative to construct the solute transport model. The solute transport model included the cumulative change of K^+ and Cl^- mass stored within sample due to mass influx and mass outflux, the K^+ and Cl^- J_{in} and J_{out}, the D^* of Cl^- and the average D^* of K^+ within the sample, the K_d and R_d of K^+, the V_{Cl} within sample, and the adsorption-desorption reactions among K^+ and other major cations originally within the sample.

7.1.1 Research Findings

The 'peak' ΔP observed from the chemical osmosis circulation system were 1.7 kPa and 1.6 kPa respectively, and the 'residual' ΔP were 0.9 kPa and 1.0 kPa respectively during the 2nd and 3rd osmotic cycles. The $\Delta \pi$ calculated based on the total major cation and anion concentration difference of the synthetic fluids (Na^+, K^+, Mg^{2+}, Cl^-, SO_4^{2-}, HCO_3^-) circulated at the top and bottom boundaries were stable, at 35.212 – 36.875 kPa and 79.987 – 82.578 kPa, respectively. The 'peak' and 'residual' ω of Pierre Shale sample were determined by comparing the 'peak' and 'residual' ΔP with the $\Delta \pi$. The 'peak' ω were respectively 0.0472 and 0.0196 during the 2nd and 3rd osmotic cycles, and the 'residual' ω were respectively 0.0250 and 0.0123. The ω values in this study were closer to zero (indicating no restriction to pore fluid flow) than to one (indicating a perfect membrane that inhibits pore fluid flow). Therefore, these values

suggested that the shale sample was far from being an impermeable membrane, but it was still a semipermeable membrane effective in restricting solute transport. The ω of Pierre Shale / Bearpaw Formation obtained by other researchers have been provided in Table 2.3. The ω of Pierre Shale sample in this research were slightly lower than those reported by Neuzil (2000) and Garavito *et al.* (2006) (0.038 – 0.14). The three main factors that contributed to the slight differences of ω between the shale samples in this research and those in the Neuzil (2000) and Garavito *et al.* (2006) were clay composition, solute chemistry, and cation exchange between K^+ and Na^+.

During the 2nd and 3rd osmotic cycles, the K^+ and Cl^- influx occurred consistently through the top boundary and the K^+ and Cl^- outflux occurred consistently through the bottom boundary. It is supported by the consistent increase of $\sum M_{in}$ and the consistent decrease of $\sum M_{out}$. The exceptions occurred during the anion exclusion periods (day 26 to day 36, day 97 to day 112, day 120 to day 127). From day 26 to day 36, Cl^- fluxed out of the top boundary as well as the bottom boundary. From day 97 to day 112 and day 120 to day 127, Cl^- influx occurred through the top boundary but at a much lower rate. The K^+ influx were consistently higher than the K^+ outflux during both 2nd and 3rd osmotic cycles, so the cumulative K^+ mass stored within sample increased consistently during both osmotic cycles. The cumulative change of Cl^- mass stored within sample largely depended on the Cl^- $\sum M_{in}$ and $\sum M_{out}$ during the anion exclusion periods. It was because the Cl^- $\sum M_{stored}$ changed most significantly during the anion exclusion periods and the Cl^- $\sum M_{stored}$ became stable after the rates of Cl^- $\sum M_{in}$ and $\sum M_{out}$ reached steady state. Due to the huge K^+ influx, the average D^* of K^+ (3.8×10^{-11} m^2/s) within sample was 2 – 3.5 times higher than the D^* of Cl^- ($1 – 2 \times 10^{-11}$ m^2/s). The K_d of K^+ during the 2nd and 3rd osmotic cycles were respectively 1.41×10^{-3} m^3/kg and 3.29×10^{-3} m^3/kg. The concomitant R_d were respectively 12.3 and 27.4. Cation exchange mainly occurred between K^+ and Ca^{2+} within the sample. K^+ was the major cation adsorbed to the sample and Ca^{2+} was the major cation desorbed from the sample. The desorption of Na^+ became significant after day 115. The three evidences to support that that the Pierre Shale sample was an efficient semipermeable membrane were the K^+ $\sum M_{in}$ consistently higher than K^+ $\sum M_{out}$, the consistent increase of K^+ $\sum M_{stored}$ and $\sum M_{solid}$, and the R_d of K^+ significantly higher than unity.

7.2 Recommendations and Limitations

7.2.1 Limitations

- The steel ring popped out 4 days 22 hours after the start of shale sample preparation. The sudden loss of lateral confinement towards the sample may have changed the physical properties of sample (expanding of the pores). Therefore, the ΔP observed in the osmotic system and the solute transportation analyses results may be misleading.
- The circulation system had to a closed system, because absolutely no leakage could be allowed during the circulation period. Any permeable connection to normally pressured surroundings would disturb the differential pressure across the sample (Neuzil & Provost, 2009). However, the osmotic system was detached on day 10, day 70 and day 105 due to the break-down of pump. The detachment caused short-term disturbance towards the differential pressure.
- The K^+ concentrations of fluids collected during day 70 to 82, and fluids synthesized and collected after day 130 were analyzed using AES tests due to the break-down of hollow cathode lamp. Due to the preparation method of testing solutions from bottom collected fluid samples, alkalinity tests could not be performed towards the bottom collected fluid samples. As a result, charge-balance errors could not be calculated for these fluids.
- The pressures at the top and bottom boundaries were measured by the line pressure transducers. The minimum readings of the transducers were 0 kPa. The pressures at the top boundary were occasionally observed to be less than 0 kPa due to osmotic suction. However, the transducers could not give accurate measurements when the readings were below 0 kPa.
- Cumulative change of shale sample height during chemical osmosis was not the main focus of this study, so dial gauge readings were not taken during 1st and 2nd osmotic cycles. There was no record for the change of sample height during the anion exclusion period in the 2nd osmotic cycle.

7.2.2 Recommendations

From the results of this study, the following recommendations are identified for consideration in future studies;

- During the sample preparation phase, the setting should prevent a concurrent high p_b and a high σ_v to avoid issues with the steel ring. The p_b should not exceed 100 kPa during saturation phase;
- The osmotic circulation system should be redesigned to consider the detachment of pump when it needs to undergo maintenance;
- A vacuum range pressure gauge should be installed at the top circulation line for accurately monitoring the negative pressure at the top boundary; and
- Since it is shown that the dial gauge readings provide useful information, the readings should be taken in the entire chemical osmosis testing. A vertical strain gauge may provide more accurate records for the cumulative change of sample height during the chemical osmosis testing.

LIST OF REFERENCES

Al-Bazali, T. M. (2005). *Experimental study of the membrane behavior of shale during interaction with water-based and oil-based muds*. The University of Texas at Austin.

Al-Bazali, T. M., Zhang, J., Atlas, B., Chenevert, M. E., & Sharma, M. M. (2006). Factors controlling the membrane efficiency of shales when interacting with water-based and oil-based muds. In *2006 SPE International Oil & Gas Conference and Exhibition*. Beijing: Society of Petroleum Engineers. https://doi.org/SPE100735

Andrade-Garda, J. M. (2009). *Basic chemometric techniques in atomic spectroscopy*. *Basic Chemometric Techniques in Atomic Spectroscopy* (1st ed.). Cambridge: RSC Publishing. https://doi.org/10.1039/9781847559661

Appelo, C. A. J., & Postma, D. (2005). *Geochemistry, groundwater and pollution* (2nd ed.). Leiden, London, New York, Philadelphia, Singapore: A.A. Balkema Publishers.

Baird, C. (2017). Mosaic celebrates the next half century in Esterhazy. Retrieved March 10, 2019, from https://leaderpost.com/news/local-news/mosaic-celebrates-the-next-half-century-in-esterhazyhttps://leaderpost.com/news/local-news/mosaic-celebrates-the-next-half-century-in-esterhazy

Bangsund, A. L. (2016a). *Origin, fate, and transport of dissolved organic gases in bedrock aquitards; Saskatchewan, Canada*. University of Saskatchewan.

Bangsund, A. L. (2016b). Squeezed data K2 only from Adrienne. Saskatoon.

Barbour, S. L. (1987). *Osmotic flow and volume change in clay soils*. University of Saskatchewan. https://doi.org/10.1139/t89-068

Barbour, S. L., & Fredlund, D. G. (1989). Mechanisms of osmotic flow and volume change in clay soils. *Canadian Geotechnical Journal*, *26*(4), 551–562.

Basc, M. E. (2014). *Seepage Induced Consolidation Test: Characterization of Mature Fine Tailings*. The University of British Columbia (Vancouver).

Bear, J., & Cheng, A. H.-D. (2010). *Modeling groundwater flow and contaminant transport*. Springer Science & Business Media.

Benn, D. I., & Evans, D. J. A. (2010). *Glaciers and glaciation*. London, UK: Hodder Education.

Berner, R. A. (1971). *Principles of chemical sedimentology (International series in the earth and planetary sciences)*. New York: McGraw-Hill Inc.

Bredehoeft, J. D., Neuzil, C. E., & Milly, P. C. D. (1983). Regional flow in the Dakota aquifer: A study of the role of confining layers. *US Geological Survey*, *2237*, 1–45.

Bresler, E. (1973). Anion exclusion and coupling effects in nonsteady transport thorugh unsaturated soils: I. Theory. *Soil Science Society of America Journal*, *37*(5), 663–669.

Brusseau, M. L., & Rao, P. S. C. (1989). The influence of sorbate-organic matter interactions on sorption nonequilibrium. *Chemosphere*, *18*(9/10), 1691–1706. https://doi.org/10.1016/0045-6535(89)90453-0

Budhu, M. (2010). *Soil Mechanics and Foundations* (3rd ed.). Arizona, US: John Wiley & Sons Inc.

Caldwell, W. G. E. (1968). *The late Cretaceous Bearpaw Formation in the South Saskatchewan River Valley*. *Saskatchewan Research Council, Geology Division*. Regina.

Cey, B. D., Barbour, S. L., & Hendry, M. J. (2001). Osmotic flow through a Cretaceous clay in southern Saskatchewan, Canada. *Canadian Geotechnical Journal*, *38*(5), 1025–1033. https://doi.org/10.1139/cgj-38-5-1025

Cherry, J. A., Parker, B. L., Bradbury, K. R., Eaton, T. T., Gotkowitz, M. G., Hart, D. J., & Borchardt, M. A. (2004). *Role of aquitards in the protection of aquifers from contamination: A "State of the Science" report*. *Awwa Research Foundation*. Denver, CO.

Curtin, D., Steppuhn, H., Mermut, A. R., & Selles, F. (1995). Sodicity in irrigated soils in Saskatchewan: Chemistry and structural stability. *Canadian Journal of Soil Science*, *75*, 177–185. Retrieved from www.nrcresearchpress.com

Curtin, D., Steppuhn, H., & Selles, F. (1994). Structural stability of Chernozemic soils as affected by exchangeable sodium and electrolyte concentration. *Canadian Journal of Soil Science*. https://doi.org/10.4141/cjss94-023

Dawson, G. (1882). Report on the country in the vicinity of the Bow and Belly Rivers. *Geological Survey of Canada*, 3–4.

Di Maio, C. (1996). Exposure of bentonite to salt solution: Osmotic and mechanical effects. *Géotechnique*, *46*(4), 695–707. https://doi.org/10.1680/geot.1996.46.4.695

Dolinar, B., Mišič, M., & Trauner, L. (2007). Correlation between surface area and Atterberg limits of fine-grained soils. *Clays and Clay Minerals*. https://doi.org/10.1346/CCMN.2007.0550506

Dolinar, B., & Trauner, L. (2004). Liquid limit and specific surface of clay particles. *Geotechnical Testing Journal*.

Fetter, C. W., Boving, T., & Kreamer, D. (2018). *Contaminant hydrogeology* (3rd ed.). Long Grove, Illinois: Waveland Press Inc. Retrieved from www.waveland.com

Fredlund, D. G., & Xing, A. (1994). Equations for the soil-water characteristic curve. *Canadian Geotechnical Journal*, *31*(4), 521–532.

Fritz, J. S., & Gjerde, D. T. (2009). *Ion chromatography* (4th ed.). Weinheim: Wiley-VCH.

Fritz, S. J. (1986). Ideality of clay membranes in osmotic processes: A review. *Clays and Clay Minerals*, *34*(2), 214–223.

Fritz, S. J., & Marine, I. W. (1983). Experimental support for a predictive osmotic model of clay membranes. *Geochimica et Cosmochimica Acta*, *47*(8), 1515–1522. https://doi.org/10.1016/0016-7037(83)90310-1

Garavito, A. M., De Cannière, P., & Kooi, H. (2007). In situ chemical osmosis experiment in the Boom Clay at the Mol underground research laboratory. *Physics and Chemistry of the Earth*, *32*, 421–433. https://doi.org/10.1016/j.pce.2006.01.004

Garavito, A. M., Kooi, H., & Neuzil, C. E. (2006). Numerical modeling of a long-term in situ chemical osmosis experiment in the Pierre Shale, South Dakota. *Advances in Water Resources*, *29*(3), 481–492. https://doi.org/10.1016/j.advwatres.2005.06.004

Gonçalvès, J., Rousseau-Gueutin, P., & Revil, A. (2007). Introducing interacting diffuse layers in TLM calculations: A reappraisal of the influence of the pore size on the swelling pressure and the osmotic efficiency of compacted bentonites. *Journal of Colloid and Interface Science*. https://doi.org/10.1016/j.jcis.2007.07.023

Grim, R. E. (1953). *Clay mineralogy*. New York, Toronto, London.

Grim, R. E. (1958). Organization of water on clay mineral surfaces and its implications for

the properties of clay-water systems.

Hach Company. (2017). *Phenolphthalein and total alkalinity method 8221: Buret titration* (9th ed.). https://doi.org/DOC316.53.01151

Hach Company. (2019). HQ40D portable multi meter pH, conductivity, salinity, TDS, dissolved oxygen (DO), ORP and ISE for water. Retrieved March 10, 2019, from https://www.hach.com/hq40d-portable-multi-meter-ph-conductivity-salinity-tds-dissolved-oxygen-do-orp-and-ise-for-water/product?id=7640501639

Hamilton Company. (2008). *Microlab ® 600 basic manual: Hardware installation and basic operation* (F).

Hatch. (2018). Esterhazy K1 and K2 expansion project, Mosaic Potash, Canada, 2008-2018. Retrieved March 10, 2019, from https://www.hatch.com/en/Projects/Metals-And-Minerals/EsterhazyK1K2Expansion-Project

Hendry, M. J., Bangsund, A. L., Schmeling, E. E., & Barbour, S. L. (2017). Measuring aqueous CH4 concentration profiles in shales and tills to define source, transport, and fate of organic gases. *Procedia Earth and Planetary Science*, *17*, 810–813. https://doi.org/10.1016/j.proeps.2017.01.048

Hendry, M. J., & Harrington, G. A. (2014). Comparing vertical profiles of natural tracers in the Williston Basin to estimate the onset of deep aquifer activation. *Water Resources Research*, *50*(8), 6496–6506. https://doi.org/10.1002/2014WR015652

Holtz, R. D., & Kovacs, W. D. (1981). *An introduction to geotechnical engineering*. Englewood Cliffs, N.J.: Prentice Hall.

Horseman, S. T., Harrington, J. F., & Noy, D. J. (2007). Swelling and osmotic flow in a potential host rock. *Physics and Chemistry of the Earth, Parts A/B/C*, *32*(1–7), 408–420. https://doi.org/10.1016/j.pce.2006.05.003

Ingebritsen, S. E., Sanford, W. E., & Neuzil, C. E. (2006). *Groundwater in geologic processes* (2nd ed.). Cambridge University Press.

Irwin, J. S. (1931). Stratigraphic correlation and nomenclature in plains of southern Alberta. *AAPG Bulletin*, *15*(10), 1129–1139.

Jafarbeglou, M., Abdouss, M., Shoushtari, A. M., & Jafarbeglou, M. (2016). Clay nanocomposites as engineered drug delivery systems. *RSC Advances*, *6*, 50002–50016. https://doi.org/10.1039/c6ra03942a

Keijzer, T. J. S., Kleingeld, P. J., & Loch, J. P. G. (1999). Chemical osmosis in compacted clayey material and the prediction of water transport. *Engineering Geology*, *53*(2), 151–159. https://doi.org/10.1016/S0013-7952(99)00028-9

Kemper, W. D., & Rollins, J. B. (1966). Osmotic efficiency coefficients across compacted clays. *Soil Science Society of America Journal*, *33*(5), 529–534.

Kharaka, Y. K., & Berry, F. A. P. (1973). Simultaneous flow of water and solutes through geological membranes: I. Experimental investigation. *Geochimica et Cosmochimica Acta*, *37*, 2577–2603. https://doi.org/10.1016/0016-7037(73)90267-6

Krupka, K. M., Kaplan, D. I., Whelan, G., Serne, R. J., & Mattigod, S. V. (1999). *Understanding variation in partition coefficient, Kd, values: Volume II. Review of geochemistry and available Kd values for cadmium, cesium, chromium, lead, plutonium, radon, strontium, thorium, tritium (3H), and uranium*. *US Environmental Protection Agency*. Washington, DC.

Kuhn, P., Di Primio, R., & Horsfield, B. (2010). Bulk composition and phase behaviour of petroleum sourced by the Bakken Formation of the Williston Basin. In B. A. Vining & S. C. Pickering (Eds.), *Petroleum Geology Conference* (Vol. 7, pp. 1065–1077). London, UK: Geological Society of London.

Langmuir, D. (1997). *Aqueous environmental geochemistry*. Upper Saddle River, N.J.: Prentice Hall.

Malusis, M. A. (2001). *Membrane behavior and coupled solute transport through a geosynthetic clay liner*. Colorado State University.

Malusis, M. A., & Shackelford, C. D. (2002). Coupling effects during steady-state solute diffusion through a semipermeable clay membrane. *Environmental Science and Technology*, *36*, 1312–1319. https://doi.org/10.1021/es011130q

Malusis, M. A., Shackelford, C. D., & Olsen, H. W. (2001). A laboratory apparatus to measure chemico-osmotic efficiency coefficients for clay soils. *Geotechnical Testing Journal*, *24*(3), 229–242. https://doi.org/10.1520/GTJ11343J

Malusis, M. A., Shackelford, C. D., & Olsen, H. W. (2003). Flow and transport through clay membrane barriers. *Engineering Geology*, *70*(3–4), 235–248. https://doi.org/10.1016/S0013-7952(03)00092-9

Marine, W. I., & Fritz, S. J. (1981). Osmotic model to explain anomalous hydraulic heads. *Water Resources Research*, *17*(1), 73–82.

Mermut, A. R., & Arshad, M. A. (1987). Significance of sulphide oxidation in soil salinization in southeastern Saskatchewan. *Soil Science Society of America Journal*, *51*(1), 247–251.

Mitchell, J. K., & Soga, K. (2005). *Fundamentals of soil behavior* (3rd ed.). Hoboken, NJ: John Wiley & Sons Inc.

Mojid, M. A., & Vereecken, H. (2005). On the physical meaning of retardation factor and velocity of a nonlinearly sorbing solute. *Journal of Hydrology*, *302*, 127–136. https://doi.org/10.1016/j.jhydrol.2004.06.041

Neuzil, C. E. (1986). Groundwater flow in low-permeability environments. *Water Resources Research*, *22*(8), 1163–1195.

Neuzil, C. E. (2000). Osmotic generation of'anomalous' fluid pressures in geological environments. *Nature*, *403*(January), 182–184.

Neuzil, C. E., & Provost, A. M. (2009). Recent experimental data may point to a greater role for osmotic pressures in the subsurface. *Water Resources Research*, *45*(3). https://doi.org/10.1029/2007WR006450

Noy, D. J., Horseman, S. T., Harrington, J. F., Bossart, P., & Fis, H. R. (2004). *Mont Terri Project — hydrogeological synthesis, osmotic flow: An experimental and modelling study of chemico-osmotic effects in the Opalinus Clay of Switzerland*. *Reports of the FOWG, Geology Series.* Bern, Switzerland: Federal Office for Water and Geology.

Oram, B. (2014). The role of alkalinity citizen monitoring. Retrieved April 18, 2019, from https://www.water-research.net/index.php/the-role-of-alkalinity-citizen-monitoring

Peltier, W. R. (1994). Ice age paleotopography. *Science*, *265*(5169), 195–201.

PetroTech Associates. (2004). Scanning electron microscope images. Retrieved November 30, 2017, from http://www.petrotech-assoc.com/prod01.htm

Rahman, M. M., Chen, Z., & Rahman, S. S. (2005). Experimental investigation of shale

membrane behavior under tri-axial condition. *Petroleum Science and Technology*, *23*(9–10), 1265–1282. https://doi.org/10.1081/LFT-200035734

Rousseau-Gueutin, P., Gonçalvès, J., & Violette, S. (2008). Osmotic efficiency in Callovo-Oxfordian argillites: Experimental vs. theoretical models. *Physics and Chemistry of the Earth*, *33*(Parts A/B/C), S106–S113. https://doi.org/10.1016/j.pce.2008.10.064

Rousseau-Gueutin, P., Greef, V. De, Gonçalvès, J., Violette, S., & Chanchole, S. (2009). Experimental device for chemical osmosis measurement on natural clay-rock samples maintained at in situ conditions: Implications for formation pressure interpretations. *Journal of Colloid And Interface Science*, *337*(1), 106–116. https://doi.org/10.1016/j.jcis.2009.04.092

Sardin, M., Schweich, D., Leij, F. J., & Van Genuchten, M. T. (1991). *Modeling the nonequilibrium transport of linearly interacting solutes in porous media: A review*. *Water Resources Research* (Vol. 27).

Schiffman, R. L., & Gibson, R. E. (1964). Consolidation of nonhomogenous clay layers. *Journal of the Soil Mechanics & Foundations Division*.

Schmitt, L., Forsans, T., & Santarelli, F. J. (1994). Shale testing and capillary phenomena. *International Journal of Rock Mechanics and Mining Sciences & Geomechanics Abstracts*, *31*(5), 411–427.

Shackelford, C. D., & Daniel, D. E. (1991). Diffusion in saturated soil: I. Background. *Journal of Geotechnical Engineering*, *117*(3), 467–484.

Shackelford, C. D., & Lee, J. M. (2003). The destructive role of diffusion on clay membrane behavior. *Clays and Clay Minerals*, *51*(2), 186–196. https://doi.org/10.1346/CCMN.2003.0510209

Shainberg, I., & Levy, G. J. (2005). Flocculation and Dispersion. In D. Hillel & J. L. Hatfield (Eds.), *Encyclopedia of soils in the environment* (3rd ed., pp. 27–34). Amsterdam: Elsevier.

Smith, L. A., van der Kamp, G., & Hendry, M. J. (2013). A new technique for obtaining high-resolution pore pressure records in thick claystone aquitards and its use to determine in situ compressibility. *Water Resources Research*, *49*(2), 732–743. https://doi.org/10.1002/wrcr.20084

Smith, L., Elwood, D., Barbour, S. L., & Hendry, M. J. (2018). Profiling the in situ compressibility of Cretaceous shale using grouted-in piezometers and laboratory testing. *Geomechanics for Energy and the Environment*, *14*, 29–37. https://doi.org/10.1016/j.gete.2018.04.003

Snoeyink, V. L., & Jenkins, D. (1980). *Water chemistry* (1st ed.). New York, Chichester, Brisbane, Toronto, Singapore: John Wiley & Sons Inc.

Sposito, G., Skipper, N. T., Sutton, R., Park, S. -h., Soper, A. K., & Greathouse, J. A. (1999). Surface geochemistry of the clay minerals. *Proceedings of the National Academy of Sciences*, *96*(7), 3358–3364. https://doi.org/10.1073/pnas.96.7.3358

Stern, O. (1924). Zur theorie der elektrolytischen doppelschicht. *Zeitschrift Für Elektrochemie Und Angewandte Physikalische Chemie*, *30*(21–22), 508–516.

Takeda, M., Hiratsuka, T., Manaka, M., Finsterle, S., & Ito, K. (2014). Experimental examination of the relationships among chemico-osmotic, hydraulic, and diffusion parameters of Wakkanai mudstones. *Journal of Geophysical Research: Solid Earth*, *119*(5), 4178–4201. https://doi.org/10.1002/2013JB010421.Received

Thermo Fisher Scientific Inc. (2010). *Thermo Scientific orion star ™ and star plus meter user guide*. Retrieved from www.thermoscientific.com/water.

Thermo Fisher Scientific Inc. (2011). *iCE 3000 series AA spectrometers operator's manual* (2.0). Cambridge. Retrieved from www.thermoscientific.com

Thermo Fisher Scientific Inc. (2012). *Dionex AS-DV autosampler operator's manual* (5th ed.).

Thermo Fisher Scientific Inc. (2016). *Dionex integrion HPIC system operator's manual* (4th ed.).

Tomkins, R. V. (1954). *Natural sodium sulphate in Saskatchewan*. Saskatchewan.

Tournassat, C., & Appelo, C. A. J. (2011). Modelling approaches for anion-exclusion in compacted Na-bentonite. *Geochimica et Cosmochimica Acta*, *75*(13), 3698–3710. https://doi.org/10.1016/j.gca.2011.04.001

van Breemen, N., Burrough, P. A., Velthorst, E. J., van Dobben, H. F., de Wit, T., Ridder, T. B., & Reijnders, H. F. R. (1982). Soil acidification from atmospheric ammonium sulphate in forest canopy throughfall. *Nature*, *299*(7), 548–550. https://doi.org/10.1038/299548a0

Weber, W. J., McGinley, P. M., & Katz, L. E. (1991). Sorption phenomena in subsurface systems: Concepts, models and effects on contaminant fate and transport. *Water Research*, *25*(5), 499–528. https://doi.org/10.1016/0043-1354(91)90125-A

Williams, G. D., & Bayliss, P. (1988). Mineralogy of the Cretaceous shales in southeastern Saskatchewan. *Bulletin of Canadian Petroleum Geology*, *36*(2), 145–157.

Yeung, A. T., & Mitchell, J. K. (1993). Coupled fluid, electrical and chemical flows in soil. *Geotechnique*, *43*(1), 121–134.

Zheng, C., & Bennett, G. D. (2002). *Applied contaminant transport modeling* (2nd ed.). New York: Wiley-Interscience.

APPENDIX A: BOREHOLE LOG

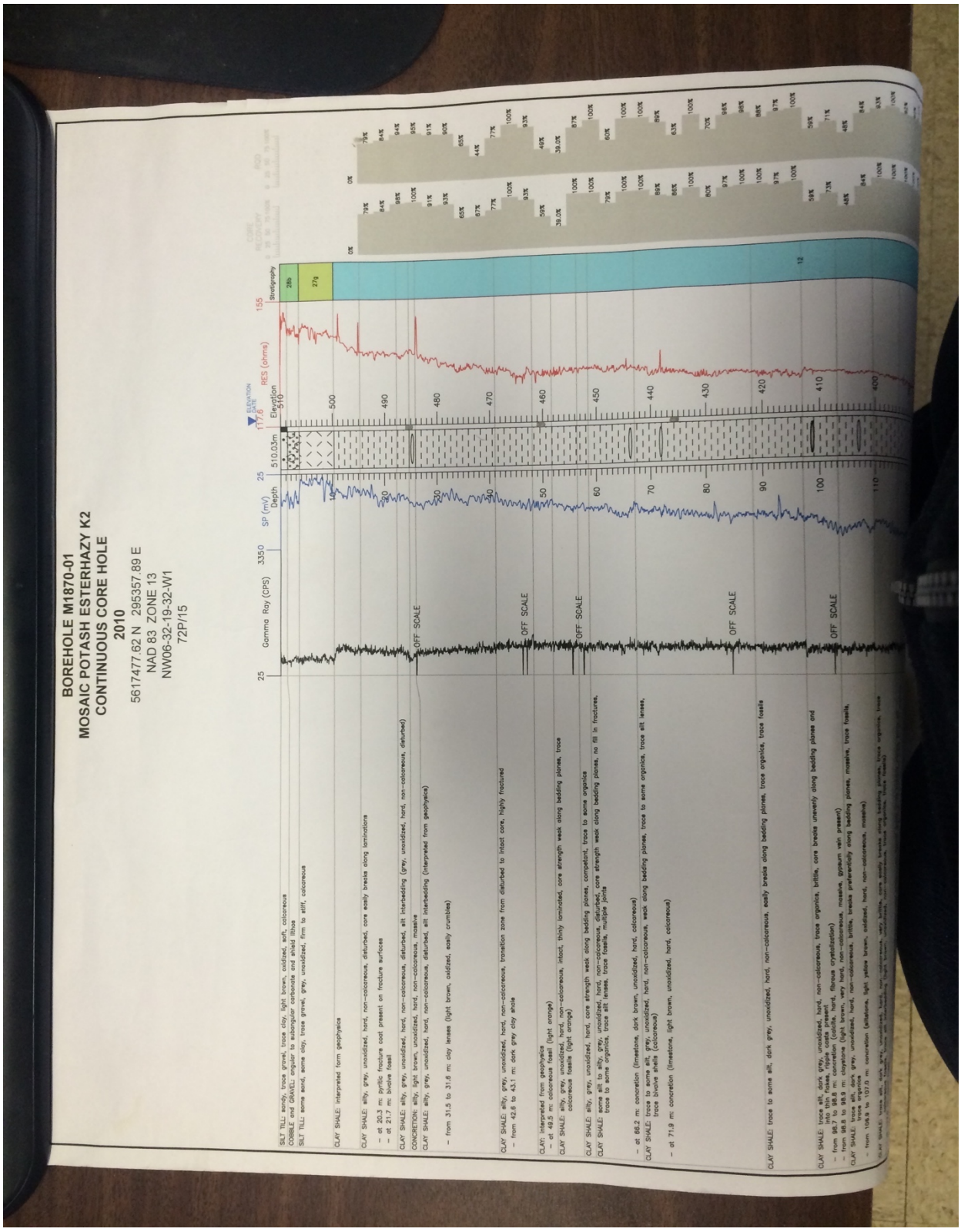

Figure A.1. Borehole log of the borehole at Mosaic's K2 mine (from 0 to 100 m BGS) (P.1 of 3); Pierre Shale sample is collected at 121 m BGS

Figure A.2. Borehole log of the borehole at Mosaic's K2 mine (from 100 to 220 m BGS) (P.2 of 3); Pierre Shale sample is collected at 121 m BGS

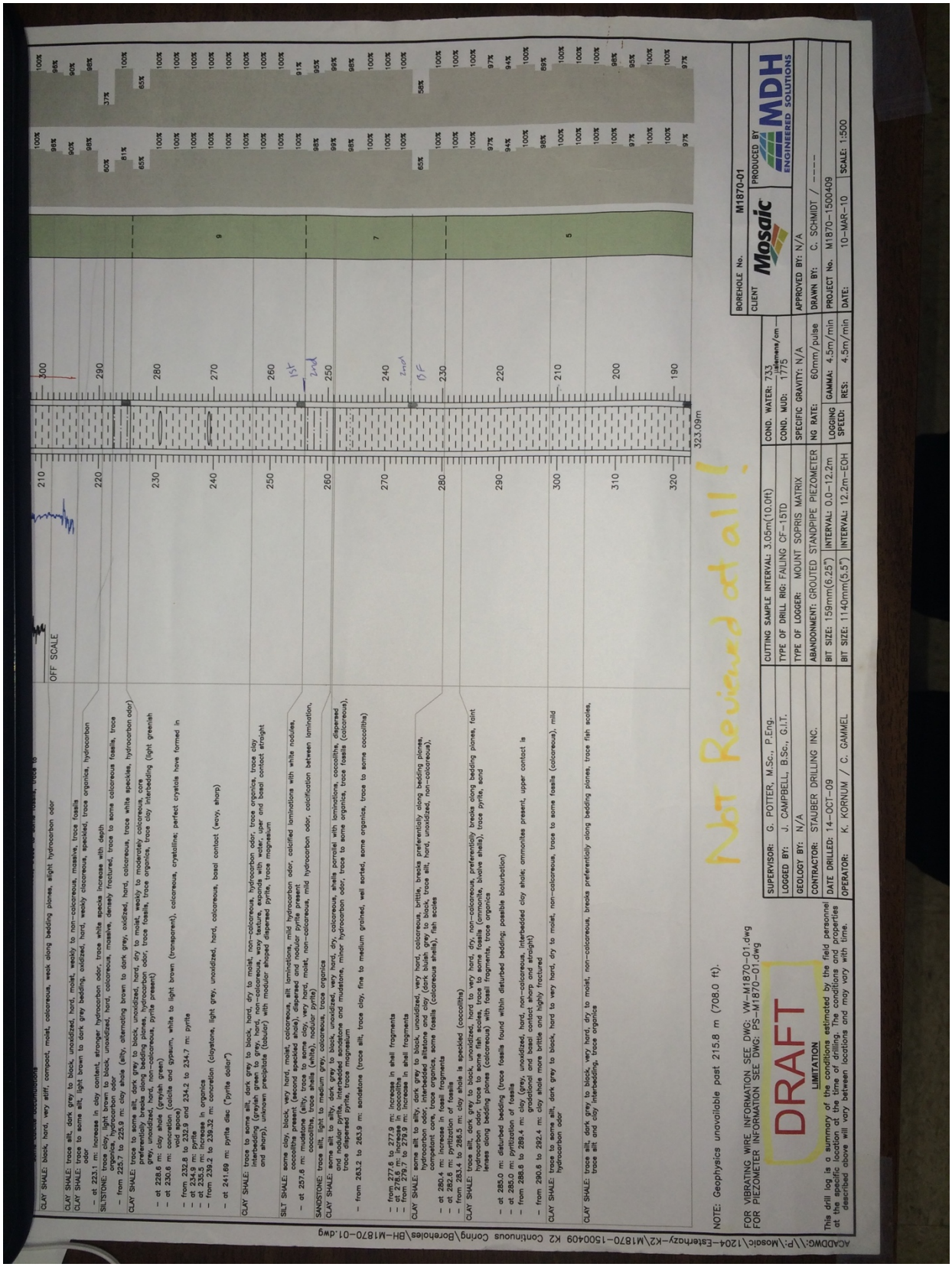

Figure A.3. Borehole log of the borehole at Mosaic's K2 mine (from 220 to 323.09 m BGS) (P.3 of 3); Pierre Shale sample is collected at 121 m BGS

APPENDIX B: LABORATORY EXPERIMENT RESULTS

Table B.1. The major cation and anion concentrations of the top synthetic fluids

Cycle	Circulation Start (From)	Circulation End (To)	Cl^- (mg/L)	SO_4^{2-} (mg/L)	HCO_3^- (mg/L)	K^+ (mg/L)	Na^+ (mg/L)	Mg^{2+} (mg/L)	TDS (mg/L)
1	**Day 1.0**	**Day 4.7**	262	15.3	6.59	0	169	4.37	457
1	**Day 4.7**	**Day 12.4**	261	14.1	5.85	0	167	4.94	453
1	**Day 13.5**	**Day 14.4**	262	11.9	6.59	0	167	4.76	452
1	**Day 14.4**	**Day 22.5**	261	14.5	5.82	0	168	4.63	454
2	**Day 22.5**	**Day 24.6**	387	14.4	6.41	150	168	5.76	731
2	**Day 24.6**	**Day 48.7**	387	11.3	4.88	152	167	4.21	726
2	**Day 48.7**	**Day 70.8**	385	11.6	4.88	148	164	4.09	718
2	**Day 73.6**	**Day 85.7**	381	12.2	6.83	148	164	4.52	717
3	**Day 85.7**	**Day 93.6**	551	11.2	8.37	319	167	4.20	1061
3	**Day 93.6**	**Day 115**	547	15.2	8.54	317	165	4.74	1057
3	**Day 115**	**Day 143**	546	14.2	7.55	314	166	4.87	1052
3	**Day 143**	**Day 150**	542	12.7	7.47	318	165	4.14	1050

Table B.2. The major cation and anion concentrations of the bottom synthetic fluids

Cycle	Circulation Start (From)	Circulation End (To)	Cl^- (mg/L)	SO_4^{2-} (mg/L)	HCO_3^- (mg/L)	K^+ (mg/L)	Na^+ (mg/L)	Mg^{2+} (mg/L)	TDS (mg/L)
1	**Day 1.0**	**Day 4.7**	262	15.3	6.59	0	169	4.37	457
1	**Day 4.7**	**Day 12.4**	261	14.1	5.85	0	167	4.94	453
1	**Day 13.5**	**Day 14.4**	262	11.9	6.59	0	167	4.76	452
1	**Day 14.4**	**Day 22.5**	261	14.5	5.82	0	168	4.63	454
2	**Day 22.5**	**Day 27.9**	261	14.5	5.82	0	168	4.63	454
2	**Day 27.9**	**Day 50.6**	261	12.9	5.61	0	168	4.17	452
2	**Day 50.6**	**Day 77.4**	260	11.5	5.61	0	167	4.63	448
2	**Day 77.4**	**Day 85.7**	254	12.4	7.32	0	164	4.37	442
3	**Day 85.7**	**Day 87.8**	254	12.4	7.32	0	164	4.37	442
3	**Day 87.8**	**Day 108**	255	12.6	7.47	0	164	4.48	443
3	**Day 108**	**Day 134**	259	14.3	7.47	0	165	5.10	451
3	**Day 134**	**Day 150**	252	14.2	4.98	0	164	4.51	439

Table B.3. The concentration difference between the top and bottom boundaries of sample

Cycle	Circulation Start (From)	Circulation End (To)	Cl^- (mg/L)	SO_4^{2-} (mg/L)	HCO_3^- (mg/L)	K^+ (mg/L)	Na^+ (mg/L)	Mg^{2+} (mg/L)	TDS (mg/L)
1	**Day 1.0**	**Day 4.7**	0	0	0	0	0	0	0
1	**Day 4.7**	**Day 12.4**	0	0	0	0	0	0	0
1	**Day 13.5**	**Day 14.4**	0	0	0	0	0	0	0
1	**Day 14.4**	**Day 22.5**	0	0	0	0	0	0	0
2	**Day 22.5**	**Day 24.6**	126	-0.08	0.59	150	0.16	1.13	277
2	**Day 24.6**	**Day 27.9**	125	-3.18	-0.94	152	-0.44	-0.42	272
2	**Day 27.9**	**Day 48.7**	126	-1.56	-0.73	152	-0.52	0.04	274
2	**Day 48.7**	**Day 50.6**	124	-1.25	-0.73	148	-3.52	-0.08	266
2	**Day 50.6**	**Day 70.8**	125	0.11	-0.73	148	-2.33	-0.54	270
2	**Day 73.6**	**Day 77.4**	121	0.73	1.22	148	-2.68	-0.11	268
2	**Day 77.4**	**Day 85.7**	127	-0.18	-0.49	148	-0.37	0.15	274
3	**Day 85.7**	**Day 87.8**	298	-1.20	1.05	319	2.51	-0.17	618
3	**Day 87.8**	**Day 93.6**	297	-1.39	0.9	319	3.36	-0.28	618
3	**Day 93.6**	**Day 108**	292	2.61	1.07	317	1.20	0.26	614
3	**Day 108**	**Day 115**	288	0.95	1.07	317	-0.71	-0.36	606
3	**Day 115**	**Day 134**	287	-0.05	0.08	314	0.44	-0.23	601
3	**Day 134**	**Day 143**	294	0.03	2.57	314	2.06	0.36	613
3	**Day 143**	**Day 150**	291	-1.46	2.49	318	1.43	-0.37	611

Table B.4. The molar concentration difference between the top and bottom boundaries of sample

Cycle	Circulation Start (From)	Circulation End (To)	Cl^- (mol/m^3)	SO_4^{2-} (mol/m^3)	HCO_3^- (mol/m^3)	K^+ (mol/m^3)	Na^+ (mol/m^3)	Mg^{2+} (mol/m^3)	TDS (mol/m^3)
1	**Day 1.0**	**Day 4.7**	0	0	0	0	0	0	0
1	**Day 4.7**	**Day 12.4**	0	0	0	0	0	0	0
1	**Day 13.5**	**Day 14.4**	0	0	0	0	0	0	0
1	**Day 14.4**	**Day 22.5**	0	0	0	0	0	0	0
2	**Day 22.5**	**Day 24.6**	3.55	-0.001	0.010	3.83	0.007	0.046	7.44
2	**Day 24.6**	**Day 27.9**	3.54	-0.033	-0.015	3.88	-0.019	-0.017	7.33
2	**Day 27.9**	**Day 48.7**	3.54	-0.016	-0.012	3.88	-0.023	0.002	7.37
2	**Day 48.7**	**Day 50.6**	3.50	-0.013	-0.012	3.78	-0.153	-0.003	7.10
2	**Day 50.6**	**Day 70.8**	3.53	0.001	-0.012	3.78	-0.101	-0.022	7.18
2	**Day 73.6**	**Day 77.4**	3.40	0.008	0.020	3.79	-0.117	-0.005	7.10
2	**Day 77.4**	**Day 85.7**	3.58	-0.002	-0.008	3.79	-0.016	0.006	7.35
3	**Day 85.7**	**Day 87.8**	8.39	-0.012	0.017	8.15	0.109	-0.007	16.7
3	**Day 87.8**	**Day 93.6**	8.37	-0.014	0.015	8.15	0.146	-0.012	16.7
3	**Day 93.6**	**Day 108**	8.24	0.027	0.018	8.10	0.052	0.011	16.5
3	**Day 108**	**Day 115**	8.13	0.010	0.018	8.10	-0.031	-0.015	16.2
3	**Day 115**	**Day 134**	8.10	-0.001	0.001	8.02	0.019	-0.009	16.1
3	**Day 134**	**Day 143**	8.30	0.000	0.042	8.02	0.090	0.015	16.5
3	**Day 143**	**Day 150**	8.20	-0.015	0.041	8.14	0.062	-0.015	16.4

Table B.5. The approximation of theoretical osmotic pressure during the chemical osmosis testing

Cycle	Circulation Start (From)	Circulation End (To)	ΔC (mol/m^3)	T (degree K)	R (kJ/mol K)	ν	Δπ
1	**Day 1.0**	**Day 4.7**	0	298	0.00831	2	0
1	**Day 4.7**	**Day 12.4**	0	298	0.00831	2	0
1	**Day 13.5**	**Day 14.4**	0	298	0.00831	2	0
1	**Day 14.4**	**Day 22.5**	0	298	0.00831	2	0
2	**Day 22.5**	**Day 24.6**	7.44	298	0.00831	2	36.9
2	**Day 24.6**	**Day 27.9**	7.33	298	0.00831	2	36.3
2	**Day 27.9**	**Day 48.7**	7.37	298	0.00831	2	36.5
2	**Day 48.7**	**Day 50.6**	7.10	298	0.00831	2	35.2
2	**Day 50.6**	**Day 70.8**	7.18	298	0.00831	2	35.6
2	**Day 73.6**	**Day 77.4**	7.10	298	0.00831	2	35.2
2	**Day 77.4**	**Day 85.7**	7.35	298	0.00831	2	36.4
3	**Day 85.7**	**Day 87.8**	16.7	298	0.00831	2	82.6
3	**Day 87.8**	**Day 93.6**	16.7	298	0.00831	2	82.6
3	**Day 93.6**	**Day 108**	16.5	298	0.00831	2	81.6
3	**Day 108**	**Day 115**	16.2	298	0.00831	2	80.4
3	**Day 115**	**Day 134**	16.1	298	0.00831	2	80.0
3	**Day 134**	**Day 143**	16.5	298	0.00831	2	81.7
3	**Day 143**	**Day 150**	16.4	298	0.00831	2	81.4

Table B.6. The major cation concentrations of the top collected fluid samples

Cycle	Circulation Start (From)	Circulation End (To)	K^+ (mg/L)	Na^+ (mg/L)	Mg^{2+} (mg/L)	Ca^{2+} (mg/L)	Fe^{3+} (mg/L)	Total (mg/L)
1	**Day 7.6**	**Day 9.6**	7.31	166	5.03	7.65	0.37	186
1	**Day 9.6**	**Day 10.6**	6.19	165	4.70	7.10	0.93	184
1	**Day 10.6**	**Day 12.4**	5.21	165	5.03	7.70	0.81	184
1	**Day 13.5**	**Day 14.4**	7.79	167	4.68	5.17	0.71	185
1	**Day 14.4**	**Day 15.8**	4.88	167	4.65	6.66	1.50	184
1	**Day 15.8**	**Day 17.5**	4.05	166	4.45	6.65	1.25	183
1	**Day 17.5**	**Day 18.8**	3.91	166	5.23	6.64	0.23	182
1	**Day 18.8**	**Day 20.5**	4.49	163	4.68	6.26	1.42	180
1	**Day 20.5**	**Day 22.5**	4.92	161	4.92	7.27	1.40	179
2	**Day 22.5**	**Day 24.6**	120	169	5.37	8.33	0.46	303
2	**Day 24.6**	**Day 26.5**	119	169	5.47	9.66	0.24	304
2	**Day 26.5**	**Day 27.9**	119	168	5.72	13.5	0.36	307
2	**Day 27.9**	**Day 29.5**	122	169	5.27	15.2	0.62	312
2	**Day 29.5**	**Day 30.9**	122	174	5.14	15.7	0.29	317
2	**Day 30.9**	**Day 32.7**	121	171	5.17	16.1	1.31	315
2	**Day 32.7**	**Day 34.4**	125	172	5.07	15.6	1.35	319
2	**Day 34.4**	**Day 36.4**	111	175	4.98	16.7	0.46	308
2	**Day 36.4**	**Day 37.9**	114	174	4.54	13.0	0.97	306
2	**Day 37.9**	**Day 39.6**	111	175	4.75	11.7	0.94	304
2	**Day 39.6**	**Day 40.9**	114	175	4.71	11.4	1.20	306
2	**Day 40.9**	**Day 42.8**	114	176	4.85	11.2	1.02	306
2	**Day 42.8**	**Day 44.8**	110	176	4.75	10.5	1.52	303
2	**Day 44.8**	**Day 46.8**	112	176	4.73	11.2	1.21	304
2	**Day 46.8**	**Day 48.7**	112	172	4.80	10.1	1.19	300
2	**Day 48.7**	**Day 50.6**	113	174	4.76	8.81	1.12	302
2	**Day 50.6**	**Day 52.4**	115	174	4.63	8.07	1.71	303
2	**Day 52.4**	**Day 54.4**	116	172	4.55	7.67	1.82	302
2	**Day 54.4**	**Day 56.5**	116	168	4.65	11.4	0.58	300
2	**Day 56.5**	**Day 58.3**	121	171	4.63	11.6	0.97	309
2	**Day 58.3**	**Day 60.4**	119	168	4.55	10.5	0.94	304
2	**Day 60.4**	**Day 61.8**	118	167	4.39	10.3	0.96	301
2	**Day 61.8**	**Day 63.6**	119	166	4.35	10.6	0.95	300
2	**Day 63.6**	**Day 65.6**	122	167	4.35	9.08	1.04	303
2	**Day 65.6**	**Day 67.5**	120	167	4.34	9.60	1.19	302
2	**Day 67.5**	**Day 69.4**	119	169	4.32	9.65	1.87	304

Cycle	Circulation Start (From)	Circulation End (To)	K^+ (mg/L)	Na^+ (mg/L)	Mg^{2+} (mg/L)	Ca^{2+} (mg/L)	Fe^{3+} (mg/L)	Total (mg/L)
2	**Day 69.4**	**Day 70.8**	127	172	4.11	8.72	2.29	314
2	**Day 73.6**	**Day 77.4**	128	174	4.08	10.7	1.99	319
2	**Day 77.4**	**Day 79.6**	124	173	4.24	12.2	1.95	315
2	**Day 79.6**	**Day 82.5**	122	172	4.14	11.7	1.35	311
3	**Day 85.7**	**Day 87.8**	255	163	6.14	21.3	0.69	446
3	**Day 87.8**	**Day 89.5**	251	167	5.54	22.2	0.14	445
3	**Day 89.5**	**Day 91.5**	243	163	6.49	28.2	0.11	441
3	**Day 91.5**	**Day 93.6**	254	163	5.84	27.5	0.68	451
3	**Day 93.6**	**Day 95.7**	258	162	5.84	27.5	0.20	454
3	**Day 95.7**	**Day 97.5**	258	165	5.03	23.1	0.64	452
3	**Day 97.5**	**Day 99.4**	265	167	5.71	23.2	0.12	461
3	**Day 99.4**	**Day 102**	252	166	6.48	24.0	0.29	449
3	**Day 102**	**Day 104**	253	173	5.75	26.4	0.24	459
3	**Day 104**	**Day 106**	252	177	5.85	21.6	0.59	457
3	**Day 107**	**Day 108**	253	176	5.06	19.7	0.76	454
3	**Day 108**	**Day 110**	250	175	5.06	19.6	0.62	451
3	**Day 110**	**Day 112**	252	175	5.07	19.0	0.47	452
3	**Day 112**	**Day 114**	253	178	5.35	20.1	0.53	458
3	**Day 114**	**Day 115**	252	178	5.20	20.6	0.68	457
3	**Day 115**	**Day 117**	255	180	4.93	19.2	0.41	459
3	**Day 117**	**Day 119**	256	178	5.50	18.0	0.41	458
3	**Day 119**	**Day 121**	255	178	4.58	16.1	0.46	454
3	**Day 121**	**Day 122**	250	180	4.52	15.7	0.55	451
3	**Day 122**	**Day 124**	258	179	5.76	20.8	0.35	464
3	**Day 124**	**Day 126**	255	179	4.56	17.4	0.26	457
3	**Day 126**	**Day 127**	257	178	4.55	16.9	0.82	457
3	**Day 127**	**Day 129**	254	177	4.92	16.0	1.21	453
3	**Day 129**	**Day 131**	258	180	4.46	17.2	0.15	460
3	**Day 131**	**Day 133**	257	179	4.45	17.1	0.79	459
3	**Day 133**	**Day 134**	252	179	4.42	18.2	0.70	455
3	**Day 134**	**Day 136**	253	176	4.47	19.1	1.24	453
3	**Day 136**	**Day 138**	250	178	4.63	18.3	1.71	452
3	**Day 138**	**Day 140**	256	179	4.59	18.4	0.89	459
3	**Day 140**	**Day 141**	263	176	4.64	18.7	1.29	464
3	**Day 141**	**Day 143**	252	179	4.76	20.6	1.15	458
3	**Day 143**	**Day 145**	253	179	4.70	17.2	1.12	455

Cycle	Circulation Start (From)	Circulation End (To)	K^+ (mg/L)	Na^+ (mg/L)	Mg^{2+} (mg/L)	Ca^{2+} (mg/L)	Fe^{3+} (mg/L)	Total (mg/L)
3	**Day 145**	**Day 146**	252	179	3.78	10.9	0.77	446
3	**Day 146**	**Day 148**	252	176	3.51	10.0	1.15	442
3	**Day 148**	**Day 150**	253	174	3.60	10.6	2.58	444

Table B.7. The major cation concentrations of the bottom collected fluid samples

Cycle	Circulation Start (From)	Circulation End (To)	K^+ (mg/L)	Na^+ (mg/L)	Mg^{2+} (mg/L)	Ca^{2+} (mg/L)	Fe^{3+} (mg/L)	Total (mg/L)
1	**Day 7.6**	**Day 9.6**	5.65	167	4.23	6.74	0.78	184
1	**Day 9.6**	**Day 10.6**	6.27	165	4.05	6.22	0.06	182
1	**Day 10.6**	**Day 12.4**	4.59	165	4.43	7.48	0.00	182
1	**Day 13.5**	**Day 14.4**	7.37	163	5.48	6.46	0.48	183
1	**Day 14.4**	**Day 15.8**	4.33	162	5.10	9.11	0.48	181
1	**Day 15.8**	**Day 17.5**	3.77	163	4.71	8.26	1.19	181
1	**Day 17.5**	**Day 18.8**	4.21	167	5.87	7.70	0.39	185
1	**Day 18.8**	**Day 20.5**	4.49	169	5.38	7.33	0.57	187
1	**Day 20.5**	**Day 22.5**	5.01	164	5.39	7.90	0.32	182
2	**Day 22.5**	**Day 24.6**	4.55	167	4.86	6.28	0.22	183
2	**Day 24.6**	**Day 26.5**	4.47	166	4.80	7.13	0.61	184
2	**Day 26.5**	**Day 27.9**	4.59	165	5.28	8.14	0.43	184
2	**Day 27.9**	**Day 29.5**	4.94	166	5.31	7.72	0.46	184
2	**Day 29.5**	**Day 30.9**	5.60	168	5.20	8.26	0.69	188
2	**Day 30.9**	**Day 32.7**	5.78	167	4.86	7.80	1.05	186
2	**Day 32.7**	**Day 34.4**	5.82	167	4.72	7.77	0.86	187
2	**Day 34.4**	**Day 36.4**	6.74	166	4.84	8.58	0.58	187
2	**Day 36.4**	**Day 37.9**	6.67	166	4.47	6.43	1.21	185
2	**Day 37.9**	**Day 39.6**	7.23	167	4.23	6.13	1.17	186
2	**Day 39.6**	**Day 40.9**	6.99	167	4.08	5.52	0.87	185
2	**Day 40.9**	**Day 42.8**	7.41	168	4.35	5.52	0.97	186
2	**Day 42.8**	**Day 44.8**	8.30	166	4.12	5.71	1.18	185
2	**Day 44.8**	**Day 46.8**	8.49	166	3.65	6.03	1.02	185
2	**Day 46.8**	**Day 48.7**	8.87	164	3.14	5.34	1.17	183
2	**Day 48.7**	**Day 50.6**	9.64	165	3.29	5.12	1.25	184
2	**Day 50.6**	**Day 52.4**	9.94	166	3.22	4.66	1.76	185
2	**Day 52.4**	**Day 54.4**	9.83	164	3.25	4.23	1.31	183
2	**Day 54.4**	**Day 56.5**	10.5	163	3.86	7.77	0.75	186
2	**Day 56.5**	**Day 58.3**	10.8	162	4.25	8.05	0.88	186
2	**Day 58.3**	**Day 60.4**	10.7	164	4.20	7.48	1.03	187
2	**Day 60.4**	**Day 61.8**	10.9	161	4.31	8.00	0.87	185
2	**Day 61.8**	**Day 63.6**	11.0	161	4.13	6.88	1.03	184
2	**Day 63.6**	**Day 65.6**	10.9	162	4.19	6.85	1.00	185
2	**Day 65.6**	**Day 67.5**	10.9	163	4.28	7.16	1.02	186
2	**Day 67.5**	**Day 69.4**	10.9	162	4.40	7.21	1.49	186

Cycle	Circulation Start (From)	Circulation End (To)	K^+ (mg/L)	Na^+ (mg/L)	Mg^{2+} (mg/L)	Ca^{2+} (mg/L)	Fe^{3+} (mg/L)	Total (mg/L)
2	**Day 69.4**	**Day 70.8**	11.3	164	3.69	6.12	1.81	187
2	**Day 73.6**	**Day 77.4**	11.3	165	4.23	6.27	0.77	187
2	**Day 77.4**	**Day 79.6**	11.7	164	4.10	7.01	0.87	188
2	**Day 79.6**	**Day 82.5**	10.8	165	3.33	6.06	1.25	187
3	**Day 85.7**	**Day 87.8**	12.3	156	7.48	16.6	1.22	194
3	**Day 87.8**	**Day 89.5**	12.8	160	4.31	9.57	0.48	187
3	**Day 89.5**	**Day 91.5**	14.5	162	3.94	10.7	0.58	191
3	**Day 91.5**	**Day 93.6**	14.7	160	4.59	11.6	0.97	192
3	**Day 93.6**	**Day 95.7**	14.7	156	4.83	11.8	0.74	188
3	**Day 95.7**	**Day 97.5**	15.0	161	4.06	8.5	0.21	189
3	**Day 97.5**	**Day 99.4**	15.9	158	4.39	9.9	0.05	189
3	**Day 99.4**	**Day 102**	18.0	158	4.82	10.4	0.06	192
3	**Day 102**	**Day 104**	19.9	159	4.86	11.0	1.02	195
3	**Day 104**	**Day 106**	20.5	163	5.69	8.72	0.43	199
3	**Day 107**	**Day 108**	16.2	165	4.33	7.29	0.94	194
3	**Day 108**	**Day 110**	17.8	164	5.05	8.01	0.84	194
3	**Day 110**	**Day 112**	18.0	166	5.02	7.20	0.62	197
3	**Day 112**	**Day 114**	17.8	170	4.81	7.09	0.41	200
3	**Day 114**	**Day 115**	18.3	168	4.62	7.20	0.56	199
3	**Day 115**	**Day 117**	17.5	171	4.38	6.67	0.19	199
3	**Day 117**	**Day 119**	19.2	167	4.54	6.92	0.01	198
3	**Day 119**	**Day 121**	19.0	171	4.53	6.45	0.39	201
3	**Day 121**	**Day 122**	19.4	172	4.43	6.53	0.48	203
3	**Day 122**	**Day 124**	21.1	172	4.78	6.82	0.64	206
3	**Day 124**	**Day 126**	20.7	171	4.77	6.74	0.57	204
3	**Day 126**	**Day 127**	21.0	169	4.63	6.90	0.22	202
3	**Day 127**	**Day 129**	19.0	171	4.69	6.91	0.29	202
3	**Day 129**	**Day 131**	19.1	174	4.39	7.49	0.59	206
3	**Day 131**	**Day 133**	18.9	174	4.43	7.65	0.53	205
3	**Day 133**	**Day 134**	16.9	175	4.32	6.71	0.33	203
3	**Day 134**	**Day 136**	16.0	173	3.97	6.39	0.76	200
3	**Day 136**	**Day 138**	17.7	172	4.33	6.42	0.71	201
3	**Day 138**	**Day 140**	17.4	170	4.00	6.69	0.85	199
3	**Day 140**	**Day 141**	19.3	172	3.70	5.52	1.03	201
3	**Day 141**	**Day 143**	16.3	170	4.14	5.97	1.20	198
3	**Day 143**	**Day 145**	16.8	171	4.01	5.72	0.84	198

Cycle	Circulation Start (From)	Circulation End (To)	K^+ (mg/L)	Na^+ (mg/L)	Mg^{2+} (mg/L)	Ca^{2+} (mg/L)	Fe^{3+} (mg/L)	Total (mg/L)
3	**Day 145**	**Day 146**	16.2	171	3.26	3.99	0.34	195
3	**Day 146**	**Day 148**	15.3	166	3.22	3.89	0.55	189
3	**Day 148**	**Day 150**	14.6	166	3.25	4.47	2.55	191

Table B.8. The major anion concentrations of the top collected fluid samples

Cycle	Circulation Start (From)	Circulation End (To)	F^- (mg/L)	Cl^- (mg/L)	SO_4^{2-} (mg/L)	HCO_3^- (mg/L)	Total (mg/L)
1	**Day 7.6**	**Day 9.6**	1.55	262	15.7	26.8	306
1	**Day 9.6**	**Day 10.6**	0.90	263	11.8	25.8	302
1	**Day 10.6**	**Day 12.4**	0.77	266	12.9	24.4	304
1	**Day 13.5**	**Day 14.4**	0.06	265	15.4	19.8	300
1	**Day 14.4**	**Day 15.8**	0.00	263	14.2	24.1	301
1	**Day 15.8**	**Day 17.5**	0.16	262	12.1	24.7	299
1	**Day 17.5**	**Day 18.8**	0.10	269	12.1	22.0	303
1	**Day 18.8**	**Day 20.5**	0.64	262	11.6	27.9	303
1	**Day 20.5**	**Day 22.5**	1.63	264	10.7	28.5	305
2	**Day 22.5**	**Day 24.6**	0.48	380	9.37	27.0	417
2	**Day 24.6**	**Day 26.5**	0.22	380	8.61	27.7	416
2	**Day 26.5**	**Day 27.9**	0.16	388	6.65	29.0	424
2	**Day 27.9**	**Day 29.5**	0	389	7.30	32.5	429
2	**Day 29.5**	**Day 30.9**	0	403	6.41	33.4	443
2	**Day 30.9**	**Day 32.7**	0	401	6.22	33.5	440
2	**Day 32.7**	**Day 34.4**	0	396	6.33	33.9	436
2	**Day 34.4**	**Day 36.4**	0	386	5.95	34.5	427
2	**Day 36.4**	**Day 37.9**	0	381	6.15	36.3	424
2	**Day 37.9**	**Day 39.6**	0	381	5.91	37.5	424
2	**Day 39.6**	**Day 40.9**	0	381	6.14	36.9	424
2	**Day 40.9**	**Day 42.8**	0	381	6.07	35.7	423
2	**Day 42.8**	**Day 44.8**	0.37	379	5.87	38.1	423
2	**Day 44.8**	**Day 46.8**	0.24	378	5.93	34.3	418
2	**Day 46.8**	**Day 48.7**	0	374	4.54	31.6	410
2	**Day 48.7**	**Day 50.6**	0	369	4.53	34.4	408
2	**Day 50.6**	**Day 52.4**	0	371	4.28	35.7	411
2	**Day 52.4**	**Day 54.4**	0	375	4.29	35.5	414
2	**Day 54.4**	**Day 56.5**	0	377	4.26	33.5	415
2	**Day 56.5**	**Day 58.3**	0	376	5.54	35.8	417
2	**Day 58.3**	**Day 60.4**	0	381	5.05	33.7	419
2	**Day 60.4**	**Day 61.8**	0	379	5.25	31.3	415
2	**Day 61.8**	**Day 63.6**	0	372	5.91	28.8	407
2	**Day 63.6**	**Day 65.6**	0	374	6.26	28.6	409
2	**Day 65.6**	**Day 67.5**	0	373	6.46	30.1	410
2	**Day 67.5**	**Day 69.4**	0	374	6.36	32.1	413

Cycle	Circulation Start (From)	Circulation End (To)	F^- (mg/L)	Cl^- (mg/L)	SO_4^{2-} (mg/L)	HCO_3^- (mg/L)	Total (mg/L)
2	**Day 69.4**	**Day 70.8**	0	383	5.38	33.3	422
2	**Day 73.6**	**Day 77.4**	0	383	8.14	42.7	433
2	**Day 77.4**	**Day 79.6**	0	378	4.68	40.7	423
2	**Day 79.6**	**Day 82.5**	0	378	5.23	30.8	414
3	**Day 85.7**	**Day 87.8**	0	522	12.6	35.9	571
3	**Day 87.8**	**Day 89.5**	0	523	7.65	37.5	568
3	**Day 89.5**	**Day 91.5**	0	524	6.80	44.0	575
3	**Day 91.5**	**Day 93.6**	0	520	7.72	43.3	571
3	**Day 93.6**	**Day 95.7**	0	521	9.05	42.7	573
3	**Day 95.7**	**Day 97.5**	0	520	10.1	39.3	570
3	**Day 97.5**	**Day 99.4**	0	532	10.6	40.0	582
3	**Day 99.4**	**Day 102**	0	537	7.34	44.5	588
3	**Day 102**	**Day 104**	0	537	7.42	35.9	581
3	**Day 104**	**Day 106**	0	536	9.30	36.6	582
3	**Day 107**	**Day 108**	0	536	13.3	35.4	585
3	**Day 108**	**Day 110**	0	533	13.6	36.6	584
3	**Day 110**	**Day 112**	0	532	13.6	39.0	585
3	**Day 112**	**Day 114**	0	522	12.4	40.3	575
3	**Day 114**	**Day 115**	0	530	11.4	37.8	579
3	**Day 115**	**Day 117**	0	521	10.9	35.4	568
3	**Day 117**	**Day 119**	0	529	12.0	25.6	567
3	**Day 119**	**Day 121**	0	530	11.1	26.8	568
3	**Day 121**	**Day 122**	0	543	11.5	23.8	578
3	**Day 122**	**Day 124**	0	544	11.3	27.9	584
3	**Day 124**	**Day 126**	0	537	11.2	28.0	576
3	**Day 126**	**Day 127**	0	536	11.2	28.3	576
3	**Day 127**	**Day 129**	0	528	11.5	26.8	566
3	**Day 129**	**Day 131**	0	528	10.7	28.9	568
3	**Day 131**	**Day 133**	0	525	10.4	29.3	565
3	**Day 133**	**Day 134**	0	528	10.6	29.3	568
3	**Day 134**	**Day 136**	0	520	10.6	31.7	562
3	**Day 136**	**Day 138**	0	522	10.6	36.2	568
3	**Day 138**	**Day 140**	0	522	10.9	37.8	570
3	**Day 140**	**Day 141**	0	530	11.5	40.3	581
3	**Day 141**	**Day 143**	0	528	11.5	37.8	577
3	**Day 143**	**Day 145**	0	526	11.2	32.9	570

Cycle	Circulation Start (From)	Circulation End (To)	F^- (mg/L)	Cl^- (mg/L)	SO_4^{2-} (mg/L)	HCO_3^- (mg/L)	Total (mg/L)
3	**Day 145**	**Day 146**	0	523	12.1	26.8	562
3	**Day 146**	**Day 148**	0	524	11.1	24.6	559
3	**Day 148**	**Day 150**	0	520	11.0	22.6	553

Table B.9. The major anion concentrations of the bottom collected fluid samples

Cycle	Circulation Start (From)	Circulation End (To)	F^- (mg/L)	Cl^- (mg/L)	SO_4^{2-} (mg/L)	HCO_3^- (mg/L)	Total (mg/L)
1	**Day 7.6**	**Day 9.6**	0	263	11.8	27.0	302
1	**Day 9.6**	**Day 10.6**	0	261	13.5	24.9	300
1	**Day 10.6**	**Day 12.4**	0	258	16.3	23.0	297
1	**Day 13.5**	**Day 14.4**	0	264	14.0	19.6	297
1	**Day 14.4**	**Day 15.8**	0	264	12.9	25.7	302
1	**Day 15.8**	**Day 17.5**	0	264	11.1	24.7	300
1	**Day 17.5**	**Day 18.8**	0	267	11.0	18.8	297
1	**Day 18.8**	**Day 20.5**	0	268	11.1	24.1	303
1	**Day 20.5**	**Day 22.5**	0	265	11.6	26.2	303
2	**Day 22.5**	**Day 24.6**	0	268	11.4	25.5	305
2	**Day 24.6**	**Day 26.5**	0	272	9.86	19.4	301
2	**Day 26.5**	**Day 27.9**	0	274	10.2	27.2	311
2	**Day 27.9**	**Day 29.5**	0	272	8.48	22.2	302
2	**Day 29.5**	**Day 30.9**	0	278	8.76	22.3	309
2	**Day 30.9**	**Day 32.7**	0	275	9.32	24.1	308
2	**Day 32.7**	**Day 34.4**	0	267	9.20	23.0	299
2	**Day 34.4**	**Day 36.4**	0	268	9.20	24.7	302
2	**Day 36.4**	**Day 37.9**	0	271	9.11	23.0	303
2	**Day 37.9**	**Day 39.6**	0	268	9.06	23.5	301
2	**Day 39.6**	**Day 40.9**	0	266	8.98	20.9	296
2	**Day 40.9**	**Day 42.8**	0	268	9.41	21.1	299
2	**Day 42.8**	**Day 44.8**	0	268	9.34	23.5	300
2	**Day 44.8**	**Day 46.8**	0	267	9.47	22.7	299
2	**Day 46.8**	**Day 48.7**	0	267	10.2	25.0	302
2	**Day 48.7**	**Day 50.6**	0	268	10.2	25.3	303
2	**Day 50.6**	**Day 52.4**	0	268	10.2	24.5	302
2	**Day 52.4**	**Day 54.4**	0	268	10.2	25.5	303
2	**Day 54.4**	**Day 56.5**	0	264	9.80	28.9	303
2	**Day 56.5**	**Day 58.3**	0	264	10.5	25.5	300
2	**Day 58.3**	**Day 60.4**	0	264	11.2	21.0	296
2	**Day 60.4**	**Day 61.8**	0	264	11.8	19.6	296
2	**Day 61.8**	**Day 63.6**	0	266	11.5	21.2	298
2	**Day 63.6**	**Day 65.6**	0	266	11.3	18.6	296
2	**Day 65.6**	**Day 67.5**	0	266	11.0	23.6	300
2	**Day 67.5**	**Day 69.4**	0	266	11.1	20.1	297

Cycle	Circulation Start (From)	Circulation End (To)	F^- (mg/L)	Cl^- (mg/L)	SO_4^{2-} (mg/L)	HCO_3^- (mg/L)	Total (mg/L)
2	**Day 69.4**	**Day 70.8**	0	262	9.36	N.I.	N.I.
2	**Day 73.6**	**Day 77.4**	0	260	11.5	N.I.	N.I.
2	**Day 77.4**	**Day 79.6**	0	261	7.59	N.I.	N.I.
2	**Day 79.6**	**Day 82.5**	0	261	10.0	N.I.	N.I.
3	**Day 85.7**	**Day 87.8**	7.10	260	12.2	33.9	314
3	**Day 87.8**	**Day 89.5**	0	260	11.7	35.2	307
3	**Day 89.5**	**Day 91.5**	0	267	11.0	29.4	307
3	**Day 91.5**	**Day 93.6**	0	267	11.8	31.7	310
3	**Day 93.6**	**Day 95.7**	0	263	12.4	34.2	309
3	**Day 95.7**	**Day 97.5**	0	266	12.2	30.5	308
3	**Day 97.5**	**Day 99.4**	0	263	12.5	28.0	304
3	**Day 99.4**	**Day 102**	0	268	13.2	29.3	310
3	**Day 102**	**Day 104**	0	274	12.5	31.7	318
3	**Day 104**	**Day 106**	0	271	12.2	31.6	314
3	**Day 107**	**Day 108**	0	268	14.4	37.8	320
3	**Day 108**	**Day 110**	0	274	14.0	30.5	319
3	**Day 110**	**Day 112**	0	276	14.6	27.5	318
3	**Day 112**	**Day 114**	0	272	13.0	27.5	313
3	**Day 114**	**Day 115**	0	273	13.1	27.5	313
3	**Day 115**	**Day 117**	0	271	12.9	27.5	311
3	**Day 117**	**Day 119**	0	269	13.6	25.6	308
3	**Day 119**	**Day 121**	0	273	13.4	25.6	312
3	**Day 121**	**Day 122**	0	278	13.7	25.0	317
3	**Day 122**	**Day 124**	0	272	13.5	27.8	314
3	**Day 124**	**Day 126**	0	277	13.0	25.6	316
3	**Day 126**	**Day 127**	0	276	12.8	25.6	314
3	**Day 127**	**Day 129**	0	276	13.1	25.0	314
3	**Day 129**	**Day 131**	0	275	11.6	N.I.	N.I.
3	**Day 131**	**Day 133**	0	276	11.7	N.I.	N.I.
3	**Day 133**	**Day 134**	0	275	11.5	N.I.	N.I.
3	**Day 134**	**Day 136**	0	273	12.2	N.I.	N.I.
3	**Day 136**	**Day 138**	0	265	12.3	N.I.	N.I.
3	**Day 138**	**Day 140**	0	268	12.2	N.I.	N.I.
3	**Day 140**	**Day 141**	0	267	12.0	N.I.	N.I.
3	**Day 141**	**Day 143**	0	269	12.2	N.I.	N.I.
3	**Day 143**	**Day 145**	0	270	11.8	N.I.	N.I.

Cycle	Circulation Start (From)	Circulation End (To)	F^- (mg/L)	Cl^- (mg/L)	SO_4^{2-} (mg/L)	HCO_3^- (mg/L)	Total (mg/L)
3	**Day 145**	**Day 146**	0	265	12.1	N.I.	N.I.
3	**Day 146**	**Day 148**	0	262	12.1	N.I.	N.I.
3	**Day 148**	**Day 150**	0	264	11.4	N.I.	N.I.

Table B.10. The CBE for the synthetic fluids

Solution Type	Fluid Production Day	Total Cation (meq/L)	Total Anion (meq/L)	CBE (%)
A	**Day 0**	7.70	-7.82	-0.78
A	**Day 2**	7.66	-7.75	-0.61
A	**Day 11**	7.65	-7.74	-0.59
A	**Day 13**	7.68	-7.76	-0.53
A	**Day 23**	7.65	-7.72	-0.51
A	**Day 47**	7.63	-7.66	-0.21
A	**Day 73**	7.51	-7.54	-0.18
A	**Day 85**	7.48	-7.57	-0.56
A	**Day 107**	7.62	-7.72	-0.66
A	**Day 129**	7.50	-7.47	0.16
B	**Day 0**	11.6	-11.3	1.27
B	**Day 24**	11.5	-11.2	1.24
B	**Day 47**	11.3	-11.2	0.36
B	**Day 73**	11.3	-11.1	0.89
C	**Day 0**	15.8	-15.9	-0.49
C	**Day 89**	15.7	-15.9	-0.71
C	**Day 112**	15.6	-15.8	-0.57
C	**Day 140**	15.7	-15.7	-0.03

Table B.11. The CBE for the top collected fluid samples

Cycle	Circulation Start (From)	Circulation End (To)	Total Cation (meq/L)	Total Anion (meq/L)	CBE (%)
1	**Day 7.6**	**Day 9.6**	8.23	-8.24	-0.05
1	**Day 9.6**	**Day 10.6**	8.12	-8.13	-0.07
1	**Day 10.6**	**Day 12.4**	8.17	-8.21	-0.26
1	**Day 13.5**	**Day 14.4**	8.13	-8.13	0.02
1	**Day 14.4**	**Day 15.8**	8.17	-8.10	0.46
1	**Day 15.8**	**Day 17.5**	8.10	-8.06	0.29
1	**Day 17.5**	**Day 18.8**	8.11	-8.21	-0.65
1	**Day 18.8**	**Day 20.5**	7.97	-8.13	-0.99
1	**Day 20.5**	**Day 22.5**	7.97	-8.23	-1.58
2	**Day 22.5**	**Day 24.6**	11.3	-11.4	-0.37
2	**Day 24.6**	**Day 26.5**	11.4	-11.4	-0.02
2	**Day 26.5**	**Day 27.9**	11.5	-11.6	-0.19
2	**Day 27.9**	**Day 29.5**	11.7	-11.7	0.04
2	**Day 29.5**	**Day 30.9**	11.9	-12.1	-0.62
2	**Day 30.9**	**Day 32.7**	11.8	-12.0	-0.56
2	**Day 32.7**	**Day 34.4**	11.9	-11.9	0.35
2	**Day 34.4**	**Day 36.4**	11.7	-11.6	0.56
2	**Day 36.4**	**Day 37.9**	11.6	-11.5	0.35
2	**Day 37.9**	**Day 39.6**	11.5	-11.5	0.04
2	**Day 39.6**	**Day 40.9**	11.5	-11.5	0.21
2	**Day 40.9**	**Day 42.8**	11.5	-11.5	0.35
2	**Day 42.8**	**Day 44.8**	11.5	-11.5	0.12
2	**Day 44.8**	**Day 46.8**	11.5	-11.4	0.66
2	**Day 46.8**	**Day 48.7**	11.3	-11.2	0.69
2	**Day 48.7**	**Day 50.6**	11.4	-11.1	1.29
2	**Day 50.6**	**Day 52.4**	11.4	-11.1	1.02
2	**Day 52.4**	**Day 54.4**	11.3	-11.2	0.37
2	**Day 54.4**	**Day 56.5**	11.2	-11.3	-0.14
2	**Day 56.5**	**Day 58.3**	11.5	-11.3	1.00
2	**Day 58.3**	**Day 60.4**	11.3	-11.4	-0.30
2	**Day 60.4**	**Day 61.8**	11.2	-11.3	-0.38
2	**Day 61.8**	**Day 63.6**	11.2	-11.1	0.37
2	**Day 63.6**	**Day 65.6**	11.2	-11.1	0.47
2	**Day 65.6**	**Day 67.5**	11.2	-11.2	0.39
2	**Day 67.5**	**Day 69.4**	11.3	-11.2	0.58

Cycle	Circulation Start (From)	Circulation End (To)	Total Cation (meq/L)	Total Anion (meq/L)	CBE (%)
2	**Day 69.4**	**Day 70.8**	11.6	-11.5	0.65
2	**Day 73.6**	**Day 77.4**	11.8	-11.7	0.70
2	**Day 77.4**	**Day 79.6**	11.7	-11.4	1.39
2	**Day 79.6**	**Day 82.5**	11.6	-11.3	1.41
3	**Day 85.7**	**Day 87.8**	15.2	-15.6	-1.13
3	**Day 87.8**	**Day 89.5**	15.2	-15.5	-0.97
3	**Day 89.5**	**Day 91.5**	15.3	-15.6	-1.26
3	**Day 91.5**	**Day 93.6**	15.5	-15.5	-0.21
3	**Day 93.6**	**Day 95.7**	15.5	-15.6	-0.23
3	**Day 95.7**	**Day 97.5**	15.4	-15.5	-0.51
3	**Day 97.5**	**Day 99.4**	15.7	-15.9	-0.62
3	**Day 99.4**	**Day 102**	15.4	-16.0	-1.85
3	**Day 102**	**Day 104**	15.8	-15.9	-0.26
3	**Day 104**	**Day 106**	15.7	-15.9	-0.58
3	**Day 107**	**Day 108**	15.6	-16.0	-1.32
3	**Day 108**	**Day 110**	15.4	-15.9	-1.53
3	**Day 110**	**Day 112**	15.5	-15.9	-1.47
3	**Day 112**	**Day 114**	15.7	-15.6	0.21
3	**Day 114**	**Day 115**	15.7	-15.8	-0.37
3	**Day 115**	**Day 117**	15.7	-15.5	0.71
3	**Day 117**	**Day 119**	15.7	-15.6	0.20
3	**Day 119**	**Day 121**	15.5	-15.6	-0.52
3	**Day 121**	**Day 122**	15.4	-15.9	-1.72
3	**Day 122**	**Day 124**	15.9	-16.1	-0.48
3	**Day 124**	**Day 126**	15.6	-15.8	-0.82
3	**Day 126**	**Day 127**	15.6	-15.8	-0.79
3	**Day 127**	**Day 129**	15.5	-15.6	-0.33
3	**Day 129**	**Day 131**	15.7	-15.6	0.20
3	**Day 131**	**Day 133**	15.6	-15.5	0.39
3	**Day 133**	**Day 134**	15.6	-15.6	-0.15
3	**Day 134**	**Day 136**	15.5	-15.4	0.30
3	**Day 136**	**Day 138**	15.5	-15.5	-0.05
3	**Day 138**	**Day 140**	15.7	-15.6	0.33
3	**Day 140**	**Day 141**	15.8	-15.8	-0.23
3	**Day 141**	**Day 143**	15.7	-15.7	-0.02
3	**Day 143**	**Day 145**	15.6	-15.6	-0.07

Cycle	Circulation Start (From)	Circulation End (To)	Total Cation (meq/L)	Total Anion (meq/L)	CBE (%)
3	**Day 145**	**Day 146**	15.1	-15.4	-0.99
3	**Day 146**	**Day 148**	14.9	-15.4	-1.50
3	**Day 148**	**Day 150**	15.0	-15.3	-0.85

Table B.12. The CBE for the bottom collected fluid samples

Cycle	Circulation Start (From)	Circulation End (To)	Total Cation (meq/L)	Total Anion (meq/L)	CBE (%)
1	**Day 7.6**	**Day 9.6**	8.12	-8.10	0.12
1	**Day 9.6**	**Day 10.6**	7.99	-8.06	-0.40
1	**Day 10.6**	**Day 12.4**	8.04	-7.98	0.35
1	**Day 13.5**	**Day 14.4**	8.08	-8.05	0.20
1	**Day 14.4**	**Day 15.8**	8.06	-8.13	-0.38
1	**Day 15.8**	**Day 17.5**	8.03	-8.08	-0.29
1	**Day 17.5**	**Day 18.8**	8.26	-8.07	1.17
1	**Day 18.8**	**Day 20.5**	8.30	-8.17	0.75
1	**Day 20.5**	**Day 22.5**	8.10	-8.15	-0.33
2	**Day 22.5**	**Day 24.6**	8.12	-8.21	-0.52
2	**Day 24.6**	**Day 26.5**	8.14	-8.20	-0.35
2	**Day 26.5**	**Day 27.9**	8.17	-8.38	-1.31
2	**Day 27.9**	**Day 29.5**	8.19	-8.21	-0.07
2	**Day 29.5**	**Day 30.9**	8.34	-8.40	-0.34
2	**Day 30.9**	**Day 32.7**	8.24	-8.34	-0.64
2	**Day 32.7**	**Day 34.4**	8.25	-8.11	0.89
2	**Day 34.4**	**Day 36.4**	8.24	-8.15	0.59
2	**Day 36.4**	**Day 37.9**	8.14	-8.21	-0.42
2	**Day 37.9**	**Day 39.6**	8.18	-8.14	0.25
2	**Day 39.6**	**Day 40.9**	8.11	-8.04	0.42
2	**Day 40.9**	**Day 42.8**	8.16	-8.10	0.37
2	**Day 42.8**	**Day 44.8**	8.11	-8.13	-0.13
2	**Day 44.8**	**Day 46.8**	8.07	-8.10	-0.14
2	**Day 46.8**	**Day 48.7**	7.96	-8.16	-1.20
2	**Day 48.7**	**Day 50.6**	8.01	-8.17	-1.03
2	**Day 50.6**	**Day 52.4**	8.06	-8.16	-0.66
2	**Day 52.4**	**Day 54.4**	7.95	-8.18	-1.39
2	**Day 54.4**	**Day 56.5**	8.11	-8.12	-0.06
2	**Day 56.5**	**Day 58.3**	8.12	-8.09	0.19
2	**Day 58.3**	**Day 60.4**	8.17	-8.03	0.90
2	**Day 60.4**	**Day 61.8**	8.09	-8.02	0.45
2	**Day 61.8**	**Day 63.6**	8.04	-8.08	-0.27
2	**Day 63.6**	**Day 65.6**	8.07	-8.04	0.15
2	**Day 65.6**	**Day 67.5**	8.12	-8.11	0.06
2	**Day 67.5**	**Day 69.4**	8.14	-8.06	0.49

Cycle	Circulation Start (From)	Circulation End (To)	Total Cation (meq/L)	Total Anion (meq/L)	CBE (%)
2	**Day 69.4**	**Day 70.8**	8.13	N.I.	N.I.
2	**Day 73.6**	**Day 77.4**	8.15	N.I.	N.I.
2	**Day 77.4**	**Day 79.6**	8.19	N.I.	N.I.
2	**Day 79.6**	**Day 82.5**	8.10	N.I.	N.I.
3	**Day 85.7**	**Day 87.8**	8.61	-8.53	0.48
3	**Day 87.8**	**Day 89.5**	8.15	-8.15	-0.04
3	**Day 89.5**	**Day 91.5**	8.29	-8.23	0.38
3	**Day 91.5**	**Day 93.6**	8.35	-8.29	0.35
3	**Day 93.6**	**Day 95.7**	8.18	-8.23	-0.29
3	**Day 95.7**	**Day 97.5**	8.18	-8.25	-0.45
3	**Day 97.5**	**Day 99.4**	8.16	-8.15	0.07
3	**Day 99.4**	**Day 102**	8.26	-8.31	-0.29
3	**Day 102**	**Day 104**	8.41	-8.51	-0.60
3	**Day 104**	**Day 106**	8.56	-8.41	0.88
3	**Day 107**	**Day 108**	8.36	-8.48	-0.69
3	**Day 108**	**Day 110**	8.47	-8.52	-0.33
3	**Day 110**	**Day 112**	8.50	-8.53	-0.18
3	**Day 112**	**Day 114**	8.62	-8.40	1.30
3	**Day 114**	**Day 115**	8.56	-8.41	0.91
3	**Day 115**	**Day 117**	8.57	-8.35	1.31
3	**Day 117**	**Day 119**	8.47	-8.28	1.11
3	**Day 119**	**Day 121**	8.62	-8.40	1.33
3	**Day 121**	**Day 122**	8.69	-8.54	0.91
3	**Day 122**	**Day 124**	8.80	-8.42	2.19
3	**Day 124**	**Day 126**	8.73	-8.51	1.26
3	**Day 126**	**Day 127**	8.62	-8.47	0.88
3	**Day 127**	**Day 129**	8.69	-8.46	1.31
3	**Day 129**	**Day 131**	8.83	N.I.	N.I.
3	**Day 131**	**Day 133**	8.81	N.I.	N.I.
3	**Day 133**	**Day 134**	8.76	N.I.	N.I.
3	**Day 134**	**Day 136**	8.62	N.I.	N.I.
3	**Day 136**	**Day 138**	8.63	N.I.	N.I.
3	**Day 138**	**Day 140**	8.56	N.I.	N.I.
3	**Day 140**	**Day 141**	8.60	N.I.	N.I.
3	**Day 141**	**Day 143**	8.53	N.I.	N.I.
3	**Day 143**	**Day 145**	8.52	N.I.	N.I.

Cycle	Circulation Start (From)	Circulation End (To)	Total Cation (meq/L)	Total Anion (meq/L)	CBE (%)
3	**Day 145**	**Day 146**	8.33	N.I.	N.I.
3	**Day 146**	**Day 148**	8.08	N.I.	N.I.
3	**Day 148**	**Day 150**	8.22	N.I.	N.I.

APPENDIX C: SOLUTE TRANSPORT ANALYSES

Table C.1. The cumulative change of total K^+ stored mass within sample due to the mass influx and mass outflux in the 2nd osmotic cycle

Circulation Start (From)	Circulation End (To)	Solute Influx (kg/m^2)	Solute Outflux (kg/m^2)	Stored Mass (kg/m^2)
Day 22.5	**Day 24.6**	5.76E-05	-8.77E-06	4.88E-05
Day 24.6	**Day 26.5**	1.19E-04	-1.74E-05	1.02E-04
Day 26.5	**Day 27.9**	1.82E-04	-2.62E-05	1.55E-04
Day 27.9	**Day 29.5**	2.38E-04	-3.58E-05	2.03E-04
Day 29.5	**Day 30.9**	2.95E-04	-4.66E-05	2.48E-04
Day 30.9	**Day 32.7**	3.54E-04	-5.77E-05	2.96E-04
Day 32.7	**Day 34.4**	4.05E-04	-6.89E-05	3.36E-04
Day 34.4	**Day 36.4**	4.84E-04	-8.19E-05	4.02E-04
Day 36.4	**Day 37.9**	5.56E-04	-9.47E-05	4.61E-04
Day 37.9	**Day 39.6**	6.33E-04	-1.09E-04	5.24E-04
Day 39.6	**Day 40.9**	7.06E-04	-1.22E-04	5.84E-04
Day 40.9	**Day 42.8**	7.79E-04	-1.36E-04	6.43E-04
Day 42.8	**Day 44.8**	8.59E-04	-1.52E-04	7.06E-04
Day 44.8	**Day 46.8**	9.35E-04	-1.69E-04	7.67E-04
Day 46.8	**Day 48.7**	1.01E-03	-1.86E-04	8.26E-04
Day 48.7	**Day 50.6**	1.08E-03	-2.04E-04	8.78E-04
Day 50.6	**Day 52.4**	1.15E-03	-2.24E-04	9.22E-04
Day 52.4	**Day 54.4**	1.21E-03	-2.43E-04	9.65E-04
Day 54.4	**Day 56.5**	1.27E-03	-2.63E-04	1.01E-03
Day 56.5	**Day 58.3**	1.32E-03	-2.84E-04	1.04E-03
Day 58.3	**Day 60.4**	1.38E-03	-3.04E-04	1.07E-03
Day 60.4	**Day 61.8**	1.43E-03	-3.25E-04	1.11E-03
Day 61.8	**Day 63.6**	1.49E-03	-3.46E-04	1.14E-03
Day 63.6	**Day 65.6**	1.54E-03	-3.67E-04	1.17E-03
Day 65.6	**Day 67.5**	1.60E-03	-3.88E-04	1.21E-03
Day 67.5	**Day 69.4**	1.65E-03	-4.10E-04	1.24E-03

Table C.2. The cumulative change of total K^+ stored mass within sample due to the mass influx and mass outflux in the 3rd osmotic cycle

Circulation Start (From)	Circulation End (To)	Solute Influx (kg/m^2)	Solute Outflux (kg/m^2)	Stored Mass (kg/m^2)
Day 85.7	**Day 87.8**	1.23E-04	-2.38E-05	9.94E-05
Day 87.8	**Day 89.5**	2.54E-04	-4.84E-05	2.06E-04
Day 89.5	**Day 91.5**	4.01E-04	-7.62E-05	3.24E-04
Day 91.5	**Day 93.6**	5.26E-04	-1.04E-04	4.22E-04
Day 93.6	**Day 95.7**	6.40E-04	-1.33E-04	5.07E-04
Day 95.7	**Day 97.5**	7.54E-04	-1.62E-04	5.92E-04
Day 97.5	**Day 99.4**	8.54E-04	-1.92E-04	6.61E-04
Day 99.4	**Day 102**	9.78E-04	-2.27E-04	7.51E-04
Day 102	**Day 104**	1.10E-03	-2.66E-04	8.35E-04
Day 104	**Day 106**	1.23E-03	-3.05E-04	9.21E-04
Day 107	**Day 108**	1.35E-03	-3.36E-04	1.01E-03
Day 108	**Day 110**	1.48E-03	-3.70E-04	1.11E-03
Day 110	**Day 112**	1.60E-03	-4.05E-04	1.20E-03
Day 112	**Day 114**	1.72E-03	-4.39E-04	1.28E-03
Day 114	**Day 115**	1.84E-03	-4.75E-04	1.37E-03
Day 115	**Day 117**	1.96E-03	-5.08E-04	1.45E-03
Day 117	**Day 119**	2.07E-03	-5.45E-04	1.52E-03
Day 119	**Day 121**	2.18E-03	-5.82E-04	1.60E-03
Day 121	**Day 122**	2.30E-03	-6.19E-04	1.69E-03
Day 122	**Day 124**	2.41E-03	-6.60E-04	1.75E-03
Day 124	**Day 126**	2.52E-03	-7.00E-04	1.82E-03
Day 126	**Day 127**	2.63E-03	-7.40E-04	1.89E-03
Day 127	**Day 129**	2.75E-03	-7.77E-04	1.97E-03
Day 129	**Day 131**	2.86E-03	-8.14E-04	2.04E-03
Day 131	**Day 133**	2.97E-03	-8.50E-04	2.12E-03
Day 133	**Day 134**	3.08E-03	-8.83E-04	2.20E-03
Day 134	**Day 136**	3.20E-03	-9.13E-04	2.29E-03
Day 136	**Day 138**	3.32E-03	-9.47E-04	2.38E-03
Day 138	**Day 140**	3.44E-03	-9.81E-04	2.45E-03
Day 140	**Day 141**	3.53E-03	-1.02E-03	2.51E-03
Day 141	**Day 143**	3.65E-03	-1.05E-03	2.60E-03
Day 143	**Day 145**	3.78E-03	-1.08E-03	2.69E-03
Day 145	**Day 146**	3.90E-03	-1.11E-03	2.79E-03
Day 146	**Day 148**	4.03E-03	-1.14E-03	2.89E-03

Circulation Start (From)	Circulation End (To)	Solute Influx (kg/m^2)	Solute Outflux (kg/m^2)	Stored Mass (kg/m^2)
Day 148	**Day 150**	4.16E-03	-1.17E-03	2.99E-03

Table C.3. The cumulative change of total Cl^- stored mass within sample due to the mass influx and mass outflux in the 2nd osmotic cycle

Circulation Start (From)	Circulation End (To)	Solute Influx (kg/m^2)	Solute Outflux (kg/m^2)	Stored Mass (kg/m^2)
Day 22.5	**Day 24.6**	1.37E-05	-1.26E-05	1.08E-06
Day 24.6	**Day 26.5**	2.70E-05	-3.35E-05	-6.50E-06
Day 26.5	**Day 27.9**	2.42E-05	-5.80E-05	-3.38E-05
Day 27.9	**Day 29.5**	1.89E-05	-7.86E-05	-5.97E-05
Day 29.5	**Day 30.9**	-1.30E-05	-1.12E-04	-1.25E-04
Day 30.9	**Day 32.7**	-3.98E-05	-1.38E-04	-1.78E-04
Day 32.7	**Day 34.4**	-5.81E-05	-1.50E-04	-2.08E-04
Day 34.4	**Day 36.4**	-5.78E-05	-1.62E-04	-2.20E-04
Day 36.4	**Day 37.9**	-4.72E-05	-1.82E-04	-2.29E-04
Day 37.9	**Day 39.6**	-3.64E-05	-1.95E-04	-2.32E-04
Day 39.6	**Day 40.9**	-2.58E-05	-2.05E-04	-2.31E-04
Day 40.9	**Day 42.8**	-1.58E-05	-2.19E-04	-2.34E-04
Day 42.8	**Day 44.8**	-8.09E-07	-2.31E-04	-2.32E-04
Day 44.8	**Day 46.8**	1.64E-05	-2.42E-04	-2.26E-04
Day 46.8	**Day 48.7**	4.13E-05	-2.54E-04	-2.13E-04
Day 48.7	**Day 50.6**	7.31E-05	-2.66E-04	-1.93E-04
Day 50.6	**Day 52.4**	1.00E-04	-2.81E-04	-1.81E-04
Day 52.4	**Day 54.4**	1.21E-04	-2.96E-04	-1.75E-04
Day 54.4	**Day 56.5**	1.36E-04	-3.03E-04	-1.67E-04
Day 56.5	**Day 58.3**	1.55E-04	-3.12E-04	-1.57E-04
Day 58.3	**Day 60.4**	1.64E-04	-3.20E-04	-1.56E-04
Day 60.4	**Day 61.8**	1.76E-04	-3.28E-04	-1.52E-04
Day 61.8	**Day 63.6**	2.01E-04	-3.39E-04	-1.38E-04
Day 63.6	**Day 65.6**	2.23E-04	-3.51E-04	-1.28E-04
Day 65.6	**Day 67.5**	2.47E-04	-3.62E-04	-1.15E-04
Day 67.5	**Day 69.4**	2.68E-04	-3.73E-04	-1.05E-04

Table C.4. The cumulative change of total Cl^- stored mass within sample due to the mass influx and mass outflux in the 3rd osmotic cycle

Circulation Start (From)	Circulation End (To)	Solute Influx (kg/m^2)	Solute Outflux (kg/m^2)	Stored Mass (kg/m^2)
Day 85.7	**Day 87.8**	5.66E-05	-1.26E-05	4.40E-05
Day 87.8	**Day 89.5**	1.11E-04	-2.29E-05	8.78E-05
Day 89.5	**Day 91.5**	1.64E-04	-4.59E-05	1.18E-04
Day 91.5	**Day 93.6**	2.24E-04	-6.95E-05	1.55E-04
Day 93.6	**Day 95.7**	2.75E-04	-8.52E-05	1.90E-04
Day 95.7	**Day 97.5**	3.26E-04	-1.07E-04	2.20E-04
Day 97.5	**Day 99.4**	3.56E-04	-1.23E-04	2.32E-04
Day 99.4	**Day 102**	3.75E-04	-1.49E-04	2.26E-04
Day 102	**Day 104**	3.94E-04	-1.86E-04	2.07E-04
Day 104	**Day 106**	4.15E-04	-2.17E-04	1.98E-04
Day 107	**Day 108**	4.36E-04	-2.43E-04	1.93E-04
Day 108	**Day 110**	4.62E-04	-2.73E-04	1.89E-04
Day 110	**Day 112**	4.91E-04	-3.06E-04	1.85E-04
Day 112	**Day 114**	5.38E-04	-3.32E-04	2.07E-04
Day 114	**Day 115**	5.70E-04	-3.58E-04	2.11E-04
Day 115	**Day 117**	6.17E-04	-3.81E-04	2.36E-04
Day 117	**Day 119**	6.49E-04	-4.00E-04	2.49E-04
Day 119	**Day 121**	6.80E-04	-4.27E-04	2.52E-04
Day 121	**Day 122**	6.86E-04	-4.64E-04	2.21E-04
Day 122	**Day 124**	6.89E-04	-4.91E-04	1.98E-04
Day 124	**Day 126**	7.06E-04	-5.26E-04	1.79E-04
Day 126	**Day 127**	7.24E-04	-5.60E-04	1.65E-04
Day 127	**Day 129**	7.59E-04	-5.92E-04	1.66E-04
Day 129	**Day 131**	7.93E-04	-6.24E-04	1.69E-04
Day 131	**Day 133**	8.32E-04	-6.58E-04	1.74E-04
Day 133	**Day 134**	8.66E-04	-6.90E-04	1.76E-04
Day 134	**Day 136**	9.17E-04	-7.26E-04	1.90E-04
Day 136	**Day 138**	9.64E-04	-7.53E-04	2.11E-04
Day 138	**Day 140**	1.01E-03	-7.85E-04	2.25E-04
Day 140	**Day 141**	1.04E-03	-8.14E-04	2.27E-04
Day 141	**Day 143**	1.08E-03	-8.49E-04	2.28E-04
Day 143	**Day 145**	1.11E-03	-8.83E-04	2.26E-04
Day 145	**Day 146**	1.15E-03	-9.08E-04	2.39E-04
Day 146	**Day 148**	1.18E-03	-9.29E-04	2.54E-04

Circulation Start (From)	Circulation End (To)	Solute Influx (kg/m^2)	Solute Outflux (kg/m^2)	Stored Mass (kg/m^2)
Day 148	**Day 150**	1.23E-03	-9.53E-04	2.74E-04

Table C.5. The cumulative change of K^+ mass stored within sample in the 2nd osmotic cycle

Circulation Start (From)	Circulation End (To)	$\sum M_{Stored}$ (kg)	M_{fluid} (kg)	$\sum M_{Solid}$ (kg)
Day 22.5	**Day 24.6**	1.55E-07	4.57E-07	-3.02E-07
Day 24.6	**Day 26.5**	3.23E-07	4.62E-07	-1.39E-07
Day 26.5	**Day 27.9**	4.92E-07	4.62E-07	2.94E-08
Day 27.9	**Day 29.5**	6.42E-07	4.62E-07	1.80E-07
Day 29.5	**Day 30.9**	7.86E-07	4.62E-07	3.23E-07
Day 30.9	**Day 32.7**	9.37E-07	4.62E-07	4.75E-07
Day 32.7	**Day 34.4**	1.06E-06	4.62E-07	6.01E-07
Day 34.4	**Day 36.4**	1.27E-06	4.62E-07	8.10E-07
Day 36.4	**Day 37.9**	1.46E-06	4.62E-07	9.97E-07
Day 37.9	**Day 39.6**	1.66E-06	4.62E-07	1.20E-06
Day 39.6	**Day 40.9**	1.85E-06	4.62E-07	1.39E-06
Day 40.9	**Day 42.8**	2.04E-06	4.62E-07	1.57E-06
Day 42.8	**Day 44.8**	2.24E-06	4.62E-07	1.77E-06
Day 44.8	**Day 46.8**	2.43E-06	4.62E-07	1.97E-06
Day 46.8	**Day 48.7**	2.62E-06	4.62E-07	2.15E-06
Day 48.7	**Day 50.6**	2.78E-06	4.57E-07	2.32E-06
Day 50.6	**Day 52.4**	2.92E-06	4.51E-07	2.47E-06
Day 52.4	**Day 54.4**	3.05E-06	4.51E-07	2.60E-06
Day 54.4	**Day 56.5**	3.18E-06	4.51E-07	2.73E-06
Day 56.5	**Day 58.3**	3.29E-06	4.51E-07	2.83E-06
Day 58.3	**Day 60.4**	3.39E-06	4.51E-07	2.94E-06
Day 60.4	**Day 61.8**	3.51E-06	4.51E-07	3.06E-06
Day 61.8	**Day 63.6**	3.62E-06	4.51E-07	3.17E-06
Day 63.6	**Day 65.6**	3.72E-06	4.51E-07	3.27E-06
Day 65.6	**Day 67.5**	3.82E-06	4.51E-07	3.37E-06
Day 67.5	**Day 69.4**	3.93E-06	4.51E-07	3.48E-06

Table C.6. The cumulative change of K^+ mass stored within sample in the 3rd osmotic cycle

Circulation Start (From)	Circulation End (To)	ΣM_{Stored} (kg)	M_{fluid} (kg)	ΣM_{Solid} (kg)
Day 85.7	**Day 87.8**	3.15E-07	5.15E-07	-2.00E-07
Day 87.8	**Day 89.5**	6.52E-07	5.15E-07	1.37E-07
Day 89.5	**Day 91.5**	1.03E-06	5.15E-07	5.13E-07
Day 91.5	**Day 93.6**	1.34E-06	5.15E-07	8.21E-07
Day 93.6	**Day 95.7**	1.61E-06	5.10E-07	1.10E-06
Day 95.7	**Day 97.5**	1.88E-06	5.09E-07	1.37E-06
Day 97.5	**Day 99.4**	2.09E-06	5.09E-07	1.59E-06
Day 99.4	**Day 102**	2.38E-06	5.09E-07	1.87E-06
Day 102	**Day 104**	2.64E-06	5.09E-07	2.14E-06
Day 104	**Day 106**	2.92E-06	5.09E-07	2.41E-06
Day 107	**Day 108**	3.21E-06	5.09E-07	2.70E-06
Day 108	**Day 110**	3.51E-06	5.09E-07	3.00E-06
Day 110	**Day 112**	3.79E-06	5.09E-07	3.28E-06
Day 112	**Day 114**	4.07E-06	5.09E-07	3.56E-06
Day 114	**Day 115**	4.33E-06	5.01E-07	3.83E-06
Day 115	**Day 117**	4.59E-06	5.00E-07	4.09E-06
Day 117	**Day 119**	4.82E-06	5.00E-07	4.32E-06
Day 119	**Day 121**	5.07E-06	5.00E-07	4.57E-06
Day 121	**Day 122**	5.34E-06	5.00E-07	4.84E-06
Day 122	**Day 124**	5.55E-06	5.00E-07	5.05E-06
Day 124	**Day 126**	5.78E-06	5.00E-07	5.28E-06
Day 126	**Day 127**	6.00E-06	5.00E-07	5.50E-06
Day 127	**Day 129**	6.25E-06	5.00E-07	5.75E-06
Day 129	**Day 131**	6.47E-06	5.00E-07	5.97E-06
Day 131	**Day 133**	6.70E-06	5.00E-07	6.20E-06
Day 133	**Day 134**	6.97E-06	5.00E-07	6.47E-06
Day 134	**Day 136**	7.25E-06	5.00E-07	6.75E-06
Day 136	**Day 138**	7.53E-06	5.00E-07	7.03E-06
Day 138	**Day 140**	7.77E-06	5.00E-07	7.27E-06
Day 140	**Day 141**	7.96E-06	5.00E-07	7.46E-06
Day 141	**Day 143**	8.24E-06	5.00E-07	7.74E-06
Day 143	**Day 145**	8.53E-06	5.12E-07	8.02E-06
Day 145	**Day 146**	8.84E-06	5.14E-07	8.33E-06
Day 146	**Day 148**	9.15E-06	5.14E-07	8.64E-06
Day 148	**Day 150**	9.46E-06	5.14E-07	8.95E-06

Table C.7. The cumulative change of Cl^- mass stored within sample in the 2nd osmotic cycle

Circulation Start (From)	Circulation End (To)	$\sum M_{Stored}$ (kg)	M_{fluid} (kg)
Day 22.5	**Day 24.6**	3.43E-09	3.84E-07
Day 24.6	**Day 26.5**	-2.06E-08	3.84E-07
Day 26.5	**Day 27.9**	-1.07E-07	3.84E-07
Day 27.9	**Day 29.5**	-1.89E-07	3.83E-07
Day 29.5	**Day 30.9**	-3.94E-07	3.83E-07
Day 30.9	**Day 32.7**	-5.63E-07	3.83E-07
Day 32.7	**Day 34.4**	-6.58E-07	3.83E-07
Day 34.4	**Day 36.4**	-6.98E-07	3.83E-07
Day 36.4	**Day 37.9**	-7.24E-07	3.83E-07
Day 37.9	**Day 39.6**	-7.34E-07	3.83E-07
Day 39.6	**Day 40.9**	-7.32E-07	3.83E-07
Day 40.9	**Day 42.8**	-7.42E-07	3.83E-07
Day 42.8	**Day 44.8**	-7.35E-07	3.83E-07
Day 44.8	**Day 46.8**	-7.15E-07	3.83E-07
Day 46.8	**Day 48.7**	-6.73E-07	3.83E-07
Day 48.7	**Day 50.6**	-6.12E-07	3.81E-07
Day 50.6	**Day 52.4**	-5.73E-07	3.76E-07
Day 52.4	**Day 54.4**	-5.54E-07	3.76E-07
Day 54.4	**Day 56.5**	-5.29E-07	3.76E-07
Day 56.5	**Day 58.3**	-4.97E-07	3.76E-07
Day 58.3	**Day 60.4**	-4.95E-07	3.76E-07
Day 60.4	**Day 61.8**	-4.81E-07	3.76E-07
Day 61.8	**Day 63.6**	-4.37E-07	3.76E-07
Day 63.6	**Day 65.6**	-4.04E-07	3.76E-07
Day 65.6	**Day 67.5**	-3.64E-07	3.76E-07
Day 67.5	**Day 69.4**	-3.34E-07	3.76E-07

Table C.8. The cumulative change of Cl^- mass stored within sample in the 3rd osmotic cycle

Circulation Start (From)	Circulation End (To)	$\sum M_{Stored}$ (kg)	M_{fluid} (kg)
Day 85.7	**Day 87.8**	1.39E-07	4.83E-07
Day 87.8	**Day 89.5**	2.78E-07	4.86E-07
Day 89.5	**Day 91.5**	3.72E-07	4.86E-07
Day 91.5	**Day 93.6**	4.90E-07	4.86E-07
Day 93.6	**Day 95.7**	6.02E-07	4.75E-07
Day 95.7	**Day 97.5**	6.96E-07	4.72E-07
Day 97.5	**Day 99.4**	7.35E-07	4.72E-07
Day 99.4	**Day 102**	7.17E-07	4.72E-07
Day 102	**Day 104**	6.56E-07	4.72E-07
Day 104	**Day 106**	6.27E-07	4.72E-07
Day 107	**Day 108**	6.12E-07	4.72E-07
Day 108	**Day 110**	5.99E-07	4.84E-07
Day 110	**Day 112**	5.86E-07	4.85E-07
Day 112	**Day 114**	6.54E-07	4.85E-07
Day 114	**Day 115**	6.69E-07	4.83E-07
Day 115	**Day 117**	7.48E-07	4.82E-07
Day 117	**Day 119**	7.90E-07	4.82E-07
Day 119	**Day 121**	7.99E-07	4.82E-07
Day 121	**Day 122**	7.01E-07	4.82E-07
Day 122	**Day 124**	6.27E-07	4.82E-07
Day 124	**Day 126**	5.68E-07	4.82E-07
Day 126	**Day 127**	5.22E-07	4.82E-07
Day 127	**Day 129**	5.27E-07	4.82E-07
Day 129	**Day 131**	5.35E-07	4.82E-07
Day 131	**Day 133**	5.52E-07	4.82E-07
Day 133	**Day 134**	5.58E-07	4.82E-07
Day 134	**Day 136**	6.03E-07	4.68E-07
Day 136	**Day 138**	6.68E-07	4.60E-07
Day 138	**Day 140**	7.14E-07	4.60E-07
Day 140	**Day 141**	7.20E-07	4.60E-07
Day 141	**Day 143**	7.23E-07	4.60E-07
Day 143	**Day 145**	7.15E-07	4.49E-07
Day 145	**Day 146**	7.56E-07	4.49E-07
Day 146	**Day 148**	8.05E-07	4.49E-07
Day 148	**Day 150**	8.68E-07	4.49E-07

Table C.9. The volume required to store Cl^- in pore fluid in the 2nd osmotic cycle

Circulation Start (From)	**Circulation End (To)**	**M_{Stored} (kg)**	**'Average' concentration in pore fluid (kg/m^3)**	**V_{Cl} (m^3)**
Day 22.5	**Day 24.6**	1.98E-06	0.324	6.11E-06
Day 24.6	**Day 26.5**	1.96E-06	0.324	6.04E-06
Day 26.5	**Day 27.9**	1.87E-06	0.324	5.78E-06
Day 27.9	**Day 29.5**	1.79E-06	0.324	5.52E-06
Day 29.5	**Day 30.9**	1.58E-06	0.324	4.89E-06
Day 30.9	**Day 32.7**	1.41E-06	0.324	4.37E-06
Day 32.7	**Day 34.4**	1.32E-06	0.324	4.07E-06
Day 34.4	**Day 36.4**	1.28E-06	0.324	3.95E-06
Day 36.4	**Day 37.9**	1.25E-06	0.324	3.87E-06
Day 37.9	**Day 39.6**	1.24E-06	0.324	3.84E-06
Day 39.6	**Day 40.9**	1.25E-06	0.324	3.85E-06
Day 40.9	**Day 42.8**	1.24E-06	0.324	3.81E-06
Day 42.8	**Day 44.8**	1.24E-06	0.324	3.84E-06
Day 44.8	**Day 46.8**	1.26E-06	0.324	3.90E-06
Day 46.8	**Day 48.7**	1.30E-06	0.324	4.03E-06
Day 48.7	**Day 50.6**	1.37E-06	0.324	4.22E-06
Day 50.6	**Day 52.4**	1.41E-06	0.323	4.36E-06
Day 52.4	**Day 54.4**	1.42E-06	0.323	4.41E-06
Day 54.4	**Day 56.5**	1.45E-06	0.323	4.49E-06
Day 56.5	**Day 58.3**	1.48E-06	0.323	4.59E-06
Day 58.3	**Day 60.4**	1.48E-06	0.323	4.60E-06
Day 60.4	**Day 61.8**	1.50E-06	0.323	4.64E-06
Day 61.8	**Day 63.6**	1.54E-06	0.323	4.77E-06
Day 63.6	**Day 65.6**	1.57E-06	0.323	4.88E-06
Day 65.6	**Day 67.5**	1.61E-06	0.323	5.00E-06
Day 67.5	**Day 69.4**	1.64E-06	0.323	5.10E-06

Table C.10. The volume required to store Cl^- in pore fluid in the 3rd osmotic cycle

Circulation Start (From)	Circulation End (To)	M_{Stored} (kg)	'Average' concentration in pore fluid (kg/m^3)	V_{Cl} (m^3)
Day 85.7	**Day 87.8**	1.78E-06	0.403	4.43E-06
Day 87.8	**Day 89.5**	1.92E-06	0.403	4.77E-06
Day 89.5	**Day 91.5**	2.02E-06	0.403	5.00E-06
Day 91.5	**Day 93.6**	2.13E-06	0.403	5.29E-06
Day 93.6	**Day 95.7**	2.25E-06	0.401	5.60E-06
Day 95.7	**Day 97.5**	2.34E-06	0.401	5.84E-06
Day 97.5	**Day 99.4**	2.38E-06	0.401	5.94E-06
Day 99.4	**Day 102**	2.36E-06	0.401	5.89E-06
Day 102	**Day 104**	2.30E-06	0.401	5.74E-06
Day 104	**Day 106**	2.27E-06	0.401	5.67E-06
Day 107	**Day 108**	2.26E-06	0.401	5.63E-06
Day 108	**Day 110**	2.24E-06	0.403	5.57E-06
Day 110	**Day 112**	2.23E-06	0.403	5.54E-06
Day 112	**Day 114**	2.30E-06	0.403	5.71E-06
Day 114	**Day 115**	2.31E-06	0.402	5.75E-06
Day 115	**Day 117**	2.39E-06	0.402	5.94E-06
Day 117	**Day 119**	2.43E-06	0.402	6.05E-06
Day 119	**Day 121**	2.44E-06	0.402	6.07E-06
Day 121	**Day 122**	2.35E-06	0.402	5.83E-06
Day 122	**Day 124**	2.27E-06	0.402	5.64E-06
Day 124	**Day 126**	2.21E-06	0.402	5.50E-06
Day 126	**Day 127**	2.17E-06	0.402	5.38E-06
Day 127	**Day 129**	2.17E-06	0.402	5.40E-06
Day 129	**Day 131**	2.18E-06	0.402	5.41E-06
Day 131	**Day 133**	2.20E-06	0.402	5.46E-06
Day 133	**Day 134**	2.20E-06	0.402	5.47E-06
Day 134	**Day 136**	2.25E-06	0.400	5.62E-06
Day 136	**Day 138**	2.31E-06	0.399	5.80E-06
Day 138	**Day 140**	2.36E-06	0.399	5.91E-06
Day 140	**Day 141**	2.36E-06	0.399	5.93E-06
Day 141	**Day 143**	2.37E-06	0.399	5.94E-06
Day 143	**Day 145**	2.36E-06	0.397	5.94E-06
Day 145	**Day 146**	2.40E-06	0.397	6.05E-06
Day 146	**Day 148**	2.45E-06	0.397	6.17E-06

Circulation Start (From)	Circulation End (To)	M_{Stored} (kg)	'Average' concentration in pore fluid (kg/m^3)	V_{Cl} (m^3)
Day 148	**Day 150**	2.51E-06	0.397	6.33E-06

Table C.11. The cumulative change of cations stored amount involved in cation exchange in the 2nd osmotic cycle

Circulation Start (From)	Circulation End (To)	K^+ (Eq)	Na^+ (Eq)	Mg^{2+} (Eq)	Ca^{2+} (Eq)	Fe^{3+} (Eq)	Net (Eq)
Day 22.5	**Day 24.6**	-7.7E-06	-2.6E-07	-1.5E-07	-4.5E-06	-2.2E-07	-1.3E-05
Day 24.6	**Day 26.5**	-3.6E-06	-2.6E-07	-4.8E-07	-9.6E-06	-5.0E-07	-1.4E-05
Day 26.5	**Day 27.9**	7.5E-07	2.7E-07	-1.6E-06	-1.6E-05	-7.6E-07	-1.7E-05
Day 27.9	**Day 29.5**	4.6E-06	4.7E-07	-2.6E-06	-2.3E-05	-1.1E-06	-2.2E-05
Day 29.5	**Day 30.9**	8.3E-06	-1.3E-06	-3.5E-06	-3.0E-05	-1.4E-06	-2.8E-05
Day 30.9	**Day 32.7**	1.2E-05	-1.9E-06	-4.4E-06	-3.8E-05	-2.2E-06	-3.4E-05
Day 32.7	**Day 34.4**	1.5E-05	-3.0E-06	-5.1E-06	-4.5E-05	-2.9E-06	-4.0E-05
Day 34.4	**Day 36.4**	2.1E-05	-4.6E-06	-5.8E-06	-5.3E-05	-3.3E-06	-4.5E-05
Day 36.4	**Day 37.9**	2.6E-05	-5.7E-06	-6.1E-06	-5.8E-05	-4.0E-06	-4.9E-05
Day 37.9	**Day 39.6**	3.1E-05	-7.6E-06	-6.4E-06	-6.4E-05	-4.7E-06	-5.2E-05
Day 39.6	**Day 40.9**	3.5E-05	-9.4E-06	-6.6E-06	-6.9E-05	-5.4E-06	-5.5E-05
Day 40.9	**Day 42.8**	4.0E-05	-1.1E-05	-7.0E-06	-7.4E-05	-6.0E-06	-5.8E-05
Day 42.8	**Day 44.8**	4.5E-05	-1.3E-05	-7.3E-06	-7.9E-05	-6.9E-06	-6.1E-05
Day 44.8	**Day 46.8**	5.0E-05	-1.5E-05	-7.3E-06	-8.4E-05	-7.6E-06	-6.4E-05
Day 46.8	**Day 48.7**	5.5E-05	-1.5E-05	-7.0E-06	-8.9E-05	-8.4E-06	-6.4E-05
Day 48.7	**Day 50.6**	5.9E-05	-1.6E-05	-6.9E-06	-9.3E-05	-9.2E-06	-6.6E-05
Day 50.6	**Day 52.4**	6.3E-05	-1.8E-05	-6.5E-06	-9.7E-05	-1.0E-05	-6.9E-05
Day 52.4	**Day 54.4**	6.7E-05	-2.0E-05	-6.1E-06	-1.0E-04	-1.1E-05	-7.1E-05
Day 54.4	**Day 56.5**	7.0E-05	-2.0E-05	-6.0E-06	-1.1E-04	-1.2E-05	-7.4E-05
Day 56.5	**Day 58.3**	7.2E-05	-2.0E-05	-6.1E-06	-1.1E-04	-1.2E-05	-7.9E-05
Day 58.3	**Day 60.4**	7.5E-05	-2.0E-05	-6.1E-06	-1.2E-04	-1.3E-05	-8.2E-05
Day 60.4	**Day 61.8**	7.8E-05	-2.0E-05	-6.1E-06	-1.2E-04	-1.4E-05	-8.5E-05
Day 61.8	**Day 63.6**	8.1E-05	-1.9E-05	-5.9E-06	-1.3E-04	-1.4E-05	-8.7E-05
Day 63.6	**Day 65.6**	8.4E-05	-1.8E-05	-5.9E-06	-1.3E-04	-1.5E-05	-8.9E-05
Day 65.6	**Day 67.5**	8.6E-05	-1.8E-05	-5.8E-06	-1.4E-04	-1.6E-05	-9.2E-05
Day 67.5	**Day 69.4**	8.9E-05	-1.8E-05	-5.8E-06	-1.4E-04	-1.7E-05	-9.6E-05

Table C.12. The cumulative change of cations stored amount involved in cation exchange in the 3rd osmotic cycle

Circulation Start (From)	Circulation End (To)	K^+ (Eq)	Na^+ (Eq)	Mg^{2+} (Eq)	Ca^{2+} (Eq)	Fe^{3+} (Eq)	Net (Eq)
Day 85.7	**Day 87.8**	-5.1E-06	3.5E-06	-2.5E-06	-1.2E-05	-6.3E-07	-1.6E-05
Day 87.8	**Day 89.5**	3.5E-06	4.6E-06	-3.1E-06	-2.1E-05	-8.3E-07	-1.7E-05
Day 89.5	**Day 91.5**	1.3E-05	6.0E-06	-4.0E-06	-3.3E-05	-1.1E-06	-1.9E-05
Day 91.5	**Day 93.6**	2.1E-05	7.9E-06	-4.9E-06	-4.5E-05	-1.6E-06	-2.3E-05
Day 93.6	**Day 95.7**	2.8E-05	1.1E-05	-5.8E-06	-5.7E-05	-1.9E-06	-2.6E-05
Day 95.7	**Day 97.5**	3.5E-05	1.2E-05	-5.7E-06	-6.7E-05	-2.2E-06	-2.8E-05
Day 97.5	**Day 99.4**	4.1E-05	1.2E-05	-6.2E-06	-7.7E-05	-2.2E-06	-3.2E-05
Day 99.4	**Day 102**	4.8E-05	1.3E-05	-7.2E-06	-8.7E-05	-2.4E-06	-3.6E-05
Day 102	**Day 104**	5.5E-05	1.2E-05	-7.9E-06	-9.9E-05	-2.8E-06	-4.2E-05
Day 104	**Day 106**	6.2E-05	9.2E-06	-9.1E-06	-1.1E-04	-3.1E-06	-4.9E-05
Day 107	**Day 108**	6.9E-05	5.8E-06	-9.2E-06	-1.2E-04	-3.7E-06	-5.4E-05
Day 108	**Day 110**	7.7E-05	3.0E-06	-9.5E-06	-1.2E-04	-4.1E-06	-5.8E-05
Day 110	**Day 112**	8.4E-05	-3.4E-09	-9.6E-06	-1.3E-04	-4.5E-06	-6.3E-05
Day 112	**Day 114**	9.1E-05	-4.8E-06	-9.8E-06	-1.4E-04	-4.8E-06	-6.9E-05
Day 114	**Day 115**	9.8E-05	-9.0E-06	-9.8E-06	-1.5E-04	-5.2E-06	-7.5E-05
Day 115	**Day 117**	1.0E-04	-1.4E-05	-9.5E-06	-1.6E-04	-5.4E-06	-8.2E-05
Day 117	**Day 119**	1.1E-04	-1.8E-05	-9.5E-06	-1.6E-04	-5.5E-06	-8.7E-05
Day 119	**Day 121**	1.2E-04	-2.2E-05	-9.1E-06	-1.7E-04	-5.8E-06	-9.2E-05
Day 121	**Day 122**	1.2E-04	-2.8E-05	-8.6E-06	-1.8E-04	-6.2E-06	-9.7E-05
Day 122	**Day 124**	1.3E-04	-3.3E-05	-8.9E-06	-1.9E-04	-6.5E-06	-1.1E-04
Day 124	**Day 126**	1.3E-04	-3.8E-05	-8.5E-06	-1.9E-04	-6.8E-06	-1.1E-04
Day 126	**Day 127**	1.4E-04	-4.2E-05	-8.1E-06	-2.0E-04	-7.1E-06	-1.2E-04
Day 127	**Day 129**	1.5E-04	-4.7E-05	-8.0E-06	-2.1E-04	-7.6E-06	-1.2E-04
Day 129	**Day 131**	1.5E-04	-5.3E-05	-7.4E-06	-2.2E-04	-7.8E-06	-1.3E-04
Day 131	**Day 133**	1.6E-04	-5.8E-05	-6.8E-06	-2.2E-04	-8.3E-06	-1.4E-04
Day 133	**Day 134**	1.7E-04	-6.5E-05	-6.2E-06	-2.3E-04	-8.6E-06	-1.4E-04
Day 134	**Day 136**	1.7E-04	-6.9E-05	-5.5E-06	-2.4E-04	-9.3E-06	-1.5E-04
Day 136	**Day 138**	1.8E-04	-7.4E-05	-5.3E-06	-2.5E-04	-1.0E-05	-1.6E-04
Day 138	**Day 140**	1.9E-04	-8.0E-05	-4.9E-06	-2.5E-04	-1.1E-05	-1.6E-04
Day 140	**Day 141**	1.9E-04	-8.4E-05	-4.3E-06	-2.6E-04	-1.1E-05	-1.7E-04
Day 141	**Day 143**	2.0E-04	-9.0E-05	-4.1E-06	-2.7E-04	-1.2E-05	-1.8E-04
Day 143	**Day 145**	2.1E-04	-9.5E-05	-3.9E-06	-2.8E-04	-1.3E-05	-1.8E-04
Day 145	**Day 146**	2.1E-04	-1.0E-04	-3.1E-06	-2.8E-04	-1.3E-05	-1.8E-04
Day 146	**Day 148**	2.2E-04	-1.0E-04	-2.1E-06	-2.9E-04	-1.4E-05	-1.8E-04

Circulation Start (From)	Circulation End (To)	K^+ (Eq)	Na^+ (Eq)	Mg^{2+} (Eq)	Ca^{2+} (Eq)	Fe^{3+} (Eq)	Net (Eq)
Day 148	**Day 150**	2.3E-04	-1.1E-04	-1.2E-06	-2.9E-04	-1.5E-05	-1.8E-04

APPENDIX D: SENSITIVITY ANALYSES

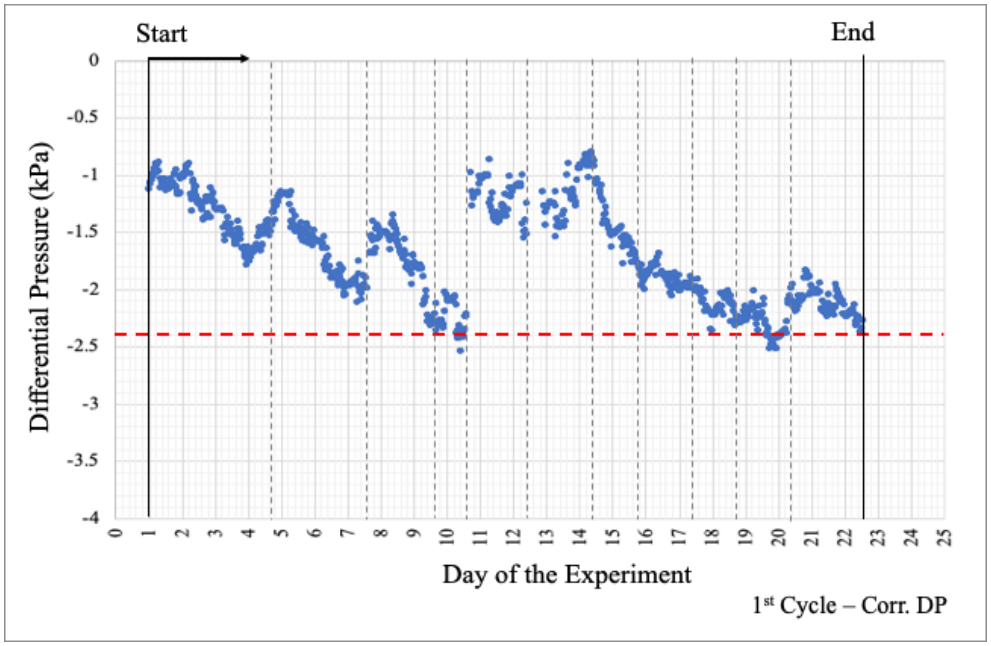

Figure D.1. Corrected DP variation during the 1st osmotic cycle (initial V_w assumed to be 1.0 $\times 10^{-5}$ m^3)

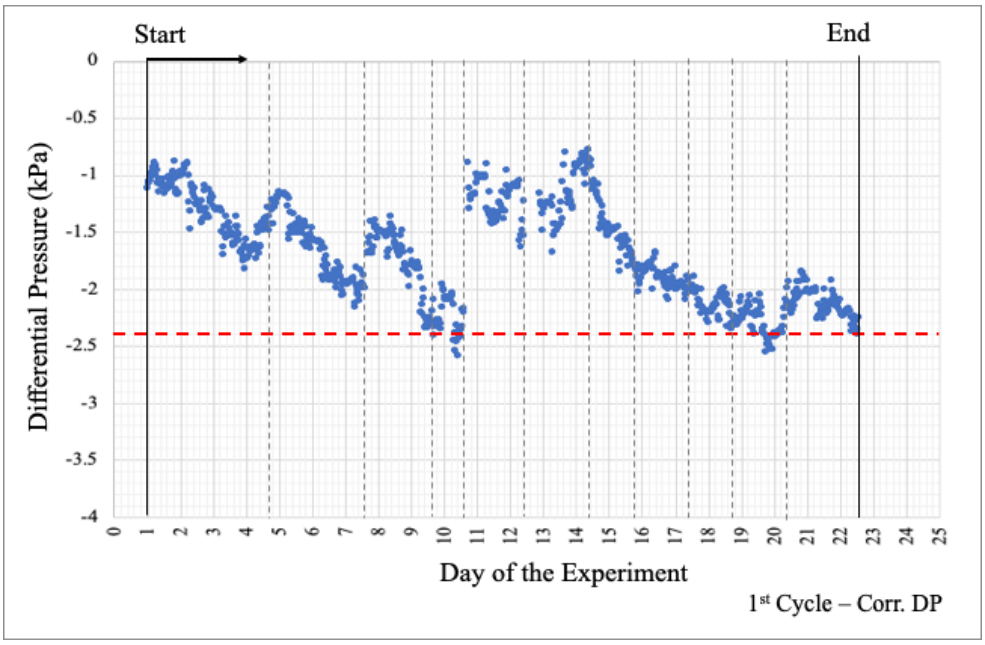

Figure D.2. Corrected DP variation during the 1st osmotic cycle (initial V_w assumed to be 1.4 $\times 10^{-5}$ m^3)

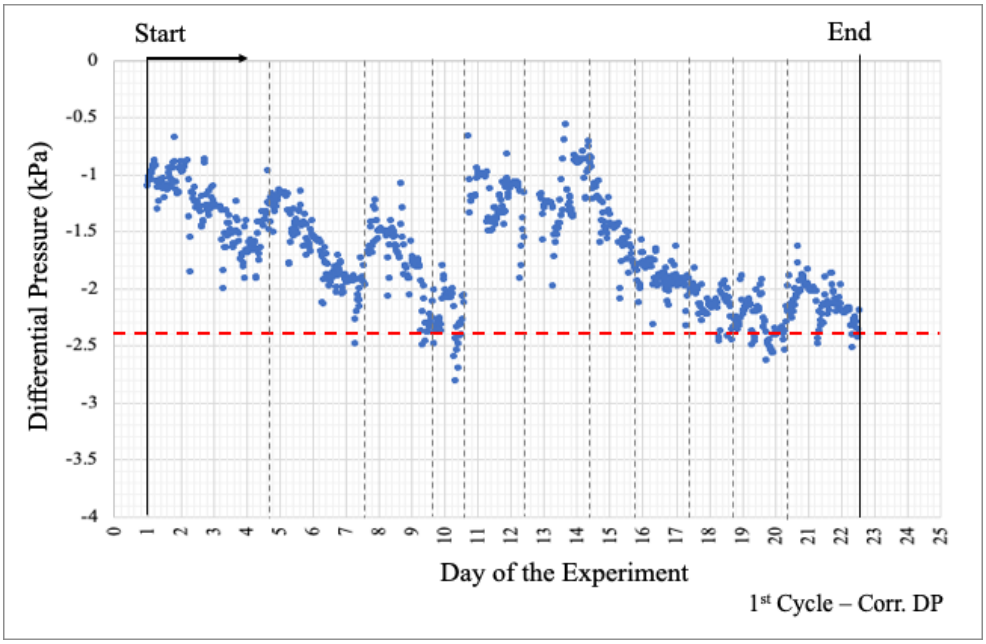

Figure D.3. Corrected DP variation during the 1st osmotic cycle (initial V_w assumed to be 2.0 $\times 10^{-5}$ m^3)

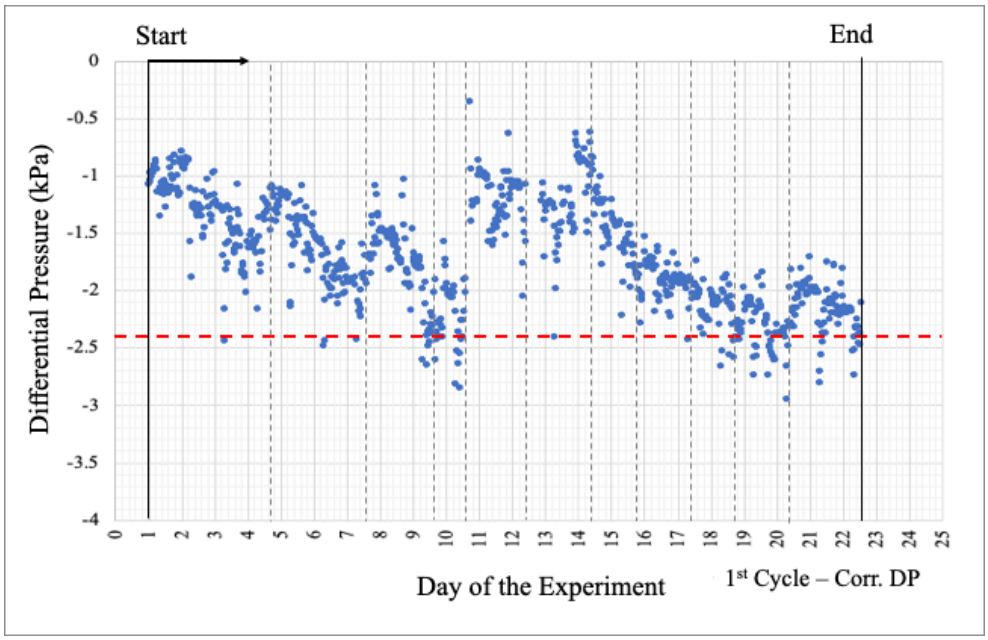

Figure D.4. Corrected DP variation during the 1st osmotic cycle (initial V_w assumed to be 3.0 $\times 10^{-5}$ m^3)

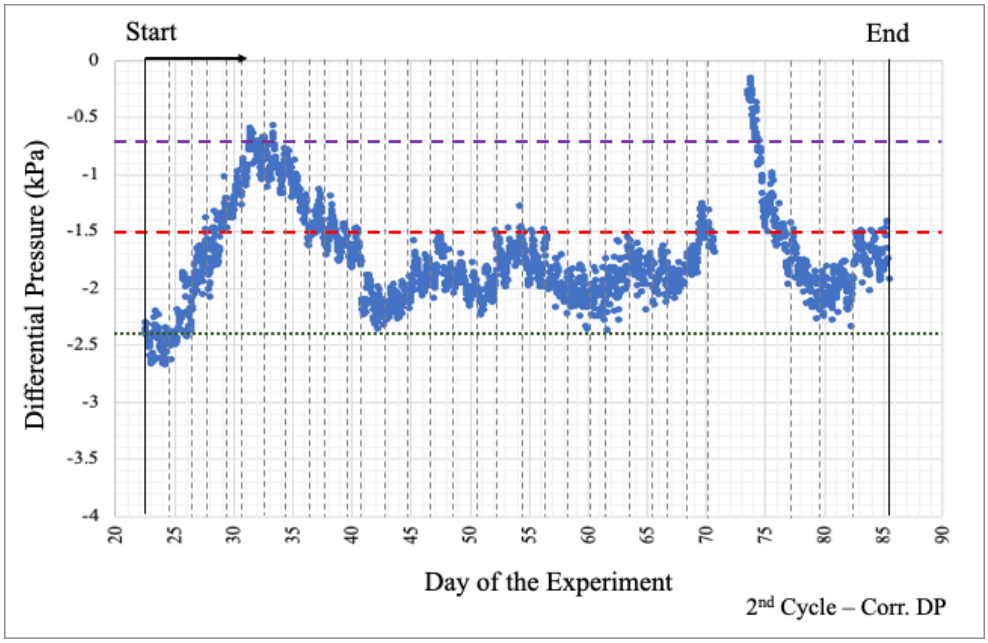

Figure D.5. Corrected DP variation during the 2nd osmotic cycle (initial V_w assumed to be 1.0 $\times 10^{-5}$ m^3)

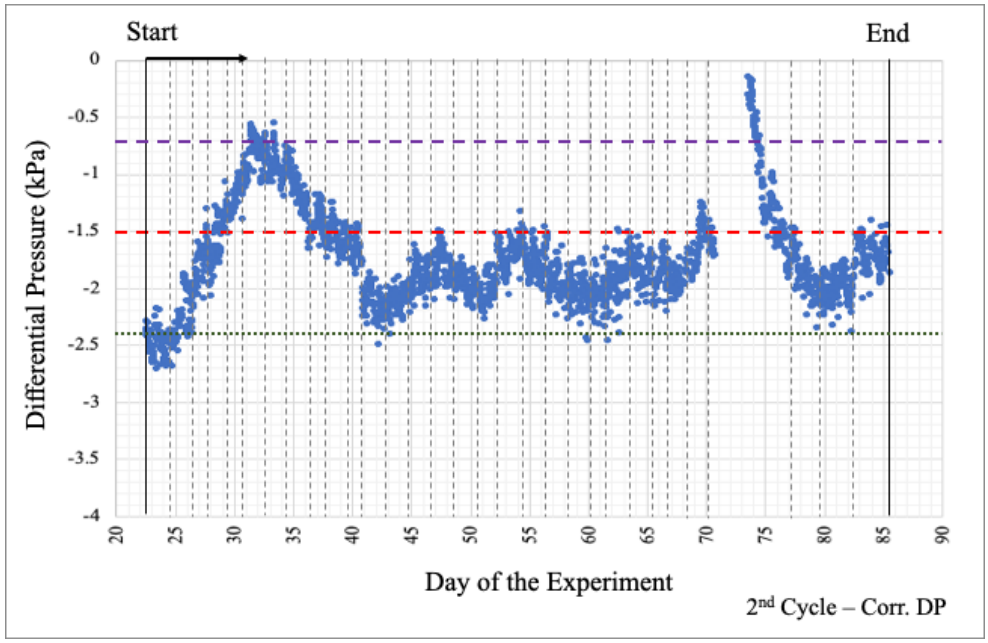

Figure D.6. Corrected DP variation during the 2nd osmotic cycle (initial V_w assumed to be 1.4 $\times 10^{-5}$ m^3)

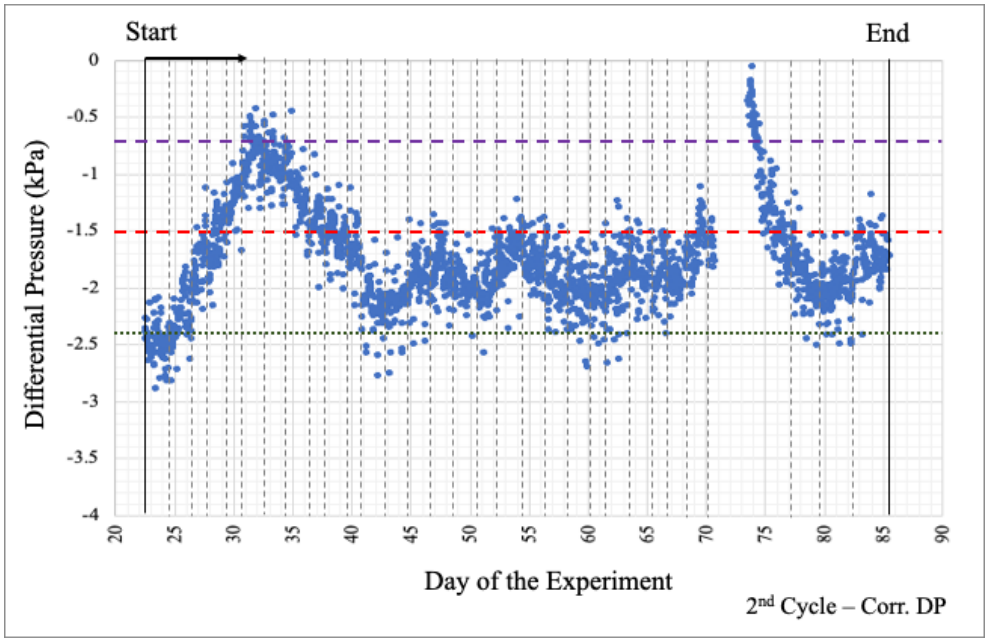

Figure D.7. Corrected DP variation during the 2nd osmotic cycle (initial V_w assumed to be 2.0 × 10^{-5} m^3)

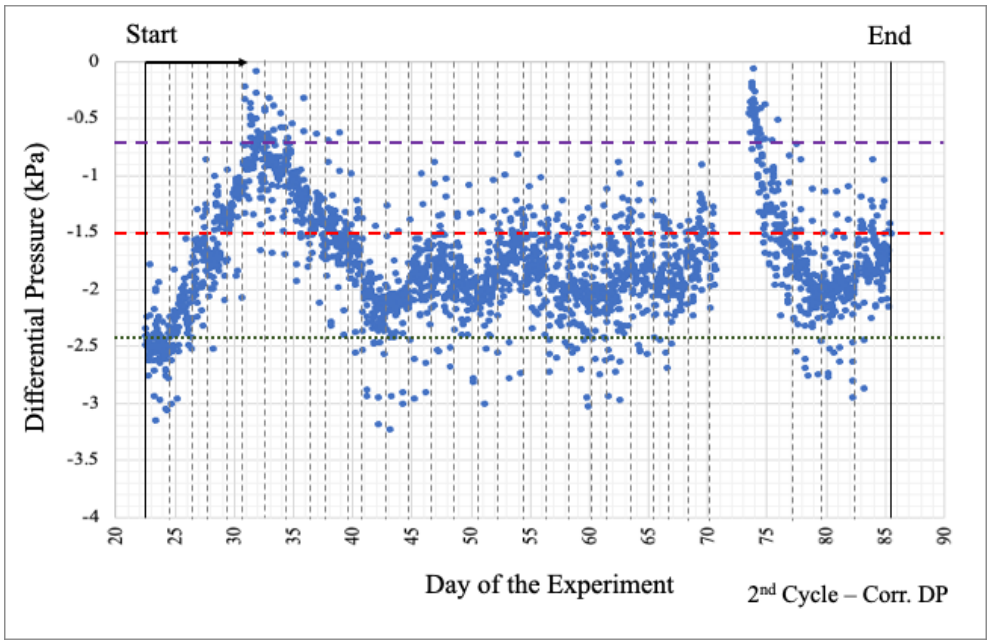

Figure D.8. Corrected DP variation during the 2nd osmotic cycle (initial V_w assumed to be 3.0 × 10^{-5} m^3)

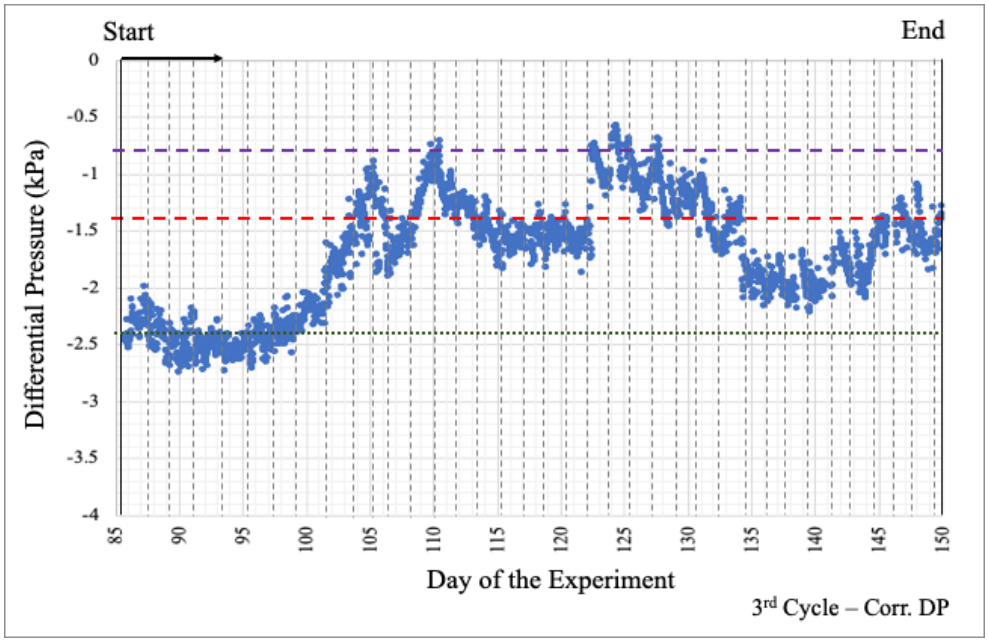

Figure D.9. Corrected DP variation during the 3rd osmotic cycle (initial V_w assumed to be 1.0 $\times 10^{-5}$ m^3)

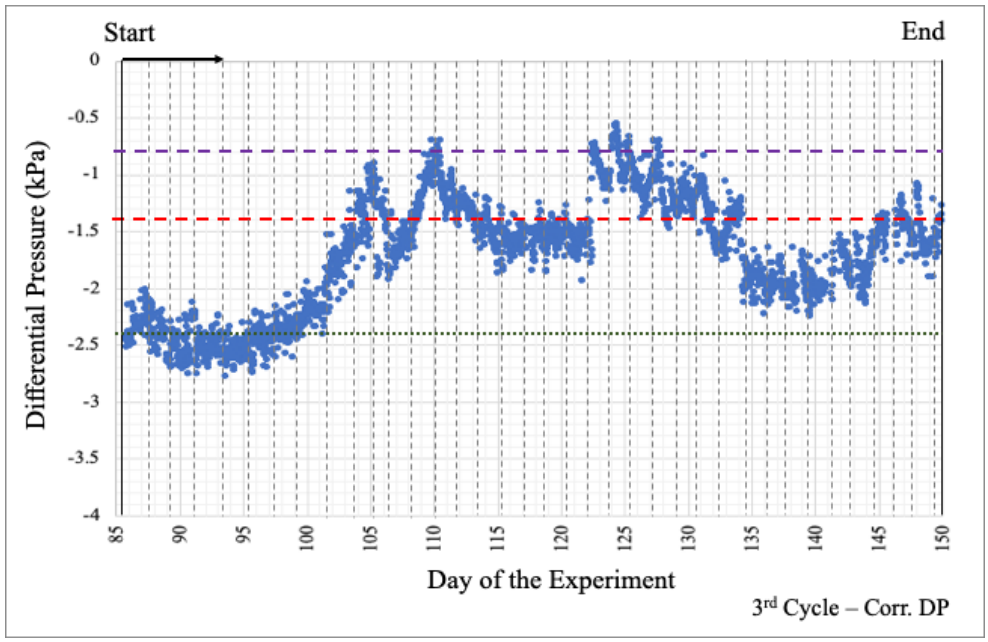

Figure D.10. Corrected DP variation during the 3rd osmotic cycle (initial V_w assumed to be 1.4 $\times 10^{-5}$ m^3)

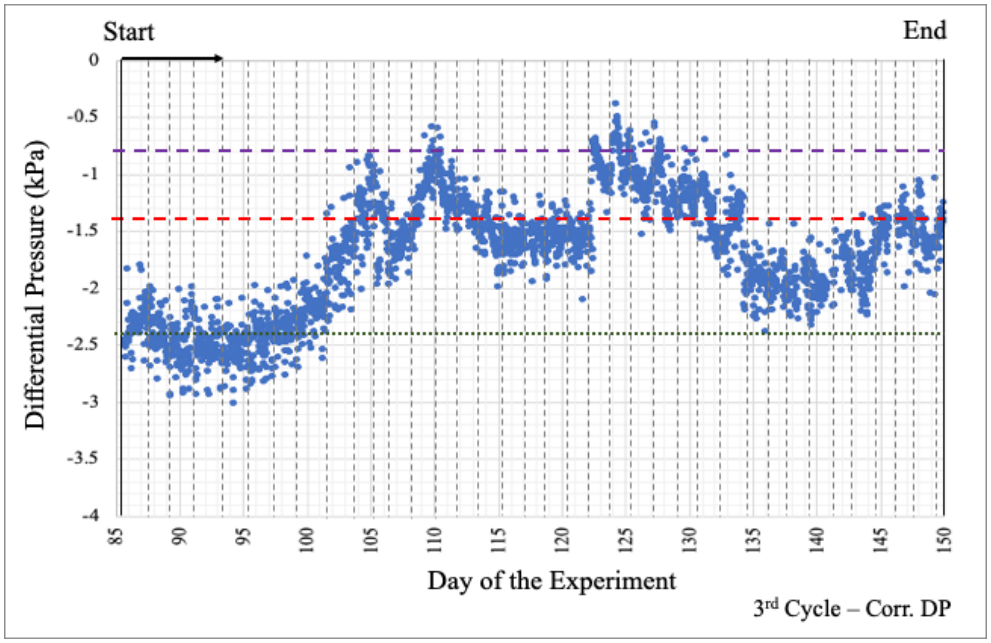

Figure D.11. Corrected DP variation during the 3rd osmotic cycle (initial V_w assumed to be 2.0×10^{-5} m^3)

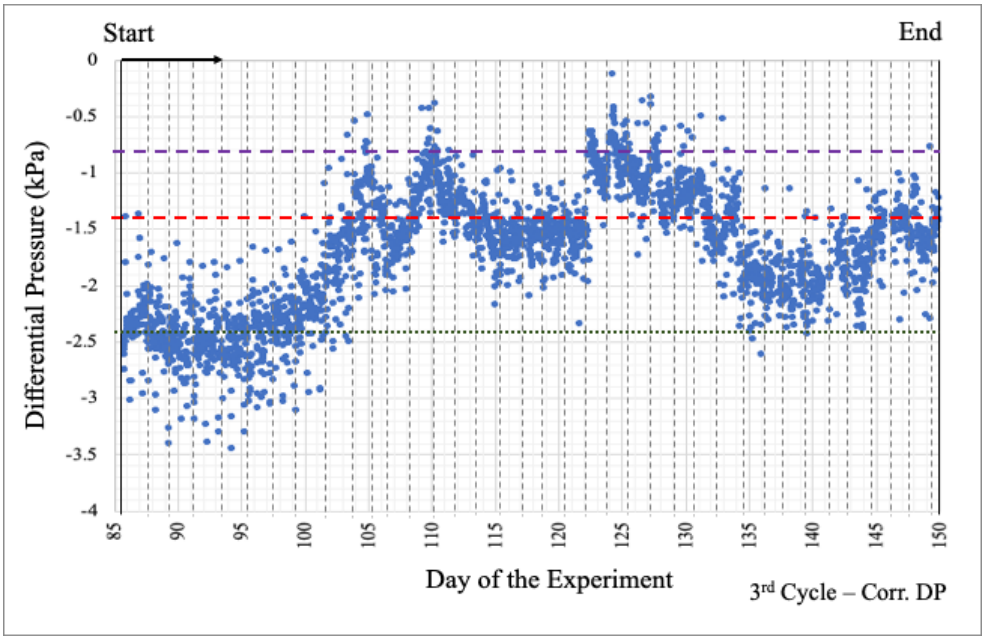

Figure D.12. Corrected DP variation during the 3rd osmotic cycle (initial V_w assumed to be 3.0×10^{-5} m^3)